UCLouvain
École polytechnique de Louvain

Institute of Condensed Matter and Nanosciences
Bio- and Soft Matter

# Nanostructured extracellular matrix-like biointerfaces

Damien LEFEVRE

Thesis submitted in fulfilment of the requirements for the Ph.D. Degree in Engineering Sciences

Thesis Committee

| | |
|---|---|
| Prof. Sophie Demoustier (Co-supervisor) | *UCLouvain/IMCN, Belgium* |
| Prof. Christine Dupont-Gillain (Co-supervisor) | *UCLouvain/IMCN, Belgium* |
| Prof. Bernard Knoops | *UCLouvain/IBST, Belgium* |
| Dr. Etienne Ferain | *UCLouvain/IMCN, Belgium* |
| Prof. Christine Jérôme | *ULiège/CERM, Belgium* |
| Prof. Deepak Kalaskar | *University College London, UK* |
| Prof. Jean-François Gohy (Chair) | *UCLouvain/IMCN, Belgium* |

Louvain-la-Neuve, 2020

# Acknowledgements

# Remerciements

Mes premiers remerciements vont à mes promotrices, les professeures Sophie Demoustier et Christine Dupont, qui ont porté ce projet depuis ses fondements jusqu'à son aboutissement. Je leur dois d'avoir su déceler et entretenir en moi, depuis mon mémoire jusqu'à la fin de ma thèse, l'attrait pour la recherche scientifique. Je leur dois également d'avoir eu confiance en ma capacité à développer ce projet aux multiples facettes et à en assumer les exigences. J'aime à penser qu'une relation de confiance réciproque s'est nouée depuis le mémoire et ne s'est jamais démentie par la suite. C'est donc avec une grande autonomie balisée et une liberté guidée que j'ai l'impression d'avoir parcouru le chemin parfois ardu de la thèse. Je les remercie d'avoir infusé nos réunions et autres discussions plus informelles de leurs nombreuses connaissances, de leur expérience et de leur grande culture scientifique. Outre la qualité de leur encadrement scientifique, j'aimerais mettre en avant leurs grandes qualités humaines. Elles ont toujours fait preuve d'une grande humanité et d'une grande capacité d'écoute à mon égard et je ne prends aucun risque à affirmer que ce ressenti prévaut largement au sein de leurs équipes. Savoir gérer une équipe, c'est pouvoir s'adapter à autant de caractères particuliers et accorder son encadrement aux besoins de chaque individu, afin que chacun puisse s'épanouir dans la réalisation de son travail. Cela restera une des nombreuses grandes qualités de mes deux promotrices.

I would like to thank all the members of the jury, the professors Jean-François Gohy, Christine Jérôme, Deepak Kalaskar, Bernard Knoops and Dr. Etienne Ferain for having accepted to review this work. I particularly would like to thank Prof. Deepak Kalaskar and Dr. Etienne Ferain for being active members of my thesis committee and for the precious advice which they provided on the occasion of my confirmation.

Je remercie vivement le Dr. Etienne Ferain et it4ip de m'avoir fourni les templates nanoporeux nécessaires à la réalisation de ce travail.

Je remercie le professeur Bernard Knoops ainsi que toute son équipe pour m'avoir accueilli au sein de leur laboratoire afin que j'y mène une grande partie des travaux cellulaires présentés dans ce manuscrit. Je remercie en particulier Sarah Becker pour avoir répondu à bons nombres de mes interrogations de novice en culture cellulaire. Je remercie également Sara Mauquoy pour la gentillesse et le sérieux avec lesquels elle m'aura prodigué une formation accélérée en bonnes pratiques de culture cellulaire.

Je voudrais remercier également Dr. Jessem Landoulsi et Dr. Elodie Colaço pour la fructueuse collaboration que nous avons pu mener dans le cadre de l'obtention de nanostructures biomimétiques minéralisées par voir biologique. Je les remercie également pour leur expertise dans les mesures de mobilité électrophorétique.

Je remercie le professeur Bernard Nysten pour, entre autres, sa connaissance pointue dans le domaine de l'AFM dont il m'aura fait bénéficier à de nombreuses reprises. Je le remercie en particulier pour l'aide apportée dans le design des expériences de nanoindentation ainsi que dans l'interprétation des résultats.

Je remercie l'ensemble des académiques rattachés à l'institut IMCN au sein du bâtiment Boltzmann : les professeur(e)s Luc Piraux, Alain Jonas, Evelyne van Ruymbeke, Christian Bailly, Karine Glinel pour m'avoir ouvert les portes de leur laboratoire et fait bénéficier de leurs connaissances. Je remercie en particulier les professeurs Alain Jonas et Karine Glinel de m'avoir permis de réaliser certaines expériences au sein de leur laboratoire de culture cellulaire.

En plus de 6 ans de thèse, j'aurais eu la chance de côtoyer un grand nombre de personnalités au sein des différentes unités de l'institut. Je tiens donc à saluer Amir, Jun, Quentin, Jeremy, Vivien, Claire, Flavio, Hamid, Vincent, Prakash, Anitha, Ronggang, Tabassum, Jie, Qian, Nassima, Imen, Imane, Aurélie, Wanlin, Sashi, Varvara, Elena, Tristan, Naïma, Waël, Pascal, Tilia, Jean-François, Cédric, Sara, Gilles, Marie, Aurélien, Simon, Mirasbek, Bruno.

Je remercie chaleureusement les secrétaires Aurore Becquevort, Anne Bouchat ainsi que les comptables Claire Umutoni, Luc Coquillart et Rose-Anne Jacob pour leur aide dans la gestion des tâches administratives et des commandes, tout autant que pour leur bonne humeur et sympathie.

J’adresse un grand merci à Pascale Lipnik pour son expérience dans l’utilisation du TEM et du microtome ainsi que pour sa sympathie et les nombreuses discussions que j’aurai eu avec elle. Merci également à Sabine Bebelman pour son expérience dans la spectroscopie infrarouge et Raman. Merci également pour ta gentillesse et ta sympathie.

Je remercie personnellement Cécile D’Haese pour son aide précieuse dans la mise en œuvre des expériences AFM. Ma maladresse lui sera éternellement reconnaissante d’avoir, à de nombreuses reprises, fixé et démonté les onéreuses pointes AFM sans jamais les casser ! Plus sérieusement, je souhaite la remercier pour sa bonne humeur, sa gentillesse ainsi que pour les nombreuses activités qu’elle a organisées.

Un grand merci à Yasmine Adriaensen pour l’encadrement des labos didactiques au cours de mes années d’étude ainsi que pour m’avoir formé à la QCM-D.

Je tiens également à remercier Delphine Magnin pour l’aide qu’elle m’aura apportée dans l’usage de nombreuses techniques, parmi lesquelles le SEM/STEM, le RX, l’ellipso, … aussi bien au cours de mon mémoire que de ma thèse. Je la remercie pour son expérience, ses conseils ainsi que pour la sympathie des nombreuses conversations que j’aurai pu échanger avec elle.

Je remercie l’ensemble du TMT : Pascal van Velthem, Delphine Magnin, Naïma Salem, et Cécile d’Haese pour l’organisation de nombreuses activités ludiques et gourmandes.

J’ai eu la chance d’encadrer 5 mémorants au cours de ma thèse, que je me fais un plaisir de remercier : Anne-Claire Timmermans, John Préat, Quentin Papeloer, Juliette Louvegny et Mathieu Naudin. Merci à vous tous, j’espère vous avoir apporté au moins autant que vous m’avez apporté.

Une thèse de plus de 6 ans doublée d’un mandat d’assistanat, c’est un périple long et sinueux. Il ne faut pas nier qu’il ne s’agit pas d’un long fleuve tranquille. Telle une vie en accéléré, la thèse est constituée d’une succession de hauts et de bas qui en font la saveur. Les aléas de la recherche expérimentale font que l’on peut tutoyer tour à tour les sommets de l’exaltation et les gouffres de la déprime. L’ensemble des galères traversées, tant au cours de cette thèse qu’en dehors, auront permis de me forger un caractère empreint d’introversion mais également d’un tempérament fort, d’une grande détermination et d’une certaine indépendance d’esprit. En

cela, je remercie les épreuves passées et souhaite continuer à en extraire le positif.

J'adresse un merci tout particulier aux personnes qui m'auront côtoyé et appris à me connaître et qui auront ainsi rendu le périple de la thèse plus doux, moins ardu et plus drôle. Il faut ainsi citer l'ensemble des personnes dont j'ai eu la chance de partager le bureau et qui auront donc également eu la chance de me supporter : Aurélie, Imen, Nassima, Sabrina, Tabassum, Florian, Guillaume, Eléana, Paul.

Catherine, je te remercie pour ta bonne humeur communicative tout au long du chemin parcouru d'abord en mémoire puis en thèse. Il était toujours agréable de commencer tôt et/ou de terminer tard quand on savait qu'il y aurait quelqu'un pour discuter de tout et de rien et pour rire aussi. Je garde le souvenir d'une grande bosseuse, toujours motivée et consciencieuse, mais également toujours disponible pour écouter les autres et discuter de choses sérieuses ou futiles au détour d'une manip.

Colette, je te remercie pour ta bonne humeur, ta gentillesse et ton dévouement. Ce fut un plaisir de te côtoyer et de discuter avec toi durant ces nombreuses années.

Florian, je te remercie pour ta présence indéfectible au laboratoire et l'aide que tu auras apportée à beaucoup de tes collègues.

Anthony, un grand merci pour ton implication dans la gestion quotidienne du labo et pour l'aide que tu auras apportée à tous.

Paul, je te remercie pour ta motivation sans faille et ta sympathie. Les aléas de la recherche ne semblent avoir aucune emprise sur toi, ta capacité à abattre une quantité impressionnante de travail demeurant inchangée quoi qu'il advienne. Un grand merci pour tous tes conseils, ton implication dans la gestion quotidienne du labo, ainsi que l'aide que tu auras apportée à tous les chercheurs y travaillant. Merci également pour les discussions plus futiles et éclats de rire échangés.

Eléana, je te remercie pour ta bonne humeur, ta capacité à pouvoir discuter de tous les sujets ainsi qu'à supporter mes blagues parfois lourdes. Je salue également ta présence au sein du labo, ton implication dans la gestion quotidienne de celui-ci, ainsi que l'aide que tu auras apportée à beaucoup de ses membres.

Paul et Eléana, vous aurez largement contribué à adoucir mes dernières années de thèse. Je vous remercie vivement pour le climat de bonne humeur qui régnait dans notre bureau.

Sabrina, je te remercie pour ton amitié, ta grande capacité d'écoute, ton humour au moins aussi scabreux que le mien, tes conseils avisés, ta présence sans faille au sein du labo, ta grande motivation dans ton travail et j'en passe. Mes premières années de thèse auront été marquées par ta présence sympathique. Tout comme Eléana, Paul et Catherine, tu es l'une des personnes avec qui il est possible de discuter des sujets les plus sérieux comme des plus drôles et futiles. Tout comme eux, ta capacité à être extrêmement consciencieuse dans ton travail tout en restant humble et modeste en ayant toujours le mot pour rire, fait de toi une amie admirable.

Je remercier chaleureusement mes amis de longue date ainsi que les amis de mes amis que j'ai la chance de côtoyer et qui rendent ma vie plus douce et pimentée à la fois : Loïc, Ronny, Maud, Anthony, Guillaume R., Guillaume S., Sébastien, Hervé, Thibaud, François F., Aurélio, Jennifer, Aurore, Baptiste. Merci de me soutenir et de me changer si agréablement les idées.

Je remercie mes compagnons à quatre pattes pour les pauses câlins impromptues : Fidji et Félicie, Chouchen et Blanco.

Enfin, j'aimerais remercier ma famille de m'avoir toujours soutenu et encouragé. Je pense bien fort à vous : papa, Chantal, mamy, marraine, Solenne, Pascal, mamy Jeanine, Roger.

En particulier, je souhaite remercier de tout cœur mon père, ma grand-mère et ma marraine, à qui je dois tout. Vous êtes, chacun, des modèles d'intégrité, de courage, de travail acharné, de force, et d'abnégation. J'espère que vous continuerez longtemps de me guider.

# Author contributions

The author contributed to the following papers :

- Saghazadeh, S., S. Zhang, D. Lefèvre, A. LeBeulze, A.M. Jonas & S. Demoustier-Champagne (2015) Universal Method to Transfer Membrane-Templated Nano-Objects to Aqueous Solutions. *Langmuir*, *31* (26), 7264-7273.
- Lefèvre, D., J. Louvegny, M. Naudin, E. Ferain, C. Dupont-Gillain & S. Demoustier-Champagne (2018) Biofunctionalized and self-supported polypyrrole frameworks as nanostructured ECM-like biointerfaces. *RSC advances*, *8* (41), 22932-22943.
- Vander Straeten, A., D. Lefèvre, S. Demoustier-Champagne & C. Dupont-Gillain. Layer-by-Layer Protein-Polyelectrolyte Assemblies. [Submitted].
- Colaço, E., D. Lefèvre, E. Maisonhaute, D. Brouri, C. Guibert, C. Dupont-Gillain, K. El Kirat, S. Demoustier-Champagne & J. Landoulsi. Confined enzyme multilayers produce highly crystalline mineralized nanostructures. [Submitted].

The author participated to the following international scientific events:

- Oral presentation at the World Biomaterials Congress (WBC), Montreal, Canada, May 2016.
- Oral presentation at the Advanced Materials for Biomedical Applications (AMBA) conference, Ghent, Belgium, September 2017.

# Abstract

The scientific community is gathering an ever-growing collection of insights into how cell fate is finely tuned in *vivo* by a complex interplay of topographical, mechanical and chemical stimuli provided through the extracellular matrix (ECM). This triggers the wish to master and replicate these cell-influencing factors. Indeed, being able to understand and control the complex mechanisms of morphogenesis, cell proliferation and differentiation found in Nature, would greatly advance technologies such as cell therapy, tissue engineering and regenerative medicine. Successful outcomes of these strategies based on the regulation and modification of cell processes are intimately linked to our capacity to develop artificial cell-educative interfaces mimicking the Nature's golden standard which is ECM. As a contribution to this challenge, we have synthesized original interfaces composed of intersected nanotubes whose structure and surface chemistry mimic that of the ECM. These ECM-like biointerfaces were synthesized *via* hard templating of biopolymers in combination with synthetic polymers or ceramic nanoparticles and subsequent dissolution of the supporting template. Whereas some of the produced biointerfaces are still lacking adequate mechanical properties for cell-based biomedical applications, other designs effectively bridge the gap between two often antagonistic factors: bioactivity and mechanical stability. In particular, matrices of intersected polypyrrole (PPy) nanotubes functionalized with a biomimetic (Collagen/Hyaluronic acid) multilayer were seeded with murine pre-osteoblast cells and observed to be cell-adhesive and to positively impact the expression of an early osteogenic marker. In addition to the projected applications as cell-influencing biomaterials, these nanostructured matrices being highly tunable and displaying a high surface area, could be useful for drug-delivery applications, biosensing or nanocatalysis.

x

# List of abbreviations

| | |
|---|---|
| **AFM** | atomic force microscopy |
| **ALP** | alkaline phosphatase |
| **AMSC(s)** | adipose-derived mesenchymal stem cell(s) |
| **BCA** | bicinchoninic acid assay |
| **BMSC(s)** | bone marrow mesenchymal stem cell(s) |
| **BSA** | bovine serum albumin |
| **Col** | collagen |
| **ECM** | extracellular matrix |
| **EDC** | 1-ethyl-3-(3-dimethylaminopropyl)carbodiimide |
| **EDX** | energy-dispersive X-ray |
| **EPM** | electrophoretic mobility |
| **ESC(s)** | embryonic stem cell(s) |
| **FAK** | focal adhesion kinase |
| **FDA** | food and drug administration |
| **Fn** | fibronectin |
| **GAG(s)** | glucosaminoglycan(s) |
| **HA** | hyaluronic acid |
| **HyAp** | hydroxyapatite |
| **IEP** | isoelectric point |
| **LbL** | layer-by-layer |
| **MSC(s)** | mesenchymal stem cell(s) |

| | |
|---|---|
| **NP(s)** | nanoparticle(s) |
| **NT(s)** | nanotube(s) |
| **OCN** | osteocalcin |
| **OPN** | osteopontin |
| **PAH** | poly(allylamine hydrochloride) |
| **PBS** | phosphate buffered saline |
| **PC** | polycarbonate |
| **PDMS** | poly(dimethylsiloxane) |
| **PE(s)** | polyelectrolyte(s) |
| **PEI** | poly(ethyleneimine) |
| **PEM** | polyelectrolyte multilayer |
| **PMMA** | poly(methylmethacrylate) |
| **PPy** | polypyrrole |
| **PSS** | poly(styrenesulfonate) |
| **Py** | pyrrole |
| **QCM-D** | Quartz crystal microbalance with dissipation monitoring |
| **RGD** | L-arginine-glycine-L-aspartic acid peptide sequence |
| **SEM** | scanning electronic microscopy |
| **s-NHS** | N-hydroxysulfosuccinimide |
| **STEM** | scanning transmission electronic microscopy |
| **TCPS** | tissue culture poly(styrene) |
| **TEM** | transmission electronic microscopy |

# List of symbols

| | |
|---|---|
| ***Ø*** | Diameter |
| ***I*** | Ionic strength |

# Table of contents

# Chapter 1

# Research context

In the contemporary context where a wide range of infectious diseases, that once used to threaten the lives of millions of individuals, have been brought under control, scientists and clinicians are left to face bigger challenges in the form of multifactorial diseases, such as genetic disorders and degenerative and chronic diseases which are prone to occur in a population with rising life expectancy. Solving such complex multifactorial issues will likely require multidisciplinary approaches and innovative technologies. The replacement of malfunctioning organs with artificial tissue-engineered constructs is likely to be part of the solution, as well as the design of new alternatives to orient and regulate the behavior of cells in the body.

Innovations of the last decades already have brought their share of advances in the supplementation of some deficient tissue functions through engineering of biomaterials and medical devices. Among those are insulin pumps, intraocular lenses, pacemakers, joint prostheses, etc. However, the treatment of more complex pathologies will probably be only attainable through the repair or replacement of dysfunctioning organs, a field of study known as **tissue engineering**, TE.

The successful development of functioning artificial tissues and organs requires that we, as scientists, work in multidisciplinary teams to first elucidate and then recapitulate the mechanisms elaborated by Nature whereby cells are taught to organize into functional tissues *in vivo.* Beyond the basic understanding of the physiological functioning of an organ, there is indeed a need to identify the key events which lead an undifferentiated mass of competent cells (i.e., multipotent **stem cells**[1]) to organize themselves and differentiate selectively into specialized tissues (i.e., the processes of **morphogenesis** and **organogenesis** whereby an organism and its constituting organs acquire their shape and function *in vivo*). This fundamental step which basically consists in observing, describing,

[1] Stem cells are cells able to both self-renew and differentiate into a range of specialized phenotypes. Multipotent cells are stem cells found in specific tissues of adult organisms and which can differentiate only in a few cell types[360].

understanding and modelling the mechanisms whereby the extracellular microenvironment (i.e, the extracellular matrix, ECM) regulates cell functions, greatly benefits from the knowledge accumulated in the fields of molecular biology, biochemistry, cellular biology and genetic engineering.

Once clearly segregated, the essential parameters guiding cell fate *in vivo* need to be recapitulated in the design of **cell-instructive materials** able to sustain basic cell processes (i.e., adhesion and proliferation) while at the same time guiding and controlling the differentiation of these cells towards the desired phenotype. The successful design of such cell-influencing biomaterials is clearly dependent on the joint progress of nanotechnology, organic chemistry, polymer and material sciences, as well as surface functionalization techniques. Provided that they are biocompatible and can encapsulate cells, such cell-instructive materials can be implanted into an organism to fulfil their mission as tissue repair or replacement, and thus play the role of **scaffolds** for tissue engineering applications.

In a pattern similar to most technological breakthroughs, the advent of **cell-educative materials** thus requires scientists to first discover and observe natural phenomena, understand them and ultimately mimic them to the benefit of mankind. The design and characterization of various cell-influencing material prototypes, to which this research project is a contribution, is thus likely to benefit the emerging field of TE and regenerative medicine. This contextual chapter will first cover the main discoveries that were made regarding the prominent influence of the immediate extracellular environment, the extracellular matrix, on cell fate *in vivo*. The principal characteristics and functions of this extracellular medium will be reviewed as well as those of two of its major components: collagen and hyaluronic acid. In a second time, various parameters regulating cell behaviour, which were isolated from the ECM will be discussed and illustrated with examples extracted from relevant studies.

## 1.1 Extracellular matrix: structure, compositions and functions

### 1.1.1 General structure and composition of the extracellular matrix

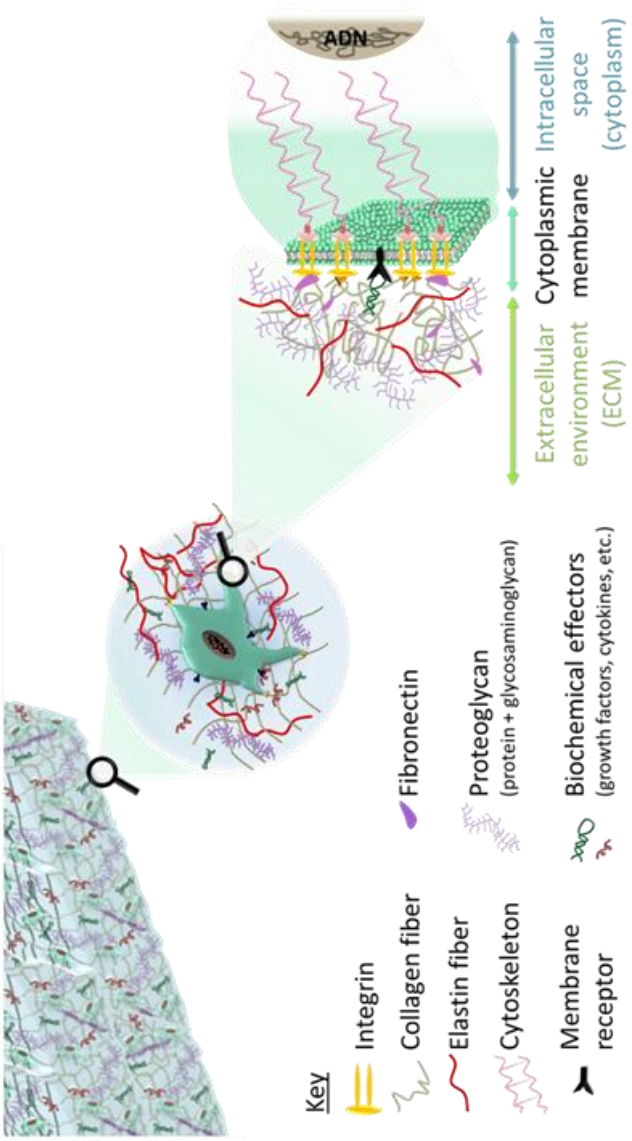


**Figure 1.1** *Schematic representation of the extracellular matrix (ECM), from the microscopic to the nanoscopic scale. [Inspired from*[1]*].*

The extracellular matrix (ECM) constitutes the native environment sheltering the cells in the body. In addition to this elemental role as mechanical support, the ECM plays a key role in collecting and transmitting a wide range of signals from and to the cells. As the platform mediating biophysical and biochemical cross-talks between the cells and their extracellular environment, the ECM plays a crucial role in tissue and organ formation and homeostasis.[2–4] Major cellular activities, including proliferation, differentiation, migration and apoptosis are actually triggered as a response to the molecular interactions with ECM effectors.[3]

The general structure of the ECM is that of an intricate 3-dimensional (3D) meshwork of fibrillar proteins interwoven within a gel of proteoglycans and glycosaminoglycans (GAGs) (*see* Figure 1.1 & 1.2). The precise composition of ECM is, however, tissue- and time-dependent as it is the combination of the cells and the ECM they are embedded in which defines the physiological properties of the tissue. For example, while the ECM of cartilage is enriched in large proteoglycans and thus highly hydrated, that of bone is highly mineralized, conferring the mechanical properties characteristic of each tissue.[2,4] The plural form *extracellular matrices* would therefore be better suited to reflect the diversity of existing extracellular media, though the singular ECM is most often used for the sake of simplicity.

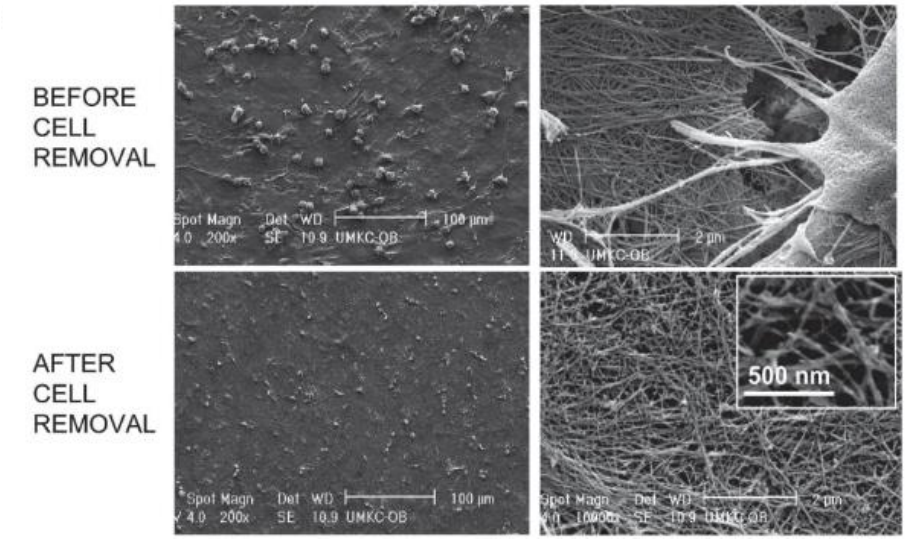


**Figure 1.2** *SEM images showing the fibrillar morphology of the native ECM produced by murine bone marrow cells, before and after the removal of cells. Left panels: low magnification. Right panels: high magnification.*[5]

Among the fibrillar proteins of the ECM are collagens (Cols) and elastin, which are members of the structural protein family as they are mainly responsible for providing tensile strength and elasticity to tissues. Other ECM-derived proteins, such as fibronectin and laminin are specialized in the anchoring of the cells to their hosting ECM and are therefore called adhesion proteins. GAGs (among which are chondroitin sulfate, heparin, hyaluronic acid, etc.), on the other hand, are long unbranched carbohydrate polymers consisting of repeating disaccharide units which mainly impart gel-like properties to the ECM thanks to their highly hydrophilic nature and present sequestered biomolecules to the hosted cells. These biomolecules are soluble biochemical effectors (growth factors, chemokines and cytokines) which are bound, stored and released by the ECM to stimulate the cells and modulate their gene expression profile.[2,6]

The nature of the external stimuli transmitted to the cells via the ECM is highly diverse: shear stresses, tensile forces, surface topography, soluble bioactive molecules, etc. These signals are transduced to the cytoskeleton and nucleus of the cell through various specific transmembrane receptors including heterodimeric integrins, receptor tyrosine kinases and phosphatases, immunoglobulin superfamily receptors, dystroglycan, and cell-surface proteoglycans.[4] Once specific binding occurs between the signalling cues and cell-surface receptors, the conveyed information is internalized by the cell through induction of complex intracellular signalling cascades which converge to regulate gene expression and ultimately establish cell phenotype and direct tissue formation, homeostasis and regeneration.[3,4]

Furthermore, ECM is not a static but rather a highly dynamic medium which is constantly degraded, remodelled and secreted by the hosted cells. The local degradation of the protein and proteoglycan components of the ECM is, for example, mediated by cell-secreted proteases, including matrix metalloproteinases (MMPs), serine proteases and hyaluronidase in order to release bioactive components and ease cell migration.[7] The flow of information between the embedded cells and their ECM is thus bidirectional, as cell behaviour is controlled by the ECM which is itself secreted and remodelled by hosted cells.[3]

### 1.1.2 Roles of the extracellular matrix *in vivo*

*a) ECM guides cell organization during morpho- and organogenesis*

The pivotal role played by the ECM during morphogenesis (i.e., the process controlling the structural organization of cells into functional tissues and organs) was mainly revealed by studies which established a clear link between mutations of genes encoding ECM macromolecules and some genetic disorders occurring both in knockout mouse models and humans (*see* Figure 1.3). For example, mice that lack the gene encoding laminin γ1 chain, the first ECM molecule to be synthesized during foetal development to serve as a matrix organizer, were found to be unable to organize a basement membrane matrix and to die before birth.[4,8] The inability to synthesize Col type I, a major component of the elastic fibers in vessel walls, was linked to the presence of lethal vascular defects in mice, leading to embryonic death following blood vessel rupture.[8,9] Similarly, the occurrence of the Ehlers-Danlos type IV syndrome in humans, causing lethal blood vessel or intestinal rupture, is associated to mutations of the gene coding for Col type III.[8] Impairment of Col type I and II synthesis respectively results in osteogenesis imperfecta (commonly called brittle bone disease) and severe chondrodysplasia, in both humans and mice.[8,10]

**Selected examples of extracellular matrix knockout mice phenotypes.**

| Gene | Phenotype |
|---|---|
| Laminin α2 | Lethal, muscular dystrophy |
| Laminin α3 | Lethal, skin blistering |
| Osteonectin/SPARC | Cataracts, osteopenia |
| Vitronectin | No phenotype |
| Fibronectin | Lethal, mesodermal and cardiovascular defects |
| Tenascin C | CNS and hematopoietic defects |
| Thrombospondin-1 | Increased vascularity, defects in lung, pancreas |
| Entactin/nidogen | Neurological defects |
| Collagen α1 (I) | Lethal, vascular defects |
| Collagen α3 (IV) | Lethal, renal failure, progressive glomerulonephritis |
| Perlecan | Lethal, cartilage defects |
| Biglycan | Osteoporosis |

CNS, central nervous system; SPARC, secreted protein acidic and rich in cysteine.

**Figure 1.3** *Examples of genetic disorders induced in knockout mouse models via selective mutation of some genes encoding ECM macromolecules.*[4]

### *b) ECM dictates the fate of multipotent cells: proliferation versus differentiation*

In addition to controlling the organization of pluripotent embryonic stem cells during early developmental stages, the ECM controls the fate of multipotent stem (i.e., cells with unlimited self-renewal and capable of differentiating into multiple phenotypes), progenitor (i.e., cells with limited self-renewal and committed to differentiate into one specific phenotype) and mature cells (i.e., fully differentiated cells) in fully developed adult organisms. The ECM maintains a balance between self-renewal and differentiation of stem cells and depending on local and temporal factors, can tilt the balance in favour of one or the other.

The bone marrow ECM is particularly important for the maintenance within the organism of a pool of self-renewing and non-differentiated cells able to differentiate into multiple phenotypes (i.e., multipotent mesenchymal stem cells, MSCs) whenever the need to remodel or repair a tissue arises. Chen *et al*. indeed demonstrated that it was possible, when culturing MSCs *in vitro*, to make them proliferate and to preserve their ability to differentiate into multiple cell types (i.e., their multipotentiality), simply by seeding them on a decellularized (i.e., cell-free) ECM extracted from the marrow of donor mice.[5] Depending on the bioactive agents added to the culture medium, MSCs grown on the marrow ECM could be directed to differentiate into osteoblasts (i.e., bone-forming cells) or adipocytes (i.e., fat-storing cells). Conversely, keeping these cells in culture on conventional tissue culture plastics resulted in the loss of their stem cell properties as they proliferated less quickly and "spontaneously" committed to the osteoblastic lineage.[5]

On the differentiation side of the balance, incubating multipotent cells isolated from a given tissue on a cell-free ECM obtained via decellularization of a similar type of tissue harvested from the same animal species orients the differentiation of the stem cells towards the phenotype of that tissue. For instance, rat MSCs harvested from bone marrow and cultured on titanium (Ti) discs covered with an MSC-derived ECM showed a much higher propensity to differentiation into osteoblasts than cells seeded onto plain Ti, even in the absence of any osteogenic chemical supplementation.[11] Another interesting study proved that it was possible to 'reprogram' (i.e., redifferentiate) human metastatic cancer cells (melanoma and breast

carcinoma) back to a benign phenotype simply by plating them on the microenvironment (i.e., the ECM) produced by human embryonic stem cells (hESCs).[12,13] This reprogramming of malignant tumor cells is actually possible because they share some similarities with multipotent stem cells, notably their ability to self-renew and generate a diverse progeny, and are therefore receptive to the signals present in their ECM.

### 1.1.3 The extracellular matrix as an ideal cell-instructive material

The instructive role of the ECM as a guide for the differentiation of multipotent cells into specific phenotypes has further been proven by the observation that natural organs which underwent a decellularization process, leaving only an intact underlying ECM, could successfully induce the differentiation of stem cells of allogeneic (i.e., cells isolated from another individual of the same species as the source of ECM) or xenogeneic (i.e., cells isolated from another species than the source of ECM) origin. As an outstanding proof of concept, Ott *et al*. managed to decellularize whole rat hearts and keep an intact ECM with 3D geometry and vasculature (Figure 1.4)[14]. Following repopulation of the construct with neonatal cardiac and aortic endothelial cells, they obtained functional contracting and drug-responsive hearts after 8 days of culture under simulated physiological conditions.

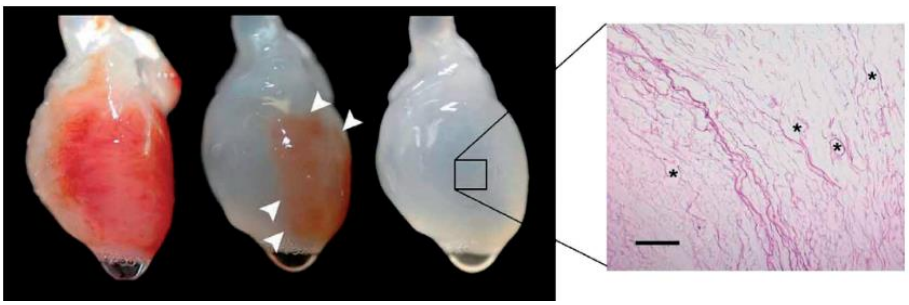

**Figure 1.4** *Sequential decellularization process of a whole rat heart, leaving an intact ECM. The inset shows that no intact cells or nuclei are present after the process and that vasculature conduits were preserved (asterisks).*[14]

The discovery of the prominent role played by the ECM in dictating and regulating cell fate *in vivo* has led to the commercialization of ECM-derived products to be used both in therapeutic applications or in *in vitro* studies. The most famous example of commercially-available ECM-derived product is Matrigel®(BD Biosciences, USA) which is a gelatinous and sterile extract of

basement membrane (i.e., a type of ECM) proteins derived from the EHS (Engelbreth-Holm-Swarm) mouse tumour and developed as early as 1983 as a substrate for cell differentiation and morphogenesis.[15] This ECM-derived substrate was shown to promote the differentiation of many different cell types as well as the outgrowth of differentiated cells from tissue explants, yielding 3D structures similar to those in the tissue of origin. Selected examples include the formation of cartilaginous nodules[15,16] and capillary-like structures[15,17,18] by chondrocytes and endothelial cells, respectively.

This further prompted the use of the ECM derived from decellularized organs as a biological scaffold for regenerative medicine applications, both in preclinical animal studies and in human clinical applications (Figure 1.5).[2,19,20] An example of such an ECM-derived bioscaffold having successfully reached the stage of implantation within humans is AlloDerm®, an acellular dermal matrix processed from the skin of human cadavers and used as treatment for burn injuries. This allograft (i.e., a graft material derived from another individual of the same species as the one implanted) enhances host cells infiltration and neovascularization as opposed to the formation of scar tissue by fibroblasts in the absence of an established dermal matrix.[21,22] Human demineralized bone matrix (DBM) is obtained after demineralization of human bone and is another example of a clinically-relevant ECM. It can be prepared from the bones of cadavers and seeded with autologous osteoprogenitor cells (i.e., cells destined to produce bone tissue and isolated from the bone marrow of the patient whose osseous defect is to be repaired) before being implanted into a patient where it will promote the differentiation of the hosted cells into functional osteoblasts.[23–27]

The use of xenogeneic ECM (i.e., ECM derived from the tissues of an animal species different than the one implanted) has also been investigated for the reconstruction of many different tissue types. Popular sources of xenogeneic ECM include the porcine-derived small intestine submucosa (SIS) which was successfully used as a vascular graft[20,28,29] and Achille's tendon repair[20,30] in the dog and as bladder wall[20,31] and dural[20,32] substitute in the rat, among others. Decellularized pig urinary bladder submucosa (UBS) has similarly been used for urethral reconstruction in a rabbit model.[20,33] Such ECM of animal origin have seemingly found their way into the clinic as Badylak stated in 2002 that "more than 100,000 human patients have now been implanted with xenogeneic ECM scaffold derived from the porcine small intestinal submucosa for a variety of applications".[34]

| Product | Company | Material | Processing | Form |
|---|---|---|---|---|
| AlloDerm | Lifecell | Human skin | Natural | Dry sheet |
| AlloPatch® | Musculoskeletal Transplant Foundation | Human fascia lata | Natural | Dry sheet |
| Axis™ dermis | Mentor | Human dermis | Natural | Dry sheet |
| Bard® Dermal Allograft | Bard | Cadaveric human dermis | Natural | Dry sheet |
| CuffPatch™ | Arthrotek | Porcine small intestinal submucosa (SIS) | Cross-linked | Hydrated sheet |
| DurADAPT™ | Pegasus Biologicals | Horse pericardium | Cross-linked | Dry sheet |
| Dura-Guard® | Synovis Surgical | Bovine pericardium | Cross-linked | Hydrated sheet |
| Durasis® | Cook SIS | Porcine small intestinal submucosa (SIS) | Natural | Dry sheet |
| Durepair® | TEI Biosciences | Fetal bovine skin | Natural | Dry sheet |
| FasLata® | Bard | Cadaveric fascia lata | Natural | Dry sheet |
| Graft Jacket® | Wright Medical Tech | Human skin | Natural | Dry sheet |
| Oasis® | Healthpoint | Porcine small intestinal submucosa (SIS) | Natural | Dry sheet |
| OrthADAPT™ | Pegasus Biologicals | Horse pericardium | Cross-linked | Dry sheet |
| Pelvicol® | Bard | Porcine dermis | Cross-linked | Hydrated sheet |
| Peri-Guard® | Synovis Surgical | Bovine pericardium | Cross-linked | Dry sheet |
| Permacol™ | Tissue Science Laboratories | Porcine skin | Cross-linked | Hydrated sheet |
| PriMatrix™ | TEI Biosciences | Fetal bovine skin | Natural | Dry sheet |
| Restore™ | DePuy | Porcine small intestinal submucosa (SIS) | Natural | Dry sheet |
| Stratasis® | Cook SIS | Porcine small intestinal submucosa (SIS) | Natural | Dry sheet |
| SurgiMend™ | TEI Biosciences | Fetal bovine skin | Natural | Dry sheet |
| Surgisis® | Cook SIS | Porcine small intestinal submucosa (SIS) | Natural | Dry sheet |
| Suspend™ | Mentor | Human fascia lata | Natural | Dry sheet |
| TissueMend® | TEI Biosciences | Fetal bovine skin | Natural | Dry sheet |
| Vascu-Guard® | Synovis Surgical | Bovine pericardium | Cross-linked | Dry sheet |
| Veritas® | Synovis Surgical | Bovine pericardium | Cross-linked | Hydrated sheet |
| Xelma™ | Molnlycke | ECM protein, PGA, water | | Gel |
| Xenform™ | TEI Biosciences | Fetal bovine skin | Natural | Dry sheet |
| Zimmer Collagen Patch® | Tissue Science Laboratories | Porcine dermis | Cross-linked | Hydrated sheet |

**Figure 1.5** *Commercially available ECM-derived products.*[20]

### 1.1.4 Integrins: main mediators of the communication between the intra- and extracellular compartments

*a) Integrins: structure and properties*

Integrins are the principal receptors of animal cells mediating the exchange of information between the extracellular environment (where the stimuli and stresses arise) and the intracellular compartment (where the genetic material and thereby the ability to respond and adapt to these stimuli reside). As such, they are key players in the regulation of cell processes such as adhesion, migration, proliferation, differentiation and apoptosis. Integrins are transmembrane heterodimeric proteins formed by the non-covalent association of one α and one β subunit. In mammals, 19 α and 8 β subunits exist, which combine to form 25 different receptor molecules.[35,36] Each subunit is composed of a large extracellular domain, a transmembrane segment and a short intracellular tail (Figure 1.6).[37]

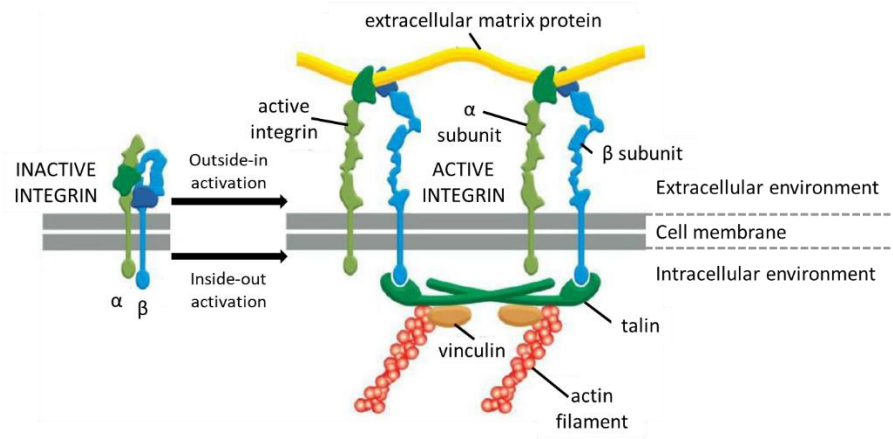


**Figure 1.6** *Schematic representation of integrins in inactive and active conformation. [Adapted from Alberts et al.*[38]*]*

*b) Integrins mediate cell adhesion*

Integrins mechanically link the ECM with the cytoskeleton (i.e., the cell's skeleton consisting in a dynamic network of interlinking protein filaments involved in all cellular events requiring motility: cell shape conservation, resistance to mechanical deformation, migration, division, intracellular transport, etc.). The extracellular domain of these transmembrane proteins constitutes the binding site for the cell-adhesive peptide motifs of ECM adhesive macromolecules (e.g., the Gxx'GEx'' sequence of some fibrillar collagens or the RGD motif of fibronectin and vitronectin, etc.), while the cytoplasmic tails interact directly or indirectly, via adapter molecules, with the actin cytoskeleton.[39]

Upon binding of an extracellular ligand, integrins switch to an activated state and translocate in the plane of the cell membrane to form clusters (Figure 1.6). In the cytoplasm, the clustering of integrins triggers the recruitment of a large number of various intracellular proteins to the activation site, which form multiprotein complexes (up to 156 distinct components can be involved)[40], ultimately anchoring the actin fibers of the cytoskeleton to the membrane receptors (Figure 1.6). Two categories are commonly distinguished among the recruited linker proteins: the proteins that directly associate with integrins (the best known being talin, α-actinin and filamin) and those that bind indirectly (the most famous being vinculin).[41,42] These transmembrane clusters of proteins are called focal complexes (small integrin clusters of 0.5-1 μm in diameter) and can either be transient or evolve into mature focal adhesions (large integrin aggregates of 3-10 μm in diameter) which mediate strong adhesion to the substrate (Figure 1.7).[42,43]

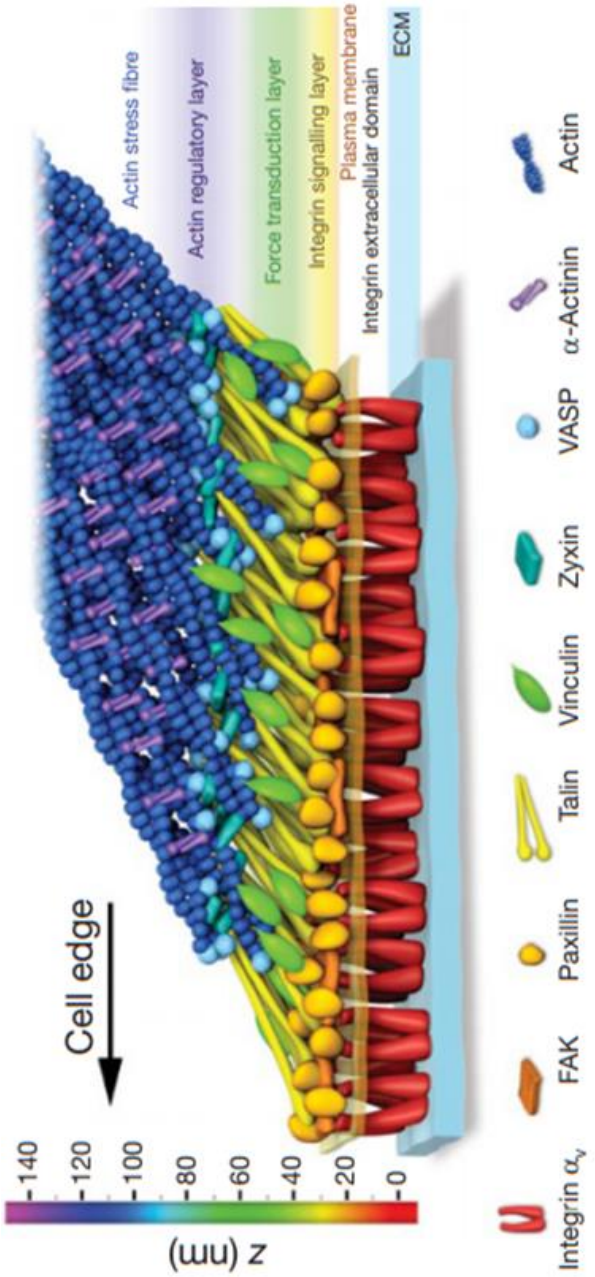


**Figure 1.7** *Schematic model of focal adhesion molecular architecture.*[44]

*c) Integrins play a role in the regulation of gene expression*

In addition to these structural proteins mediating the coupling between integrin receptors and the cytoskeleton, adhesion to ECM proteins also mobilizes cytoplasmic enzymes (e.g., tyrosine kinases such as FAK [Focal Adhesion Kinase][45] and serine/threonine kinases such as those involved in the MAPK cascade [Mitogen-Activated Protein Kinase][46]) having signalling properties. Activation of these enzymes in turn initiates complex signalling pathways ultimately regulating cell proliferation and gene expression (e.g., MAP-kinase and Jun kinase pathways) as well as locomotion (i.e., Rho-family GTPases mainly including Rho, Rac and Cdc42) (Figure 1.8).[35,47–50]

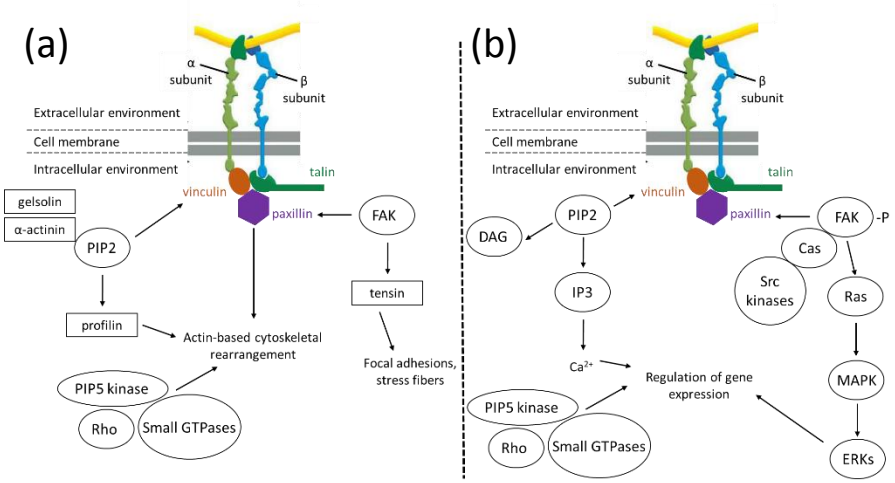


**Figure 1.8** *Schematic representation of some of the intracellular signaling cascades which are locally initiated when integrins bind to an extracellular ligand. (a) Integrin-dependent cytoskeletal rearrangement. (b) Integrin-dependent mediation of gene expression and cell proliferation. [Adapted from Giliberti et al.*[51]*].*

Beside this direct implication of integrins in the activation of signalling pathways, integrins are also involved in "collaborative signalling" as their activation by ECM ligands is required for the transduction of signals initiated by other cellular receptors such as growth factor receptors and ion channels. For instance, integrin activation is often necessary in order for the biochemical signals perceived by growth factor and cytokine receptors to be efficiently transduced to the nucleus and influence gene expression.[47,52,53]

*d) Integrins play a role in the regulation of cell survival and death (apoptosis)*

Integrins thus exert a real control over the cell cycle and most cells require appropriate anchorage to ECM macromolecules in order to proliferate and differentiate.[47] As such, integrin-matrix interactions are critical for the survival of many cell types (e.g., epithelial, endothelial and muscle cells, etc.) which can undergo a special type of apoptosis (i.e., programmed cell death where cells trigger they self-destruction), named anoikis, when losing their contact with ECM.[54,55] This mechanism appears to be an important safeguard for the organism as it prevents cells detached from their native environment from reattaching to new matrices and colonizing other tissues. Alteration of this mechanism can lead to anoikis resistance and anchorage-independent growth, which is characteristic of metastatic tumour cells.[56,57]

*e) Integrins as mechanosensors*

Apart from simply mediating the adhesion of the cell to its external environment, integrins work as mechanosensors able to probe the rigidity of the extracellular environment and transmit mechanical stresses bidirectionally to either side of the cell membrane. Indeed, when an external mechanical tension is applied to the cell, the formation of focal adhesions can be enhanced and those can be reinforced with increased actin polymerization into larger stress fibers. Contractile microfilaments can also be synthesized via incorporation of myosin II. These reinforcement mechanisms allow the cell to withstand greater external forces as well as to pull harder on its surrounding substrate in order to counter the tensile force applied to it and adapt to its environment (a phenomenon termed '**mechanotransduction**').[35,42,47,58,59]

### 1.1.5 Collagens: major proteins of the ECM

*a) The Collagen superfamily[35,37,60–65]*

Collagens are the most abundant structural components of the ECMs. Although their primary sequence (i.e., the sequence of amino acids in the polypeptide chain) varies, collagens share a common backbone which consists in three polypeptide α chains which can either be identical (homotrimeric form) or different (heterotrimeric form). These 3 α chains are

supercoiled around a central axis in a right-handed manner to form a triple helix of 1.5 nm diameter. To date, 42 different genes coding for more than 28 different types of collagens have been identified in the superfamily of vertebrate collagens. The amino acid sequence of each α chain variant is encoded by a distinct gene, yet all subunits share a common (glycine, Gly)-X-Y repetitive motif which can be repeated any number of times along the polypeptide backbone. This repetitive sequence contains a glycine residue in every third position and about 20% proline and hydroxyproline residues in position X and Y. The Gly residues of all three α chains constituting the collagen molecule are positioned in the centre of the triple helix, while all bulky amino acid residue side chains are exposed to the surface of the triple helix and enable the interaction with other matrix components and the self-assembly with other collagen molecules (in the case of fibril-forming collagens). The stability of the triple helix structure is maintained thanks to hydrogen bridges formed between the OH-groups of 4-hydroxyproline and the OH-, NH- or carbonyl groups of adjacent residues.

Collagens are classified into fibril-forming collagens (i.e., collagen type I, II, III, V and XI, accounting for 90% of all collagens) and non-fibrillar collagens. The synthesis of fibril-forming collagens begins with the production inside the cells of procollagens which contain large globular propeptides at each end of the triple helix. After secretion into the extracellular space, the terminal propeptides are enzymatically cleaved, resulting in mature collagen molecules with a characteristic 300-nm-long triple helical rod-like shape. The formation of collagen fibrils then follows as collagen molecules self-assemble longitudinally head-to-tail and aggregate laterally in a quarter-staggered manner, giving rise to fibrils exhibiting a characteristic striation with a 67-nm periodicity (Figure 1.9 (a)). Upon crosslinking, collagen fibrils are finally assembled into fibres.

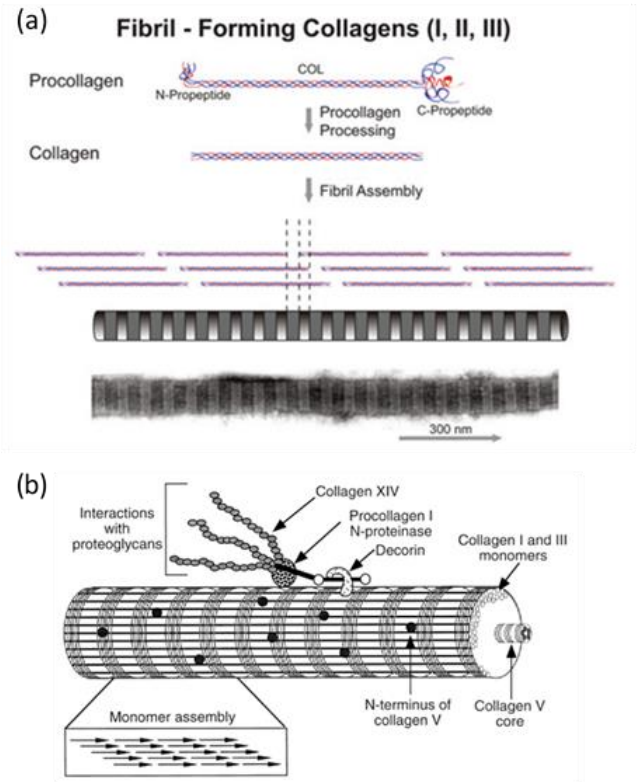


**Figure 1.9** *(a) Schematic representation of the processing and assembly of fibril-forming collagens into fibrils. Within the fibril, the collagen molecules are staggered N to C which gives rise to the characteristic D-periodic repeat (~ 67 nm). The electron micrograph of a collagen fibril from tendon is presented at the bottom of the panel. The negatively stained fibril displays the characteristic alternating light/dark pattern representing the gap (dark) and overlap (light) regions of the fibril.*[66] *(b) Model of a collagen I-containing fibre.*[37]

### *b) Collagen type I*

The collagen molecule used in this study, type I collagen (Col), is the longest known and most intensely studied collagen type as it is the main structural backbone of mammalian connective tissues including bone, skin, tendon, etc. Col is a heterotrimer of two $\alpha_1$ and one $\alpha_2$ polypeptide chains, each forming a left-handed α-helix. These 3 α-chains assemble together to give the characteristic right-handed triple helix structure. Col being a fibril-forming collagen, it self-assembles into fibres. However, it is noteworthy to

mention that Col-containing fibres are never composed solely of collagen type I *in vivo*, as they contain up to 25% of type III and V collagens depending on the tissue and their external surface is decorated with fibril-associated collagens with interrupted triple helix (FACIT collagens, Figure 1.9 (b)).

Besides its importance as a structural protein, Col is also endowed with a cell adhesive activity as it contains small sequences responsible for binding to cell transmembrane receptors, mainly integrins as discussed in section 1.1.4. The main amino acid sequence mediating the adhesion of collagen types I, II and III to cell integrins is the Gxx'GEx'' motif (where G = glycine, x is a hydrophobic residue (often phenylalanine), x' is usually O (hydroxyproline) and x'' is often R (arginine)) which is located in the triple helical domain of the molecules.[67–70] Preservation of the triple helical conformation appears to be important for the recognition of the Gxx'GEx'' sequence by the integrins $\alpha_1\beta_1$ and $\alpha_2\beta_1$.[35,37] It is important to mention that, although Col do contain many RGD (arginine-glycine-aspartic acid) peptide sequences, well-known for mediating the binding of cell integrins to most adhesive matrix glyproteins (e.g., fibronectin, vitronectin, etc.), these epitopes are not involved in the cell-adhesive properties of native Col.[35,37] It is only upon unfolding of the triple helix conformation (such as in heat-denaturated Col or gelatin, for example) that some of the RGD motifs substitute for the inactivated Gxx'GEx'' sequences and start to interact with the RGD-specific integrins $\alpha_V\beta_1$, $\alpha_V\beta_3$ and $\alpha_{IIb}\beta_3$.

Col is ubiquitous across animal and plant kingdoms and has maintained a highly conserved amino acid sequence through the course of evolution.[34,60] This observation justifies the use of allogeneic and xenogeneic sources of Col as tissue repair material with low antigenic potential. As such, Col extracted from animal tissues accounts for more than 90% of the mass of Col used in biomedical applications such as dressings and sponges for wound repair, as catgut in surgery, or as 3D scaffolds and surface coatings in tissue engineering.[35,63,71]

### 1.1.6 Hyaluronic acid: a polysaccharide of the ECM

#### *a) HA: structure and properties*

Hyaluronic acid (HA, also termed hyaluronan or sodium hyaluronate in its salt form) is a linear natural polysaccharide composed of a repeating disaccharide unit based on alternated β 1-4-D-glucuronic acid and β 1-3-*N*-

acetyl-D-glucosamine residues (Figure 1.10).[72,73] This relatively simple structure is conserved throughout all mammals[73,74], which results in HA being non-antigenic and non-immunogenic. Commercial sources of HA thus mainly involve its extraction from animal tissues, including bovine vitreous humour, rooster combs, umbilical cords or its production by bacteria such as *Streptococcus zooepidermicus.*[72] In the body, HA is produced by specific enzymes, HA synthases, localized in the plasma membrane of cells and is concomitantly extruded into the ECM and can sometimes be tethered to the cell surface by retention in the synthase.[75] Under normal homeostatic conditions, the molar mass of this polysaccharide can be as high as ~ 4 million Da and it is packed under a highly hydrated random coil conformation (with a hydrodynamic radius ~200 nm[72,76], while its fully extended length could reach ~10 µm[77]) stabilized via hydrogen bonding between the hydroxyl groups along the chain. HA is a member of the group of glycosaminoglycans (GAGs, polysaccharides also including chondroitin sulfate, dermatan sulfate, keratin sulfate, heparan sulfate and heparin) and has the most simple chemical structure of them all.[72] Contrary to more complex GAGs, HA is not sulphated and is never covalently linked to a protein core in the form of a proteoglycan. Due to the presence of a carboxyl group on each glucuronic acid unit, HA shows a polyanionic character at physiological pH[78,79] ($pK_a$ of the polymer estimated to be 2.9[78,80]). HA is a major component of soft connective tissues (e.g., joint synovial fluid, vitreous humor of the eye, skin, umbilical cord, etc) where its physicochemical roles are mainly the control of tissue hydration, joint lubrication and shock absorbance.[81] Indeed, due to its high molecular weight and anionic polyelectrolyte behaviour[79], it is highly hydrophilic and shows high osmotic pressure and viscosity.

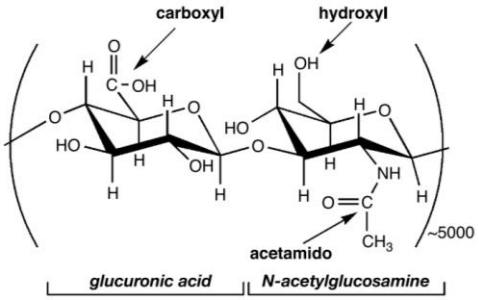


**Figure 1.10** *Chemical structure of native HA.*[75]

### *b) Main applications of HA*

The viscoelastic properties of HA, coupled to its biocompatibility and non-immunogenicity led to the use of HA in a number of pre-clinical and clinical applications (Figure 1.11). Notable amongst those are the supplementation of joint fluid in arthritis via intra-articular injections[77,82,83], ophthalmologic surgery[77], scaffolding material for wound-healing applications (HYAFF® scaffold consisting of a benzyl ester-derivative of HA, developed by Fidia (Abano Terme, Italy))[84–87], moisturizer in cosmetics, and drug-delivery agents.[88–90] Due to its high hydrophilicity, HA also displays antifouling properties and has proven to be well suited to applications requiring minimal cell adhesion. Hence, HA was used to coat endovascular stents and efficiently reduced platelet adhesion, preventing thrombus formation.[91,92]

| Application | Tradename | Approval type | Company |
|---|---|---|---|
| Osteoarthritis | Hyalgan | Premarket | Fidia |
| | Synvisc | Premarket | Biomatrix/Genzyme |
| | Supartz | Premarket | Seikagaku |
| | Hylashield | 510 k | Biomatrix |
| Ophthalmology | Healon | Premarket | Pharmacia |
| | Amvisc | Premarket | Bausch and Lomb |
| | Coease, Shellgel, Staarvisc | Premarket | Anika Therapeutics |
| | Amo Vitrax, Vitrax | Premarket | Allergan/Medtronic |
| | Provisc, Viscoat | Premarket | Alcon Laboratories |
| Wound healing | Bionect | 510 k | Fidia |
| | Ialuset | 510 k | IBSA |
| Postsurgical adhesions | Adcon | Premarket | Gliatech |
| | Intergel | Premarket | LifeCore Biomedical |
| | Seprafilm | Premarket | Genzyme |
| Surgical scaffolding | Hyalomatrix | 510 k | Fidia |
| | Hylasine | 510 k | Biomatrix |
| Gastrourology | Deflux | Premarket | Q-Med |

**Figure 1.11** *Table displaying a selection of FDA-approved HA products.*[75]

### *c) Bioactivity of HA*

In addition to these structural properties associated with the physicochemical characteristics of HA, this polysaccharide is also endowed with biological activity. Quite similarly to the adhesion proteins extensively described previously, HA was indeed found to bind to specific cell surface receptors and modulate cell motility, adhesion, proliferation and gene expression. The most documented HA-binding proteins, named *hyaladherins*, are the cell surface receptors CD44 and RHAMM (Receptor for HA-Mediated Motility).[93] CD44 is a transmembrane glycoprotein which is expressed in most mammalian cell types. Upon specific binding with HA macromolecules present in the ECM, it activates cytoplasmic signalling proteins (e.g., Rho GTPases such as RhoA and Rac1 proteins for example)

which ultimately leads to the reorganization of the cell cytoskeleton and the promotion of lamellipodial protrusions (Figure 1.12).[94,95] This receptor is also involved in the intracellular uptake and degradation of HA.[96] On the other hand, RHAMM is a HA-binding protein which is ubiquitously distributed into cell compartments including the cell surface, cytoplasm, mitochondria and nucleus.[95] Its specific interaction with HA stimulates the phosphorylation of several cytoplasmic proteins, including key components of focal adhesions (e.g., focal adhesion kinase, FAK) and, as such, regulates the focal adhesion turnover and promotes cell locomotion.[96–98] Overexpression of CD44 and RHAMM has been linked to the development of tumour cells and their metastatic proliferation, migration and invasion.[95,96,98,99]

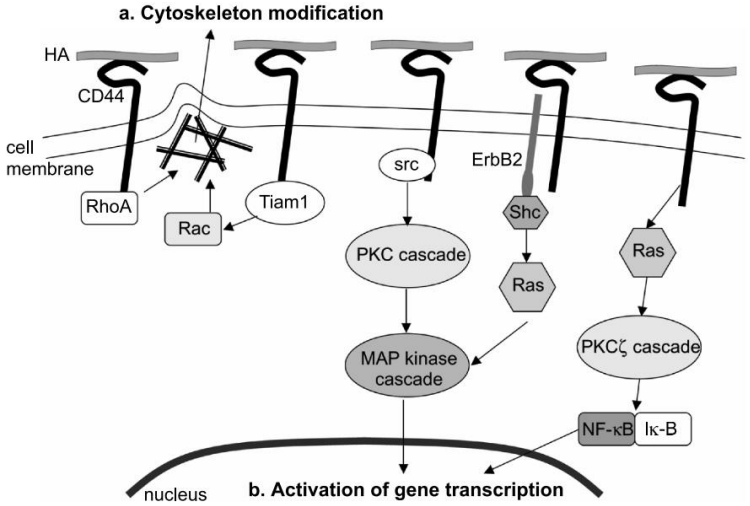


**Figure 1.12** *Schematic representation of some signaling pathways initiated by the binding of HA to the CD44 receptor. The binding of HA to CD44 results in signaling cascades which can affect: a) the organization of cytoskeletal proteins, leading to changes in cell migration, and b) the activation of gene transcription, leading to changes in cell proliferation.*[75,99]

In view of this, the biological functions of HA can be ascribed to a combination of both its physicochemical properties (i.e., its strong hygroscopic character which provides expanded, hydrated matrices promoting cell migration and mitosis) and its ability to specifically interact with cells.[93] As a promoter of cell migration, HA plays a significant role in morphogenesis, normal regenerative processes (i.e., wound healing and tissue regeneration and remodelling) as well as in malignant diseases (i.e.,

tumour cell invasion and metastasis) and its concentration is correspondingly elevated in the ECM of embryos, wound beds and tumours.[100,101] HA was also discovered to have size-dependent effects.[102] Indeed, although HA is originally synthesized as large 100-1000 kDa unbranched chains, it can be degraded in the matrix by specific enzymes called hyaluronidases, to give rise to small oligosaccharides (4-25 disaccharide units). These low molar mass HA oligosaccharides have been shown to be angiogenic in several experimental models[103–106], while angiogenesis inhibition is in contrast shown to occur with high molar mass HA.[103,105]

***In summary, the ECM is the source of many parameters influencing cell behavior and the mediator of all signals which need to be transmitted to cells to regulate their processes (i.e., from adhesion to differentiation). Most of these cross-talks between cells and their ECM are mediated via the coupling of the cell cytoskeleton and ECM proteins through integrin receptors. The design of systems mimicking the instructive role of native ECM is thus particularly relevant for the advent of successful TE and regenerative medicine applications. Although the use of natural decellularized ECMs of allogeneic or xenogeneic origin has already proven useful for therapeutic applications or in vitro studies, issues might arise regarding the risk of pathogen transmission. Furthermore, even though immunogenicity is not a concern with these biological scaffolds as most of their constituting molecules are conserved across species, the need for a thorough sterilization often has detrimental effects on their mechanical properties. Hence, isolating the specific contribution of each of the numerous cell-influencing cues present in the ECM in order to subsequently recapitulate them in the design of cell-instructive biomaterials with tailored properties probably is the best option for TE and regenerative medicine applications. This has been the focus of many research works, as will be highlighted in the next section.***

## 1.2 Cell-influencing cues

### 1.2.1 Influence of surface chemistry

As discussed in section 1.1.4, the adhesion of cells to their extracellular environment is mediated by specific integrin-ligand interactions and hence, is conditioned upon the presence of such ligands on the surface to be explored. Whenever cells encounter a surface, be it *in vivo* or *in vitro*, their ability to successfully adhere to it will thus initially depend on the presence of adhesive proteins under the appropriate conformation recognized by integrins. When implanting a biomaterial in the body, the proteins interacting with its surface will mainly be the ones circulating in the bloodstream (e.g., human serum albumin, fibronectin, vitronectin, etc.) or naturally present within the tissue of implantation (e.g. collagens, fibronectin, etc.). When dealing with mammalian cell culture experiments *in vitro*, it is common practice to supplement the culture medium with fetal bovine serum (FBS), so that the proteins it contains will be the ones (i.e., mostly FN present in a concentration as high as 300 µg/mL in the plasma[35]) interfacing the culture substrate. The nature of the proteins which will effectively interact with the culture substrate/implanted biomaterial surface and adhere to it, itself depends on the physicochemical properties of the surface: surface charge and chemistry[107], wettability[108–110], and topography/roughness.[111–114] Hence, the physicochemical properties of the surface will ultimately govern the processes of cell adhesion and spreading.

Bearing in mind the prime importance of this initial protein-material interaction, it is thus possible to engineer a material's surface accordingly with a view to control the adsorption of proteins and ultimately regulate cell adhesion and spreading. As such, it is common practice to functionalize a biomaterial surface with cell-adhesive biomacromolecules or peptide sequences derived therefrom, to render the material more cytophilic. However, one has to keep in mind that once brought in contact with serum proteins (either *in vitro* or *in vivo*), the surface composition will likely change along with the adsorption of exogeneous proteins and the surface properties might consequently be affected.

Slightly hydrophilic surfaces (45°≤ water contact angle ≤ 75°) are generally described as being more conducive to protein adsorption and hence, to cell adhesion (Figure 1.13).[115,116] In contrast, hydrophobic surfaces with a water contact angle higher higher than 80° favour the adsorption of non-adhesive proteins which restricts the access of the surface to adhesive proteins and limits cell adhesion. This is the reasoning behind the use of hydrophilic plasticware as cell culture consumables, their original polystyrene (PS) surface being plasma-treated to become more hydrophilic and thus more cytophilic (i.e., the widespread tissue culture PS, TCPS). Moreover, it has been documented that proteins adsorbing on hydrophobic surfaces tend to do so by changing their conformation so as to expose their hydrophobic core towards the substrate and maximize hydrophobic interactions.[110] This can lead to the denaturation of the protein and/or hiding of the adhesive epitopes, resulting in the inability to bind to integrins and to interact with cells. For instance, the adsorption of FN on a hydrophobic surface (i.e., substrate functionalized with a monolayer of self-assembled $CH_3$-terminated alkanethiols), was shown to affect its cell-adhesivity due to denaturation of its integrin-binding motif.[107] Conversely, cell adhesion was the highest when FN was adsorbed on highly hydrophilic OH-terminated alkanethiols and slightly reduced on less hydrophilic COOH- and $NH_2$-terminated substrates.

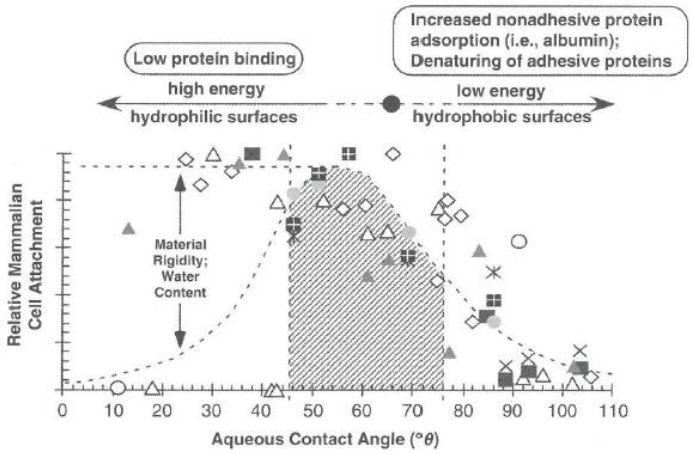


**Figure 1.13** *Cell adhesion as a function of surface wettability.*[115]

This observation was corroborated by Lin and coworkers who demonstrated that the cell-binding domains of FN were more accessible when the protein was adsorbed on highly hydrophilic OH-terminated SAMs

compared to $NH_2$- and $CH_3$-terminated SAMs.[117] The success of initial cell adhesion on a material can thus be predicted with fair accuracy from its hydrophilic character. However, other factors come into play to determine how tightly cells anchor to their substrate and spread at later culture stages. Indeed, the same authors evidenced that, after 12 h of seeding, the factor which determined the extent of FAs formation (i.e., late cell-adhesion events) in adhered cells was the adhesion force between FN and its underlying substrate. Adhered cells were actually found to generate traction forces on their substrate and, correspondingly, anchored better (i.e., formed more numerous and larger FAs) to surfaces to which FN was more tightly linked (i.e., $NH_2$-terminated SAMs where FN was stabilized via electrostatic interactions).

In an early study by Schakenraad et al., the relationship between surface free energy, protein adsorption and cell spreading was clearly established.[118] In the absence of serum supplementation, the relationship between the relative spreading of cells (i.e., spreading of human fibroblasts with the spreading area on TCPS used as reference) and the surface free energy of the substrate follows a sigmoidal trend (Figure 1.14 (a)). The most hydrophilic substrates tested (i.e., glass, TCPS and poly(methyl methacrylate), PMMA) were also the ones with the highest surface free energies and showed the highest relative cell spreading in the absence of any interfacial protein layer (i.e., no added serum). At the opposite end of the spectrum, hydrophobic polymers (e.g., fluoroethylenepropylene copolymer and poly(tetrafluoroethylene)) had the lowest surface free energies and correspondingly, the lowest relative cell spreading values. Upon addition of serum in the culture medium, the absolute values of cell spreading were increased on all substrates, highlighting the fact that adhesive proteins are naturally present in serum and positively impact cell adhesion. However, the presence of serum proteins in the culture medium did not change the minimal level of surface free energy required to reach effective cell spreading. Indeed, most polymers tested in the presence of serum induced a similar cell spreading which was much lower than that obtained on TCPS (Figure 1.14 (b)). Only glass and polycarbonate (PC) displayed spreading values very close to or 50% that of TCPS, respectively. Altogether, these results indicate that the incubation with serum proteins does not drastically improve the cell-adhesivity of low surface energy polymers, either because the amount of proteins which adsorb on these substrates is low or because

they adsorb under a denatured conformation which inactivates their integrin-binding motifs.

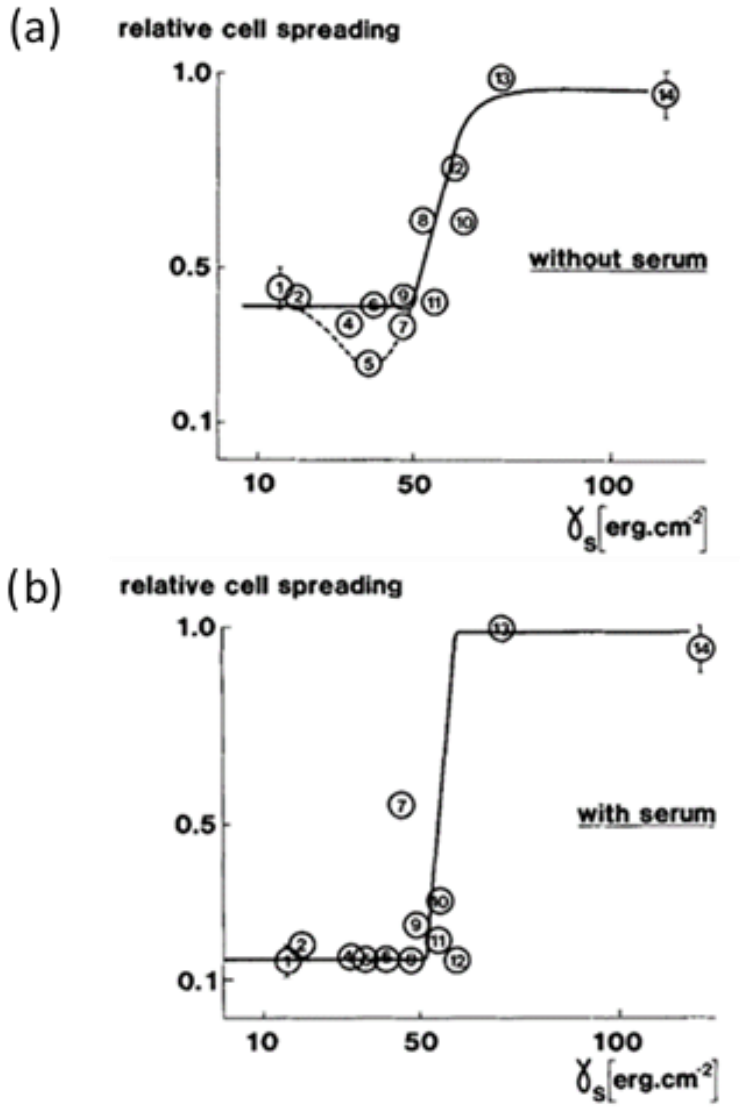


**Figure 1.14** *Relative cell spreading (reference = 13: TCPS) as a function of the substratum surface free energy, a) without serum and b) with serum. Selected examples include: 1: fluoroethylenepropylene copolymers, 3: polytetrafluoroethylene, 4: silicon rubber, 7: PC, 12: PMMA, 14: Glass.*

### 1.2.2 Influence of soluble (bio)chemical effectors

Beyond the effect of surface chemistry on cell adhesion and spreading, soluble (bio)chemical effectors are known to direct the differentiation of multipotent cells cultured *in vitro* to particular lineages. Hence, it is common practice to add a 'cocktail' of differentiation factors (i.e., growth factors, cytokines or even non-natural chemical products) to the culture medium of multipotent cells in order to guide their fate towards differentiation into a specific phenotype. For instance, Pittenger *et al.* proved that multipotent hMSCs present in adult bone marrow can be induced to selectively differentiate into, for example, adipocytes (i.e., fat-storing cells), chondrocytes (i.e., cartilage cells) or osteoblasts (i.e., bone-forming cells), depending on the nature of the chemical effectors added to the culture medium.[119]

### 1.2.3 Influence of geometric cues

#### *a) Control of cell viability and growth*

Controlling the extent to which cells are able to spread on a surface appears to be one of the prime mechanism to control their viability and switch their fate between the two extremes which are apoptosis and growth. Patterning a surface with islands of cell-adhesive ligands has thus been widely explored as a way to influence cell behaviour.

In a founding study, Chen et al. varied the extent of cell spreading while maintaining a constant total cell-matrix contact area and evidenced that the level of DNA synthesis (i.e., a direct indicator of cell activity) measured in adherent cells was directly proportional to their projected area (Figure 1.15).[120] In other words, cells which spread across multiple small adhesive FN-coated islands and hence displayed a stretched morphology were more active than rounded cells which were adhering to a single adhesive island of larger size. Furthermore, the proportion of cells undergoing apoptosis was much higher in rounded cells than in well-spread cells, independently of the total area of cell-matrix contact. Cell viability and activity was thus shown to be dependent on the projected cell area (i.e., the spreading of cell bodies) rather than on the total cell-adhesive contact area.

Arnold et al. further refined the maximum spacing between adhesive ligands to maintain effective cell spreading.[121] They patterned a non-

adhesive substrate with cell-adhesive gold nanodots (< 8 nm diameter) coated with a cyclic RGD peptide sequence and uniformly spaced by a distance of 28, 58, 73 or 85 nm. Each Au dot allowed the anchoring of a single cellular integrin since the average diameter of integrins embedded in the cell membrane is between 8-12 nm. For distances ≥ 73 nm between the adhesive sequences, cell adhesion was limited and the formation of FAs and actin stress fibres greatly reduced and attributed to the inability to cluster integrins. The maximum spacing between adhesive ligands enabling integrin clustering and thus FA formation and effective cell spreading was therefore determined to be between 58 and 73 nm for a variety of cell types: mouseMC3T3-E1 osteoblasts, 3T3-fibroblasts, B16-melanocytes and rat REF52-fibroblasts.[121,122]

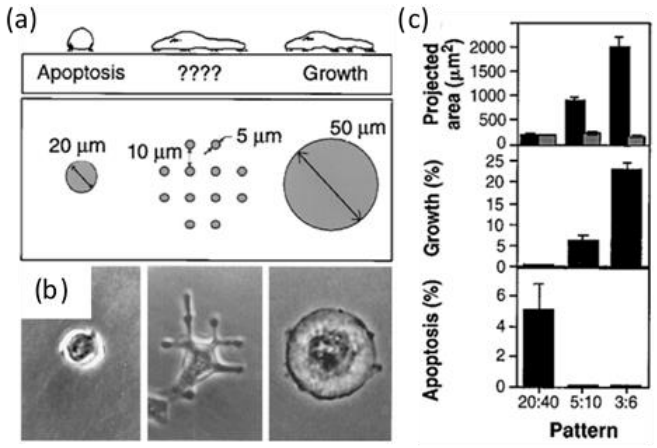


**Figure 1.15** *Cell-ECM contact area versus cell spreading as a regulator of cell fate. (a) Diagram of substrates used to vary cell shape independently of the cell-ECM contact area. Substrates were patterned with small, closely spaced circular FN-coated islands. (b) Phase-contrast micrographs of cells spread on single 20- or 50-µm-diameter circles or multiple 5-µm circles patterned as shown in (a). (c) Plot of projected cell area (black bars) and total ECM contact area (grey bars) per cell (top), growth index (middle), and apoptotic index (bottom) when cells are cultured on single 20-µm circles or on multiple circles 5 or 3 µm in diameter separated by 40, 10, and 6 µm, respectively.[Adapted from Chen et al.*[120]*].*

### *b) Control of cell differentiation*

Kilian et al. published a striking study where the fate of human mesenchymal stem cells (hMSCs) could be directed towards either the osteogenic or adipogenic lineages simply by varying the area and shape of a pattern of adhesive ECM protein (i.e., FN) designed to contain a single cell.[123] While maintaining a constant chemical composition of the culture medium (supplementation with a 1:1 mixture of adipogenesis and osteogenesis-promoting growth factors), hMSCs plated on small adhesive islands (1,000 $\mu m^2$) showed a higher tendency to differentiate into adipocytes whereas the osteogenic lineage was favored on large adhesive islands (5,000 $\mu m^2$) (Figure 1.16 (a)). When selecting an adhesive area of intermediate size (2,500 $\mu m^2$), a mixed population of differentiated cells was initially obtained and could be further selectively oriented towards one of the two phenotypes by simply dictating cell shape while keeping the adhesive surface area constant. Using pentagonal shaped patterns of adhesive protein, individual hMSCs were forced into the shape of either a flower (i.e., pentagon with convex edges), a common pentagon (i.e., straight edges) or a star (i.e., concave edges). The proportion of osteoblastic phenotypes was shown to increase from the flower shape (~ 40% osteoblasts) to the pentagon shape (~ 50% osteoblasts) and towards the star shape (~ 60% osteoblasts) (Figure 1.16 (b)). This trend was demonstrated to be in line with the increase in cytoskeleton contractility within the cells, the cells in star shapes showing larger FAs and stress fibres than those in flower shapes (Figure 1.16 (c-d)). Geometric feature were thus proven to influence the way cells organize their cytoskeleton and shapes that increase actomyosin contractility triggered the promotion of osteogenesis.[124,125]

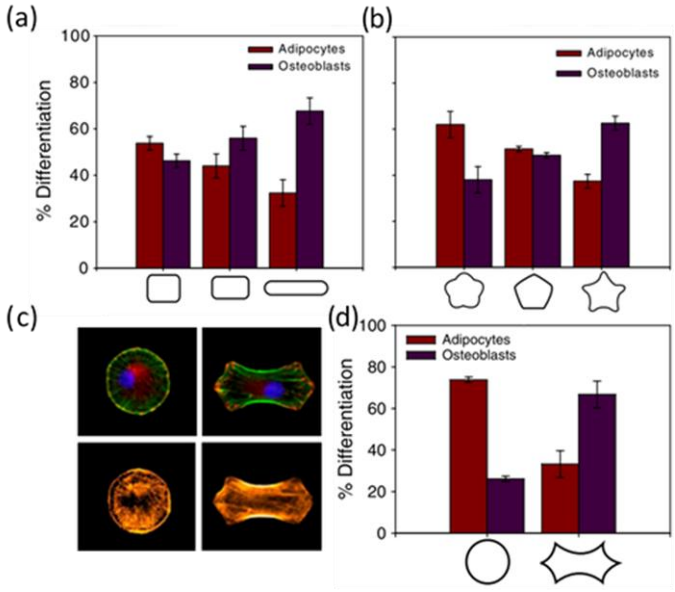


**Figure 1.16** *(a) Percentage of cells captured on adhesive FN rectangles of varying aspect ratio differentiating to adipocyte or osteoblast lineage. (b) Percentage of cells differentiating to either lineage when captured on adhesive FN surfaces with fivefold symmetric shapes. (c) Cell in a circle shape showing low contractility by F-actin (green) and vinculin (red) with nuclei in blue compared to a holly leaf shape yielding large stress fibres along the concave long edge of the cell [top panel]. Myosin IIa immunofluorescent staining [bottom panel]. (d) Corresponding differentiation of cells in both shapes.[Adapted from Kilian et al.*[124]*]*

### 1.2.4 Influence of topographical cues

Research conducted in recent years has highlighted that nanotopographical features are often superior to plain surfaces in terms of their ability to positively impact cell behaviour.

*a) Nanopits*

The use of vertically oriented and close-packed titania (i.e., $TiO_2$) NTs as culture substrate has been a popular way to investigate the effect of tube diameter on cell behaviour. When it comes to favoring cell adhesion and

spreading, it has been documented that tube diameters below 30 nm score better than larger NTs and flat surfaces. Park *et al.* varied the diameter of anodized $TiO_2$ NTs between 15 and 100 nm and evidenced that the adhesion, spreading and proliferation of rat MSCs were all highest on the 15-nm diameter NTs and were declining with increasing tube diameter (Figure 1.17).[126] Interestingly, the cellular activity (i.e., adhesion, proliferation and migration) was higher on the 15-nm diameter NTs as compared to plain $TiO_2$ surfaces. On the contrary, adhesion and spreading of cells were severely impaired when plated on NTs with a diameter > 50 nm, leading to a drastic increase in cell death (i.e., anoikis). In line with the conclusions drawn from the geometric patterning of flat substrates, the decrease in cell activity with increasing tube diameter was related to the inability of cells to cluster integrins anchored more than 30 nm apart (though a maximum distance between 58-73 nm was found on flat substrates) to form stable FAs and efficiently activate intracellular signalling cascades. Similarly, Oh and coworkers reported the initial density of adherent cells to be inversely proportional to the diameter of $TiO_2$ NTs (the tube diameter being varied between 30, 50, 70 and 100 nm).[127] This observation was linked to the adsorption of serum proteins in higher amounts on low diameter NTs. The group of Popat reached similar conclusions using human adipose-derived stem cells (ADSCs), the best adhesion and proliferation results being obtained for the lower diameters tested (i.e., 70 and 110-nm diameter tubes).[128] Brammer et *al.* found primary bovine chondrocytes to be most active in the secretion of *de novo* ECM when seeded on 70-nm $TiO_2$ NTs as compared to flat Ti substrates and NTs of a different diameter (in the range 30-100 nm).[129]

Using yet another sample preparation technique (i.e., polymer demixing) and another cell line (i.e., human foetal osteoblastic (hFOB) cells), Lim and coworkers synthesized thin films with nanoscale pits of homogeneous depth of 14, 29 or 45 nm.[130] The surface chemistry being identical to pure PLLA in all substrates and the total surface area being almost constant (difference < 1%), the nanotextured films allowed to study the effect of topography on cells, independently of surface chemistry effects. hFOB cells cultured on the 14- and 29-nm deep pits adhered more, spread better and synthesized more FA proteins compared with the surface with 45-nm deep pits and flat PLLA substrates.

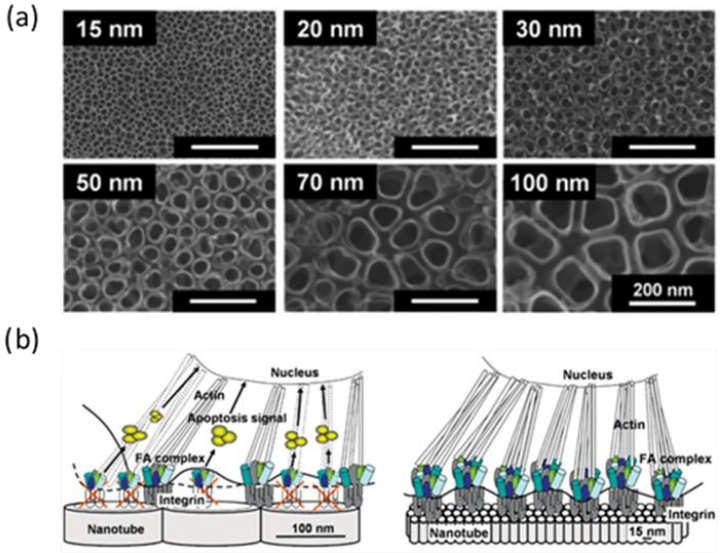


**Figure 1.17** *(a) SEM images of self-assembled layers of vertically-oriented $TiO_2$ NTs with varying diameter generated by anodization of titanium sheets. (b) Hypothetical model showing how the lateral spacing of focal contacts on NTs of different diameters might direct cell fate. A spacing of 15 nm seems optimal for integrin clustering into focal contacts, thus inducing assembly of actin filaments and signalling to the nucleus. NTs larger than 70 nm diameter do not support focal contact formation and cell signalling, thus leading to apoptosis (anoikis).[Adapted from Park et al.*[126]*]*

Observations regarding the impact of NT diameter on cell differentiation are yet divergent, although a consensus can be reached as to the positive effect of nanotopography compared to plain surfaces. Park *et al*. showed that the osteogenic differentiation of rat MSCs was promoted on lower diameter NTs (i.e., 15-nm diameter NTs) in the presence of biochemical inducers.[126] After biochemical induction of the osteogenic pathway, Popat *et al.* showed a similar increase in osteoblastic phenotypes when hADSCs were cultured on nanotubular substrates compared to flat Ti and a decreasing trend with the increase in tube diameter.[128] Oh *et al*. evidenced the opposite trend in the absence of any biochemical inducer, as hMSCs showed a higher propensity to differentiate into osteoblasts when seeded on larger tube diameters (i.e., 100 nm) (Figure 1.18).[127] The conclusion drawn by the latter authors was that the lower density of serum proteins adsorbed on larger diameter NTs force

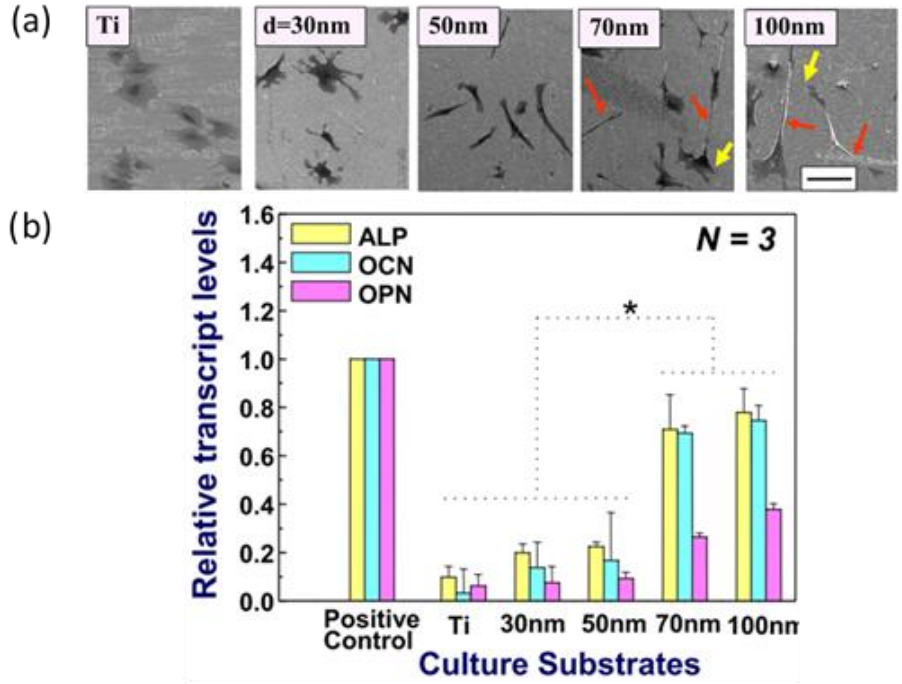


**Figure 1.18** *(a) SEM micrographs of hMSCs on flat Ti and 30-, 50-, 70-, and 100-nm diameter $TiO_2$ NT surfaces after 24 h of culture. Extraordinary cell elongation is induced on NTs with diameters of 70 and 100 nm (see red arrows). Cells are more elongated on the bigger $TiO_2$ NTs. (b) Quantitative PCR analysis for alkaline phosphatase (ALP, early marker of osteogenic differentiation), osteocalcin and osteopontin (OCN and OPN, respectively, late markers of osteogenic differentiation). Plastic cell culture plate with osteogenic inducing media was used as positive control of osteogenic differentiation. *, significant differences between Ti, 30-, and 50-nm NTs vs. 70- and 100-nm NTs for ALP, OCN and OPN gene expressions ($p < 0.01$). [Adapted from Oh et al.[127]].*

the cells to stretch to find anchoring points and the higher cytoskeletal tension generated inside stretched cells in turn favours their differentiation towards the osteogenic lineage. In another study, Popat *et al.* used nanoporous (average pore diameter ~ 72 nm) alumina surfaces as culture substrates for mouse MSCs and concluded that the well-defined nanoporosity enhanced cell adhesion and proliferation compared with plain alumina surfaces (both conditions in presence of serum).[131] Upon administration of osteogenic differentiation medium, MSCs seeded on the

nanostructured interfaces showed a higher tendency to differentiate into osteoblasts than the cells seeded on flat substrates. Both the synthesis of ALP and the *de novo* production of mineralized ECM were indeed upregulated. A clear link between a spread morphology, increased cytoskeleton contractility and differentiation towards the osteogenic lineage seems to emerge from cells forced to stretch across nanopits. Zouani *et al*. synthesized RGD-functionalized PET substrates with a controlled nanotopography (i.e., 10-nm or 100-nm deep nanopits) and highlighted the correlation between the higher projected area of cells having to stretch along the depth of deeper pits, their cytoskeleton organization and their increased tendency to selectively differentiate into osteoblasts.[132] After 2 h of culture, the projected area of hMSCs was the highest on the deeper pits (i.e., 100-nm deep pits) in comparison with shallower pits and flat PET surfaces. This increase in cell spreading on 100-nm deep pits later associated with organization of mature FAs (after 6 h incubation) and upregulation of osteogenic genes (after 12 days of incubation) even in the absence of osteogenic medium. Osteoblastic differentiation was later proven to be related to the increased cytoskeletal tension generated on deeper nanopits as disruption of actin polymerization (using cytocholasin D) fully inhibited the differentiation of hMSCs.

### *b) Micro- and nanogrooved substrates*

Microgrooved substrates produced from titanium or various polymers (e.g., PLA and PS) have been explored in terms of their effect on cell processes. Adherent cells such as osteoblasts, fibroblasts, epithelial and endothelial cells have all been documented to align with the microfabricated grooves and to spread and migrate along the axis of these grooves (a phenomenon termed 'contact or topographic guidance').[133–136] In addition to regulate cell orientation and migration, microgrooved patterns were shown to influence the differentiation of some cell types. Matsusaka *et al*. demonstrated that rat bone marrow (RBM) cells cultured on microtextured surfaces of PS or PLA (displaying grooves with a depth of 0.5, 1.0, or 1.5 µm and a width of 1, 2, 5, or 10 µm) aligned along the micro-channels after 8 days of culture.[137] After 16 days of culture within osteogenic medium, the osteogenic differentiation of cells grown on micropatterned substrates was significantly enhanced (as proven by the higher ALP activity) compared with that of cells seeded on smooth surfaces. In particular, PLA surfaces with 1.0 µm-deep grooves and 1 or 2-µm wide grooves had the highest level of ALP activity and of mineralized matrix secretion.

Lee *et al*. demonstrated that human embryonic stem cells (hESCs) seeded on nanogrooved patterns (ridges of 500 nm height and 350 nm width) elongated along the direction of the grooves and differentiated into neuronal lineages after only 5 days of incubation in the absence of any biochemical inducer of differentiation (Figure 1.19).[138] To explain this observation, the authors proposed that the change in morphology of cells guided by the grooved patterns results in a transfer of tensional force to the nucleus, which in turn influences gene expression.

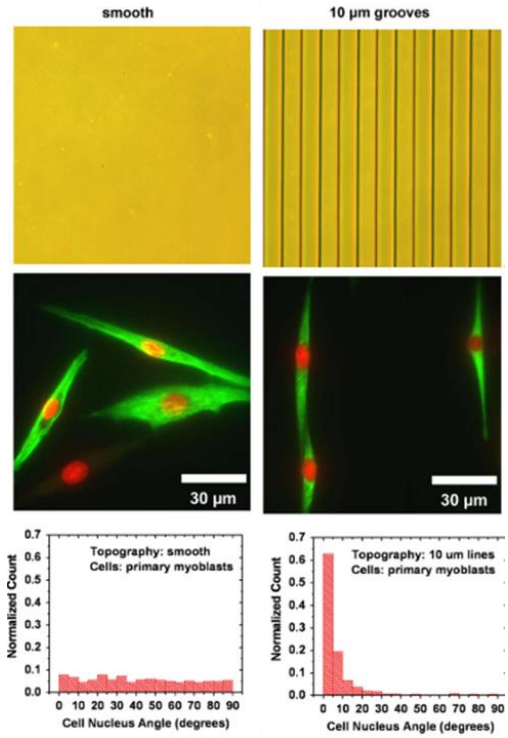


**Figure 1.19** *Cellorientation (primary myoblast cells) influenced by surface topography, as shown by immunostaining of sarcomeric myosin (green) and nuclei (red). Histograms show the distribution of cell alignment angles. Cells orient randomly on smooth substrates and parallel to 10-µm wide grooves.[Adapted from Charest et al.*[136]*]*

*c) Nanopillars*

As a general observation, seeding of cells on substrates consisting of spaced and rigid nanopillars seems to disturb the normal organization of the cells cytoskeleton as they attempt to endocytose the protruding nanotopographies which they find on their path.

Human fibroblasts seeded on cylindrical PMMA nanocolumns (160-nm high, 100-nm diameter and 230-nm centre-centre spacing) were discovered to produce many filopodia to interact with the columns and to attempt to internalize them via endocytosis (Figure 1.20 (a)).[139] Cells which adhered on the nanopillars had poorly organized actin cytoskeleton and smaller FAs as compared to flat substrates of identical chemistry. Quite similarly, Kim *et al.* plated mammalian cells (i.e., mouse embryonic stem cells and human embryonic kidney cells) on silicon substrates with vertically aligned Si nanowires (SiNWs) of varying diameter (Ø = 30-400 nm, length = 3-6 µm) (Figure 1.20 (b)).[140] NWs were reported to penetrate through the cell membrane within the first hours after seeding and the longevity of the resulting pierced cells was found to be dependent on the diameter of the NWs: cell death occurred within a day when the culture was carried out on large diameter SiNWs (Ø ~ 400 nm), whereas cells grown on smaller diameter NWs (Ø ~ 30 nm) were viable for more than 5 days. Interestingly, functionalization of the NWs with electrostatically-bound DNA enabled the successful delivery of exogenous DNA inside the pierced cells.

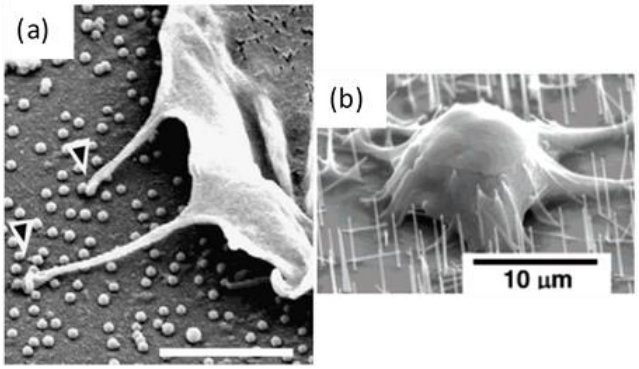


**Figure 1.20** *(a) SEM image of human fibroblast filopodia interacting with nanocolumns (arrowheads) (scale bar = 1 µm). [Adapted from Dalby et al.*[139]*] (b) SEM image of individual mouse embryonic stem cell penetrated with silicon NWs. The diameter and the length of the NWs are ~ 90 nm and ~ 6 µm, respectively.[Adapted from Kim et al.*[140]*].*

*d) Nanofibrils*

A simple and robust way to synthesize fibrous scaffolds mimicking the protein meshwork of native ECM is through electrospinning of polymers (of either synthetic or natural origin or a composite thereof). Hence, this technique has been widely investigated with a view to synthesize ECM-like scaffolds able to host cells and influence their behaviour. For instance, seeding mouse MC3T3-E1 osteoprogenitor cells on electrospun PMMA fibers (1.153±0.310 µm diameter) was shown to facilitate their osteogenic differentiation as compared to cells cultured on flat PMMA surfaces (a 2-fold increase in ALP activity was measured for cells grown on fibres).[141] This enhanced osteoblastic differentiation was associated with an increase (1.5-fold increase) in the elastic modulus of the cells cultured on fibres compared to plain substrates. Stretching of the cells to anchor across distinct fibres of the fibrous substrates thus generates an increased intracellular tension which in turn promotes the osteoblastic phenotype.

### 1.2.5 Influence of mechanical cues

As developed in section 1.1.4, cells can sense the stiffness of their microenvironment as their intracellular cytoskeleton is coupled to the ECM through anchorage points (i.e., FAs and other types of adhesion structures). The cells are usually documented to exert traction forces on their extracellular environment to probe its resistance and to organize their cytoskeleton accordingly in order to withstand the level of mechanical stress present in the extracellular medium. This mechanism of stress accommodation further initiates signalling cascades which ultimately result in changes in gene expression and modification of cell behaviour.

*a) Influence of substrate stiffness on cell adhesion and spreading*

When it comes to adhesion and spreading, a general rule seems to be that, all other parameters being held constant (e.g., density of cell-adhesive ligands), most cells spread more and display more organized FAs and actin stress fibres on stiffer substrates, a phenomenon termed 'durotaxis'. [142–144] Pelham and Wang evidenced that cells (rat kidney epithelial cells and 3T3 fibroblasts in this case) tended to organize more stable FAs and spread better on stiffer substrates.[142] In contrast, cells grown on softer substrates displayed more dynamic FAs and correspondingly lower projected area and higher motility. Engler *et al.* later demonstrated that the projected area of smooth

muscle cells (SMCs, derived from rat aorta) followed a saturable hyperbolic trend with the increase in the elastic modulus of the substrate, the saturation being reached for cells grown on glass (Figure 1.21).[143,145] Yeung *et al*. clearly highlighted a shift in the morphology of adherent fibroblast (mouse NIH-3T3) and endothelial (from bovine aorta) cells when increasing the substrate's modulus above 2,000 Pa, with cells developing a spread morphology and visible actin stress fibres only above this level.[146] Moving away from polyacrylamide gels, Picart and colleagues designed biocompatible multilayer films made of poly(L-lysine) and HA, which were chemically cross-linked to modulate the Young's modulus of the film from ~ 3 kPa (native films), ~ 100 kPa (weakly cross-linked films) and up to ~ 400 kPa (highly cross-linked films).[147] Mouse C2C212 myoblast cells were found to adhere better, form more numerous and larger FAs and proliferate better with increasing stiffness of the underlying multilayer. Upon incubation with differentiation medium, cells seeded on stiffer substrates differentiated into larger and more mature myotubes (i.e., precursors of contractile skeletal muscle cells) but this morphological change was not associated with an overexpression of muscle-specific proteins.

Degand *et al.* synthesized substrates with mechanical nanoheterogeneities by depositing silica colloids (Ø 500 nm, E ~ 70 GPa) on glass slides and subsequently spin-coating them with a PDMS gel of tunable elasticity (soft, $E_{soft}$ ~ 1 kPa versus stiff, $E_{stiff}$ ~ 1 MPa PDMS gels).[148] MC3T3-E1 preosteoblasts cultured on substrates with mechanical heterogeneities formed more developed FAs, cytoskeleton and proliferated better after 3 days of incubation than cells seeded on homogeneous PDMS films and that, irrespective of the stiffness of the PDMS gels. Moreover, the characteristics of the cells grown on substrates with subcellular mechanical heterogeneities made of silica were similar to those of cells seeded on homogeneously stiff glass slides.

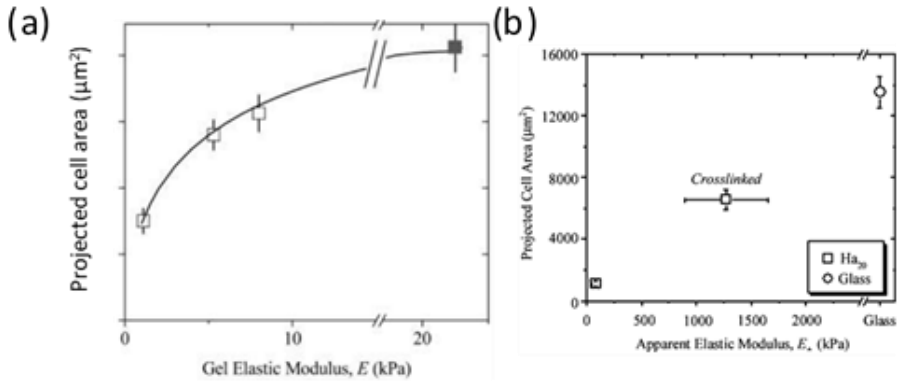


**Figure 1.21** *(a) Projected area of SMCs as a function of the elastic modulus of the substrate 4 h after plating them on polyacrylamide gels with a varying Young's modulus (open squares) or on glass (black square).*[143] *(b) Projected area of SMCs seeded on either native or cross-linked (PLL/HA)$_{20}$ multilayer films or on glass, as a function of the substrate's elastic modulus.*[145]

As often argued in the present dissertation for other kinds of cues, the response to materials stiffness appears to be quite logically cell-type dependent as highly motile, non anchorage-dependent cells such as human neutrophils, for instance, seem to be insensitive to matrix stiffness.

### *b) Influence of substrate stiffness on cell differentiation*

Besides influencing the spreading and cytoskeletal organization of cells, mechanical cues appear to be potent inducers of differentiation in multipotent cells.

A general rule seems to be that exposing multipotent cells to mechanical properties similar to those naturally present *in vivo* in a selected tissue greatly contributes to selectively orient their differentiation into the phenotype of the selected tissue. For instance, Altman and coworkers demonstrated that bovine bone marrow cells could be induced to selectively differentiate into ligament fibroblast cells when seeded in a Col gel submitted to a combination of forces mimicking the mechanical strains to which ligament is naturally exposed *in vivo*.[149] This selective differentiation could be achieved in the absence of any biochemical effector and was clearly evidenced by a distinct alignment of the cells in the direction of mechanical loading and the upregulation of specific ligament fibroblast markers.

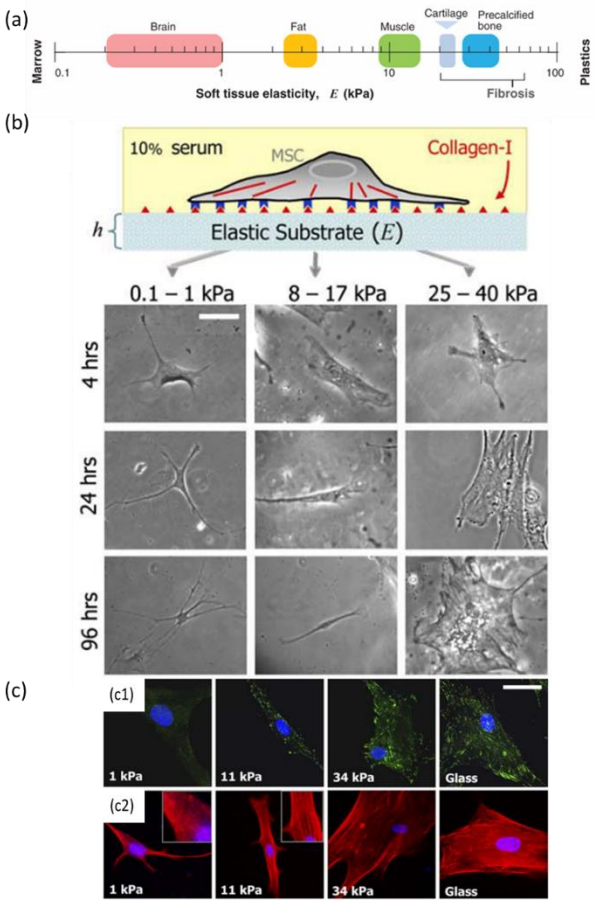


**Figure 1.22** *(a) Soft tissue elasticity scale ranging from soft brain, fat, and striated muscle, to stiff cartilage and precalcified bone.*[150] *(b) Differentiation of naive hMSCs as a function of the elastic modulus of polyacrylamide gel substrates. Naive hMSCs are initially small and round but develop increasingly branched, spindle, or polygonal shapes when grown on matrices respectively in the range typical of* $E_{brain}$ *(~ 0.1-1 kPa),* $E_{muscle}$ *(8-17 kPa) or stiff cross-linked matrices (E ~ 25-40 kPa). Scale bar is 20 µm.*[151] *(c) Adhesions grow and cytoskeletal organization increases with substrate stiffness. (c1) Paxillin-labeled adhesions grow from undetectable diffuse "contacts" on neurogenic soft gels (1 kPa) to punctate adhesions on stiffer, myogenic gels (11 kPa). On the stiffest, osteogenic gels (34 kPa), the adhesions are long and thin and slightly more peripheral than they appear on glass. (c2) F-actin organization shows a similar trend, from diffuse on soft gels to progressively organized on stiffer substrates (as stress fibers). Scale bar is 20 µm.*[151]

In a remarkable study, Engler and coworkers proved that matrix stiffness could drive the lineage commitment of naïve MSCs, without requiring any soluble inducer (i.e., other than serum supplementation) (Figure 1.22).[151] MSCs seeded onto soft polyacrylamide gels with a stiffness mimicking that of brain tissue ($E_{brain}$ ~ 0.1-1 kPa) showed both a morphology and a transcriptional profile similar to those of neurons, whereas plating these multipotent cells on harder substrates approaching the elasticity of striated muscle ($E_{muscle}$ ~ 8-17 kPa) and osteoids ($E_{bone}$ ~ 25-40 kPa) resulted in cells with a shape and gene transcript profile close to that of myoblasts and osteoblasts, respectively.

Chen *et al*. designed arrays of PDMS microposts whose height was varied in order to modulate their spring constant and hence the rigidity sensed by the cells seeded on top of them.[152] Micropost rigidity clearly impacted the cultured hMSCs, with rigid posts favouring the emergence of well-spread cells with highly organized actin stress fibers and large FAs whereas soft pillars gave rise to a rounded cell morphology, disorganized actin filaments and small adhesion complexes (Figure 1.23 (a)). In the absence of biochemical inducers, substrate rigidity alone was not potent in modulating cell fate. However, after a 2-week period incubation in a bipotential differentiation medium (i.e., mixture of both osteogenic and adipogenic effectors), micropost rigidity could tilt the balance of hMSCs differentiation: arrays of stiff microposts favored the osteogenic lineage while soft substrates enhanced adipogenic differentiation (Figure 1.23 (b1-2)). Moreover, a striking conclusion was that the commitment of single hMSCs could be predicted at early stages (between 1-3 days after differentiation medium addition) simply based on the level of traction forces exerted by individual cells. Indeed, hMSCs that underwent osteogenic differentiation displayed higher traction forces that non-differentiating cells while cells that committed to the adipogenic lineage displayed lower contractility that undifferentiated cells.

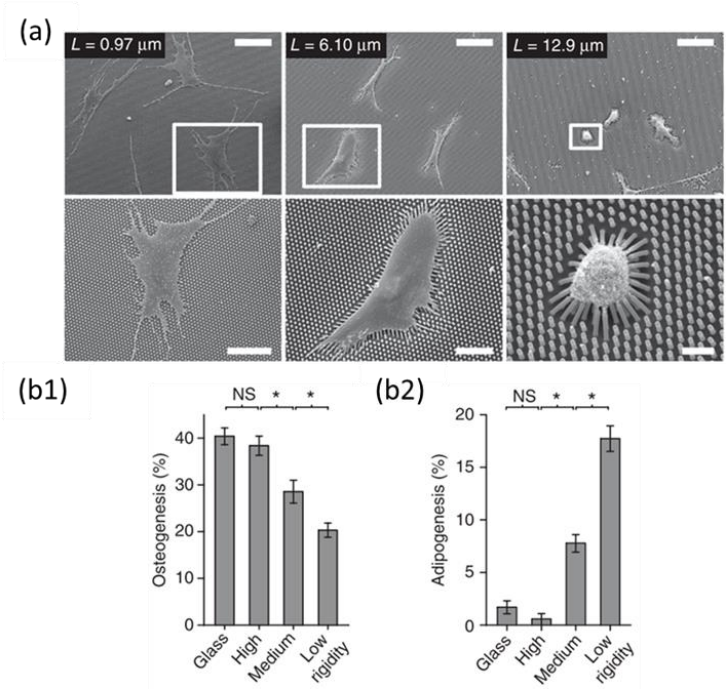


**Figure 1.23** *(a) SEM micrographs of hMSCs plated on PDMS micropost arrays of the indicated heights. Images at the bottom are magnifications of the boxed regions in the top images. Scale bars : 100 µm (top) and, from bottom left to right, 50, 30 and 10 µm. (b) Mean percentages of hMSCs osteogenesis (b1) and adipogenesis (b2) as a function of micropost rigidity. Glass served as a control. Error bars, standard error of the mean (n ≥ 3). NS, not significant (p > 0.05), *p < 0.05; Student's t-test. [Adapted from Fu et al.*[152]*].*

### *c) Stiffness in 2D versus 3D microenvironments*

Most of the observations linking substrate mechanics to cell fate have been collected from 2D tissue culture models but seem to hold also, at least in part, for more physiologically-relevant 3D microenvironments. When encapsulating naive mouse MSCs (mMSCs) into 3D alginate hydrogels (i.e., ionically cross-linked gels) modified to present RGD peptide epitopes and a tunable elastic modulus (varied between 2.5 and 110 kPa), Huebsch *et al.* observed a predominant osteogenic commitment of mMSCs after 1 week inside matrices with intermediate stiffness ($E$ ~ 1-30 kPa).[153] Softer gels ($E$ ~ 2.5-5 kPa), on the contrary, promoted the adipogenic lineage. However, in striking contrast with studies on 2D models, the difference in stiffness was

not associated with a significant change in cell morphology as cells remained grossly spherical under all conditions.

Baker *et al*. unveiled a previously unrecognized mechanism which cells seem to use to transduce matrix stiffness in fibrous 3D microenvironments: fibre recruitment.[154] These authors engineered fibrous environments recapitulating the architecture of native ECM via electrospinning of dextran methacrylate fibers, consecutive photocrosslinking to tune their stiffness (varied between 450 Pa and 45 kPa) and incorporation of RGD sequences to enable cell attachment (Figure 1.24). The response of hMSCs seeded inside these 3D fibrillar meshworks was inverted compared to that on commonly investigated 2D hydrogels, as cells formed more numerous FAs of higher size on softer fibre networks, where they were able to pull and deform the architecture so as to recruit nearby fibres and form dense clusters. This led to a local increase in adhesive ligand density, enhanced adhesive signalling and proliferation. Conversely, cells were unable to pull on and remodel networks of stiffer fibres, resulting in downregulated adhesion and proliferation.

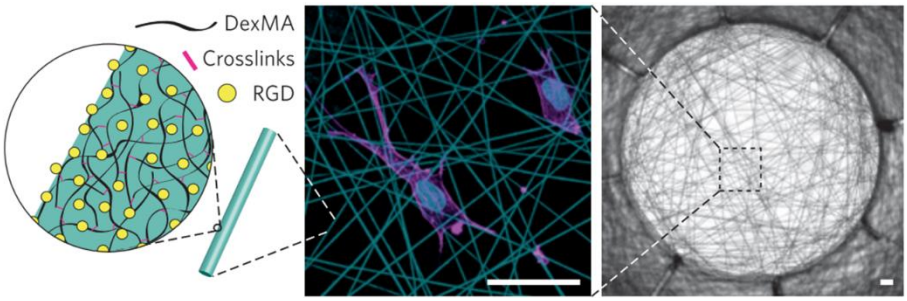


**Figure 1.24** *Cell-adhesive networks of dextran methacrylate fibres with tunable mechanical and architectural features. Scale bars, 100 µm.*[154]

### *d) Influence of viscoelastic properties*

In line with these recent observations, Chaudhuri *et al*. confirmed that cells not only sense and react to the stiffness of the substrate but also to its viscoelastic properties and stress relaxation profile.[155] Indeed, most conclusions regarding the way cells sense the elasticity of their environment by exerting traction forces have been achieved on purely elastic substrates (e.g., covalently cross-linked gels), whereas the physiological ECM is viscoelastic. On the contrary to purely elastic materials (i.e., displaying a constant resistance to traction forces over time), the viscoelastic ECM

exhibits stress relaxation over time, meaning that the resistance to the traction forces exerted by the cells decreases over time as some of the energy imparted by the cells is consumed to generate a remodelling (i.e., plastic deformation) of the matrix. In parallel to stiffness, plastic deformation of the substrate allows integrin clustering and thus similarly activates intracellular signalling processes. Evidences indeed highlighted that increased stress relaxation could compensate for matrices with a lower stiffness, as the spreading and proliferation of cells (human osteosarcoma U2OS cell line) were increased on substrates with stress relaxation (i.e., ionically cross-linked alginate hydrogels) compared to elastic substrates (i.e., covalently cross-linked alginate hydrogels) with the same initial elastic modulus.

***In summary, chemical, topographical/geometrical and mechanical signals are the main parameters which are presented to the cells through the ECM and which regulate their behaviour. Most of these cues are transmitted to the cells via the cytoskeleton/ECM coupling through the integrins and are thus actually subordinated to the successful anchoring of the integrins to adhesion proteins present in the extracellular medium. The design and characterization of cell-instructive biomaterials mimicking both the structure and functions of the ECM and thus recapitulating most of the documented cell-influencing cues is likely to be beneficial for TE and regenerative medicine applications.***

***Following discoveries on how ECM influences cell fate, a new paradigm emerged among scientists which consists in engineering artificial ECM analogs combining as many cell-influencing cues as possible and using them as scaffolds for tissue engineering and repair.***

## 1.3 Artificial ECM analogs

As an alternative to the biological scaffolds (described in section 1.1.3) derived from the top-down processing (i.e., decellularization) of native tissue ECM, artificial ECM-like materials can be built from a bottom-up approach, using synthetic or biological building blocks[156]. The development of bioinspired artificial matrices has become one of the most important paradigms in tissue engineering research nowadays. Compared to acellular tissues of natural sources, artificial matrices enable to circumvent concerns over pathogen transmission, immune rejection, batch-to-batch consistency and their design allows for more control over the composition, mechanical properties and biodegradability so as to orient cell processes in a specific manner. Such engineered matrices should chemically and structurally mimic the native ECM and its characteristic cell-influencing cues (described in section 1.2) so as to induce particular types of cells to function in their native manner and ultimately restore, maintain or improve damaged tissues and organs. Synthetic mimics of the natural ECM have mainly been produced in the form of hydrogels, micro- and macro-porous polymeric foams and nanofiber mats.

### 1.3.1 Hydrogels

Hydrogels are formed *via* cross-linking of polymers into an insoluble network which can adsorb high amounts of water without dissolving. By appropriately tailoring the polymer chemistry and cross-linking density, the physical properties of the hydrogel, such as its water content, mechanical strength and elasticity, and its biodegradability can be manipulated to resemble those of particular natural tissues. Furthermore, biological cues such as bioactive peptides, proteins and proteoglycans can be integrated into hydrogels through either covalent linkages or non-covalent interactions. Hydrogels can serve as 2-D substrates for cell culture or as 3-D micro-environments, with cells being seeded on top or encapsulated during the cross-linking process.[156] Being intrinsically permeable to oxygen, nutrients and other water-soluble compounds and enabling angiogenesis and osteoconductivity, hydrogels are attractive materials for tissue

engineering.[157,158] Hydrogels have been developed from synthetic polymers such as poly(ethylene glycol) (PEG)[159,160] and from natural polymers such as agarose[161,162], alginate[163–165], HA[82,166,167] and Col[168,169]. Composite hydrogels, combining synthetic and natural polymers and/or ceramic particles were developed to compensate for the uncontrolled degradation of biopolymers and to allow better control over mechanical properties.[170,171] Bioinert hydrogels (e.g., alginate, PEG) have usually been covalently functionalized with adhesive RGD peptides to facilitate cell adhesion and spreading.[159,163] Growth factors[167], drugs[157] and ceramic particles[170] have also been encapsulated within hydrogels to increase their bioactivity. MacDonald et *al*. incorporated single-walled carbon nanotubes (SWCNTs) into a Col hydrogel in order to take advantage of their high aspect ratio and outstanding mechanical and electrical properties.[172] Main advantages of hydrogels include their tunable mechanical properties as well as the fact that they can easily be loaded with cells and drugs and injected into the body in a minimally invasive manner.[157,173–176] More recently, the 3D printing technology has enabled the use of hydrogels as a bioink and opened the possibility of their patterning into complex 3-D shapes mimicking tissue macro- and microarchitectures.[157,158,165,177] The main drawback of hydrogel biomaterials is their low mechanical strength which limits their use in load-bearing applications (e.g., bone tissue engineering).[157,173] Moreover, the micro- and nano-architectures of gel biomaterials cannot be easily tailored which restricts the possibility to present encapsulated cells with topographical cues.

### 1.3.2 Microporous polymeric scaffolds

The production of microporous polymeric membranes/scaffolds mainly involves the introduction of a porogen into a polymer solution or melt; casting of the mixture into a mould of the desired shape, hardening of the polymer around the porogen and subsequent dissolution of the porogen to leave pores in the polymer matrix.[157,173] Traditionally used porogens include water (i.e., freeze-drying), $CO_2$ (i.e., gaz foaming), organic solvents (i.e., phase separation) or water-soluble salt particles (i.e., solvent casting and particulate leaching).[157,173] Many research groups focussed on the processing of ECM-derived biopolymers into microporous ECM analogs *via* freeze-drying and explored their potential as scaffolds for tissue engineering[178]. Col scaffolds with pores of a hundred microns were obtained via carbodiimide cross-linking (i.e., use of EDC, 1-ethyl-3-(3-dimethylaminopropyl)-

carbodiimide) of native collagen followed by freeze-drying and were seeded with fibroblasts.[179] Composite Col/HA[180,181], Col/Chondroitin-6-sulfate (CS)[182,183] and Col/elastin[184] sponges were produced in a similar manner and investigated as skin or blood vessels substitutes. Synthetic bioresorbable and FDA-approved polymers such as aliphatic polyesters, including poly(glycolic acid) (PGA), poly(L-lactid acid) (PLLA), poly(Ɛ-caprolactone) and their copolymers, have been widely used for the preparation of microporous scaffolds.[185–187]

In order to impart microporous scaffolds with electrical conductivity and offer the possibility to electrically stimulate the hosted cells, composite biomaterials including conducting polymers were produced. Sajesh *et al.* synthesized a conducting scaffold *via* freeze-drying and chemical cross-linking of a mixture containing a polypyrrole (PPy, a conducting polymer)-alginate blend dispersed in a chitosan solution.[188] Baniasadi *et al.* prepared a highly conductive chitosan/gelatin porous scaffold (with a pore size in the range 100-300 µm) loaded with PPy/graphene nanocomposite particles and highlighted promising results for nerve regeneration applications.[189]

Natural bone tissue being a biocomposite in which inorganic apatite (i.e., calcium phosphate mainly in the form of hydroxyapatite, HyAp, chemical formula $Ca_{10}(PO_4)_6(OH)_2$) crystals are nucleated on Col fibers, a great deal of research has explored the production of organic/inorganic composite scaffolds for bone tissue engineering. The bioceramic particles can be added as a filler during the manufacture of the scaffold, in the form of a commercial powder[190,191] or a precipitate[192] or, alternatively, can be nucleated *in situ*, after completion of the scaffold processing, *via* an alternate soaking process[193] or through incubation in a simulated body fluid (SBF)[194]. The group of Kaplan prepared a silk fibroin/polyaspartic acid scaffold (pore size ~750±20 µm) *via* a solvent casting/particulate leaching method and subsequently mineralized it with calcium phosphate using an alternate soaking process (i.e., cyclic exposure to $CaCl_2$ and $Na_2HPO_4$ solutions).[193] Liao et al. mineralized Col fibril *via* precipitation of HyAp nanocrystals in a Col solution, freeze-dried the mixture and suspended the resulting powder in a PLLA/dioxane solution which was casted and freeze-dried to produce a porous PLLA matrix (pore size 100-400 µm) uniformly filled with Col/HyAp nanocomposites.[192] Polymer/carbon nanotube (CNT) composite scaffolds were also produced, either from natural[195–198] or synthetic[199,200] polymers, with a view to taking advantage of the high mechanical strength and high

specific surface area developed by the nanostructured CNT. In addition to providing nanotopographical cues reminiscent of the structure of native ECM proteins, CNT showed strong protein adsorption which favoured cell adhesion, proliferation and differentiation.[195–200] In order to enhance the cell-material interactions, the surface of scaffolds derived from synthetic polymers can be modified with bioactive polymers either *via* covalent bonding[201] or through the layer-by-layer (LbL) assembly technique (developed in section…) based on weak interactions. For instance, Gong *et al.* functionalized the surface of a microporous aminolyzed PLLA scaffold with a LbL-assembled CS/Col multilayer and evidenced improved adhesion and proliferation of chondrocytes.[202] Although polymeric microporous scaffolds offer the possibility to physically support cell growth in a 3-D micro-environment and present them with various bioactive cues, these systems lack adequate mechanical properties for load-bearing applications and the nanoscale topography in contact with cells cannot be easily manipulated.

### 1.3.3 Nanofibrous polymeric mats

Nanofiber mats have attracted considerable attention as their structure recapitulates the nanofibrillar topography of native ECM (e.g., collagen fiber bundles with diameter in the range 50-500 nm).[203,204] Their large surface area advantageously increases the amount of adsorbed proteins and biochemical effectors which can be presented to the cells in a fashion much similar to *in vivo* conditions, leading to enhanced cellular responses. Moreover, the microporosity inbetween fibers enables the mass transport of nutrients and waste products.[204,205]Biomaterials which mimic the architecture of structural proteins within ECM have mostly been produced using electrospinning, phase separation and self-assembly.[204,206,207] The electrospinning technique entails application of a high voltage to a polymer solution or melt in order to form a charged jet which is collected onto a grounded substrate and solidified into continuous fibers with a diameter ranging from several microns down to 50 nm. This technology has been used extensively to synthesize nanofibers out of natural and synthetic polymers or even composites and to organize them into randomly- or preferentially-oriented fiber mats.[204,208]

Electrospun Col fibers of various diameters (from 50 to 1000 nm), either chemically cross-linked *via* EDC[209] or not[210], were produced by different groups starting from a Col solution in HFP (1,1,1,3,3,3 hexafluoro-2-propanol) and showed promising results for the growth of hMSCs and their

osteogenic differentiation. Venugopal *et al*. synthesized biomimetic nanofibers much similar to the bone ECM *via* co-precipitation of a chitosan/HyAp nanocomposite, redispersion in an aqueous acetic acid/dimethyl sulfoxide (DMSO) system and subsequent co-electrospinning of the solution with a poly(ethylene oxide) additive.[211] The use of nanofiber mats, endowed with electrical conductivity through functionalization with a conducting polymer shell, was investigated for neural tissue engineering. Thunberg *et al.* synthesized a matrix of electrospun cellulose nanofibers which were functionalized via in situ chemical polymerization of pyrrole monomers. Human neuroblastoma cells (SH-SY5Y) showed increased adhesion on the PPy-modified mats and adopted a neuron-like morphology.[212] Martin's group used an electrospun mat of PLLA nanofibers, supported on a neural microelectrode, as template for the electrochemical deposition of poly(3,4-ethylenedioxythiophene) (PEDOT) or PPy. After dissolution of the PLLA core, the matrix of conducting-polymer NTs was used for the culture of primary neurons.[213] In another study, Martin *et al.* prepared poly(L, D-lactic acid) (PLDLA) nanofibers loaded with an anti-inflammatory drug (dexamethasone), supported on a microelectrode, and subsequently functionalized with a PEDOT shell and encapsulated within an alginate hydrogel.[214]

In order to combine the better stability of synthetic polymers with the bioactivity of natural ones, a wide range of composite nanofibrous scaffolds were developed. For this purpose, biopolymers were introduced in the system either *via* co-electrospinning[215,216] or by adsorption[217], covalent binding or LbL assembly[205,218] on the surface of the processed matrix. In recent years, electrospun systems of increasing complexity have been created with a view to better emulate the structure, composition and functions of native ECM. These complex fibrous matrices most often combine a synthetic polymer core (providing mechanical stability and delayed degradability), biopolymer (providing cell-adhesive cues) and conducting polymer (enabling electro-stimulation of seeded cells) coatings and growth factors (stimulating the growth and differentiation of cells) and/or bioceramic (imparting osteoinductivity as well as a composition and mechanical properties close to bone tissue) functionalisations. Such systems were mainly investigated for bone and nerve tissues regeneration. Meaningful examples include the synthesis of synthetic polymer nanofibers, polymerization of a conducting polymer shell and subsequent adsorption of a cell-adhesive biopolymer such as CoI.[219–221]

Zeng *et al*. prepared an electrospun PLLA matrix which was further coated with a poly(glutamic acid) and sodium dodecyl sulfate (SDS) co-doped PPy shell and covalently functionalized first with poly(L-lysine) (PLL) and then with nerve growth factor (NGF) *via* EDC chemistry.[222] Zhang *et al.* produced core-shell nanofibers through co-axial electrospinning of a lysine-doped solution containing NGF as the core and a PLLA/silk protein as the shell. This system was evaluated as a guide for nerve regeneration in a rat model.[223] HyAp NPs were also introduced in nanofibrous matrices either *via* dispersion in a polymer solution and co-electrospinning[224] or by nucleation (i.e., alternate soaking process in $CaCl_2$ and $Na_2HPO_4$)[225] on the fiber surface. Wang et al. demonstrated the possibility to stack sheets of electrospun PCL/Col/HyAp composite nanofibers seeded with mouse BMSCs (stacking of 20 sheets, leading to a thickness of ~200 µm) to produce a biomimetic tissue-engineered periosteum. The resulting flexible tissue membrane was wrapped around a structural bone allograft and shown to improve the healing of a bone defect in the mouse femur.[226]

Despite its versatility in tailoring nanoscaled fibers of tunable compositions and diameters mimicking those of the native ECM environment, electrospinning has the disadvantage of being hardly scalable for the production of complex 3-D shapes. Indeed, most electrospun nanofibrous mats have a thickness in the range of 30 to 50 µm, which positions them rather as cell-influencing membranes than as implantable 3D scaffolds. Moreover, the electrospinning process requires organic solvents which could potentially cause deleterious effects on the bioactivity of any protein compound added in the electrospun mixture.

## 1.4 Layer-by-layer (LbL) assembly

As already evidenced in the previous section, the LbL self-assembly is an easy and versatile method to functionalize the surface of materials with nanostructured films imparting interesting properties such as cell-adhesivity, catalytic activity, drug loading and delivery, etc. Since its introduction by Decher and co-workers in 1991[227,228], the LbL assembly has become the prevalent method to functionalize surfaces, especially those of biomaterials. The LbL process indeed offers many advantages: it is a simple and inexpensive technique, it is highly versatile as it allows a wide variety of materials to be incorporated within the multilayer, it generates stable multilayered films whose layering sequence and nanometer thickness can be

finely tuned and it can be efficiently used to functionalize substrates with complex structures and irregular topographies.[229–232] Moreover, the LbL assembly can be achieved under soft aqueous conditions in a manner similar to the natural physiological processes through which individual molecules spontaneously self-assemble into complex architectures in the body (e.g., nucleic acid and protein assembly). In view of this, the LbL technique has supplanted earlier surface functionalization techniques such as Langmuir-Blodgett (LB) deposition[233–235] and self-assembled monolayers (SAMs)[236,237] which suffer from various flaws. Among the drawbacks of the LB deposition are the need for expensive instrumentation and long fabrication periods, the limited range of molecules that can be assembled as the technique is restricted to the use of amphiphilic components, and the rather low stability of the resulting film. Surface functionalization with SAMs, on the other hand, is limited to the construction of a monolayer of thiolated or silanized compounds on noble metals or silica surfaces, respectively, which further limits the loading capacity of biomolecules within the film and offers low stability under physiological conditions.[229–232]

The LbL assembly has preponderantly been conducted relying on electrostatic interactions between oppositely-charged polymers, alternately adsorbed on a substrate, to produce multilayered thin films of controlled nanometer thickness. The driving force for such assemblies based on electroattractive interactions is the excess adsorption of each charged compound during each layer deposition and the charge overcompensation and charge reversal which result from it.[230,238] Since the original introduction of the LbL method based on electrostatic interactions, many other types of intermolecular interactions were investigated, including covalent bond[239–242], hydrogen bonding[243–247], charge transfer[248], host-guest[249–252], coordination bond[253–258], hydrophobic[259,260] and specific biological interactions (i.e., avidin-biotin[261–263], antibody-antigen[264,265], lectin-polysaccharides[266,267] and fibronectin (FN)-ECM proteins and glycosaminoglycans[268–272]). Moreover, researchers have extended the LbL technique to assemble not only conventional water-soluble synthetic polymers[238,273–276] but also viruses[277], proteins[278–280], silica colloids[281–283], metal NPs[284], dyes[285,286], metal oxides[287,288], clays[289,290], PS nanospheres[291,292] and living cells[268–272].

### 1.4.1 Template-assisted LbL assembly

The LbL process being achievable on any charged surface, it can be carried out on micro- or nano-structured substrates in order to organize the assembling molecules into complex supramolecular micro- or nanostructures. As such, assembling polymers in a LbL fashion onto the surface of colloidal particles used as hard templates is a widely used method to produce hollow capsules after dissolution of the colloidal core.[282,293] These hollow capsules were mainly used for the encapsulation and controlled release of guest substances.[294–301] Similarly, conducting the LbL assembly within a membrane with cylindrical nanopores (*i.e.*, the template synthesis method reported by Martin *et al*[302,303]), enables the production of NTs.[304–308]

Many research groups achieved the synthesis of protein-based NTs *via* this template-assisted LbL method carried out either within the nanopores of anodic aluminium oxide (AAO) or track-etched PC membranes. Martin and co-workers produced glucose oxidase (Gox) and hemoglobin (Hb) NTs through alternate filtration of protein solution and glutaraldehyde (GA) cross-linker. Gox- and Hb-based NTs were shown to retain their catalytic activity and electroactivity, respectively.[305] Li and co-workers synthesized cytochrome-C NTs *via* covalent binding using GA or electrostatic interactions with the strong PE poly(styrene sulfonate) (PSS).[309] The same group designed single-component human serum albumin (HSA) NTs and phospholipid/HSA NTs through electrostatic interactions.[310] The group of Liang produced single-component avidin and bovine serum albumin (BSA) NTs through electrostatic assembly.[311,312] The group of Komatsu focussed on the engineering of HSA-based NTs electrostatically-assembled in combination with various synthetic polycations such as poly(allylamine hydrochloride) (PAH), poly(L-arginine) (PLA), poly(L-lysine hydrobromide) (PLL), poly(ethylene imine) (PEI).[313–316] They further demonstrated the opportunity to functionalize the inner surface of the protein NTs with an enzyme[317], antibody[280], or avidin[318] layer or with gold[319] or Pt[320] NPs. PLA/ferritin[314,321,322] and PLA/myoglobin[314] NTs were also produced. Sadeghi *et al*. synthesized poly(D-lysine)/BSA NTs.[323] Jiao *et al*. produced PEI/BSA NTs which were shown to entrap DNA with high affinity.[324] The group of Demoustier-Champagne and Jonas evidenced the production of enzymatically-active PEI/Gox NTs[325] and PLA or PAH/ovalbumin NTs[326] which were successfully internalized by dendritic cells. Maldonado and Kokini elaborated edible BSA/alginate NTs.[327]

Recently, ion track-etched polymer templates of increasing complexity were developed, displaying a 3-D network of interconnected nanochannels whose dimensions can be tuned.[328,329] Combining the LbL assembly process with such templates displaying a nanostructured porosity of complex and tunable architecture, could potentially lead to the organization of biological molecules into complex 3-D networks offering the combined advantages of macroscaled dimensions and the display of cell-influencing cues at the nanoscale.

### 1.4.2 LbL assembly of biopolymers for cell-contacting applications

Owing to its versatility and its ability to be carried out under soft biomimetic conditions, the LbL technique has been widely employed to synthetize polymeric coatings, membranes and NTs out of natural macromolecules, with a view to target cell-contacting applications.

Many researchers developed Col-containing thin films built *via* LbL assembly in order to improve the cell-adhesion properties of various substrates. Col/HA coatings were assembled on titanium[330,331] and silica substrates[332] and evidenced to positively impact the adhesion and proliferation of hMSCs and mouse preosteoblasts. Grant *et al.* built Col/PSS thin films on the bottom of Petri dishes and investigated their biological properties using C2C12 myoblast and PC12 pheochromocytoma cells.[333]Mhanna et *al.* functionalized PDMS substrates with Col/chondroitin sulfate and Col/heparin films and used these systems for the culture of bovine chondrocytes.[334] Col was LbL-assembled in combination with alginate on the surface of glass slides and PLA electrospun scaffolds by *Li et al*. The biocompatible coating was evidenced to improve the adhesion and proliferation of human periodontal ligament cells.[335] Chaubaroux et al. similarly produced Col/alginate coatings but chemically cross-linked the multilayer using a natural agent, genipin, and evaluated their cell compatibility with human umbilical vein endothelial cells.[336] Lin *et al.* coated the surface of a stainless steel stent with a Col/heparin multilayer which was cross-linked with glutaraldehyde and further functionalized with an anti-CD34 antibody. The authors evidenced that the anti-CD34-functionalized Col/heparin coating could selectively promote the attachment and growth of vascular endothelial cells (bearing CD34 antigen on their surface), at the expense of smooth muscle cells, therefore reducing the risks of in-stent restenosis.[337] Gao *et al*. functionalized the surface of a poly(ethylene terephthalate) (PET) vascular graft with a Col/chondroitin sulfate multilayer

and showed that the attachment, growth and viability of endothelial cells on the graft was enhanced.[338]

Picart and co-workers produced an abundant literature on the development of polysaccharide-based multilayers, the modification of their mechanical properties via chemical EDC/s-NHS cross-linking and the corresponding influence on the behaviour of seeded cells.[339–341] The group mainly investigated the buildup of PLL/HA[342–350], chitosan/HA[345,348,351], HA/Col[352], PLL/chondroitin sulfate and PLL/heparin multilayered films[350]. In a recent paper, the group engineered free-standing (thickness ~ 50 µm) membranes based on the electrostatic LbL assembly of two polysaccharides, alginate and chitosan, which were further chemically cross-linked and loaded with the osteoinductive growth factor bone morphogenetic protein 2 (BMP-2). The more cross-linked membranes showed myoconductive and osteoinductive capacities both *in vitro* when seeded with murine C2C12 skeletal myoblasts and *in vivo* when implanted in a mouse ectopic model.[353] Fujie *et al.* synthesized a free-standing Col/HA thin film (i.e., denoted as ECM-nanosheet; ~ 62 nm thick) by initiating the LbL assembly of Col and HA on a $SiO_2$ substrate covered with a water-soluble poly(vinyl alcohol) supporting film. Incubation of the ECM-nanosheets under physiological conditions (i.e., PBS buffer at 37°C) led to partial dissociation of HA and reorganization of the remaining HA-depleted Col layers into microfibrils, which further increased the spreading of the seeded NIH-3T3 cells.[354]

The group of Matsusaki recreated a nanostructured ECM-like meshwork on the surface of living cells (e.g., mouse L929 fibroblast, human umbilical vein endothelial, human hepatocellular carcinoma cells, etc.) using the LbL assembly of FN/gelatin or FN/dextran sulfate based on specific interactions between FN and the FN-binding domain found in many ECM molecules.[268,272] By stacking several layers of FN/gelatin-functionalized cells, they further managed to build complex 3-D cellular multilayers mimicking natural tissue constructs within incubation times as low as 1 day.[270–272]

The group of Dupont-Gillain and Demoustier-Champagne elaborated Col/PSS NTs displaying Col in their outermost layer[355–357] which were further collected on a glass substrate by electrophoretic deposition and seeded with mouse MC3T3-E1 preosteoblasts. The cells were observed to specifically interact with Col-based NTs through filopodia.[358,359]

## 1.5 References

(1) Campbell, N. A.; Reece, J. B. Biology, Pearson.; Cummings, B., Ed.; Boston, MA, 2005.

(2) Fernandes, H.; Moroni, L.; van Blitterswijk, C.; de Boer, J. Extracellular Matrix and Tissue Engineering Applications. J. Mater. Chem. 2009, 19 (31), 5474. https://doi.org/10.1039/b822177d.

(3) Lutolf, M. P.; Hubbell, J. A. Synthetic Biomaterials as Instructive Extracellular Microenvironments for Morphogenesis in Tissue Engineering. Nat. Biotechnol. 2005, 23 (1), 47–55. https://doi.org/10.1038/nbt1055.

(4) Kleinman, H. K.; Philp, D.; Hoffman, M. P. Role of the Extracellular Matrix in Morphogenesis. Curr. Opin. Biotechnol. 2003, 14 (5), 526–532. https://doi.org/10.1016/j.copbio.2003.08.002.

(5) Chen, X. D.; Dusevich, V.; Feng, J. Q.; Manolagas, S. C.; Jilka, R. L. Extracellular Matrix Made by Bone Marrow Cells Facilitates Expansion of Marrow-Derived Mesenchymal Progenitor Cells and Prevents Their Differentiation into Osteoblasts. J. Bone Miner. Res. 2007, 22 (12), 1943–1956. https://doi.org/10.1359/jbmr.070725.

(6) Ramirez, F.; Rifkin, D. B. Cell Signaling Events: A View from the Matrix. Matrix Biol. 2003, 22 (2), 101–107. https://doi.org/10.1016/S0945-053X(03)00002-7.

(7) Streuli, C. Extracellular Matrix Remodelling and Cellular Differentiation. Curr. Opin. Cell Biol. 1999, 11 (5), 634–640. https://doi.org/10.1016/S0955-0674(99)00026-5.

(8) Gustafsson, E.; Fässler, R. Insights into Extracellular Matrix Functions from Mutant Mouse Models. Exp. Cell Res. 2000, 261 (1), 52–68. https://doi.org/10.1006/excr.2000.5042.

(9) Löhler, J.; Timpl, R.; Jaenisch, R. Embryonic Lethal Mutation in Mouse Collagen I Gene Causes Rupture of Blood Vessels and Is Associated

with Erythropoietic and Mesenchymal Cell Death. Cell 1984, 38 (2), 597–607. https://doi.org/10.1016/0092-8674(84)90514-2.

(10) Snead, M. P.; Yates, J. R. W. Clinical and Molecular Genetics of Stickler Syndrome. J. Med. Genet. 1999, 36 (5), 353–359. https://doi.org/10.1136/jmg.36.5.353.

(11) Datta, N.; Pham, Q. P.; Sharma, U.; Sikavitsas, V. I.; Jansen, J. A.; Mikos, A. G. In Vitro Generated Extracellular Matrix and Fluid Shear Stress Synergistically Enhance 3D Osteoblastic Differentiation. Proc. Natl. Acad. Sci. 2006, 103 (8), 2488–2493. https://doi.org/10.1073/pnas.0505661103.

(12) Hendrix, M. J. C.; Seftor, E. A.; Seftor, R. E. B.; Kasemeier-Kulesa, J.; Kulesa, P. M.; Postovit, L.-M. Reprogramming Metastatic Tumour Cells with Embryonic Microenvironments. Nat. Rev. Cancer 2007, 7 (4), 246–255. https://doi.org/10.1038/nrc2108.

(13) Postovit, L.-M.; Margaryan, N. V.; Seftor, E. A.; Kirschmann, D. A.; Lipavsky, A.; Wheaton, W. W.; Abbott, D. E.; Seftor, R. E. B.; Hendrix, M. J. C. Human Embryonic Stem Cell Microenvironment Suppresses the Tumorigenic Phenotype of Aggressive Cancer Cells. Proc. Natl. Acad. Sci. 2008, 105 (11), 4329–4334. https://doi.org/10.1073/pnas.0800467105.

(14) Ott, H. C.; Matthiesen, T. S.; Goh, S. K.; Black, L. D.; Kren, S. M.; Netoff, T. I.; Taylor, D. A. Perfusion-Decellularized Matrix: Using Nature's Platform to Engineer a Bioartificial Heart. Nat. Med. 2008, 14 (2), 213–221. https://doi.org/10.1038/nm1684.

(15) Kleinman, H. K.; Martin, G. R. Matrigel: Basement Membrane Matrix with Biological Activity. Semin. Cancer Biol. 2005, 15 (5), 378–386. https://doi.org/10.1016/j.semcancer.2005.05.004.

(16) Bradham, D. M.; Passaniti, A.; Horton, W. E. Mesenchymal Cell Chondrogenesis Is Stimulated by Basement Membrane Matrix and Inhibited by Age-Associated Factors. Matrix Biol. 1995, 14 (7), 561–571. https://doi.org/10.1016/S0945-053X(05)80005-8.

(17) Kubota, Y.; Kleinman, H. K.; Martin, G. R.; Lawley, T. J. Role of Laminin and Basement Membrane in the Morphological Differentiation of

Human Endothelial Cells into Capillary-like Structures. J. Cell Biol. 1988, 107 (4), 1589–1598. https://doi.org/10.1083/jcb.107.4.1589.

(18) Nicosia, R. F.; Ottinetti, A. Cultures of Rat Aorta : A Comparative Study Of. 1990, No. February, 119–128.

(19) Brizzi, M. F.; Tarone, G.; Defilippi, P. Extracellular Matrix, Integrins, and Growth Factors as Tailors of the Stem Cell Niche. Curr. Opin. Cell Biol. 2012, 24 (5), 645–651. https://doi.org/10.1016/j.ceb.2012.07.001.

(20) Badylak, S. F.; Freytes, D. O.; Gilbert, T. W. Extracellular Matrix as a Biological Scaffold Material: Structure and Function. Acta Biomater. 2009, 5 (1), 1–13. https://doi.org/10.1016/j.actbio.2008.09.013.

(21) Wainwright, D. J. Use of an Acellular Allograft Dermal Matrix (AlloDerm) in the Management of Full-Thickness Burns. Burns 1995, 21 (4), 243–248. https://doi.org/10.1016/0305-4179(95)93866-I.

(22) Jung, S. N.; Chung, J. W.; Yim, Y. M.; Kwon, H. One-Stage Skin Grafting of the Exposed Skull with Acellular Human Dermis (AlloDerm). J. Craniofac. Surg. 2008, 19 (6), 1660–1662. https://doi.org/10.1097/SCS.0b013e31818ac258.

(23) Hofmann, A.; Konrad, L.; Gotzen, L.; Printz, H.; Ramaswamy, A.; Hofmann, C. Bioengineered Human Bone Tissue Using Autogenous Osteoblasts Cultured on Different Biomatrices. J. Biomed. Mater. Res. - Part A 2003, 67 (1), 191–199. https://doi.org/10.1002/jbm.a.10594.

(24) Mauney, J. R.; Blumberg, J.; Pirun, M.; Volloch, V.; Vunjak-; Kaplan, D. L. Osteogenic Differentiation of Human Bone Marrow Stromal. Tissue Eng. 2004, 10 (1), 81–92.

(25) Delloye, C.; De Nayer, P.; Malghem, J.; Noel, H. Induced Healing of Aneurysmal Bone Cysts by Demineralized Bone Particles: A Report of Two Cases. Arch. Orthop. Trauma Surg. 1996, 115 (3–4), 141–145. https://doi.org/10.1007/BF00434541.

(26) Rosenthal, R. K.; Folkman, J.; Glowacki, J. Demineralized Bone Implants for Nonunion Fractures, Bone Cysts, and Fibrous Lesions. Clin. Orthop. Relat. Res. 1999, No. 364, 61–69. https://doi.org/10.1097/00003086-199907000-00009.

(27) Rougraff, B. T.; Kling, T. J. Treatment of Active Unicameral Bone Cysts with Percutaneous Injection of Demineralized Bone Matrix and Autogenous Bone Marrow. J. Bone Jt. Surg. - Ser. A 2002, 84 (6). https://doi.org/10.2106/00004623-200206000-00005.

(28) Badylak, S. F.; Lantz, G. C.; Coffey, A.; Geddes, L. A. Small Intestinal Submucosa as a Large Diameter Vascular Graft in the Dog. J. Surg. Res. 1989, 47 (1), 74–80. https://doi.org/10.1016/0022-4804(89)90050-4.

(29) Sandusky, G. E.; Lantz, G. C.; Badylak, S. F. Healing Comparison of Small Intestine Submucosa and EPTFE Grafts in the Canine Carotid Artery. J. Surg. Res. 1995, 58 (4), 415–420. https://doi.org/10.1006/jsre.1995.1064.

(30) Badylak, S. F.; Tullius, R.; Kokini, K.; Shelbourne, K. D.; Klootwyk, T.; Voytik, S. L.; Kraine, M. R.; Simmons, C. The Use of Xenogeneic Small Intestinal Submucosa as a Biomaterial for Achille's Tendon Repair in a Dog Model. J. Biomed. Mater. Res. 1995, 29 (8), 977–985. https://doi.org/10.1002/jbm.820290809.

(31) Kropp, B. P.; Eppley, B. L.; Prevel, C. D.; Rippy, M. K.; Harruff, R. C.; Badylak, S. F.; Adams, M. C.; Rink, R. C.; Keating, M. A. Experimental Assessment of Small Intestinal Submucosa as a Bladder Wall Substitute. Urology 1995, 46 (3), 396–400. https://doi.org/10.1016/S0090-4295(99)80227-1.

(32) Cobb, M. A.; Badylak, S. F.; Janas, W.; Simmons-Byrd, A.; Boop, F. A. Porcine Small Intestinal Submucosa as a Dural Substitute. Surg. Neurol. 1999, 51 (1), 99–104. https://doi.org/10.1016/S0090-3019(97)00475-8.

(33) Chen, F.; Yoo, J. J.; Atala, A. Acellular Collagen Matrix as a Possible "off the Shelf" Biomaterial for Urethral Repair. Urology 1999, 54 (3), 407–410. https://doi.org/10.1016/S0090-4295(99)00179-X.

(34) Badylak, S. F. The Extracellula Matrix as a Scaffold for Tissue Reconstruction. Cell Dev. Biol. 2002, 13, 377–383. https://doi.org/10.1016/S1084-9521(02)00094-0.

(35) von der Mark, K.; Park, J. Engineering Biocompatible Implant Surfaces. Prog. Mater. Sci. 2013, 58 (3), 327–381. https://doi.org/10.1016/j.pmatsci.2012.09.002.

(36) Hynes, R. O. Integrins: A Family of Cell Adhesion Receptors. Cell 1987, 48, 549–554.

(37) Aumailley, M.; Gayraud, B. Structure and Biological Activity of the Extracellular Matrix. J. Mol. Med. 1998, 76 (3–4), 253–265. https://doi.org/10.1007/s001090050215.

(38) Alberts, B.; Johnson, A.; Lewis, J.; Raff, M.; Roberts, K.; Walter, P. Molecular Biology of The Cell, 5th ed.; Garland Sciences, 2008.

(39) Hynes, R. O. Integrins. Cell 2002, 110 (6), 673–687. https://doi.org/10.1016/S0092-8674(02)00971-6.

(40) Kim, S. H.; Turnbull, J.; Guimond, S. Extracellular Matrix and Cell Signalling: The Dynamic Cooperation of Integrin, Proteoglycan and Growth Factor Receptor. J. Endocrinol. 2011, 209 (2), 139–151. https://doi.org/10.1530/JOE-10-0377.

(41) Di Cio, S.; Gautrot, J. E. Cell Sensing of Physical Properties at the Nanoscale: Mechanisms and Control of Cell Adhesion and Phenotype. Acta Biomater. 2016, 30, 26–48. https://doi.org/10.1016/j.actbio.2015.11.027.

(42) Geiger, B.; Bershadsky, A.; Pankov, R.; Yamada, K. M. Transmembrane Crosstalk between the Extracellular Matrix and the Cytoskeleton. Nat. Rev. Mol. Cell Biol. 2001, 2 (11), 793–805. https://doi.org/10.1038/35099066.

(43) Cukierman, E.; Pankov, R.; Yamada, K. M. Cell Interactions with Three-Dimensional Matrices. Curr. Opin. Cell Biol. 2002, 14 (5), 633–640. https://doi.org/10.1016/S0955-0674(02)00364-2.

(44) Kanchanawong, P.; Shtengel, G.; Pasapera, A. M.; Ramko, E. B.; Davidson, M. W.; Hess, H. F.; Waterman, C. M. Nanoscale Architecture of Integrin-Based Cell Adhesions. Nature 2010, 468 (7323), 580–584. https://doi.org/10.1038/nature09621.

(45) Hanks, S. K.; Polte, T. R. Signaling through Focal Adhesion Kinase. BioEssays 1997, 19 (2), 137–145.

(46) Zhu, X.; Assoian, R. K. Integrin-Dependent Activation of MAP Kinase: A Link to Shape-Dependent Cell Proliferation. Mol. Biol. Cell 1995, 6 (3), 273–282. https://doi.org/10.1091/mbc.6.3.273.

(47) Giancotti, F. G.; Ruoslahti, E. Integrin Signaling. Science (80-. ). 1999, 285 (5430), 1028–1033. https://doi.org/10.1126/science.285.5430.1028.

(48) Legate, K. R.; Wickström, S. A.; Fässler, R. Genetic and Cell Biological Analysis of Integrin Outside-in Signaling. Genes Dev. 2009, 23 (4), 397–418. https://doi.org/10.1101/gad.1758709.

(49) Nobes, C. D.; Hall, A. Rho GTPases Control Polarity, Protrusion, and Adhesion during Cell Movement. J. Cell Biol. 1999, 144 (6), 1235–1244. https://doi.org/10.1083/jcb.144.6.1235.

(50) Burridge, K.; Chrzanowska-Wodnicka, M. Focal Adhesions, Contractility, and Signaling. Annu. Rev. Cell Dev. Biol. 1996, 12 (1), 463–519. https://doi.org/10.1146/annurev.cellbio.12.1.463.

(51) Giliberti, D. C.; White, K. K.; Dee, K. C. Control of Cell-Biomaterial Interactions. In Polymeric Biomaterials; Dumitriu, S., Ed.; Marcel Dekker, Inc.: New York, NY, 2002; pp 361–375.

(52) Howe, A.; Aplin, A. E.; Alahari, S. K.; Juliano, R. Integrin Signaling and Cell Growth Control. Curr. Opin. Cell Biol. 1998, 10 (2), 220–231. https://doi.org/10.1016/S0955-0674(98)80144-0.

(53) Miyamoto, S.; Teramoto, H.; Gutkind, J. S.; Yamada, K. M. Integrins Can Collaborate with Growth Factors for Phosphorylation of Receptor Tyrosine Kinases and MAP Kinase Activation: Roles of Integrin Aggregation and Occupancy of Receptors. J. Cell Biol. 1996, 135 (6), 1633–1642. https://doi.org/10.1083/jcb.135.6.1633.

(54) Frisch, S. M.; Vuori, K.; Ruoslahti, E.; Chan-Hui, P.-Y. Control of Adhesion-Dependent Cell Survival by Focal Adhesion Kinase. J. Cell Biol. 1996, 134 (3), 793–799. https://doi.org/10.1083/jcb.134.3.793.

(55) Frisch, S. M.; Francis, H. Disruption of Epithelial Cell-Matrix Interactions Induces Apoptosis. J. Cell Biol. 1994, 124 (4), 619–626. https://doi.org/10.1083/jcb.124.4.619.

(56) Frisch, S. M.; Ruoslahti, E. Integrins and Anoikis. Curr. Opin. Cell Biol. 1997, 9 (5), 701–706. https://doi.org/10.1016/S0955-0674(97)80124-X.

(57) Guo, W.; Giancotti, F. G. Integrin Signalling during Tumour Progression. Nat. Rev. Mol. Cell Biol. 2004, 5 (10), 816–826. https://doi.org/10.1038/nrm1490.

(58) Goldmann, W. H. Mechanotransduction in Cells. Cell Biol. Int. 2012, 36 (6), 567–570. https://doi.org/10.1042/cbi20120071.

(59) Goldmann, W. H. Mechanotransduction and Focal Adhesions. Cell Biol. Int. 2012, 36 (7), 649–652. https://doi.org/10.1042/cbi20120184.

(60) van der Rest, M.; Garrone, R. Collagen Family of Proteins. FASEB J. 1991, 5 (13), 2814–2823. https://doi.org/10.1096/fasebj.5.13.1916105.

(61) Prockop, D. J.; Fertala, A. The Collagen Fibril: The Almost Crystalline Structure. J. Struct. Biol. 1998, 122 (1–2), 111–118. https://doi.org/10.1006/jsbi.1998.3976.

(62) Hulmes, D. J. S. Collagen Diversity, Synthesis and Assembly. Collagen Struct. Mech. 2008, 15–47. https://doi.org/10.1007/978-0-387-73906-9_2.

(63) P.Fratzl. Collagen: Structure and Mechanics; Fratzl, P., Ed.; Springer US: Boston, MA, 2008. https://doi.org/10.1007/978-0-387-73906-9.

(64) Asgari, M.; Latifi, N.; Heris, H. K.; Vali, H.; Mongeau, L. In Vitro Fibrillogenesis of Tropocollagen Type III in Collagen Type i Affects Its Relative Fibrillar Topology and Mechanics. Sci. Rep. 2017, 7 (1), 1–10. https://doi.org/10.1038/s41598-017-01476-y.

(65) Karsdal, M. A.; Manon-Jensen, T.; Genovese, F.; Kristensen, J. H.; Nielsen, M. J.; Sand, J. M. B.; Hansen, N. U. B.; Bay-Jensen, A. C.; Bager, C. L.; Krag, A.; et al. Novel Insights into the Function and Dynamics of Extracellular Matrix in Liver Fibrosis. Am. J. Physiol. - Gastrointest. Liver

Physiol. 2015, 308 (10), G807–G830. https://doi.org/10.1152/ajpgi.00447.2014.

(66) Birk, D. E.; Brückner, P. Collagens, Suprastructures, and Collagen Fibril Assembly. In The Extracellular Matrix: an Overview; Mecham, R. P., Ed.; Springer Berlin Heidelberg: Berlin, Heidelberg, 2011; pp 77–115. https://doi.org/10.1007/978-3-642-16555-9_3.

(67) Gullberg, D. I Domain Integrins; Gullberg, D., Ed.; Advances in Experimental Medicine and Biology; Springer Netherlands: Dordrecht, 2014; Vol. 819. https://doi.org/10.1007/978-94-017-9153-3.

(68) Knight, C. G.; Morton, L. F.; Peachey, A. R.; Tuckwell, D. S.; Farndale, R. W.; Barnes, M. J. The Collagen-Binding A-Domains of Integrins α 1 β 1 and α 2 β 1 Recognize the Same Specific Amino Acid Sequence, GFOGER, in Native (Triple-Helical) Collagens. J. Biol. Chem. 2000, 275 (1), 35–40. https://doi.org/10.1074/jbc.275.1.35.

(69) Emsley, J.; Knight, C. G.; Farndale, R. W.; Barnes, M. J.; Liddington, R. C. Structural Basis of Collagen Recognition by Integrin A2β1. Cell 2000, 101 (1), 47–56. https://doi.org/10.1016/S0092-8674(00)80622-4.

(70) Jokinen, J.; Dadu, E.; Nykvist, P.; Käpylä, J.; White, D. J.; Ivaska, J.; Vehviläinen, P.; Reunanen, H.; Larjava, H.; Häkkinen, L.; et al. Integrin-Mediated Cell Adhesion to Type I Collagen Fibrils. J. Biol. Chem. 2004, 279 (30), 31956–31963. https://doi.org/10.1074/jbc.M401409200.

(71) Glowacki, J.; Mizuno, S. Collagen Scaffolds for Tissue Engineering. Biopolymers 2008, 89 (5), 338–344. https://doi.org/10.1002/bip.20871.

(72) Lapčík, L.; De Smedt, S.; Demeester, J.; Chabreček, P. Hyaluronan: Preparation, Structure, Properties, and Applications. Chem. Rev. 1998, 98 (8), 2663–2684. https://doi.org/10.1021/cr941199z.

(73) Kogan, G.; Šoltés, L.; Stern, R.; Gemeiner, P. Hyaluronic Acid: A Natural Biopolymer with a Broad Range of Biomedical and Industrial Applications. Biotechnol. Lett. 2007, 29 (1), 17–25. https://doi.org/10.1007/s10529-006-9219-z.

(74) Morra, M. Engineering of Biomaterials Surfaces by Hyaluronan. Biomacromolecules 2005, 6 (3), 1205–1223. https://doi.org/10.1021/bm049346i.

(75) Leach, J. B.; Schmidt, C. E. Hyaluronan. In Encyclopedia of Biomaterials and Biomedical Engineering; Wnek, G. E., Bowlin, G. L., Eds.; Marcel Dekker: Boca Raton, 2008; p 3552. https://doi.org/10.1081/E-EBBE2-120007317.

(76) E. Fouissac; Milas, M.; Rinaudo, M.; Borsali, R. Influence of the Ionic Strength on the Dimensions of Sodium Hyaluronate. Macromolecules 1992, 25 (2), 5613–5617.

(77) Necas, J.; Bartosikova, L.; Brauner, P.; Kolar, J. Hyaluronic Acid (Hyaluronan): A Review. Vet. Med. (Praha). 2008, 53 (8), 397–411.

(78) Cleland, R. L.; Wang, J. L.; Detweiler, D. M.; Wang, J. L. Polyelectrolyte Properties of Sodium Hyaluronate, 2. Potentiometric Titration of Hyaluronic Acid. Macromolecules 1982, 15 (2), 386–395. https://doi.org/10.1021/ma00230a037.

(79) Cleland, R. L.; College, D. Polyelectrolyte Behavior of Hyaluronate with That of Carboxymethyl Cellulose .* Preparation of Material. 1968, 6.

(80) Reed, C. E.; Li, X.; Reed, W. F. The Effects of PH on Hyaluronate as Observed by Light Scattering. Biopolymers 1989, 28 (11), 1981–2000. https://doi.org/10.1002/bip.360281114.

(81) Laurent, T. C.; Laurent, U. B.; Fraser, J. R. The Structure and Function of Hyaluronan: An Overview. Immunol. Cell Biol. 1996, 74, A1–A7. https://doi.org/10.1002/yea.

(82) Barbucci, R.; Lamponi, S.; Borzacchiello, A.; Ambrosio, L.; Fini, M.; Torricelli, P.; Giardino, R. Hyaluronic Acid Hydrogel in the Treatment of Osteoarthritis. Biomaterials 2002, 23, 4503–4513.

(83) Uthman, I.; Raynauld, J. P.; Haraoui, B. Intra - Articular Therapy in Osteoarthritis. Postgradual Med. J. 2003, 79, 449–453.

(84) Mori, M.; Yamaguchi, M.; Sumitomo, S.; Takai, Y. Hyaluronan-Based Biomaterials in Tissue Engineering. Acta Histochem. Cytochem. 2004, 37 (1), 1–5. https://doi.org/10.1267/ahc.37.1.

(85) Galassi, G.; Brun, P.; Radice, M.; Cortivo, R.; Zanon, G. F.; Genovese, P.; Abatangelo, G. In Vitro Reconstructed Dermis Implanted in Human Wounds: Degradation Studies of the HA-Based Supporting Scaffold. Biomaterials 2000, 21 (21), 2183–2191. https://doi.org/10.1016/S0142-9612(00)00147-2.

(86) Zacchi, V.; Soranzo, C.; Cortivo, R.; Radice, M.; Brun, P.; Abatangelo, G. In Vitro Engineering of Human Skin-like Tissue. J. Biomed. Mater. Res. 1998, 40 (2), 187–194. https://doi.org/10.1002/(SICI)1097-4636(199805)40:2<187::AID-JBM3>3.0.CO;2-H.

(87) Campoccia, D.; Doherty, P.; Radice, M.; Brun, P.; Abatangelo, G.; Williams, D. F. Semisynthetic Resorbable Materials from Hyaluronan Esterification. Biomaterials 1998, 19 (23), 2101–2127. https://doi.org/10.1016/S0142-9612(98)00042-8.

(88) Hume, L. R.; Lee, H. K.; Benedetti, L.; Sanzgiri, Y. D.; Topp, E. M.; Stella, V. J. Ocular Sustained Delivery of Prednisolone Using Hyaluronic Acid Benzyl Ester Films. Int. J. Pharm. 1994, 111, 295–298. https://doi.org/10.1016/0378-5173(95)04332-2.

(89) Illum, L.; Farraj, N. F.; Fisher, A. N.; Gill, I.; Miglietta, M.; Benedetti, L. M. Hyaluronic Acid Ester Microspheres as a Nasal Delivery System for Insulin. J. Control. Release 1994, 29 (1–2), 133–141. https://doi.org/10.1016/0168-3659(94)90129-5.

(90) Esposito, E.; Menegatti, E.; Cortesi, R. Hyaluronan-Based Microspheres as Tools for Drug Delivery: A Comparative Study. Int. J. Pharm. 2005, 288 (1), 35–49. https://doi.org/10.1016/j.ijpharm.2004.09.001.

(91) Thierry, B.; Winnik, F. M.; Merhi, Y.; Silver, J.; Tabrizian, M. Bioactive Coatings of Endovascular Stents Based on Polyelectrolyte Multilayers. Biomacromolecules 2003, 4 (6), 1564–1571. https://doi.org/10.1021/bm0341834.

(92) Verheye, S.; Markou, C. P.; Salame, M. Y.; Wan, B.; King, S. B.; Robinson, K. a; Chronos, N. a; Hanson, S. R. Reduced Thrombus Formation by Hyaluronic Acid Coating of Endovascular Devices. Arterioscler. Thromb. Vasc. Biol. 2000, 20, 1168–1172. https://doi.org/10.1161/01.ATV.20.4.1168.

(93) Toole, B. P. Hyaluronan in Morphogenesis. J. Intern. Med. 1997, 242, 35–40. https://doi.org/10.1006/scdb.2000.0244.

(94) Oliferenko, S.; Kaverina, I.; Small, J. V.; Huber, L. A. Hyaluronic Acid (HA) Binding to CD44 Activates Rac1 and Induces Lamellipodia Outgrowth. J. Cell Biol. 2000, 148 (6), 1159–1164. https://doi.org/10.1083/jcb.148.6.1159.

(95) Turley, E. A.; Noble, P. W.; Bourguignon, L. Y. W. Signaling Properties of Hyaluronan Receptors. J. Biol. Chem. 2002, 277 (7), 4589–4592. https://doi.org/10.1074/jbc.R100038200.

(96) Sherman, L.; Sleeman, J.; Herrlich, P.; Ponta, H. Hyaluronate Receptors: Key Players in Growth, Differentiation, Migration and Tumor Progression. Curr. Opin. Cell Biol. 1994, 6 (5), 726–733. https://doi.org/10.1016/0955-0674(94)90100-7.

(97) Hall, C. L.; Wang, C.; Lange, L. A.; Turley, E. A. Hyaluronan and the Hyaluronan Receptor RHAMM Promote Focal Adhesion Turnover and Transient Tyrosine Kinase Activity. J. Cell Biol. 1994, 126 (2), 575–588. https://doi.org/10.1083/jcb.126.2.575.

(98) Entwistle, J.; Hall, C. L.; Turley, E. A. HA Receptors: Regulators of Signalling to the Cytoskeleton. J. Cell. Biochem. 1996, 61 (4), 569–577. https://doi.org/10.1002/(SICI)1097-4644(19960616)61:4<569::AID-JCB10>3.0.CO;2-B.

(99) Lee, J. Y.; Spicer, A. P. Hyaluronan: A Multifunctional, MegaDalton, Stealth Molecule. Curr. Opin. Cell Biol. 2000, 12 (5), 581–586. https://doi.org/10.1016/S0955-0674(00)00135-6.

(100) Knudson, C. B.; Knudson, W. Hyaluronan-Binding Proteins in Development , Tissue Homeostasis, and Disease. Faseb 1993, 7 (13), 1233–1241.

(101) Toole, B. P. The CD147-HYALURONAN Axis in Cancer. Anat. Rec. 2019, No. November 2018. https://doi.org/10.1002/ar.24147.

(102) Noble, P. W. Hyaluronan and Its Catabolic Products in Tissue Injury and Repair. Matrix Biol. 2002, 21 (1), 25–29. https://doi.org/10.1016/S0945-053X(01)00184-6.

(103) West, D. C.; Kumar, S. The Effect of Hyaluronate and Its Oligosaccharides on Endothelial Cell Proliferation and Monolayer Integrity. Exp. Cell Res. 1989, 183 (1), 179–196. https://doi.org/10.1016/0014-4827(89)90428-X.

(104) West, D. C.; Hampson, I. N.; Arnold, F.; Kumar, S. Angiogenesis Induced by Degradation Products of Hyaluronic Acid. Science (80-. ). 1985, 228 (4705), 1324–1326. https://doi.org/10.1126/science.2408340.

(105) Arnold, F.; Jia, C.; He, C.; Cherry, G. W.; Carbow, B.; Meyer-Ingold, W.; Bader, D.; West, D. C. Hyaluronan, Heterogeneity, and Healing: The Effects of Ultrapure Hyaluronan of Defined Molecular Size on the Repair of Full-thickness Pig Skin Wounds. Wound Repair Regen. 1995, 3 (3), 299–310. https://doi.org/10.1046/j.1524-475X.1995.30310.x.

(106) Sattar, A.; Rooney, P.; Kumar, S.; Pye, D.; West, D. C.; Scott, I.; Ledger, P. Application of Angiogenic Oligosaccharides of Hyaluronan Increases Blood Vessel Numbers in Rat Skin. J. Invest. Dermatol. 1994, 103 (4), 576–579. https://doi.org/10.1111/1523-1747.ep12396880.

(107) Keselowsky, B. G.; Collard, D. M.; García, A. J. Surface Chemistry Modulates Fibronectin Conformation and Directs Integrin Binding and Specificity to Control Cell Adhesion. J. Biomed. Mater. Res. - Part A 2003, 66 (2), 247–259. https://doi.org/10.1002/jbm.a.10537.

(108) Allen, L. T.; Tosetto, M.; Miller, I. S.; O'Connor, D. P.; Penney, S. C.; Lynch, I.; Keenan, A. K.; Pennington, S. R.; Dawson, K. A.; Gallagher, W. M. Surface-Induced Changes in Protein Adsorption and Implications for Cellular Phenotypic Responses to Surface Interaction. Biomaterials 2006, 27 (16), 3096–3108. https://doi.org/10.1016/j.biomaterials.2006.01.019.

(109) Barrias, C. C.; Martins, M. C. L.; Almeida-Porada, G.; Barbosa, M. A.; Granja, P. L. The Correlation between the Adsorption of Adhesive Proteins and Cell Behaviour on Hydroxyl-Methyl Mixed Self-Assembled Monolayers. Biomaterials 2009, 30 (3), 307–316. https://doi.org/10.1016/j.biomaterials.2008.09.048.

(110) Xu, L. C.; Siedlecki, C. A. Effects of Surface Wettability and Contact Time on Protein Adhesion to Biomaterial Surfaces. Biomaterials 2007, 28 (22), 3273–3283. https://doi.org/10.1016/j.biomaterials.2007.03.032.

(111) González-García, C.; Sousa, S. R.; Moratal, D.; Rico, P.; Salmerón-Sánchez, M. Effect of Nanoscale Topography on Fibronectin Adsorption, Focal Adhesion Size and Matrix Organisation. Colloids Surfaces B Biointerfaces 2010, 77 (2), 181–190. https://doi.org/10.1016/j.colsurfb.2010.01.021.

(112) Pegueroles, M.; Aparicio, C.; Bosio, M.; Engel, E.; Gil, F. J.; Planell, J. A.; Altankov, G. Spatial Organization of Osteoblast Fibronectin Matrix on Titanium Surfaces: Effects of Roughness, Chemical Heterogeneity and Surface Energy. Acta Biomater. 2010, 6 (1), 291–301. https://doi.org/10.1016/j.actbio.2009.07.030.

(113) Dolatshahi-Pirouz, A.; Rechendorff, K.; Hovgaard, M. B.; Foss, M.; Chevallier, J.; Besenbacher, F. Bovine Serum Albumin Adsorption on Nano-Rough Platinum Surfaces Studied by QCM-D. Colloids Surfaces B Biointerfaces 2008, 66 (1), 53–59. https://doi.org/10.1016/j.colsurfb.2008.05.010.

(114) Hovgaard, M. B.; Rechendorff, K.; Chevallier, J.; Foss, M.; Besenbacher, F. Fibronectin Adsorption on Tantalum: The Influence of Nanoroughness. J. Phys. Chem. B 2008, 112 (28), 8241–8249. https://doi.org/10.1021/jp801103n.

(115) Harbers, G. M.; Grainger, D. W. Cell-Material Interactions: Fundamental Design Issues for Tissue Engineering and Clinical Considerations. In An Introduction to Biomaterials; CRC Press, 2006; pp 15–45. https://doi.org/10.1201/b11561.

(116) Ruardy, T. G.; Schakenraad, J. M.; van der Mei, H. C.; Busscher, H. J. Adhesion and Spreading of Human Skin Fibroblasts on Physicochemically Characterized Gradient Surfaces. J. Biomed. Mater. Res. 1995, 29 (11), 1415–1423. https://doi.org/10.1002/jbm.820291113.

(117) Lin, M.; Wang, H.; Ruan, C.; Xing, J.; Wang, J.; Li, Y.; Wang, Y.; Luo, Y. Adsorption Force of Fibronectin on Various Surface Chemistries and Its Vital Role in Osteoblast Adhesion. Biomacromolecules 2015, 16 (3), 973–984. https://doi.org/10.1021/bm501873g.

(118) Schakenraad, J. M.; Busscher, H. J.; Wildevuur, C. R. H.; Arends, J. The Influence of Substratum Surface Free Energy on Growth and Spreading

of Human Fibroblasts in the Presence and Absence of Serum Proteins. J. Biomed. Mater. Res. 1986, 20 (6), 773–784. https://doi.org/10.1002/jbm.820200609.

(119) Pittenger, M. F. Multilineage Potential of Adult Human Mesenchymal Stem Cells. Science (80-. ). 1999, 284 (5411), 143–147. https://doi.org/10.1126/science.284.5411.143.

(120) Chen, C. S.; Mrksich, M.; Huang, S.; Whitesides, G. M.; Ingber, D. E. Geometric Control of Cell Life and Death. Science (80-. ). 1997, 276 (5317), 1425–1428. https://doi.org/10.1126/science.276.5317.1425.

(121) Arnold, M.; Cavalcanti-Adam, E. A.; Glass, R.; Blümmel, J.; Eck, W.; Kantlehner, M.; Kessler, H.; Spatz, J. P. Activation of Integrin Function by Nanopatterned Adhesive Interfaces. ChemPhysChem 2004, 5 (3), 383–388. https://doi.org/10.1002/cphc.200301014.

(122) Cavalcanti-Adam, E. A.; Volberg, T.; Micoulet, A.; Kessler, H.; Geiger, B.; Spatz, J. P. Cell Spreading and Focal Adhesion Dynamics Are Regulated by Spacing of Integrin Ligands. Biophys. J. 2007, 92 (8), 2964–2974. https://doi.org/10.1529/biophysj.106.089730.

(123) Kilian, K. A.; Mrksich, M. Directing Stem Cell Fate by Controlling the Affinity and Density of Ligand – Receptor Interactions at the Biomaterials Interface ** Angewandte. 2012, 2, 4891–4895. https://doi.org/10.1002/anie.201108746.

(124) Kilian, K. A.; Bugarija, B.; Lahn, B. T.; Mrksich, M. Geometric Cues for Directing the Differentiation of Mesenchymal Stem Cells. Proc. Natl. Acad. Sci. U. S. A. 2010, 107 (11), 4872–4877. https://doi.org/10.1073/pnas.0903269107.

(125) McBeath, R.; Pirone, D. M.; Nelson, C. M.; Bhadriraju, K.; Chen, C. S. Cell Shape, Cytoskeletal Tension, and RhoA Regulate Stem Cell Lineage Commitment. Dev. Cell 2004, 6 (4), 483–495. https://doi.org/10.1016/S1534-5807(04)00075-9.

(126) Park, J.; Bauer, S.; von der Mark, K.; Schmuki, P. Nanosize and Vitality: TiO2 Nanotube Diameter Directs Cell Fate. Nano Lett. 2007, 7 (6), 1686–1691.

(127) Oh, S.; Brammer, K. S.; Li, Y. S. J.; Teng, D.; Engler, A. J.; Chien, S.; Jin, S. Stem Cell Fate Dictated Solely by Altered Nanotube Dimension. Proc. Natl. Acad. Sci. U. S. A. 2009, 106 (7), 2130–2135. https://doi.org/10.1073/pnas.0813200106.

(128) Cowden, K.; Dias-Netipanyj, M. F.; Popat, K. C. Effects of Titania Nanotube Surfaces on Osteogenic Differentiation of Human Adipose-Derived Stem Cells. Nanomedicine Nanotechnology, Biol. Med. 2019, 17, 380–390. https://doi.org/10.1016/j.nano.2019.01.008.

(129) Brammer, K. S.; Oh, S.; Frandsen, C. J.; Varghese, S.; Jin, S. Nanotube Surface Triggers Increased Chondrocyte Extracellular Matrix Production. Mater. Sci. Eng. C 2010, 30 (4), 518–525. https://doi.org/10.1016/j.msec.2010.01.013.

(130) Lim, J. Y.; Dreiss, A. D.; Zhou, Z.; Hansen, J. C.; Siedlecki, C. A.; Hengstebeck, R. W.; Cheng, J.; Winograd, N.; Donahue, H. J. The Regulation of Integrin-Mediated Osteoblast Focal Adhesion and Focal Adhesion Kinase Expression by Nanoscale Topography. Biomaterials 2007, 28 (10), 1787–1797. https://doi.org/10.1016/j.biomaterials.2006.12.020.

(131) Popat, K. C.; Chatvanichkul, K.-I.; Barnes, G. L.; Latempa, T. J.; Grimes, C. A.; Desai, T. A. Osteogenic Differentiation of Marrow Stromal Cells Cultured on Nanoporous Alumina Surfaces. J. Biomed. Mater. Res. Part A 2007, 80A (4), 955–964. https://doi.org/10.1002/jbm.a.31028.

(132) Zouani, O. F.; Chanseau, C.; Brouillaud, B.; Bareille, R.; Deliane, F.; Foulc, M. P.; Mehdi, A.; Durrieu, M. C. Altered Nanofeature Size Dictates Stem Cell Differentiation. J. Cell Sci. 2012, 125 (5), 1217–1224. https://doi.org/10.1242/jcs.093229.

(133) Eisenbarth, E.; Linez, P.; Biehl, V.; Velten, D.; Breme, J.; Hildebrand, H. F. Cell Orientation and Cytoskeleton Organisation on Ground Titanium Surfaces. Biomol. Eng. 2002, 19 (2–6), 233–237. https://doi.org/10.1016/S1389-0344(02)00028-X.

(134) Brunette, D. M.; Chehroudi, B. The Effects of the Surface Topography of Micromachined Titanium Substrata on Cell Behavior in Vitro and in Vivo. J. Biomech. Eng. 1999, 121 (1), 49–57. https://doi.org/10.1115/1.2798042.

(135) Dalby, M. J.; Riehle, M. O.; Yarwood, S. J.; Wilkinson, C. D. W.; Curtis, A. S. G. Nucleus Alignment and Cell Signaling in Fibroblasts: Response to a Micro-Grooved Topography. Exp. Cell Res. 2003, 284 (2), 272–280. https://doi.org/10.1016/S0014-4827(02)00053-8.

(136) Charest, J. L.; García, A. J.; King, W. P. Myoblast Alignment and Differentiation on Cell Culture Substrates with Microscale Topography and Model Chemistries. Biomaterials 2007, 28 (13), 2202–2210. https://doi.org/10.1016/j.biomaterials.2007.01.020.

(137) Matsuzaka, K.; Walboomers, X. F.; De Ruijter, J. E.; Jansen, J. A. The Effect of Poly-L-Lactic Acid with Parallel Surface Micro on Groove on Osteoblast-like Cells in Vitro. Biomaterials 1999, 20 (14), 1293–1301. https://doi.org/10.1016/S0142-9612(99)00029-0.

(138) Lee, M. R.; Kwon, K. W.; Jung, H.; Kim, H. N.; Suh, K. Y.; Kim, K.; Kim, K. S. Direct Differentiation of Human Embryonic Stem Cells into Selective Neurons on Nanoscale Ridge/Groove Pattern Arrays. Biomaterials 2010, 31 (15), 4360–4366. https://doi.org/10.1016/j.biomaterials.2010.02.012.

(139) Dalby, M. J.; Berry, C. C.; Riehle, M. O.; Sutherland, D. S.; Agheli, H.; Curtis, A. S. G. Attempted Endocytosis of Nano-Environment Produced by Colloidal Lithography by Human Fibroblasts. Exp. Cell Res. 2004, 295 (2), 387–394. https://doi.org/10.1016/j.yexcr.2004.02.004.

(140) Kim, W.; Ng, J. K.; Kunitake, M. E.; Conklin, B. R.; Yang, P. Interfacing Silicon Nanowires with Mammalian Cells. J. Am. Chem. Soc. 2007, 129 (23), 7228–7229. https://doi.org/10.1021/ja071456k.

(141) Ozdemir, T.; Xu, L. C.; Siedlecki, C.; Brown, J. L. Substrate Curvature Sensing through Myosin IIa Upregulates Early Osteogenesis. Integr. Biol. (United Kingdom) 2013, 5 (11), 1407–1416. https://doi.org/10.1039/c3ib40068a.

(142) Pelham, R. J.; Wang, Y. -l. Cell Locomotion and Focal Adhesions Are Regulated by Substrate Flexibility. Proc. Natl. Acad. Sci. 1997, 94 (25), 13661–13665. https://doi.org/10.1073/pnas.94.25.13661.

(143) Engler, a.; Sheehan, M.; Sweeney, H. L.; Discher, D. E. Substrate Compliance vs Ligand Density in Cell on Gel Responses. Eur. Cells

Mater. 2003, 6 (SUPPL. 1), 7–8. https://doi.org/10.1016/S0006-3495(04)74140-5.

(144) Lo, C. M.; Wang, H. B.; Dembo, M.; Wang, Y. L. Cell Movement Is Guided by the Rigidity of the Substrate. Biophys. J. 2000, 79 (1), 144–152. https://doi.org/10.1016/S0006-3495(00)76279-5.

(145) Engler, A. J.; Richert, L.; Wong, J. Y.; Picart, C.; Discher, D. E. Surface Probe Measurements of the Elasticity of Sectioned Tissue, Thin Gels and Polyelectrolyte Multilayer Films: Correlations between Substrate Stiffness and Cell Adhesion. Surf. Sci. 2004, 570 (1–2), 142–154. https://doi.org/10.1016/j.susc.2004.06.179.

(146) Yeung, T.; Georges, P. C.; Flanagan, L. A.; Marg, B.; Ortiz, M.; Funaki, M.; Zahir, N.; Ming, W.; Weaver, V.; Janmey, P. A. Effects of Substrate Stiffness on Cell Morphology, Cytoskeletal Structure, and Adhesion. Cell Motil. Cytoskeleton 2005, 60 (1), 24–34. https://doi.org/10.1002/cm.20041.

(147) Ren, K.; Crouzier, T.; Roy, C.; Picart, C. Polyelectrolyte Multilayer Films of Controlled Stiffness Modulate Myoblast Cell Differentiation. Adv. Funct. Mater. 2008, 18 (9), 1378–1389. https://doi.org/10.1002/adfm.200701297.

(148) Degand, S.; Knoops, B.; Dupont-Gillain, C. C. Design and Characterization of Surfaces Presenting Mechanical Nanoheterogeneities for a Better Control of Cell-Material Interactions. Colloids Surfaces A Physicochem. Eng. Asp. 2014, 442, 164–172. https://doi.org/10.1016/j.colsurfa.2013.05.024.

(149) Altman, G. H.; Horan, R. L.; Martin, I.; Farhadi, J.; Stark, P. R. H.; Volloch, V.; Richmond, J. C.; Vunjak-Novakovic, G.; Kaplan, D. L. Cell Differentiation by Mechanical Stress. FASEB J. 2002, 16 (2), 270–272.

(150) Discher, D. E.; Mooney, D. J.; Zandstra, P. W. Growth Factors, Matrices, and Forces Combine and Control Stem Cells. Science (80-. ). 2009, 324 (5935), 1673–1677. https://doi.org/10.1126/science.1171643.

(151) Engler, A. J.; Sen, S.; Sweeney, H. L.; Discher, D. E. Matrix Elasticity Directs Stem Cell Lineage Specification. Cell 2006, 126, 677–689. https://doi.org/10.1016/j.cell.2006.06.044.

(152) Fu, J.; Wang, Y. K.; Yang, M. T.; Desai, R. A.; Yu, X.; Liu, Z.; Chen, C. S. Mechanical Regulation of Cell Function with Geometrically Modulated Elastomeric Substrates. Nat. Methods 2010, 7 (9), 733–736. https://doi.org/10.1038/nmeth.1487.

(153) Huebsch, N.; Arany, P. R.; Mao, A. S.; Shvartsman, D.; Ali, O. A.; Bencherif, S. A.; Rivera-Feliciano, J.; Mooney, D. J. Harnessing Traction-Mediated Manipulation of the Cell/Matrix Interface to Control Stem-Cell Fate. Nat. Mater. 2010, 9 (6), 518–526. https://doi.org/10.1038/nmat2732.

(154) Baker, B. M.; Trappmann, B.; Wang, W. Y.; Sakar, M. S.; Kim, I. L.; Shenoy, V. B.; Burdick, J. A.; Chen, C. S. Cell-Mediated Fibre Recruitment Drives Extracellular Matrix Mechanosensing in Engineered Fibrillar Microenvironments. Nat. Mater. 2015, 14 (12), 1262–1268. https://doi.org/10.1038/nmat4444.

(155) Chaudhuri, O.; Gu, L.; Darnell, M.; Klumpers, D.; Bencherif, S. A.; Weaver, J. C.; Huebsch, N.; Mooney, D. J. Substrate Stress Relaxation Regulates Cell Spreading. Nat. Commun. 2015, 6 (1), 6365. https://doi.org/10.1038/ncomms7365.

(156) Green, J. J.; Elisseeff, J. H. Mimicking Biological Functionality with Polymers for Biomedical Applications. https://doi.org/10.1038/nature21005.

(157) Turnbull, G.; Clarke, J.; Picard, F.; Riches, P.; Jia, L.; Han, F.; Li, B.; Shu, W. 3D Bioactive Composite Scaffolds for Bone Tissue Engineering. Bioact. Mater. 2018, 3 (3), 278–314. https://doi.org/10.1016/j.bioactmat.2017.10.001.

(158) Stanton, M. M.; Samitier, J.; Sánchez, S. Bioprinting of 3D Hydrogels. Lab Chip 2015, 15 (15), 3111–3115. https://doi.org/10.1039/c5lc90069g.

(159) Burdick, J. A.; Anseth, K. S. Photoencapsulation of Osteoblasts in Injectable RGD-Modified PEG Hydrogels for Bone Tissue Engineering. Biomaterials 2002, 23 (22), 4315–4323. https://doi.org/10.1016/S0142-9612(02)00176-X.

(160) Lutolf, M. P.; Weber, F. E.; Schmoekel, H. G.; Schense, J. C.; Kohler, T.; Müller, R.; Hubbell, J. A. Repair of Bone Defects Using Synthetic Mimetics of Collagenous Extracellular Matrices. Nat. Biotechnol. 2003, 21 (5), 513–518. https://doi.org/10.1038/nbt818.

(161) Shin, H.; Jo, S.; Mikos, A. G. Biomimetic Materials for Tissue Engineering. Biomaterials 2003, 24, 4353–4364. https://doi.org/10.1016/j.addr.2007.08.041.

(162) Bellamkonda, R.; Ranieri, J. P.; Aebischer, P. Laminin Oligopeptide Derivatized Agarose Gels Allow Three-dimensional Neurite Extension in Vitro. J. Neurosci. Res. 1995, 41 (4), 501–509. https://doi.org/10.1002/jnr.490410409.

(163) Alsberg, E.; Anderson, K. W.; Albeiruti, A.; Rowley, J. A.; Mooney, D. J. Engineering Growing Tissues. Proc. Natl. Acad. Sci. U. S. A. 2002, 99 (19), 12025–12030. https://doi.org/10.1073/pnas.192291499.

(164) Kuo, C. K.; Ma, P. X. Ionically Crosslinked Alginate Hydrogels as Scaffolds for Tissue Engineering: Part 1. Structure, Gelation Rate and Mechanical Properties. Biomaterials 2001, 22 (6), 511–521. https://doi.org/10.1016/S0142-9612(00)00201-5.

(165) Tabriz, A. G.; Hermida, M. A.; Leslie, N. R.; Shu, W. Three-Dimensional Bioprinting of Complex Cell Laden Alginate Hydrogel Structures. Biofabrication 2015, 7 (4). https://doi.org/10.1088/1758-5090/7/4/045012.

(166) Gerecht, S.; Burdick, J. A.; Ferreira, L. S.; Townsend, S. A.; Langer, R.; Vunjak-Novakovic, G. Hyaluronic Acid Hydrogel for Controlled Self-Renewal and Differentiation of Human Embryonic Stem Cells. Proc. Natl. Acad. Sci. U. S. A. 2007, 104 (27), 11298–11303. https://doi.org/10.1073/pnas.0703723104.

(167) Kim, J.; Kim, I. S.; Cho, T. H.; Lee, K. B.; Hwang, S. J.; Tae, G.; Noh, I.; Lee, S. H.; Park, Y.; Sun, K. Bone Regeneration Using Hyaluronic Acid-Based Hydrogel with Bone Morphogenic Protein-2 and Human Mesenchymal Stem Cells. Biomaterials 2007, 28 (10), 1830–1837. https://doi.org/10.1016/j.biomaterials.2006.11.050.

(168) Fujiyama, C.; Masaki, Z.; Sugihara, H. Reconstruction of the Urinary Bladder Mucosa in Three-Dimensional Collagen Gel Culture: Fibroblast-Extracellular Matrix Interactions on the Differentiation of Transitional Epithelial Cells. J. Urol. 1995, 153 (6), 2060–2067. https://doi.org/10.1016/S0022-5347(01)67402-0.

(169) Vernon, R. B.; Gooden, M. D.; Lara, S. L.; Wight, T. N. Native Fibrillar Collagen Membranes of Micron-Scale and Submicron Thicknesses for Cell Support and Perfusion. Biomaterials 2005, 26 (10), 1109–1117. https://doi.org/10.1016/j.biomaterials.2004.04.019.

(170) Fellah, B. H.; Weiss, P.; Gauthier, O.; Rouillon, T.; Pilet, P.; Daculsi, G.; Layrolle, P. Bone Repair Using a New Injectable Self-Crosslinkable Bone Substitute. J. Orthop. Res. 2006, 24 (4), 628–635. https://doi.org/10.1002/jor.20125.

(171) Baldwin, A. D.; Kiick, K. L. Polysaccharide-Modified Synthetic Polymeric Biomaterials. Biopolymers 2010, 94 (1), 128–140. https://doi.org/10.1002/bip.21334.

(172) MacDonald, R. a.; Laurenzi, B. F.; Viswanathan, G.; Ajayan, P. M.; Stegemann, J. P. Collagen-Carbon Nanotube Composite Materials as Scaffolds in Tissue Engineering. J. Biomed. Mater. Res. - Part A 2005, 74 (3), 489–496. https://doi.org/10.1002/jbm.a.30386.

(173) Liu, X.; Ma, P. X. Polymeric Scaffolds for Bone Tissue Engineering. Ann. Biomed. Eng. 2004, 32 (3), 477–486. https://doi.org/10.1023/B:ABME.0000017544.36001.8e.

(174) Nie, T.; Baldwin, A.; Yamaguchi, N.; Kiick, K. L. Production of Heparin-Functionalized Hydrogels for the Development of Responsive and Controlled Growth Factor Delivery Systems. J. Control. Release 2007, 122 (3), 287–296. https://doi.org/10.1016/j.jconrel.2007.04.019.

(175) Liang, Y.; Kiick, K. L. Heparin-Functionalized Polymeric Biomaterials in Tissue Engineering and Drug Delivery Applications. Acta Biomater. 2014, 10 (4), 1588–1600. https://doi.org/10.1016/j.actbio.2013.07.031.

(176) Ossipov, D. A. Bisphosphonate-Modified Biomaterials for Drug Delivery and Bone Tissue Engineering. Expert Opin. Drug Deliv. 2015, 12 (9), 1443–1458. https://doi.org/10.1517/17425247.2015.1021679.

(177) Chimene, D.; Lennox, K. K.; Kaunas, R. R.; Gaharwar, A. K. Advanced Bioinks for 3D Printing: A Materials Science Perspective. Ann. Biomed. Eng. 2016, 44 (6), 2090–2102. https://doi.org/10.1007/s10439-016-1638-y.

(178) Von Heimburg, D.; Zachariah, S.; Kühling, H.; Heschel, I.; Schoof, H.; Hafemann, B.; Pallua, N. Human Preadipocytes Seeded on Freeze-Dried Collagen Scaffolds Investigated in Vitro and in Vivo. Biomaterials 2001, 22 (5), 429–438. https://doi.org/10.1016/S0142-9612(00)00186-1.

(179) Ma, L.; Gao, C.; Mao, Z.; Zhou, J.; Shen, J. Enhanced Biological Stability of Collagen Porous Scaffolds by Using Amino Acids as Novel Cross-Linking Bridges. Biomaterials 2004, 25 (15), 2997–3004. https://doi.org/10.1016/j.biomaterials.2003.09.092.

(180) Park, S. N.; Park, J. C.; Kim, H. O.; Song, M. J.; Suh, H. Characterization of Porous Collagen/Hyaluronic Acid Scaffold Modified by 1-Ethyl-3-(3-Dimethylaminopropyl)Carbodiimide Cross-Linking. Biomaterials 2002, 23 (4), 1205–1212. https://doi.org/10.1016/S0142-9612(01)00235-6.

(181) Kirk, J. J. F.; Ritter, G.; Finger, I.; Sankar, D.; Reddy, J. D.; Talton, J. D.; Nataraj, C.; Narisawa, S.; Millán, J. L.; Cobb, R. R. Mechanical and Biocompatible Characterization of a Cross-Linked Collagen-Hyaluronic Acid Wound Dressing. Biomatter 2013, 3 (4), 1–14. https://doi.org/10.4161/biom.25633.

(182) Powell, H. M.; Boyce, S. T. EDC Cross-Linking Improves Skin Substitute Strength and Stability. 2006, 27, 5821–5827. https://doi.org/10.1016/j.biomaterials.2006.07.030.

(183) Pieper, J. S.; Hafmans, T.; Veerkamp, J. H.; Van Kuppevelt, T. H.; Van Wachem, P. B.; Van Luyn, M. J. A.; Brouwer, L. A. Attachment of Glycosaminoglycans to Collagenous Matrices Modulates the Tissue Response in Rats. Biomaterials 2000, 21 (16), 1689–1699. https://doi.org/10.1016/S0142-9612(00)00052-1.

(184) Buijtenhuijs, P.; Buttafoco, L.; Poot, A. A.; Daamen, W. F.; Van Kuppevelt, T. H.; Dijkstra, P. J.; De Vos, R. A. I.; Sterk, L. M. T.; Geelkerken, B. R. H.; Feijen, J.; et al. Tissue Engineering of Blood Vessels: Characterization of Smooth-Muscle Cells for Culturing on Collagen-and-Elastin-Based Scaffolds. Biotechnol. Appl. Biochem. 2004, 39 (2), 141–149. https://doi.org/10.1042/BA20030105.

(185) Ma, P. X.; Choi, J. W. Biodegradable Polymer Scaffolds with Well-Defined Interconnected Spherical Pore Network. Tissue Eng. 2001, 7 (1), 23–33. https://doi.org/10.1089/107632701300003269.

(186) Ma, P. X.; Zhang, R. Microtubular Architecture of Biodegradable Polymer Scaffolds. J. Biomed. Mater. Res. 2001, 56 (4), 469–477. https://doi.org/10.1002/1097-4636(20010915)56:4<469::AID-JBM1118>3.0.CO;2-H.

(187) Zhang, R.; Ma, P. X. Synthetic Nano-Fibrillar Extracellular Matrices with Predesigned Macroporous Architectures. J. Biomed. Mater. Res. 2000, 52 (2), 430–438. https://doi.org/10.1002/1097-4636(200011)52:2<430::AID-JBM25>3.0.CO;2-L.

(188) Sajesh, K. M.; Jayakumar, R.; Nair, S. V.; Chennazhi, K. P. Biocompatible Conducting Chitosan/Polypyrrole-Alginate Composite Scaffold for Bone Tissue Engineering. Int. J. Biol. Macromol. 2013, 62, 465–471. https://doi.org/10.1016/j.ijbiomac.2013.09.028.

(189) Baniasadi, H.; Ahmad Ramazani, S. A.; Mashayekhan, S.; Farani, M. R.; Ghaderinezhad, F.; Dabaghi, M. Design, Fabrication, and Characterization of Novel Porous Conductive Scaffolds for Nerve Tissue Engineering. Int. J. Polym. Mater. Polym. Biomater. 2015, 64 (18), 969–977. https://doi.org/10.1080/00914037.2015.1038817.

(190) Kim, S.-S.; Sun Park, M.; Jeon, O.; Yong Choi, C.; Kim, B.-S. Poly(Lactide-Co-Glycolide)/Hydroxyapatite Composite Scaffolds for Bone Tissue Engineering. Biomaterials 2006, 27 (8), 1399–1409. https://doi.org/10.1016/j.biomaterials.2005.08.016.

(191) Wei, G.; Ma, P. X. Structure and Properties of Nano-Hydroxyapatite/Polymer Composite Scaffolds for Bone Tissue Engineering. Biomaterials 2004, 25 (19), 4749–4757. https://doi.org/10.1016/j.biomaterials.2003.12.005.

(192) Liao, S. S.; Cui, F. Z.; Zhu, Y. Osteoblasts Adherence and Migration through Three-Dimensional Porous Mineralized Collagen Based Composite: NHAC/PLA. J. Bioact. Compat. Polym. 2004, 19 (2), 117–130. https://doi.org/10.1177/0883911504042643.

(193) Kim, H. J.; Kim, U. J.; Kim, H. S.; Li, C.; Wada, M.; Leisk, G. G.; Kaplan, D. L. Bone Tissue Engineering with Premineralized Silk Scaffolds. Bone 2008, 42 (6), 1226–1234. https://doi.org/10.1016/j.bone.2008.02.007.

(194) Chou, Y. F.; Dunn, J. C. Y.; Wu, B. M. In Vitro Response of MC3T3-E1 Preosteoblasts within Three-Dimensional Apatite-Coated PLGA Scaffolds. J. Biomed. Mater. Res. - Part B Appl. Biomater. 2005, 75 (1), 81–90. https://doi.org/10.1002/jbm.b.30261.

(195) Hirata, E.; Uo, M.; Takita, H.; Akasaka, T.; Watari, F.; Yokoyama, A. Development of a 3D Collagen Scaffold Coated with Multiwalled Carbon Nanotubes. J. Biomed. Mater. Res. - Part B Appl. Biomater. 2009, 90 B (2), 629–634. https://doi.org/10.1002/jbm.b.31327.

(196) Hirata, E.; Uo, M.; Takita, H.; Akasaka, T.; Watari, F.; Yokoyama, A. Multiwalled Carbon Nanotube-Coating of 3D Collagen Scaffolds for Bone Tissue Engineering. Carbon N. Y. 2011, 49 (10), 3284–3291. https://doi.org/10.1016/j.carbon.2011.04.002.

(197) Hirata, E.; Uo, M.; Nodasaka, Y.; Takita, H.; Ushijima, N.; Akasaka, T.; Watari, F.; Yokoyama, A. 3D Collagen Scaffolds Coated with Multiwalled Carbon Nanotubes: Initial Cell Attachment to Internal Surface. J. Biomed. Mater. Res. - Part B Appl. Biomater. 2010, 93 (2), 544–550. https://doi.org/10.1002/jbm.b.31613.

(198) Abarrategi, A.; Gutiérrez, M. C.; Moreno-Vicente, C.; Hortigüela, M. J.; Ramos, V.; López-Lacomba, J. L.; Ferrer, M. L.; del Monte, F. Multiwall Carbon Nanotube Scaffolds for Tissue Engineering Purposes. Biomaterials 2008, 29 (1), 94–102. https://doi.org/10.1016/j.biomaterials.2007.09.021.

(199) Verdejo, R.; Jell, G.; Safinia, L.; Bismarck, A.; Stevens, M. M.; Shaffer, M. S. P. Reactive Polyurethane Carbon Nanotube Foams and Their Interactions with Osteoblasts. J. Biomed. Mater. Res. - Part A 2009, 88 (1), 65–73. https://doi.org/10.1002/jbm.a.31698.

(200) Sitharaman, B.; Shi, X.; Walboomers, X. F.; Liao, H.; Cuijpers, V.; Wilson, L. J.; Mikos, A. G.; Jansen, J. A. In Vivo Biocompatibility of Ultra-Short Single-Walled Carbon Nanotube/Biodegradable Polymer Nanocomposites for Bone Tissue Engineering. Bone 2008, 43 (2), 362–370. https://doi.org/10.1016/j.bone.2008.04.013.

(201) Más, B. A.; Cattani, S. M. de M.; Rangel, R. de C. C.; Ribeiro, G. de A.; Cruz, N. C.; Leite, F. de L.; Nascente, P. A. de P.; Duek, E. A. de R. Surface Characterization and Osteoblast-like Cells Culture on Collagen Modified PLDLA Scaffolds. Mater. Res. 2014, 17 (6), 1523–1534. https://doi.org/10.1590/1516-1439.269414.

(202) Gong, Y.; Zhu, Y.; Liu, Y.; Ma, Z.; Gao, C.; Shen, J. Layer-by-Layer Assembly of Chondroitin Sulfate and Collagen on Aminolyzed Poly(l-Lactic Acid) Porous Scaffolds to Enhance Their Chondrogenesis. Acta Biomater. 2007, 3 (5), 677–685. https://doi.org/10.1016/j.actbio.2007.04.007.

(203) Shekaran, A.; García, A. J. Extracellular Matrix-Mimetic Adhesive Biomaterials for Bone Repair. J. Biomed. Mater. Res. Part A 2011, 96A (1), 261–272. https://doi.org/10.1002/jbm.a.32979.

(204) Wei, G.; Ma, P. X. Nanostructured Biomaterials for Regeneration. Adv. Funct. Mater. 2008, 18 (22), 3568–3582. https://doi.org/10.1002/adfm.200800662.

(205) He, L.; Shi, Y.; Han, Q.; Zuo, Q.; Ramakrishna, S.; Xue, W.; Zhou, L. Surface Modification of Electrospun Nanofibrous Scaffolds via Polysaccharide–Protein Assembly Multilayer for Neurite Outgrowth. J. Mater. Chem. 2012, 22 (26), 13187. https://doi.org/10.1039/c2jm32332j.

(206) Hosseinkhani, H.; Hosseinkhani, M.; Tian, F.; Kobayashi, H.; Tabata, Y. Osteogenic Differentiation of Mesenchymal Stem Cells in Self-Assembled Peptide-Amphiphile Nanofibers. Biomaterials 2006, 27 (22), 4079–4086. https://doi.org/10.1016/j.biomaterials.2006.03.030.

(207) Genové, E.; Shen, C.; Zhang, S.; Semino, C. E. The Effect of Functionalized Self-Assembling Peptide Scaffolds on Human Aortic Endothelial Cell Function. Biomaterials 2005, 26 (16), 3341–3351. https://doi.org/10.1016/j.biomaterials.2004.08.012.

(208) Hardy, J. G.; Lee, J. Y.; Schmidt, C. E. Biomimetic Conducting Polymer-Based Tissue Scaffolds. Curr. Opin. Biotechnol. 2013, 24 (5), 847–854. https://doi.org/10.1016/j.copbio.2013.03.011.

(209) Shih, Y.-R. V; Chen, C.-N.; Tsai, S.-W.; Wang, Y. J.; Lee, O. K. Growth of Mesenchymal Stem Cells on Electrospun Type I Collagen Nanofibers. Stem Cells 2006, 24 (11), 2391–2397. https://doi.org/10.1634/stemcells.2006-0253.

(210) Schofer, M. D.; Boudriot, U.; Wack, C.; Leifeld, I.; Gräbedünkel, C.; Dersch, R.; Rudisile, M.; Wendorff, J. H.; Greiner, A.; Paletta, J. R. J.; et al. Influence of Nanofibers on the Growth and Osteogenic Differentiation of Stem Cells: A Comparison of Biological Collagen Nanofibers and Synthetic PLLA Fibers. J. Mater. Sci. Mater. Med. 2009, 20 (3), 767–774. https://doi.org/10.1007/s10856-008-3634-8.

(211) Zhang, Y.; Venugopal, J. R.; El-Turki, A.; Ramakrishna, S.; Su, B.; Lim, C. T. Electrospun Biomimetic Nanocomposite Nanofibers of Hydroxyapatite/Chitosan for Bone Tissue Engineering. Biomaterials 2008, 29 (32), 4314–4322. https://doi.org/10.1016/j.biomaterials.2008.07.038.

(212) Thunberg, J.; Kalogeropoulos, T.; Kuzmenko, V.; Hägg, D.; Johannesson, S.; Westman, G.; Gatenholm, P. In Situ Synthesis of Conductive Polypyrrole on Electrospun Cellulose Nanofibers: Scaffold for Neural Tissue Engineering. Cellulose 2015, 22 (3), 1459–1467. https://doi.org/10.1007/s10570-015-0591-5.

(213) Abidian, M. R.; Corey, J. M.; Kipke, D. R.; Martin, D. C. Conducting-Polymer Nanotubes Improve Electrical Properties, Mechanical Adhesion, Neural Attachment and Neurite Outgrowth of Neural Electrodes. Small 2010, 6 (3), 421–429. https://doi.org/10.1002/smll.200901868.

(214) Abidian, M. R.; Martin, D. C. Multifunctional Nanobiomaterials for Neural Interfaces. Adv. Funct. Mater. 2009, 19 (4), 573–585. https://doi.org/10.1002/adfm.200801473.

(215) Venugopal, J. R.; Zhang, Y.; Ramakrishna, S. In Vitro Culture of Human Dermal Fibroblasts on Electrospun Polycaprolactone Collagen Nanofibrous Membrane. Artif. Organs 2006, 30 (6), 440–446.

(216) Lee, S. J.; Yoo, J. J.; Lim, G. J.; Atala, A.; Stitzel, J. In Vitro Evaluation of Electrospun Nanofiber Scaffolds for Vascular Graft Application. J. Biomed. Mater. Res. Part A 2007, 83A (4), 999–1008. https://doi.org/10.1002/jbm.a.31287.

(217) Venugopal, J.; Ma, L. L.; Yong, T.; Ramakrishna, S. In Vitro Study of Smooth Muscle Cells on Polycaprolactone and Collagen Nanofibrous Matrices. Cell Biol. Int. 2005, 29 (10), 861–867. https://doi.org/10.1016/j.cellbi.2005.03.026.

(218) He, L.; Tang, S.; Prabhakaran, M. P.; Liao, S.; Tian, L.; Zhang, Y.; Xue, W.; Ramakrishna, S. Surface Modification of PLLA Nano-Scaffolds with Laminin Multilayer by LbL Assembly for Enhancing Neurite Outgrowth. Macromol. Biosci. 2013, 13 (11), 1601–1609. https://doi.org/10.1002/mabi.201300177.

(219) Hardy, J. G.; Villancio-wolter, M. K.; Sukhavasi, R. C.; Mouser, D. J.; Jr, D. A.; Geissler, S. A.; Kaplan, D. L.; Schmidt, C. E. Electrical Stimulation of Human Mesenchymal Stem Cells on Conductive Nanofi Bers Enhances Their Differentiation toward Osteogenic Outcomes. Macromol. Rapid Commun. 2015, 36, 1884–1890. https://doi.org/10.1002/marc.201500233.

(220) Naghavi Alhosseini, S.; Moztarzadeh, F.; Karkhaneh, A.; Dodel, M.; Khalili, M.; Eslami Arshaghi, T.; Elahirad, E.; Mozafari, M. Improved Cellular Response on Functionalized Polypyrrole Interfaces. J. Cell. Physiol. 2019, 234 (9), 15279–15287. https://doi.org/10.1002/jcp.28173.

(221) Zhou, X.; Yang, A.; Huang, Z.; Yin, G.; Pu, X.; Jin, J. Enhancement of Neurite Adhesion, Alignment and Elongation on Conductive Polypyrrole-Poly(Lactide Acid) Fibers with Cell-Derived Extracellular Matrix. Colloids Surfaces B Biointerfaces 2017, 149, 217–225. https://doi.org/10.1016/j.colsurfb.2016.10.014.

(222) Zeng, J.; Huang, Z.; Yin, G.; Qin, J.; Chen, X.; Gu, J. Fabrication of Conductive NGF-Conjugated Polypyrrole-Poly(l-Lactic Acid) Fibers and Their Effect on Neurite Outgrowth. Colloids Surfaces B Biointerfaces 2013, 110, 450–457. https://doi.org/10.1016/j.colsurfb.2013.05.012.

(223) Zhang, H.; Wang, K.; Xing, Y.; Yu, Q. Lysine-Doped Polypyrrole/Spider Silk Protein/Poly(l-Lactic) Acid Containing Nerve Growth Factor Composite Fibers for Neural Application. Mater. Sci. Eng. C 2015, 56, 564–573. https://doi.org/10.1016/j.msec.2015.06.024.

(224) Venugopal, J.; Vadgama, P.; Sampath Kumar, T. S.; Ramakrishna, S. Biocomposite Nanofibres and Osteoblasts for Bone Tissue Engineering. Nanotechnology 2007, 18 (5). https://doi.org/10.1088/0957-4484/18/5/055101.

(225) Ngiam, M.; Liao, S.; Patil, A. J.; Cheng, Z.; Yang, F.; Gubler, M. J.; Ramakrishna, S.; Chan, C. K. Fabrication of Mineralized Polymeric Nanofibrous Composites for Bone Graft Materials. Tissue Eng. Part A 2009, 15 (3), 535–546. https://doi.org/10.1089/ten.tea.2008.0011.

(226) Wang, T.; Zhai, Y.; Nuzzo, M.; Yang, X.; Yang, Y.; Zhang, X. Layer-by-Layer Nanofiber-Enabled Engineering of Biomimetic Periosteum for Bone Repair and Reconstruction. Biomaterials 2018, 182 (May), 279–288. https://doi.org/10.1016/j.biomaterials.2018.08.028.

(227) Decher, G.; Hong, J. -D. Buildup of Ultrathin Multilayer Films by a Self-assembly Process, 1 Consecutive Adsorption of Anionic and Cationic Bipolar Amphiphiles on Charged Surfaces. Makromol. Chemie. Macromol. Symp. 1991, 46 (1), 321–327. https://doi.org/10.1002/masy.19910460145.

(228) Decher, G. Fuzzy Nanoassemblies: Toward Layered Polymeric Multicomposites. Science (80-. ). 1997, 277 (5330), 1232–1237. https://doi.org/10.1126/science.277.5330.1232.

(229) Matsusaki, M.; Ajiro, H.; Kida, T.; Serizawa, T.; Akashi, M. Layer-by-Layer Assembly through Weak Interactions and Their Biomedical Applications. Adv. Mater. 2012, 24 (4), 454–474. https://doi.org/10.1002/adma.201103698.

(230) Ariga, K.; Hill, J. P.; Ji, Q. Layer-by-Layer Assembly as a Versatile Bottom-up Nanofabrication Technique for Exploratory Research and Realistic Application. Phys. Chem. Chem. Phys. 2007, 9 (19), 2319–2340. https://doi.org/10.1039/b700410a.

(231) Azzaroni, O.; Lau, K. H. A. Layer-by-Layer Assemblies in Nanoporous Templates: Nano-Organized Design and Applications of Soft Nanotechnology. Soft Matter 2011, 7 (19), 8709–8724. https://doi.org/10.1039/c1sm05561e.

(232) Tang, Z.; Wang, Y.; Podsiadlo, P.; Kotov, N. A. Biomedical Applications of Layer-by-Layer Assembly: From Biomimetics to Tissue Engineering. Adv. Mater. 2006, 18 (24), 3203–3224. https://doi.org/10.1002/adma.200600113.

(233) Langmuir-Blodgett Films; Roberts, G., Ed.; Springer US: Boston, MA, 1990. https://doi.org/10.1007/978-1-4899-3716-2.

(234) Langmuir, I.; Schaefer, V. J. Monolayers and Multilayers of Chlorophyll. J. Am. Chem. Soc. 1937, 59 (10), 2075–2076. https://doi.org/10.1021/ja01289a506.

(235) Blodgett, K. B. Films Built by Depositing Successive Monomolecular Layers on a Solid Surface. J. Am. Chem. Soc. 1935, 57 (6), 1007–1022. https://doi.org/10.1021/ja01309a011.

(236) Nuzzo, R. G.; Allara, D. L. Adsorption of Bifunctional Organic Disulfides on Gold Surfaces. J. Am. Chem. Soc. 1983, 105 (13), 4481–4483. https://doi.org/10.1021/ja00351a063.

(237) Bain, C. D.; Whitesides, G. M. Formation of Monolayers by the Coadsorption of Thiols on Gold: Variation in the Length of the Alkyl Chain. J. Am. Chem. Soc. 1989, 111 (18), 7164–7175. https://doi.org/10.1021/ja00200a040.

(238) Ladam, G.; Schaad, P.; Voegel, J. C.; Schaaf, P.; Decher, G.; Cuisinier, F. In Situ Determination of the Structural Properties of Initially Deposited Polyelectrolyte Multilayers. Langmuir 2000, 16 (3), 1249–1255. https://doi.org/10.1021/la990650k.

(239) Feng, Z.; Wang, Z.; Gao, C.; Shen, J. Direct Covalent Assembly to Fabricate Microcapsules with Ultrathin Walls and High Mechanical Strength. Adv. Mater. 2007, 19 (21), 3687–3691. https://doi.org/10.1002/adma.200700541.

(240) Li, M.; Ishihara, S.; Akada, M.; Liao, M.; Sang, L.; Hill, J. P.; Krishnan, V.; Ma, Y.; Ariga, K. Electrochemical-Coupling Layer-by-Layer (ECC-LbL)

Assembly. J. Am. Chem. Soc. 2011, 133 (19), 7348–7351. https://doi.org/10.1021/ja202768k.

(241) Manna, U.; Dhar, J.; Nayak, R.; Patil, S. Multilayer Single-Component Thin Films and Microcapsules via Covalent Bonded Layer-by-Layer Self-Assembly. Chem. Commun. 2010, 46 (13), 2250–2252. https://doi.org/10.1039/b924240f.

(242) Seo, J.; Schattling, P.; Lang, T.; Jochum, F.; Nilles, K.; Theato, P.; Char, K. Covalently Bonded Layer-by-Layer Assembly of Multifunctional Thin Films Based on Activated Esters. Langmuir 2010, 26 (3), 1830–1836. https://doi.org/10.1021/la902574z.

(243) Stockton, W. B.; Rubner, M. F. Molecular-Level Processing of Conjugated Polymers. 4. Layer-by-Layer Manipulation of Polyaniline via Hydrogen-Bonding Interactions. Macromolecules 1997, 30 (9), 2717–2725. https://doi.org/10.1021/ma9700486.

(244) Wang, L.; Wang, Z.; Zhang, X.; Shen, J.; Chi, L.; Fuchs, H. A New Approach for the Fabrication of an Alternating Multilayer Film of Poly(4-Vinylpyridine) and Poly(Acrylic Acid) Based on Hydrogen Bonding. Macromol. Rapid Commun. 1997, 18 (6), 509–514. https://doi.org/10.1002/marc.1997.030180609.

(245) Quinn, J. F.; Caruso, F. Facile Tailoring of Film Morphology and Release Properties Using Layer-by-Layer Assembly of Thermoresponsive Materials. Langmuir 2004, 20 (1), 20–22. https://doi.org/10.1021/la0360310.

(246) Huo, F.; Xu, H.; Zhang, L.; Fu, Y.; Wang, Z.; Zhang, X. Hydrogen-Bonding Based Multilayer Assemblies by Self-Deposition of Dendrimer. Chem. Commun. 2003, 3 (7), 874–875. https://doi.org/10.1039/b300405h.

(247) Lu, Y.; Choi, Y. J.; Lim, H. S.; Kwak, D.; Shim, C.; Lee, S. G.; Cho, K. PH-Induced Antireflection Coatings Derived from Hydrogen-Bonding-Directed Multilayer Films. Langmuir 2010, 26 (22), 17749–17755. https://doi.org/10.1021/la103260g.

(248) Shimazaki, Y.; Mitsuishi, M.; Ito, S.; Yamamoto, M. Preparation of the Layer-by-Layer Deposited Ultrathin Film Based on the Charge-Transfer

Interaction. Langmuir 1997, 13 (6), 1385–1387. https://doi.org/10.1021/la9609579.

(249) Crespo-Biel, O.; Dordi, B.; Reinhoudt, D. N.; Huskens, J. Supramolecular Layer-by-Layer Assembly: Alternating Adsorptions of Guest- and Host-Functionalized Molecules and Particles Using Multivalent Supramolecular Interactions. J. Am. Chem. Soc. 2005, 127 (20), 7594–7600. https://doi.org/10.1021/ja051093t.

(250) Ikeda, A.; Hatano, T.; Shinkai, S.; Akiyama, T.; Yamada, S. Efficient Photocurrent Generation in Novel Self-Assembled Multilayers Comprised of [60]Fullerene-Cationic Homooxacalix[3]Arene Inclusion Complex and Anionic Porphyrin Polymer [2]. J. Am. Chem. Soc. 2001, 123 (20), 4855–4856. https://doi.org/10.1021/ja015596k.

(251) Kida, T.; Minabe, T.; Nakano, S.; Akashi, M. Fabrication of Novel Multilayered Thin Films Based on Inclusion Complex Formation Between Amylose Derivatives and Guest Polymers. Langmuir 2008, 24 (17), 9227–9229. https://doi.org/10.1021/la801811r.

(252) Gao, S.; Yuan, D.; Lü, J.; Cao, R. In Situ Synthesis of Ag Nanoparticles in Aminocalix[4]Arene Multilayers. J. Colloid Interface Sci. 2010, 341 (2), 320–325. https://doi.org/10.1016/j.jcis.2009.09.025.

(253) Kurth, D. G.; Osterhout, R. In Situ Analysis of Metallosupramolecular Coordination Polyelectrolyte Films by Surface Plasmon Resonance Spectroscopy. Langmuir 1999, 15 (14), 4842–4846. https://doi.org/10.1021/la981760e.

(254) Ginzburg, M.; Galloro, J.; Jäkle, F.; Power-Billard, K. N.; Yang, S.; Sokolov, I.; Lam, C. N. C.; Neumann, A. W.; Manners, I.; Ozin, G. A. Layer-by-Layer Self-Assembly of Organic-Organometallic Polymer Electrostatic Superlattices Using Poly(Ferrocenylsilanes). Langmuir 2000, 16 (24), 9609–9614. https://doi.org/10.1021/la0012283.

(255) Qian, D. J.; Nakamura, C.; Ishida, T.; Wenk, S. O.; Wakayama, T.; Takeda, S.; Miyake, J. Palladium-Mediated Stepwise Assembly of Three-Dimensional Organized Multiporphyrin Arrays Directly on Solid Substrates. Langmuir 2002, 18 (26), 10237–10242. https://doi.org/10.1021/la0205654.

(256) Altman, M.; Shukla, A. D.; Zubkov, T.; Evmenenko, G.; Dutta, P.; Van Der Boom, M. E. Controlling Structure from the Bottom-up: Structural and Optical Properties of Layer-by-Layer Assembled Palladium Coordination-Based Multilayers. J. Am. Chem. Soc. 2006, 128 (22), 7374–7382. https://doi.org/10.1021/ja061026e.

(257) Zhao, W.; Tong, B.; Shi, J.; Pan, Y.; Shen, J.; Zhi, J.; Chan, W. K.; Dong, Y. Fabrication and Optoelectronic Properties of Novel Films Based on Functionalized Multiwalled Carbon Nanotubes and (Phthalocyaninato)Ruthenium(II) via Coordination Bonded Layer-by-Layer Self-Assembly. Langmuir 2010, 26 (20), 16084–16089. https://doi.org/10.1021/la1022196.

(258) Welterlich, I.; Tieke, B. Conjugated Polymer with Benzimidazolylpyridine Ligands in the Side Chain: Metal Ion Coordination and Coordinative Self-Assembly into Fluorescent Ultrathin Films. Macromolecules 2011, 44 (11), 4194–4203. https://doi.org/10.1021/ma200126e.

(259) Xu, L.; Zhu, Z.; Sukhishvili, S. A. Polyelectrolyte Multilayers of Diblock Copolymer Micelles with Temperature-Responsive Cores. Langmuir 2011, 27 (1), 409–415. https://doi.org/10.1021/la1038014.

(260) Al-Hariri, L. A.; Reisch, A.; Schlenoff, J. B. Exploring the Heteroatom Effect on Polyelectrolyte Multilayer Assembly: The Neglected Polyoniums. Langmuir 2011, 27 (7), 3914–3919. https://doi.org/10.1021/la104109f.

(261) He, P.-G.; Takahashi, T.; Hoshi, T.; Anzai, J. -i.; Suzuki, Y.; Osa, T. Preparation of Enzyme Multilayers on Electrode Surface by Use of Avidin and Biotin-Labeled Enzyme for Biosensor Applications. Mater. Sci. Eng. C 1994, 2 (1–2), 103–106. https://doi.org/10.1016/0928-4931(94)90037-X.

(262) Müller, W.; Ringsdorf, H.; Suci, P.; Herron, J. N.; Ebato, H.; Okahata, Y. Docking of a Second Functional Protein Layer to a Streptavidin Matrix on a Solid Support: Studies with a Quartz Crystal Microbalance. Angew. Chemie Int. Ed. English 1992, 31 (8), 1087–1090. https://doi.org/10.1002/anie.199210871.

(263) Anzai, J. I.; Kobayashi, Y.; Nakamura, N.; Nishimura, M.; Hoshi, T. Layer-by-Layer Construction of Multilayer Thin Films Composed of Avidin and Biotin-Labeled Poly(Amine)S. Langmuir 1999, 15 (1), 221–226. https://doi.org/10.1021/la980743m.

(264) Bourdillon, C.; Demaille, C.; Moiroux, J.; Saveant, J.-M. Step-by-Step Immunological Construction of a Fully Active Multilayer Enzyme Electrode. J. Am. Chem. Soc. 1994, 116 (22), 10328–10329. https://doi.org/10.1021/ja00101a074.

(265) Bourdillon, C.; Demaille, C.; Moiroux, J.; Savéant, J.-M. Catalysis and Mass Transport in Spatially Ordered Enzyme Assemblies on Electrodes. J. Am. Chem. Soc. 1995, 117 (46), 11499–11506. https://doi.org/10.1021/ja00151a013.

(266) Anzai, J.-I.; Kobayashi, Y.; Nakamura, N. Alternate Deposition of Concanavalin a and Mannose-Labelled Enzymes on a Solid Surface to Prepare Catalytically Active Enzyme Thin Films. J. Chem. Soc. Perkin Trans. 2 1998, No. 3, 461–462. https://doi.org/10.1039/a709286e.

(267) Zhu, Y.; Tong, W.; Gao, C. Molecular-Engineered Polymeric Microcapsules Assembled from Concanavalin A and Glycogen with Specific Responses to Carbohydrates. Soft Matter 2011, 7 (12), 5805–5815. https://doi.org/10.1039/c1sm05047h.

(268) Kadowaki, K.; Matsusaki, M.; Akashi, M. Control of Cell Surface and Functions by Layer-by-Layer Nanofilms. Langmuir 2010, 26 (8), 5670–5678. https://doi.org/10.1021/la903738n.

(269) Matsuzawa, A.; Matsusaki, M.; Akashi, M. Effectiveness of Nanometer-Sized Extracellular Matrix Layer-by-Layer Assembled Films for a Cell Membrane Coating Protecting Cells from Physical Stress. Langmuir 2013, 29 (24), 7362–7368. https://doi.org/10.1021/la303459v.

(270) Nishiguchi, A.; Yoshida, H.; Matsusaki, M.; Akashi, M. Rapid Construction of Three-Dimensional Multilayered Tissues with Endothelial Tube Networks by the Cell-Accumulation Technique. Adv. Mater. 2011, 23 (31), 3506–3510. https://doi.org/10.1002/adma.201101787.

(271) Matsusaki, M.; Kadowaki, K.; Nakahara, Y.; Akashi, M. Fabrication of Cellular Multilayers with Nanometer-Sized Extracellular Matrix Films. Angew. Chemie - Int. Ed. 2007, 46 (25), 4689–4692. https://doi.org/10.1002/anie.200701089.

(272) Matsusaki, M. Development of Three-Dimensional Tissue Models Based on Hierarchical Cell Manipulation Using Nanofilms. Bull. Chem. Soc. Jpn. 2012, 85 (4), 401–414. https://doi.org/10.1246/bcsj.20110194.

(273) Sui, Z.; Salloum, D.; Schlenoff, J. B. Effect of Molecular Weight on the Construction of Polyelectrolyte Multilayers: Stripping versus Sticking. Langmuir 2003, 19 (6), 2491–2495. https://doi.org/10.1021/la026531d.

(274) Dubas, S. T.; Schlenoff, J. B. Factors Controlling the Growth of Polyelectrolyte Multilayers. Macromolecules 1999, 32 (24), 8153–8160. https://doi.org/10.1021/ma981927a.

(275) Burke, S. E.; Barrett, C. J. Acid-Base Equilibria of Weak Polyelectrolytes in Multilayer Thin Films. Langmuir 2003, 19 (8), 3297–3303. https://doi.org/10.1021/la026500i.

(276) Mendelsohn, J. D.; Yang, S. Y.; Hiller, J. a.; Hochbaum, A. I.; Rubner, M. F. Rational Design of Cytophilic and Cytophobic Polyelectrolyte Multilayer Thin Films. Biomacromolecules 2003, 4 (1), 96–106. https://doi.org/10.1021/bm0256101.

(277) Lvov, Y.; Haas, H.; Decher, G.; Moehwald, H.; Mikhailov, A.; Mtchedlishvily, B.; Morgunova, E.; Vainshtein, B. Successive Deposition of Alternate Layers of Polyelectrolytes and a Charged Virus. Langmuir 1994, 10 (11), 4232–4236. https://doi.org/10.1021/la00023a052.

(278) Lvov, Y.; Ariga, K.; Ichinose, I.; Kunitake, T. Assembly of Multicomponent Protein Films by Means of Electrostatic Layer-by-Layer Adsorption. J. Am. Chem. Soc. 1995, 117 (22), 6117–6123. https://doi.org/10.1021/ja00127a026.

(279) Ariga, K.; McShane, M.; Lvov, Y. M.; Ji, Q.; Hill, J. P. Layer-by-Layer Assembly for Drug Delivery and Related Applications. Expert Opin.

Drug Deliv. 2011, 8 (5), 633–644. https://doi.org/10.1517/17425247.2011.566268.

(280) Komatsu, T.; Qu, X.; Ihara, H.; Fujihara, M.; Azuma, H.; Ikeda, H. Virus Trap in Human Serum Albumin Nanotube. J. Am. Chem. Soc. 2011, 133 (10), 3246–3248. https://doi.org/10.1021/ja1096122.

(281) Lvov, Y.; Ariga, K.; Onda, M.; Ichinose, I.; Kunitake, T. Alternate Assembly of Ordered Multilayers of SiO 2 and Other Nanoparticles and Polyions. Langmuir 1997, 13 (23), 6195–6203. https://doi.org/10.1021/la970517x.

(282) Caruso, F.; Caruso, R. A.; Möhwald, H. Nanoengineering of Inorganic and Hybrid Hollow Spheres by Colloidal Templating. Science (80-. ). 1998, 282 (5391), 1111–1114. https://doi.org/10.1126/science.282.5391.1111.

(283) Li, Q.; Quinn, J. F.; Wang, Y.; Caruso, F. Preparation of Nanoporous Polyelectrolyte Multilayer Films via Nanoparticle Templating. Chem. Mater. 2006, 18 (23), 5480–5485. https://doi.org/10.1021/cm061626c.

(284) Shchukln, D. G.; Ustinovich, E. A.; Sukhorukov, G. B.; Möhwald, H.; Sviridov, D. V. Metallized Polyelectrolyte Microcapsules. Adv. Mater. 2005, 17 (4), 468–472. https://doi.org/10.1002/adma.200401031.

(285) Ariga, K.; Lvov, Y.; Kunitake, T. Assembling Alternate Dye-Polyion Molecular Films by Electrostatic Layer-by-Layer Adsorption. J. Am. Chem. Soc. 1997, 119 (9), 2224–2231. https://doi.org/10.1021/ja963442c.

(286) Linford, M. R.; Auch, M.; Möhwald, H. Nonmonotonic Effect of Ionic Strength on Surface Dye Extraction Durins Dye-Polyelectrolyte Multilayer Formation. J. Am. Chem. Soc. 1998, 120 (1), 178–182. https://doi.org/10.1021/ja972133z.

(287) Zebli, B.; Susha, A. S.; Sukhorukov, G. B.; Rogach, A. L.; Parak, W. J. Magnetic Targeting and Cellular Uptake of Polymer Microcapsules Simultaneously Functionalized with Magnetic and Luminescent Nanocrystals. Langmuir 2005, 21 (10), 4262–4265. https://doi.org/10.1021/la0502286.

(288) Hu, S. H.; Tsai, C. H.; Liao, C. F.; Liu, D. M.; Chen, S. Y. Controlled Rupture of Magnetic Polyelectrolyte Microcapsules for Drug Delivery. Langmuir 2008, 24 (20), 11811–11818. https://doi.org/10.1021/la801138e.

(289) Kotov, N. A.; Haraszti, T.; Turi, L.; Zavala, G.; Geer, R. E.; Dékány, I.; Fendler, J. H. Mechanism of and Defect Formation in the Self-Assembly of Polymeric Polycation-Montmorillonite Ultrathin Films. J. Am. Chem. Soc. 1997, 119 (29), 6821–6832. https://doi.org/10.1021/ja964409t.

(290) Hua, F.; Cui, T.; Lvov, Y. M. Ultrathin Cantilevers Based on Polymer-Ceramic Nanocomposite Assembled through Layer-by-Layer Adsorption. Nano Lett. 2004, 4 (5), 823–825. https://doi.org/10.1021/nl0498031.

(291) Serizawa, T.; Akashi, M. Accumulation of Cationic-Polymer Grafted Poly(Styrene) Nanospheres onto an Anionic-Polymer Surface. Chem. Lett. 1997, No. 8, 809–810. https://doi.org/10.1246/cl.1997.809.

(292) Serizawa, T.; Kamimura, S.; Akashi, M. Electrostatic Adsorption of Polystyrene Particles with Different Surface Charges onto the Surface of an Ultrathin Polymer Film. Colloids Surfaces A Physicochem. Eng. Asp. 2000, 164 (2–3), 237–245. https://doi.org/10.1016/S0927-7757(99)00399-4.

(293) Donath, E.; Sukhorukov, G. B.; Caruso, F.; Davis, S. A.; Möhwald, H. Novel Hollow Polymer Shells by Colloid-Templated Assembly of Polyelectrolytes. Angew. Chemie - Int. Ed. 1998, 37 (16), 2202–2205.

(294) Lvov, Y.; Antipov, A. A.; Mamedov, A.; Möhwald, H.; Sukhorukov, G. B. Urease Encapsulation in Nanoorganized Microshells. Nano Lett. 2001, 1 (3), 125–128. https://doi.org/10.1021/nl0100015.

(295) Liang, Z.; Susha, A.; Caruso, F. Gold Nanoparticle-Based Core-Shell and Hollow Spheres and Ordered Assemblies Thereof. Chem. Mater. 2003, 15 (16), 3176–3183. https://doi.org/10.1021/cm031014h.

(296) Volodkin, D. V.; Petrov, A. I.; Prevot, M.; Sukhorukov, G. B. Matrix Polyelectrolyte Microcapsules: New System for Macromolecule Encapsulation. Langmuir 2004, 20 (8), 3398–3406. https://doi.org/10.1021/la036177z.

(297) Park, M. K.; Deng, S.; Advincula, R. C. Sustained Release Control via Photo-Cross-Linking of Polyelectrolyte Layer-by-Layer Hollow Capsules. Langmuir 2005, 21 (12), 5272–5277. https://doi.org/10.1021/la047008x.

(298) Mauser, T.; Déjugnat, C.; Möhwald, H.; Sukhorukov, G. B. Microcapsules Made of Weak Polyelectrolytes: Templating and Stimuli-Responsive Properties. Langmuir 2006, 22 (13), 5888–5893. https://doi.org/10.1021/la060088f.

(299) De Geest, B. G.; Jonas, A. M.; Demeester, J.; De Smedt, S. C. Glucose-Responsive Polyelectrolyte Capsules. Langmuir 2006, 22 (11), 5070–5074. https://doi.org/10.1021/la053368o.

(300) Shchukin, D. G.; Möhwald, H. Urea Photosynthesis inside Polyelectrolyte Capsules: Effect of Confined Media. Langmuir 2005, 21 (12), 5582–5587. https://doi.org/10.1021/la050429+.

(301) Sousa, F.; Kreft, O.; Sukhorukov, G. B.; Möhwald, H.; Kokol, V. Biocatalytic Response of Multi-Layer Assembled Collagen/Hyaluronic Acid Nanoengineered Capsules. J. Microencapsul. 2014, 31 (3), 270–276. https://doi.org/10.3109/02652048.2013.834995.

(302) Martin, C. R. Nanomaterials: A Membrane-Based Synthetic Approach. Science (80-. ). 1994, 266 (5193), 1961–1966. https://doi.org/10.1126/science.266.5193.1961.

(303) Cepak, V. M.; Martin, C. R. Preparation of Polymeric Micro- and Nanostructures Using a Template-Based Deposition Method. Chem. Mater. 1999, 11 (5), 1363–1367. https://doi.org/10.1021/cm9811500.

(304) Liang, Z.; Susha, A. S.; Yu, A.; Caruso, F. Nanotubes Prepared by Layer-by-Layer Coating of Porous Membrane Templates. Adv. Mater. 2003, 15 (21), 1849–1853. https://doi.org/10.1002/adma.200305580.

(305) Hou, S.; Wang, J.; Martin, C. R. Template-Synthesized Protein Nanotubes. Nano Lett. 2005, 5 (2), 231–234. https://doi.org/10.1021/nl048305p.

(306) Li, J.; Cui, Y. Template-Synthesized Nanotubes through Layer-by-Layer Assembly under Charge Interaction. J. Nanosci. Nanotechnol. 2006, 6 (6), 1552–1556. https://doi.org/10.1166/jnn.2006.251.

(307) He, Q.; Cui, Y.; Ai, S.; Tian, Y.; Li, J. Self-Assembly of Composite Nanotubes and Their Applications. Curr. Opin. Colloid Interface Sci. 2009, 14 (2), 115–125. https://doi.org/10.1016/j.cocis.2008.09.005.

(308) Hou, S.; Harrell, C. C.; Trofin, L.; Kohli, P.; Martin, C. R. Layer-by-Layer Nanotube Template Synthesis. J. Am. Chem. Soc. 2004, 126 (18), 5674–5675. https://doi.org/10.1021/ja049537t.

(309) Tian, Y.; He, Q.; Cui, Y.; Li, J. Fabrication of Protein Nanotubes Based on Layer-by-Layer Assembly. Biomacromolecules 2006, 7 (9), 2539–2542. https://doi.org/10.1021/bm060412l.

(310) Lu, G.; Ai, S.; Li, J. Layer-by-Layer Assembly of Human Serum Albumin and Phospholipid Nanotubes Based on a Template. Langmuir 2005, 21 (5), 1679–1682. https://doi.org/10.1021/la047771r.

(311) Dougherty, S. a.; Zhang, D.; Liang, J. Fabrication of Protein Nanotubes Using Template-Assisted Electrostatic Layer-by-Layer Methods. Langmuir 2009, 25 (22), 13232–13237. https://doi.org/10.1021/la901909n.

(312) Zhang, D.; Dougherty, S. A.; Liang, J. Fabrication of Bovine Serum Albumin Nanotubes through Template-Assisted Layer by Layer Assembly. J. Nanoparticle Res. 2011, 13 (4), 1563–1571. https://doi.org/10.1007/s11051-011-0254-x.

(313) Lu, G.; Tsuchida, E.; Komatsu, T. Human Serum Albumin Nanotubes Comprising Layer-by-Layer Assembly with Polycation. Chem. Lett. 2008, 37 (9), 972–973. https://doi.org/10.1246/cl.2008.972.

(314) Qu, X.; Lu, G.; Tsuchida, E.; Komatsu, T. Protein Nanotubes Comprised of an Alternate Layer-by-Layer Assembly Using a Polycation as an Electrostatic Glue. Chem. - A Eur. J. 2008, 14 (33), 10303–10308. https://doi.org/10.1002/chem.200800771.

(315) Komatsu, T. Protein-Based Nanotubes for Biomedical Applications. Nanoscale 2012, 4 (6), 1910–1918. https://doi.org/10.1039/C1NR11224D.

(316) Komatsu, T.; Sato, T.; Boettcher, C. Human Serum Albumin Nanotubes with Esterase Activity. Chem. - An Asian J. 2012, 7 (1), 201–206. https://doi.org/10.1002/asia.201100606.

(317) Komatsu, T.; Terada, H.; Kobayashi, N. Protein Nanotubes with an Enzyme Interior Surface. Chem. - A Eur. J. 2011, 17 (6), 1849–1854. https://doi.org/10.1002/chem.201001937.

(318) Qu, X.; Komatsu, T. Molecular Capture in Protein Nanotubes. ACS Nano 2010, 4 (1), 563–573. https://doi.org/10.1021/nn901474y.

(319) Goto, S.; Amano, Y.; Akiyama, M.; Böttcher, C.; Komatsu, T. Gold Nanoparticle Inclusion into Protein Nanotube as a Layered Wall Component. Langmuir 2013, 29 (46), 14293–14300. https://doi.org/10.1021/la403283x.

(320) Kobayakawa, S.; Nakai, Y.; Akiyama, M.; Komatsu, T. Self-Propelled Soft Protein Microtubes with a Pt Nanoparticle Interior Surface. Chem. - A Eur. J. 2017, 23 (21), 5044–5050. https://doi.org/10.1002/chem.201605055.

(321) Qu, X.; Kobayashi, N.; Komatsu, T. Solid Nanotubes Comprising α-$Fe_2O_3$ Nanoparticles Prepared from Ferritin Protein. ACS Nano 2010, 4 (3), 1732–1738. https://doi.org/10.1021/nn901879d.

(322) Kato, R.; Komatsu, T. Structure and Photocatalytic Activity of Iron Oxide Nanotubes Prepared from Ferritin. J. Inorg. Organomet. Polym. Mater. 2013, 23 (1), 167–171. https://doi.org/10.1007/s10904-012-9725-5.

(323) Sadeghi, R.; Kalbasi, a.; Emam-jomeh, Z.; Razavi, S. H.; Kokini, J.; Moosavi-Movahedi, a. a. Biocompatible Nanotubes as Potential Carrier for Curcumin as a Model Bioactive Compound. J. Nanoparticle Res. 2013, 15 (11), 1–11. https://doi.org/10.1007/s11051-013-1931-8.

(324) Jiao, P.; Guo, Y.; Niu, A.; Kang, X. Layer-by-Layer Assembled Protein Nanotubes with High DNA Affinity. RSC Adv. 2015, 5 (47), 37130–37137. https://doi.org/10.1039/c5ra04725k.

(325) Zhang, S.; Demoustier-Champagne, S.; Jonas, A. M. Quantitative Collection and Enzymatic Activity of Glucose Oxidase Nanotubes Fabricated by Templated Layer-by-Layer Assembly. Biomacromolecules 2015, 16 (8), 2382–2393. https://doi.org/10.1021/acs.biomac.5b00628.

(326) Ramírez-Wong, D. G.; Saghazadeh, S.; Van Herck, S.; De Geest, B. G.; Jonas, A. M.; Demoustier-Champagne, S. Uptake of Long Protein-Polyelectrolyte Nanotubes by Dendritic Cells. Biomacromolecules 2017, acs.biomac.7b01353. https://doi.org/10.1021/acs.biomac.7b01353.

(327) Maldonado, L.; Kokini, J. An Optimal Window for the Fabrication of Edible Polyelectrolyte Complex Nanotubes (EPCNs) from Bovine Serum Albumin (BSA) and Sodium Alginate. Food Hydrocoll. 2018, 77, 336–346. https://doi.org/10.1016/j.foodhyd.2017.10.010.

(328) Piraux, L.; Antohe, V.; Ferain, E.; Lahem, D. Self-Supported Three-Dimensionally Interconnected Polypyrrole Nanotubes and Nanowires for Highly Sensitive Chemiresistive Gas Sensing. RSC Adv. 2016, 6, 21808–21813. https://doi.org/10.1039/C6RA03439J.

(329) Rauber, M.; Alber, I.; Muöller, S.; Neumann, R.; Picht, O.; Roth, C.; Schoökel, A.; Toimil-Molares, M. E.; Ensinger, W. Highly-Ordered Supportless Three-Dimensional Nanowire Networks with Tunable Complexity and Interwire Connectivity for Device Integration. Nano Lett. 2011, 11 (6), 2304–2310. https://doi.org/10.1021/nl2005516.

(330) Ao, H.; Xie, Y.; Tan, H.; Yang, S.; Li, K.; Wu, X.; Zheng, X.; Tang, T. Fabrication and in Vitro Evaluation of Stable Collagen/Hyaluronic Acid Biomimetic Multilayer on Titanium Coatings. J. R. Soc. Interface 2013, 10 (84), 20130070. https://doi.org/10.1098/rsif.2013.0070.

(331) Li, X.; Luo, Q.; Huang, Y.; Li, X.; Zhang, F.; Zhao, S. The Responses of Preosteoblasts to Collagen/Hyaluronic Acid Polyelectrolyte Multilayer Coating on Titanium. Polym. Adv. Technol. 2012, 23 (4), 756–764. https://doi.org/10.1002/pat.1953.

(332) Johansson, J. Å.; Halthur, T.; Herranen, M.; Söderberg, L.; Elofsson, U.; Hilborn, J. Build-up of Collagen and Hyaluronic Acid Polyelectrolyte Multilayers. Biomacromolecules 2005, 6 (3), 1353–1359. https://doi.org/10.1021/bm0493741.

(333) Grant, G. G. S.; Koktysh, D. S.; Yun, B.; Matts, R. L.; Kotov, N. a. Layer-by-Layer Assembly of Collagen Thin Films: Controlled Thickness and Biocompatibility. Biomed. Microdevices 2001, 3 (4), 301–306. https://doi.org/10.1023/A:1012456714628.

(334) Mhanna, R. F.; Vörös, J.; Zenobi-Wong, M. Layer-by-Layer Films Made from Extracellular Matrix Macromolecules on Silicone Substrates. Biomacromolecules 2011, 12 (3), 609–616. https://doi.org/10.1021/bm1012772.

(335) Li, W.; Zhao, P.; Lin, C.; Wen, X.; Katsanevakis, E.; Gero, D.; Félix, O.; Liu, Y. Natural Polyelectrolyte Self-Assembled Multilayers Based on Collagen and Alginate: Stability and Cytocompatibility. Biomacromolecules 2013, 14 (8), 2647–2656. https://doi.org/10.1021/bm4005063.

(336) Chaubaroux, C.; Vrana, E.; Debry, C.; Schaaf, P.; Senger, B.; Voegel, J. C.; Haikel, Y.; Ringwald, C.; Hemmerlé, J.; Lavalle, P.; et al. Collagen-Based Fibrillar Multilayer Films Cross-Linked by a Natural Agent. Biomacromolecules 2012, 13 (7), 2128–2135. https://doi.org/10.1021/bm300529a.

(337) Lin, Q.; Ding, X.; Qiu, F.; Song, X.; Fu, G.; Ji, J. In Situ Endothelialization of Intravascular Stents Coated with an Anti-CD34 Antibody Functionalized Heparin-Collagen Multilayer. Biomaterials 2010, 31 (14), 4017–4025. https://doi.org/10.1016/j.biomaterials.2010.01.092.

(338) Liu, Y.; He, T.; Song, H.; Gao, C. Layer-by-Layer Assembly of Biomacromolecules on Poly(Ethylene Terephthalate) Films and Fiber Fabrics to Promote Endothelial Cell Growth. J. Biomed. Mater. Res. Part A 2007, 81A (3), 692–704. https://doi.org/10.1002/jbm.a.31102.

(339) Boudou, T.; Crouzier, T.; Ren, K.; Blin, G.; Picart, C. Multiple Functionalities of Polyelectrolyte Multilayer Films: New Biomedical Applications. Adv. Mater. 2010, 22 (4), 441–467. https://doi.org/10.1002/adma.200901327.

(340) Gribova, V.; Auzely-Velty, R.; Picart, C. Polyelectrolyte Multilayer Assemblies on Materials Surfaces: From Cell Adhesion to Tissue Engineering. Chem. Mater. 2012, 24 (5), 854–869. https://doi.org/10.1021/cm2032459.

(341) Bouyer, M.; Guillot, R.; Lavaud, J.; Plettinx, C.; Olivier, C.; Curry, V.; Boutonnat, J.; Coll, J. L.; Peyrin, F.; Josserand, V.; et al. Surface Delivery of Tunable Doses of BMP-2 from an Adaptable Polymeric Scaffold

Induces Volumetric Bone Regeneration. Biomaterials 2016, 104, 168–181. https://doi.org/10.1016/j.biomaterials.2016.06.001.

(342) Picart, C.; Lavalle, P.; Hubert, P.; Cuisinier, F. J. G.; Decher, G.; Schaaf, P.; Voegel, J.-C. Buildup Mechanism for Poly( l -Lysine)/Hyaluronic Acid Films onto a Solid Surface. Langmuir 2001, 17 (23), 7414–7424. https://doi.org/10.1021/la010848g.

(343) Picart, C.; Mutterer, J.; Richert, L.; Luo, Y.; Prestwich, G. D.; Schaaf, P.; Voegel, J.-C.; Lavalle, P. Molecular Basis for the Explanation of the Exponential Growth of Polyelectrolyte Multilayers. Proc. Natl. Acad. Sci. 2002, 99 (20), 12531–12535. https://doi.org/10.1073/pnas.202486099.

(344) Richert, L.; Engler, A. J.; Discher, D. E.; Picart, C. Elasticity of Native and Cross-Linked Polyelectrolyte Multilayer Films. Biomacromolecules 2004, 5 (5), 1908–1916. https://doi.org/10.1021/bm0498023.

(345) Richert, L.; Lavalle, P.; Payan, E.; Shu, X. Z.; Prestwich, G. D.; Stoltz, J.; Schaaf, P.; Voegel, J.; Picart, C. Layer by Layer Buildup of Polysaccharide Films : Physical Chemistry and Cellular Adhesion Aspects Layer by Layer Buildup of Polysaccharide Films : Physical Chemistry and Cellular Adhesion Aspects. Society 2004, No. 9, 448–458. https://doi.org/10.1021/la035415n.

(346) Richert, L.; Boulmedais, F.; Lavalle, P.; Mutterer, J.; Ferreux, E.; Decher, G.; Schaaf, P.; Voegel, J.-C.; Picart, C. Improvement of Stability and Cell Adhesion Properties of Polyelectrolyte Multilayer Films by Chemical Cross-Linking. Biomacromolecules 2004, 5 (2), 284–294. https://doi.org/10.1021/bm0342281.

(347) Schneider, A.; Obeid, R.; Schwinte, P.; Hemmerle, J.; Schaaf, P.; Voegel, J.; Senger, B.; Picart, C.; Dentaire, D. C.; Pasteur, L.; et al. Polyelectrolyte Multilayers with a Tunable Young ' s Modulus : Influence of Film Stiffness on Cell Adhesion. Langmuir 2006, 22 (3), 1193–1200.

(348) Boudou, T.; Crouzier, T.; Auzély-Velty, R.; Glinel, K.; Picart, C. Internal Composition versus the Mechanical Properties of Polyelectrolyte Multilayer Films: The Influence of Chemical Cross-Linking. Langmuir 2009, 25 (24), 13809–13819. https://doi.org/10.1021/la9018663.

(349) Crouzier, T.; Fourel, L.; Boudou, T.; Albigès-Rizo, C.; Picart, C. Presentation of BMP-2 from a Soft Biopolymeric Film Unveils Its Activity on Cell Adhesion and Migration. Adv. Mater. 2011, 23 (12), H111–H118. https://doi.org/10.1002/adma.201004637.

(350) Crouzier, T.; Picart, C. Ion Pairing and Hydration in Polyelectrolyte Multilayer Films Containing Polysaccharides. Biomacromolecules 2009, 10 (2), 433–442. https://doi.org/10.1021/bm8012378.

(351) Picart, B. C.; Schneider, A.; Etienne, O.; Mutterer, J.; Schaaf, P.; Egles, C.; Jessel, N.; Voegel, J. Controlled Degradability of Polysaccharide Multilayer Films In Vitro and In Vivo. Adv. Funct. Mater. 2005, 15, 1771–1780. https://doi.org/10.1002/adfm.200400588.

(352) Zhang, J.; Senger, B.; Vautier, D.; Picart, C.; Schaaf, P.; Voegel, J.-C.; Lavalle, P. Natural Polyelectrolyte Films Based on Layer-by Layer Deposition of Collagen and Hyaluronic Acid. Biomaterials 2005, 26 (16), 3353–3361. https://doi.org/10.1016/j.biomaterials.2004.08.019.

(353) Caridade, S. G.; Monge, C.; Almodóvar, J.; Guillot, R.; Lavaud, J.; Josserand, V.; Coll, J.; Mano, J. F.; Picart, C. Myoconductive and Osteoinductive Free-Standing Polysaccharide Membranes. Acta Biomater. 2015, 15, 139–149. https://doi.org/10.1016/j.actbio.2014.12.027.

(354) Fujie, T.; Furutate, S.; Niwa, D.; Takeoka, S. A Nano-Fibrous Assembly of Collagen–Hyaluronic Acid for Controlling Cell-Adhesive Properties. Soft Matter 2010, 6 (19), 4672. https://doi.org/10.1039/c0sm00527d.

(355) Landoulsi, J.; Roy, C. J.; Dupont-Gillain, C.; Demoustier-Champagne, S. Synthesis of Collagen Nanotubes with Highly Regular Dimensions through Membrane-Templated Layer-by-Layer Assembly. Biomacromolecules 2009, 10 (5), 1021–1024. https://doi.org/10.1021/bm900245h.

(356) Landoulsi, J.; Demoustier-Champagne, S.; Dupont-Gillain, C. Self-Assembled Multilayers Based on Native or Denatured Collagen: Mechanism and Synthesis of Size-Controlled Nanotubes. Soft Matter 2011, 7 (7), 3337. https://doi.org/10.1039/c0sm00918k.

(357) Poleunis, C.; Dupont-Gillain, C.; Demoustier-Champagne, S.; Delcorte, A.; Kalaskar, D. Characterisation of Protein Nanotubes by ToF-SIMS Imaging. Surf. Interface Anal. 2013, 45 (1), 333–337. https://doi.org/10.1002/sia.5037.

(358) Kalaskar, D. M.; Poleunis, C.; Dupont-Gillain, C.; Demoustier-Champagne, S. Elaboration of Nanostructured Biointerfaces with Tunable Degree of Coverage by Protein Nanotubes Using Electrophoretic Deposition. Biomacromolecules 2011, 12 (11), 4104–4111. https://doi.org/10.1021/bm2011592.

(359) Kalaskar, D. M.; Demoustier-Champagne, S.; Dupont-Gillain, C. C. Interaction of Preosteoblasts with Surface-Immobilized Collagen-Based Nanotubes. Colloids Surfaces B Biointerfaces 2013, 111, 134–141. https://doi.org/10.1016/j.colsurfb.2013.05.035.

(360) Ilic, D.; Polak, J. M. Stem Cells in Regenerative Medicine: Introduction. Br. Med. Bull. 2011, 98 (1), 117–126. https://doi.org/10.1093/bmb/ldr012.

# Chapter 2

# Aim of the thesis

The scientific community is gathering an ever-growing collection of insights into how cell fate is finely tuned *in vivo* by a complex interplay of topographical, mechanical and chemical stimuli provided through the extracellular matrix (ECM). This triggers the wish to master and replicate these cell-influencing factors. Indeed, being able to understand and control the complex mechanisms of morphogenesis, cell proliferation and differentiation found in Nature, would greatly advance technologies such as cell therapy, tissue engineering and regenerative medicine; which are currently still in their infancy. Successful outcomes of these strategies based on the regulation and modification of cell processes are intimately linked to our capacity to develop artificial cell-educative interfaces mimicking the Nature's golden standard which is ECM.

In addition to hosting the cells and providing them with mechanical support, such an ideal biointerface should be free of any harmful effect on human health. It should also present the cells with all the physical stimuli and biochemical epitopes able to trigger their adhesion on the materials surface, sustain their proliferation and guide their differentiation towards a selected phenotype. Hence, along with being biocompatible, the engineered ECM mimic should also be bioactive. All the featured signals should also be implemented at an appropriate length scale for the cells to be able to sense them and react accordingly. The cell-material cross-talks occur via internalisation of small molecules by the cells or the membrane-based recognition of molecular sequences of a few nanometers in length. The appropriate length scale will thus be the nanoscale. The best available option to combine biocompatibility and bioactivity remains to select building blocks directly in the pool of molecules invented by Nature and having successfully passed through the filter of evolution. Native ECM proteins and polysaccharides however have the drawback of lacking the adequate mechanical properties required to handle them and organize them into complex supra-molecular architectures *ex vivo*. Special care must therefore be taken when designing biomimetic interfaces to elaborate strategies which can compensate for the weak mechanical properties of biomacromolecules.

The aim of this thesis is to propose a contribution to the challenge of producing a cell-influencing interface inspired from nature's ECM. The synthesized biointerfaces will be designed to accommodate as many cell-influencing factors natively found in ECM as possible. Biopolymers originating from the ECM will be used as building blocks and driven to self-assemble into fibrous nanostructures, similar to the organization naturally taken by a large part of ECM proteins *in vivo*. The use of natural polymers will ensure biocompatibility as well as bioactivity of the resulting nanostructures. The mechanical properties of the designed architectures will also be tailored, in a way to ensure easy handling of the structures as well as to offer an additional possibility to regulate cell behaviour.

As a contribution to the development of multi-functional cell-influencing platforms, the produced biointerfaces could lead to future applications in the field of tissue engineering and regenerative medicine. More readily achievable, direct applications would be to use the synthesized biomimetic interfaces as model substrates for studying the effect of a set of finely-tuned physicochemical parameters on cell behaviour.

The successive objectives of this thesis will thus be:

1) The synthesis and characterization of ECM-like biointerfaces combining biocompatibility, bioactivity and mechanical integrity.

2) The investigation of the ability of the synthesized biointerfaces to sustain cell adhesion, proliferation and differentiation.

The research strategy elaborated to reach these goals will be developed in the next section.

# Chapter 3

# Research strategy

The prerequisite to work with natural compounds leads us to consider only bottom-up techniques able to organize the biological matter under soft, non-denaturing conditions so as to preserve the bioactivity of the natural polymers. Putting the biopolymers in a position to self-assemble into supra-molecular structures, similarly to what is occurring *in vivo*, appears to be the most natural way of organizing them. It was therefore decided to rely on the layer-by-layer (LbL) self-assembly of the chosen biopolymers to build ECM-like biointerfaces. The focus was put on Col as it is ubiquitously present as a structural protein in the ECM.[1,2] Type I Col, in particular, is well-known for featuring peptide sequences (i.e., GFOGER[3,4] and DGEA[5,6] motifs, etc.) responsible for triggering integrin-mediated cell adhesion.[7,8] It was also demonstrated to play a role in cell differentiation, especially towards the osteoblastic lineage.[5,9] In order to benefit from these bioactive properties, Col was selected as the main protein of interest and the requirement to incorporate Col in the cell-contacting outermost layer of our biointerfaces was implemented in their design. HA, a linear glycosaminoglycan copolymer of D-glucuronic acid and N-acetyl-D-glucosamide also abundantly present in native ECM[10] was more recently discovered to be granted with numerous biological functions. HA is indeed involved in cell signalling, including proliferation[11], migration[12] and adhesion.[13,14] HA was therefore selected as second partner for the LbL assembly of the biomimetic multilayer, in combination with Col.

Guidance of the biopolymers assembly into nanostructured arrangements was made possible thanks to the use of a mold (or template) with a peculiar structure designed at the nanoscale. Polycarbonate (PC) templates were selected due to the high versatility of their characteristics (i.e., thickness, pore density and average pore diameter) as well as to their ease of dissolution within organic solvents (in contrast with alumina templates, for instance, which require alkaline pH and high temperature conditions to be dissolved, incompatible with the use of biomolecules). Moreover, a high degree of knowledge and experience was accumulated in the design and use of these PC templates by researchers working in the laboratory and its partner company, *it4ip*. While templates with cylindrical

nanopores are classically produced and used to synthesize nanotubes (NTs), the templates used throughout this study were custom-designed to present a network of intersected nanopores (figure 3.1.a). Such nanoporous membranes are traditionally prepared via a track-etching process which, in this case, involved sequential rather than a single irradiation of a PC film using heavy energetic ions propelled at various incident angles, so as to create intersecting damaged tracks along the PC matrix. The created tracks along which the polymer has been degraded are then chemically etched to reveal intersecting pores which follow the infiltration path of heavy ions.

The resulting interconnected porosity of the template works as a negative of the desired structure, which is replicated thanks to the LbL deposition of the biopolymers along the pore walls and sacrificed in a final step to reveal the architecture of interest (figure 3.1.b). As a direct consequence of the high tunability of the PC templates (i.e., thickness, pore density and average pore diameter), nanostructures with highly versatile characteristics can be designed. A structure made of intersecting nanocylinders was chosen for our engineered matrices due to the set of advantages it presents:

- The high aspect ratio and high specific surface area developed by the NTs are likely to emulate those developed by the protein nanofibers present in native ECM (i.e., collagen, fibronectin, etc.).

- The inner and outer linings of the multilayered NTs can be separately and selectively functionalized.

- The existence of a hollow compartment inside the cylindrical building blocks entails the possibility of further filling them with a bioactive drug in a post-production fashion.

- Macroscopic interfaces composed of a high number of nano-sized units combine mechanical integrity and ease of handling at the macro-scale with a nano-scale precision in the distribution of cell-influencing cues.

- The high level of interconnected porosity of the resulting matrix allows the circulation of nutrients and waste products which will be respectively consumed and produced by the hosted cells.

- Cell-influencing factors are presented in a three-dimensional (3D) environment at the cellular level; similarly to *in vivo* design rules.

Compared to more conventional ECM substitutes (i.e., hydrogels, nanofiber mats, microporous polymeric foams, etc.), the designed process (i.e., template-assisted LbL assembly within custom-made templates displaying a complex and tunable network of nanostructured pores) should offer the possibility to guide the assembly of biomolecules into complex supramolecular architectures while still conserving a nano-scale precision in the distribution of cell-influencing cues.

It is noteworthy to mention that the projected biointerfaces do not constitute scaffolding materials as the dimensions of their interconnected porosity (defined by the intertubular space) is in the nanometer range (i.e., from a few nanometers to a few hundreds of nanometers) and hence, too low to allow the penetration of cells within the structure. A pore size greater than the diameter of a mammalian cell in suspension (i.e., 10-15 µm) would indeed be the required minimum for cells to be able to infiltrate the matrices.[15] However, we could expect that, in cases where the biointerfaces would be biodegradable, cells could progressively degrade the material and progressively embed themselves within the engineered matrices as they synthesize their own ECM at the same time.[16]

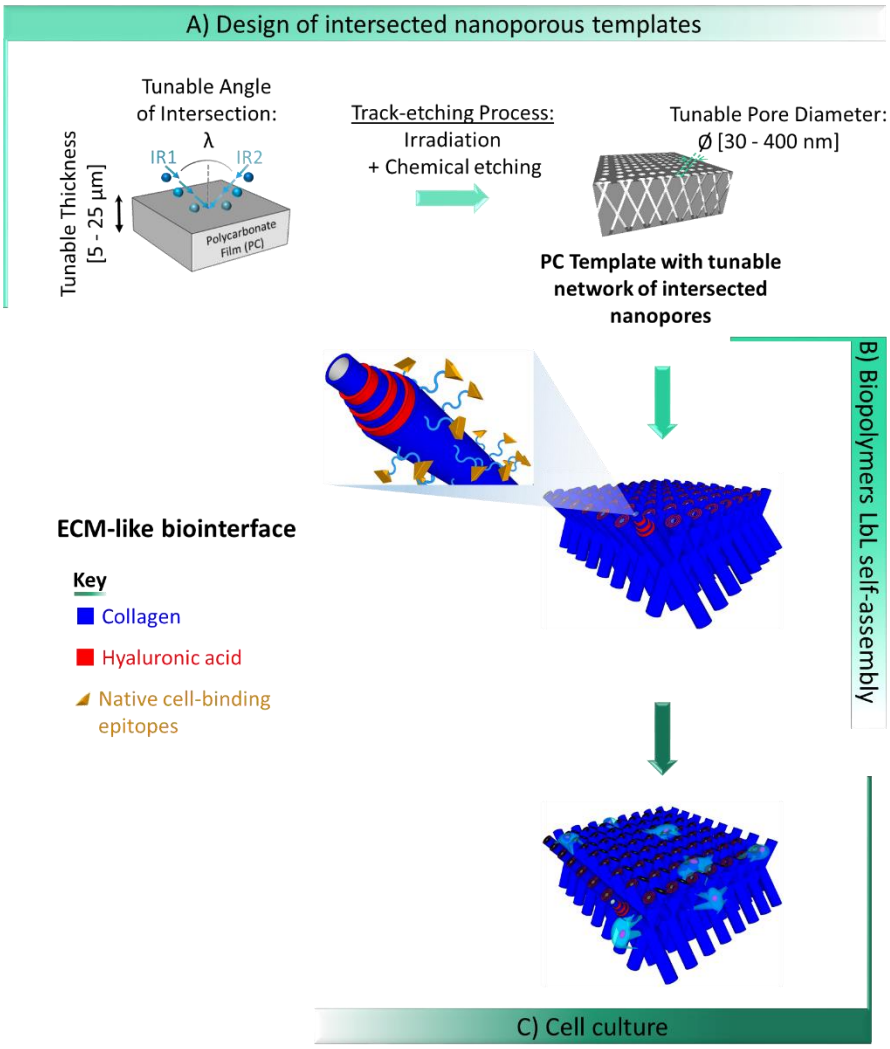


**Figure 3.1** *Schematic illustration of the general research strategy. (a) Design and synthesis of nanostructured PC templates displaying a network of intersected nanopores via a track-etching process [partnership with it4ip]. (b) Use of the produced templates to guide the LbL self-assembly of two ECM-derived biomacromolecules: Col and HA. (c) Evaluation of the performances of the as-synthesized nanostructured biointerfaces as cytocompatible and cell-influencing surfaces*

Despite the great interest of Col and HA as bioactive ECM-derived polymers, reports focussing on their LbL assembly remain scarce in the literature[17–20], probably due to the complexity of the selection of adequate assembly conditions. In the frame of this thesis, the work developed in ***Chapter 4. LbL self-assembly of ECM-like thin films, NTs and biointerfaces*** was thus dedicated to the identification of adequate conditions for triggering the Col/HA self-assembly.

First attempts at templating the optimized Col/HA assembly within nanoporous membranes so as to organize the biomacromolecules into a matrix of intersected NTs led to collapsed structures with evidently low mechanical properties (Figure 3.4). The need for easy-to-handle self-supported biointerfaces, prompted us to consider two different approaches to impart mechanical stability to the designed nanostructures while at the same time preserving their biocompatibility and bioactivity.

The first proposed approach, developed in ***Chapter 5***, focusses on the production of composite biomaterials, combining the bioactivity of ECM-derived polymers with the mechanical stiffness of ceramic nanoparticles (NPs). This was achieved thanks to the incorporation of silica NPs during the LbL assembly of Col/HA multilayers, giving rise to composite NTs and artificial matrices made thereof (Figure 3.2).

The second approach, reported in ***Chapter 6***, is based on the polymerization of a stiff polymer, PPy, inside the nanostructured template so as to firstly synthesize a rigid framework of intersected PPy NTs which is then, in a consecutive step, functionalized with a self-assembled Col/HA multilayer (Figure 3.3).

Following the successful synthesis of self-supported biointerfaces in ***Chapter 6***, their ability to favour cell adhesion was investigated using murine osteoprogenitor cells (MC3T3-E1 cell line). Furthermore, their ability to trigger and influence the early differentiation phase of MC3T3-E1 cells towards their committed phenotype (i.e., osteoblasts) was assessed.

The outline of the present thesis is summarized in Figures 3.4 & 3.5

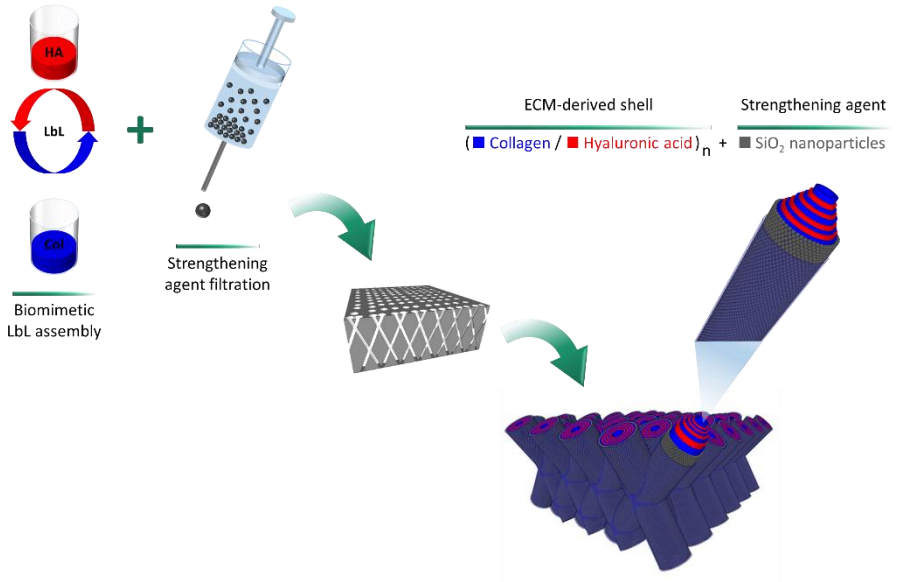


**Figure 3.2** *Schematic representation of the first approach to synthesize biointerfaces combining increased mechanical properties with bioactivity, relying on the production of nanocomposite interfaces. The stiffness of the nanotubular Col/HA multilayers is improved via incorporation of ceramic NPs, leading to nanocomposite ECM-like biointerfaces*

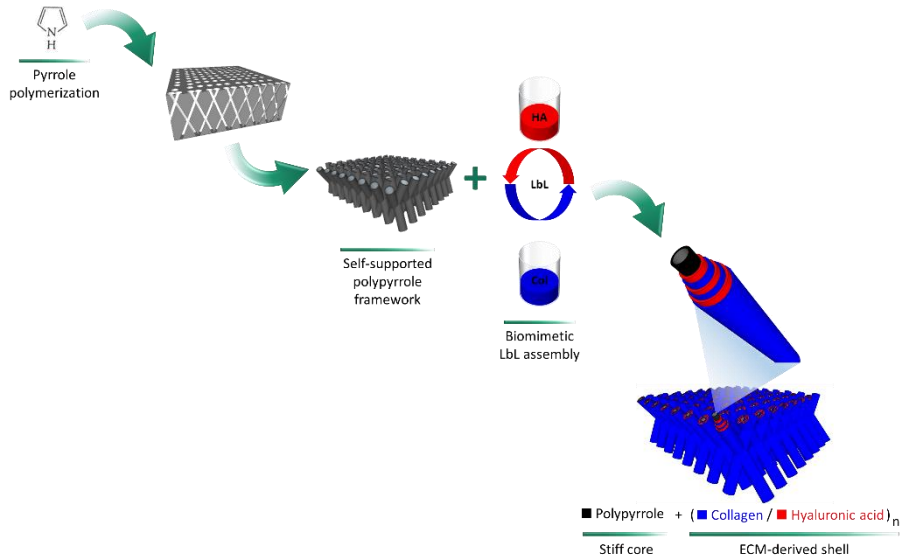


**Figure 3.3** *Schematic representation of the second approach used for the production of biointerfaces with increased mechanical stability. A self-supported framework of intersected PPy NTs is first polymerized before being functionalized with a Col/HA ECM-like multilayer.*

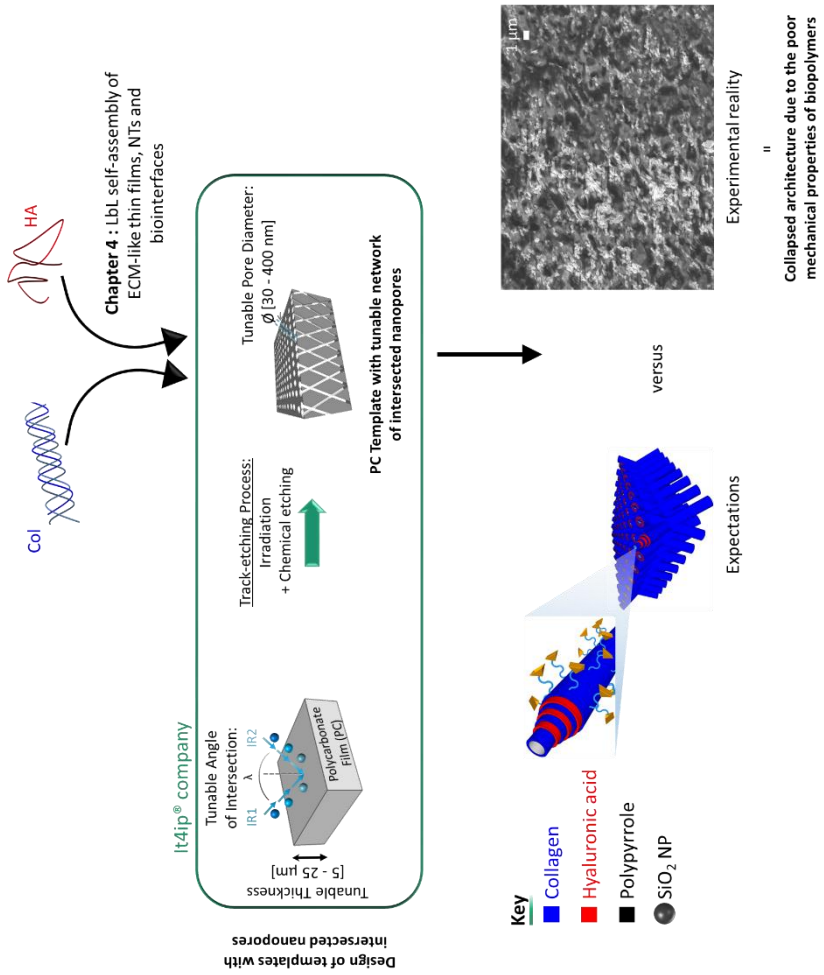


**Figure 3.4** *Thesis outline (Part A)*

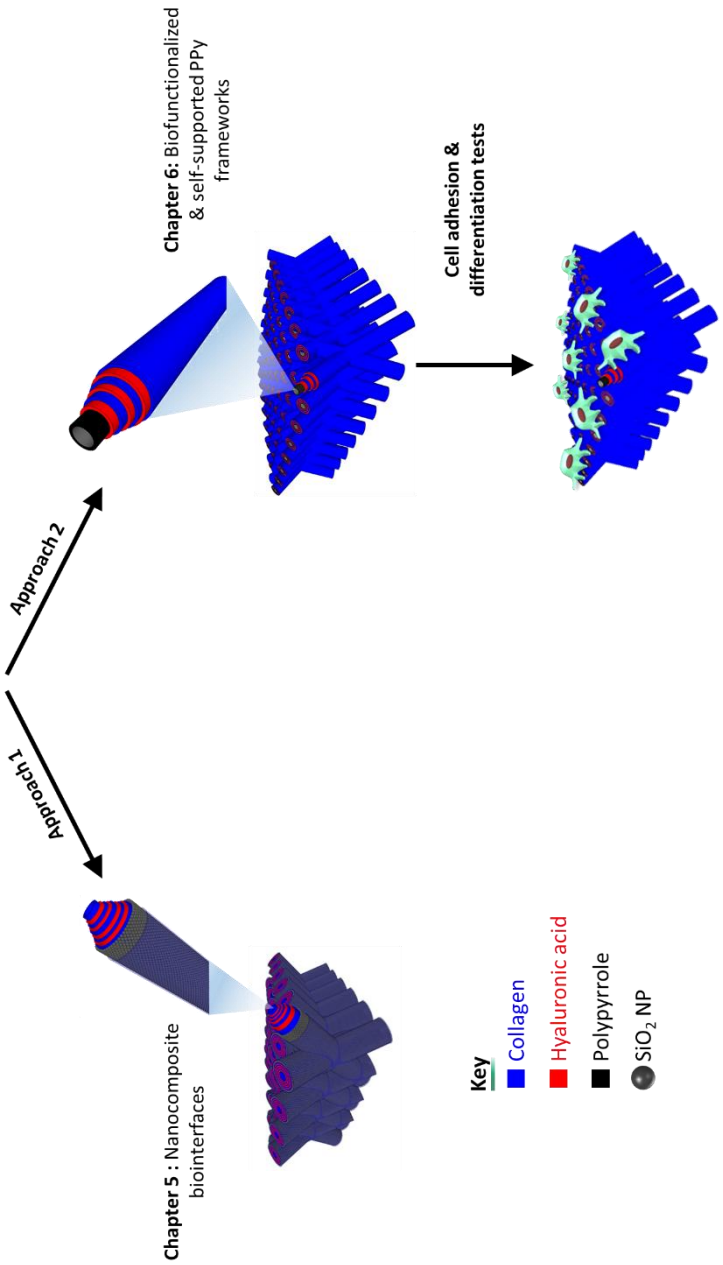


**Figure 3.5** *Thesis outline (Part B)*

## References

(1) Beckman, M. J.; Shields, K. J.; Diegelmann, R. F. Collagen. *Encyclopedia of Biomaterials and Biomedical Engineering*; Wnek, G. E., Bowlin, G. L., Eds.; New-York, 2004; pp 324–334. https://doi.org/10.1081/E-EBBE120007271.

(2) Piez, K. A. Collagen. *Encyclopedia of Polymer Sciences and Engineering*; Kroschwitz, J., 1985; pp 699–727.

(3) Von Der Mark, K.; Park, J.; Bauer, S.; Schmuki, P. Nanoscale Engineering of Biomimetic Surfaces: Cues from the Extracellular Matrix. *Cell Tissue Res.* **2010**, *339* (1), 131–153. https://doi.org/10.1007/s00441-009-0896-5.

(4) Emsley, J.; Knight, C. G.; Farndale, R. W.; Barnes, M. J.; Liddington, R. C. Structural Basis of Collagen Recognition by Integrin A2β1. *Cell* **2000**, *101* (1), 47–56. https://doi.org/10.1016/S0092-8674(00)80622-4.

(5) Mizuno, M.; Fujisawa, R.; Kuboki, Y. Type I Collagen-Induced Osteoblastic Differentiation of Bone-Marrow Cells Mediated by Collagen-A2β1 Integrin Interaction M. *J. Cell. Physiol.* **2000**, *184*, 207–213.

(6) Mizuno, M.; Kuboki, Y. Osteoblast-Related Gene Expression of Bone Marrow Cells during the Osteoblastic Differentiation Induced by Type I Collagen. *J. Biochem* **2001**, *129* (1), 133–138.

(7) Nykvist, P.; Tu, H.; Ivaska, J.; Ka, J.; Pihlajaniemi, T. Distinct Recognition of Collagen Subtypes by A1β1 and A2β1 Integrins. *J. Biol. Chem.* **2000**, *275* (11), 8255–8261.

(8) Schiro, J. A.; Chan, B. M. C.; Roswit, W. T.; Kassner, P. D.; Pentland, A. P.; Hemler, M. E.; Eisen, A. Z.; Kupper, T. S. Integrin A2β1 (VLA-2) Mediates Reorganization and Contraction of Collagen Matrices by Human Cells. *Cell* **1991**, *67* (2), 403–410. https://doi.org/10.1016/0092-8674(91)90191-Z.

(9) Salasznyk, R. M.; Williams, W. A.; Boskey, A.; Batorsky, A.; Plopper, G. E. Adhesion to Vitronectin and Collagen I Promotes Osteogenic Differentiation of Human Mesenchymal Stem Cells. *J. Biomed. Biotechnol.* **2004**, *2004* (1), 24–34.

https://doi.org/10.1155/S1110724304306017.

(10) Laurent, T. C.; Laurent, U. B.; Fraser, J. R. The Structure and Function of Hyaluronan: An Overview. *Immunol. Cell Biol.* **1996**, *74*, A1–A7. https://doi.org/10.1002/yea.

(11) Yoneda, M.; Shimizu, S.; Nishi, Y.; Yamagata, M.; Suzuki, S.; Kimata, K. Hyaluronic Acid-Dependent Change in the Extracellular Matrix of Mouse Dermal Fibroblasts That Is Conducive to Cell Proliferation. *J. Cell Sci.* **1988**, *90 ( Pt 2)*, 275–286.

(12) Nishida, T.; Nakamura, M.; Hiroshi, M.; Otori, T. Hyaluronan Stimulates Corneal Epithelial Migration. *Exp. Eye Res.* **1991**, *53* (6), 753–758.

(13) Turley, E. A.; Noble, P. W.; Bourguignon, L. Y. W. Signaling Properties of Hyaluronan Receptors. *J. Biol. Chem.* **2002**, *277* (7), 4589–4592. https://doi.org/10.1074/jbc.R100038200.

(14) Underhill, C. B.; Toole, B. P. Binding of Hyaluronate to the Surface of Cultured Cells. *J. Cell Biol.* **1979**, *82* (2), 475–484.

(15) Chaikof, E. L.; Matthew, H.; Kohn, J.; Mikos, A. G.; Prestwich, G. D.; Yip, C. M. Biomaterials and Scaffolds in Reparative Medicine. *Ann. N. Y. Acad. Sci.* **2002**, *961*, 96–105. https://doi.org/10.1111/j.1749-6632.2002.tb03057.x.

(16) Reilly, G. C.; Engler, A. J. Intrinsic Extracellular Matrix Properties Regulate Stem Cell Differentiation. *J. Biomech.* **2010**, *43* (1), 55–62. https://doi.org/10.1016/j.jbiomech.2009.09.009.

(17) Ao, H.; Xie, Y.; Tan, H.; Yang, S.; Li, K.; Wu, X.; Zheng, X.; Tang, T. Fabrication and in Vitro Evaluation of Stable Collagen/Hyaluronic Acid Biomimetic Multilayer on Titanium Coatings. *J. R. Soc. Interface* **2013**, *10* (84), 20130070. https://doi.org/10.1098/rsif.2013.0070.

(18) Johansson, J. Å.; Halthur, T.; Herranen, M.; Söderberg, L.; Elofsson, U.; Hilborn, J. Build-up of Collagen and Hyaluronic Acid Polyelectrolyte Multilayers. *Biomacromolecules* **2005**, *6* (3), 1353–1359. https://doi.org/10.1021/bm0493741.

(19) Zhang, J.; Senger, B.; Vautier, D.; Picart, C.; Schaaf, P.; Voegel, J.-C.; Lavalle, P. Natural Polyelectrolyte Films Based on Layer-by Layer Deposition of Collagen and Hyaluronic Acid. *Biomaterials* **2005**, *26* (16), 3353–3361.

https://doi.org/10.1016/j.biomaterials.2004.08.019.

(20) Li, X.; Luo, Q.; Huang, Y.; Li, X.; Zhang, F.; Zhao, S. The Responses of Preosteoblasts to Collagen/Hyaluronic Acid Polyelectrolyte Multilayer Coating on Titanium. *Polym. Adv. Technol.* **2012**, *23* (4), 756–764. https://doi.org/10.1002/pat.1953.

# Chapter 4

# LbL self-assembly of ECM-like thin films, NTs and biointerfaces

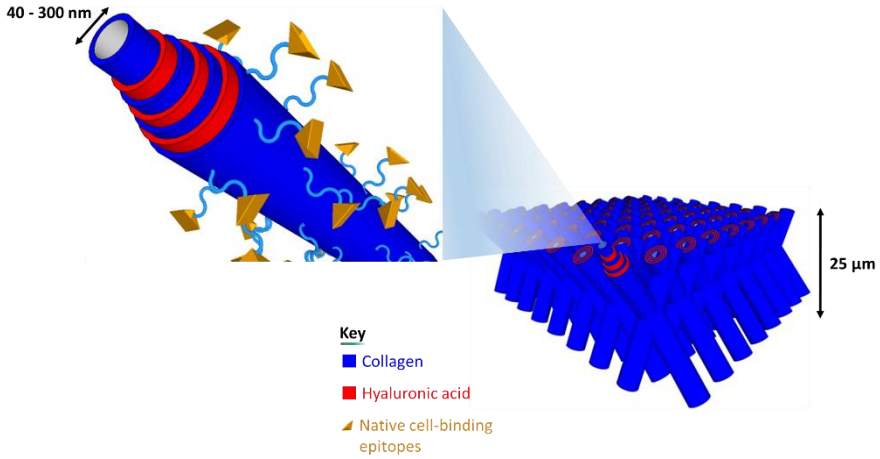


## Abstract

The assembly of two ECM-derived biopolymers, Col and HA, into supra-molecular architectures, be it in the form of planar thin films, capsules or nanotubes, would hold many promises for the advancement of implantable technologies. Reports focussing on this matter remain however scarce in the literature. This lack of background can, at least partly, be explained by the inherent complexity which exists in pinpointing the optimal conditions able to trigger successful interactions between biomacromolecules of large dimensions, non-homogeneous charge density and limited stability. In this regard, the parameters leading to the assembly of multilayered $(Col/HA)_x$ thin films and NTs are identified. The isoelectric point (iep) of Col is experimentally determined to be in the range ]5;6[ in UPW and ]4;5[ in 0.15 M NaCl aqueous solution, while the iep of HA is below 3 in both cases. Adapting the pH of the biopolymer aqueous solutions to a value of 4.0 imparts them with a global charge of opposite polarity, the ζ-potential of Col being +14.4 mV in UPW (+2.8 mV in 0.15 M NaCl) and that of HA -31.1 mV (-13.1 mV in NaCl 0.15 M). A sustainable LbL growth is observed for a $(Col/HA)_{2.5}$ film built under such pH 4.0 condition (either in UPW or 0.15 M

NaCl aqueous solution). The optimal conditions leading to (Col/HA) self-assembly are found to be substrate-dependent. While low *I* (UPW, $I = 10^{-4}$ M) favours the deposition of thicker layers on planar substrates, no nanotube could be obtained when transposing the assembly inside nanoporous templates under these conditions. The synthesis of biomimetic NTs is thus favoured under higher *I* conditions (*I* = 0.15 M), on the contrary to what is observed on flat surfaces. ECM-inspired biointerfaces of intersected NTs issuing from the (Col/HA) assembly inside custom-made templates are produced but show a collapsed morphology due to a lack of mechanical stability. Introduction of an internal core made of common synthetic polymers, PAH and PSS, inside the biomimetic NTs did not further succeed in improving the mechanical integrity of the interfaces. The discovery that interfaces built entirely out of synthetic polymers (with either 6 or 10 (PAH/PSS) bilayers) were equally collapsed leads to the conclusion that stacking a high number of polymer layers, be it synthetic or natural, would not be sufficient to drastically enhance the mechanical properties of the architectures. Hence, the development of new strategies to compensate for the low mechanical properties of (bio)polymers and reach the requirement of a self-supported biomaterial will be the focus of further research.

## 4.1 Strategy

To synthesize the aimed ECM-inspired biointerfaces, biopolymers need to be organized under mild conditions. For that purpose, the LbL assembly technique was selected as it is a versatile, solvent-free process relying on attractive forces which naturally exist between molecules (hydrogen bonds, electrostatic interactions, hydrophobic forces, specific recognition, etc.). In the case of this study, it was decided to capitalize on electroattractive forces occurring between two oppositely-charged biomolecules to assemble supramolecular architectures. The first stage in this process is to clearly identify the surface charge borne by the Col and HA biomolecules as well as to monitor its evolution as a function of pH and ionic strength (*I*) conditions. This will allow to solubilize the polymers under conditions in which they will both be imparted with a stable electrical charge of opposite polarity (Figure 4.1.a). Surface charge of colloidal particles dispersed in liquid phase can be deduced from the velocity they achieve once brought in an electric field (electrophoretic mobility determination; EPM), as developed in ***Theoretical appendix 4.I***. After selecting the optimal conditions to ensure stable charges of opposite polarity for both Col and HA macromolecules, their ability to self-assemble into multilayered thin films is assessed *in situ* using quartz crystal microbalance (QCM; ***Theoretical appendix 4.II***) (Figure 4.1.b). The possibility to carry out this LbL assembly inside a nanoporous template so as to yield individual ECM-like nanotubes is then evaluated (Figure 4.1.c).

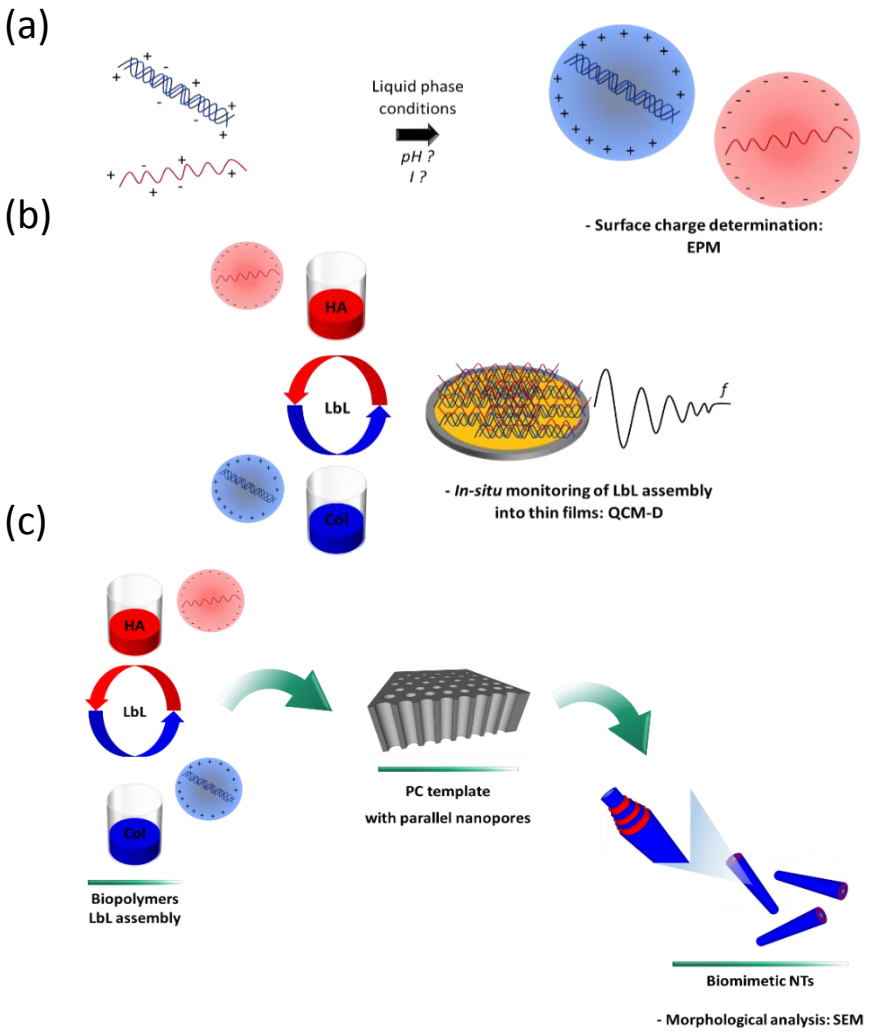


**Figure 4.1** *Schematic illustration of the successive steps of the process used for the successful production of LbL-assembled ECM-like thin films and NTs. The aqueous conditions leading to a stable charge of opposite polarity for both biopolymers are first determined using EPM (a). The opportunity to use the as-charged biopolymers to build multilayered thin films via LbL assembly is then evaluated using QCM-D (b) before finally investigating the feasibility of building biopolymer NTs thanks to the completion of the LbL assembly inside a template with parallel nanopores (c).*

## 4.2 Results and discussion

### 4.2.1 LbL self-assembly of ECM-like thin films and NTs

*a) Optimal pH selection*

Screening of the set of appropriate parameters able to elicit the self-assembly of Col and HA molecules in a LbL fashion was first initiated with the monitoring of their electrophoretic mobility ($U_E$) as a function of the pH and *I* of the solution.

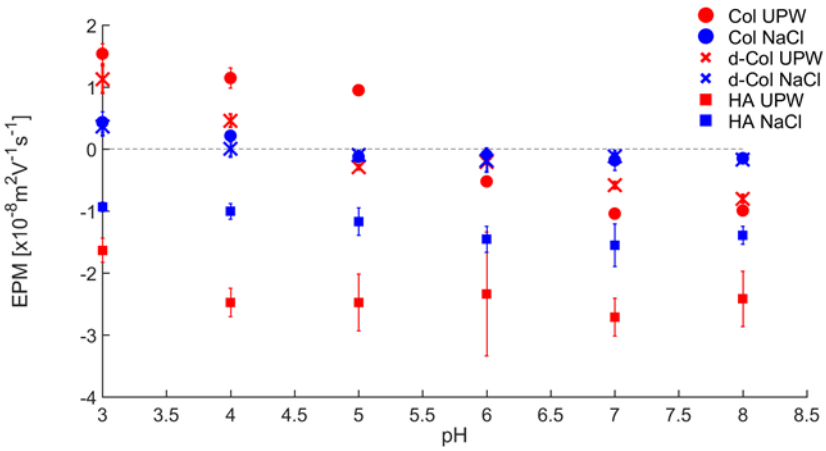


**Figure 4.2** *Evolution of the electrophoretic mobility of biomacromolecules in function of pH and ionic strength (ultrapure water, I = $10^{-5}$ M, red color or 0.15 M NaCl aqueous solution, I = 0.15 M, blue color): native (Col, circle) or denaturated (d-Col, cross) collagen and HA (square).*

As seen in Figure 4.2, Col biopolymer, whether native (Col) or denaturated (d-Col) seems to follow the same mobility pattern in function of pH. As expected, the presence of salt in the solution dampens the migration velocity of the molecules as the increased charge-screening capacity of the electrolyte solution leads to an attenuation of their ζ-potential. As such, while the isoelectric point[2] (iep) of Col is experimentally determined to be comprised between ]5;6[ in ultrapure water, it falls to ]4;5[ in 0.15 M NaCl

[2] pH value for which the charges carried by a molecule equilibrate, leading to a net charge of 0

solution. Although keeping the same evolution trend as Col, d-Col shows a slightly lower magnitude of mobility, depicting a lower density of surface charges. The iep of d-Col is thus found between ]4;5[ in ultrapure water and lowers to ~ 4 in the presence of salt. HA is always negatively charged under all studied conditions, its charge being slightly reduced in higher ionic strength environments. In order to promote the electrostatic interactions between the Col (or d-Col) and HA partners, assumed to be the driving force for their LbL assembly, the pH of the construction medium was set at 4, in such a way that Col (or d-Col) are globally positively charged and can interact interact with negatively-charged HA. Both low ($I$ = $10^{-4}$ M) and physiological ($I$ = 0.15 M) ionic strength conditions were assessed relative to their efficiency in yielding stable/fruitful self-assemblies. Computing the ζ-potential of the biopolymers of interest from their electrophoretic mobility at pH 4 yields: +14.4 mV for Col in UPW ($I$ = $10^{-4}$ M) compared to +2.8 mV in 0.15 M NaCl, +5.7 mV for d-Col in UPW compared to +0.035 mV in 0.15 M NaCl and -31.1 mV for HA compared to -13.1 mV in NaCl 0.15 M (all values obtained using equation 4.8, assuming validity of the Smoluchowski approximation, *see* ***Theroretical appendix 4.I***).

To further evidence the utter importance of fixing the pH of the construction medium at an appropriate value for which a sustainable LbL growth occurs between Col and HA molecules, QCM-D monitoring of the assembly process was carried out with or without preliminarily fixing the pH of the macromolecule solutions at 4.0 (Figures 4.3 & 4.4). Figure 4.3.(a) corresponds to the adsorption kinetics obtained from solutions of Col and HA where the polymers were simply solubilized in a 0.15 M NaCl aqueous solution, without any further pH adjustment; whereas Figure 4.4 (a) shows the adsorption profile recorded from polymer solutions whose pH was adjusted to 4.0 after dissolution of the corresponding biomacromolecule.

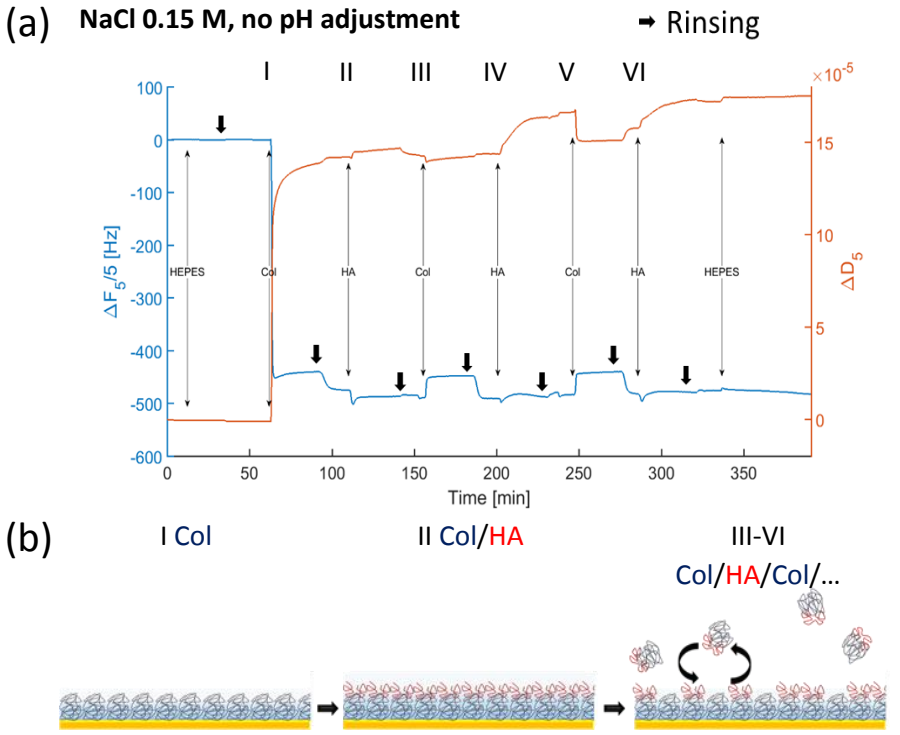


**Figure 4.3** *(a) Real time QCM-D monitoring of the frequency ($\Delta f_5/5$, left axis) and dissipation ($\Delta D_5$, right axis) shifts for the assembly of a $(Col/HA)_3$ film built with polymers dissolved in a 0.15 M NaCl aqueous solution without further pH adjustment. (b) Schematic interpretation of the adsorption sequence occurring at the crystal-liquid interface.*

The lack of a net evolution of the frequency signal in profile (a) (Figure 4.3.a) despite the alternate circulation of Col and HA solutions clearly indicates that no LbL growth is taking place on the crystal surface in absence of any pH adjustment. Only the first Col injection gives rise to a significant frequency drop, with the signal falling to -449 Hz in about 15 min, indicating a quick saturation of the quartz surface with a Col monolayer. The concomitant increase of the dissipation signal, as sudden as the frequency shift, illustrates the adsorption of Col as a highly hydrated, viscous layer which seems to swell even more through the rinsing step (joint increase in ΔD and decrease in Δf; Figure 4.3.b step I). Injection of the first HA solution leads to a further decrease of the frequency which quickly stabilizes after less than 10 min, implying the fast saturation of the previously-adsorbed Col molecules with a monolayer of HA (Figure 4.3.b step II). The multilayer growth seems to stop after the deposition of this Col/HA bilayer as the

system reaches a dynamic equilibrium with the Δf signal oscillating around a more or less constant value. Indeed, an increase in Δf is recorded whenever Col is injected, exceeding the downward shift reported during the previous HA adsorption step, likely hinting towards the formation of soluble Col-HA complexes, peeling off some previously adsorbed molecules from the crystal surface. The frequency signal then stabilizes back to its original value while rinsing, only to slightly decrease upon injection of HA, before quickly reverting back to equilibrium after rinsing and starting a new oscillation when Col is introduced. This dynamic equilibrium supports the hypothesis of the formation of soluble Col-HA complexes (Figure 4.3.b steps III to VI), as the introduction of Col would trigger a partial removal of the previously-adsorbed HA monolayer, leading to a simultaneous increase in Δf and decrease in ΔD (as observed in Figure 4.3.a), followed by a replenishment of the lost mass via adsorption of hydrated HA molecules during the next step (characterized by a drop in Δf and an increase in ΔD). Without pH adjustment, the Col solution (1 mg/mL in 0.15 M NaCl aqueous solution) features a pH of ~2.56 while the pH of the HA solution (1 mg/mL in 0.15 M NaCl aqueous solution) is equal to ~4.54. The formation of complexes might be favoured by the increased difference in surface charge of the two partners as compared to the situation which prevails when they are both adjusted at pH 4.0. The absolute value of the difference between the surface potential of the two LbL partners, $|\Delta\zeta|$, is indeed much higher at pH 2.5 (pH condition corresponding to Col injection) than it is at pH 4.0 (Figure 4.2).

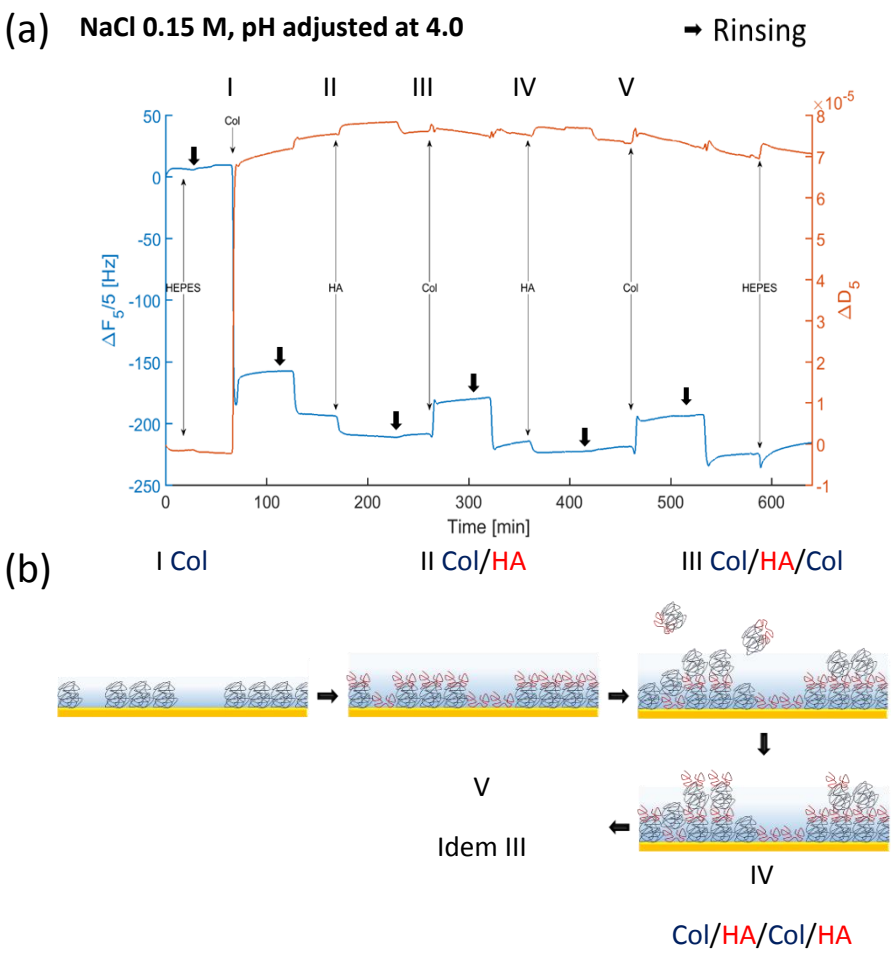


**Figure 4.4** *(a) Real time QCM-D monitoring of the frequency ($\Delta f_5/5$, left axis) and dissipation ($\Delta D_5$, right axis) shifts for the assembly of a $(Col/HA)_{2.5}$ film built with polymers dissolved in a 0.15 M NaCl aqueous solution consecutively adjusted at pH 4.0. (b) Schematic interpretation of the adsorption sequence occurring at the crystal-liquid interface.*

On the contrary, profile 4.4.a shows a net decrease in frequency following the alternate injection of Col and HA, indicative of a sustainable LbL growth under fixed pH (pH = 4.0) conditions. The frequency signal equilibrates to ~ - 158 Hz after 35 min of Col circulation; the saturation of the crystal surface is thus slower and less pronounced than when Col is adsorbed from a pH 2.5 solution (stabilization at ~ -449 Hz in 15 min, Figure 4.3.a). This probably results from the lower charge density carried by Col at pH 4.0 than

at pH 2.5. Rinsing further increases the drop in frequency and dissipation shift as water molecules are incorporated in the viscous, gel-like Col film, identically to the observations made in the absence of pH adjustment (Figure 4.3.a). Again similarly to case 4.3, the injection of HA produces an appreciable shift in both frequency and dissipation, testifying the adsorption of HA molecules over the Col layer (Figure 4.4.b steps I-II). After these two first adsorption events, introduction of Col is marked by an increase of the frequency signal, as previously observed in Figure 4.3.a, but the rinsing step yields a negative frequency shift which fully outperforms the initial increase, contrarily to what was previously observed in absence of pH adaptation. This leads to a net decrease in frequency and hence a net increase in deposited mass compared to situation 4.3. Similarly, injection of HA produces a substantial frequency shift which is not reverted upon rinsing. Surprisingly enough, the dissipation factor equilibrates at a value twice lower than in the case without pH adjustment and does not evolve much after the first Col/HA bilayer adsorption or even shows a slightly decreasing trend, suggesting a compaction of the multilayer. The increase in deposited mass cannot thus be solely explained by an accumulation of water within the film. Moreover, circulation of HEPES buffer at pH 7.4 does not seem to disturb the construction, as only a slightly positive frequency shift is recorded, evidencing the stability of the Col/HA self-assembly even in the absence of any cross-linking step.

### *b) Optimal ionic strength selection*

In order to determine whether the biomimetic Col/HA self-assembly is favoured under conditions where the biopolymers have a higher ζ-potential (in UPW, $I = 10^{-4}$ M) or rather in physiological conditions (in 0.15 M NaCl, $I$ = 0.15 M) where the ζ-potential is lower, QCM-D monitoring was carried out and compared under both conditions while keeping the pH fixed at 4.0 (Figure 4.4 & 4.5).

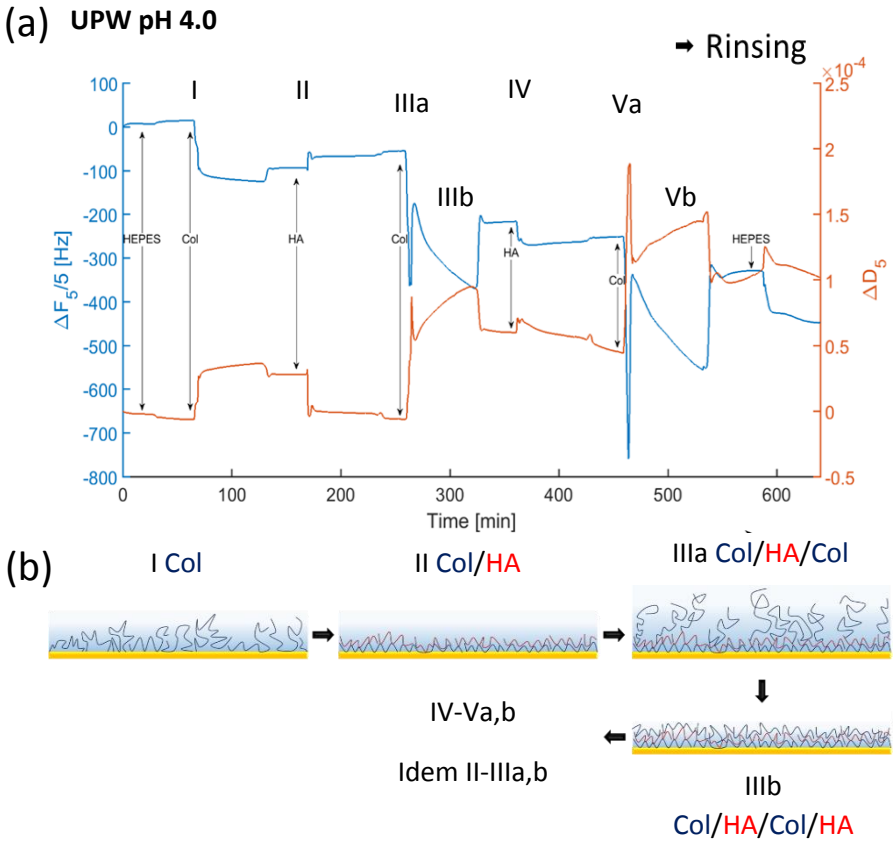


**Figure 4.5** *(a) Real time QCM-D monitoring of the frequency ($\Delta f_5/5$, left axis) and dissipation ($\Delta D_5$, right axis) shifts for the assembly of a $(Col/HA)_{2.5}$ film built with polymers dissolved in UPW adapted at pH 4.0. (b) Schematic interpretation of the adsorption sequence occurring at the crystal-liquid interface.*

The first addition of Col produces a drop in the frequency signal in both cases, although of lower magnitude in the absence of salt (Figure 4.5). The value obtained for the dissipation shift is equally lower (~3.4 x $10^{-5}$ in UPW pH 4.0 compared to ~7.7 x $10^{-5}$ in 0.15 M NaCl pH 4.0). Both observations suggest that the Col molecules adsorb on the quartz surface in a flat conformation in the absence of salt, increasing the number of interaction sites with the crystal and hence giving rise to a thinner film containing a lower density of well-extended Col polymers, occupying a larger area of the crystal surface per molecule, and a lower amount of physisorbed water (as highlighted by the lower recorded dissipation factor). The flat, worm-like

conformation adopted by Col under low ionic strength conditions is indeed justified by the lower charge-screening capacity of UPW as compared to saline solutions, leading to a higher intramolecular repulsion between identically-charged moieties and thus increasing the hydrodynamic radius of the protein. Adsorption plateau could not reach full equilibrium even after 1 h of circulation of Col in the absence of salt, on the contrary to what is observed under physiological conditions. This probably points to a progressive saturation of the crystal surface as Col molecules first adsorb rapidly as the whole quartz surface is initially available until a second, slower kinetics is reached where the adsorption of Col molecules in a rod-shaped conformation is hindered by the fact that only small portions of the surface are left available for interaction, between the pre-adsorbed protein chains. The adsorption of Col as a thin monolayer of extended, worm-like molecules in water, is further evidenced by the fact that rinsing evacuates weakly adsorbed molecules and excess water (concomitant increase in Δf and decrease in ΔD, Figure 4.5). In contrast, the rinsing step simply increases the swelling of the layer when Col is adsorbed under physiological conditions (simultaneous decrease in Δf and increase in ΔD, Figure 4.4), which points towards the fact that the biopolymers probably adsorb under a loopier, water-swellable conformation in this case.

The first injection of HA under low *I* conditions is marked by an increase of the frequency (i.e. loss of adsorbed mass) and a decrease of the dissipation factor. This can be explained by a displacement of the water molecules adsorbed to the quartz surface or to Col chains upon HA adsorption as well as by the detachment of loosely attached Col molecules from the substrate following the formation of soluble Col-HA complexes. The kinetics of Col adsorption is then radically different under the two chosen *I* conditions. While the injection of Col is followed by a decrease of adsorbed mass (i.e., increase in Δf) in 0.15 M NaCl, the opposite is true in UPW. The duality of the Col adsorption pattern then becomes more evident than during the first step: Col molecules first adsorb very quickly on the surface in a highly hydrated conformation, producing a sudden and sharp drop in Δf and peak in ΔD, before some kind of rearrangement/relaxation occurs where the system drastically loses water (as shown by the sudden and simultaneous increase of the frequency and decrease of the dissipation). We can potentially attribute this relaxation process to the fact that Col biopolymers first adsorb rapidly in a highly hydrated end-on conformation on top of the preceding layer (Figure 4.5.b, step IIIa) before creating more interaction sites with the surface and anchoring tightly to it, leading to the collapse of the brush

structure and the release of water (Figure 4.5.b, step IIIb). The colloidal charge being increasingly screened with the distance under saline conditions (Figure 4.2), the Col molecules of identical polarity can probably adsorb more easily on each other, which explains the slow but continuous increase in adsorbed mass (i.e., decrease in Δf) recorded until rinsing almost fully washes away these weakly interacting molecules.

The total change in frequency measured at the end of the self-assembly is twice larger in the absence of salt than it is under physiological conditions. This leads to a doubling of the deposited mass under low *I*. We hypothesize that this difference is due to the adsorption of Col molecules as worm-like threads at low electrolyte concentration, giving rise to thin monolayers of tightly adsorbed molecules, potentially more favourable to a sustainable stepwise LbL deposition than the adsorption of polymer chains in a more flexible and hydrated conformation as is the case for Col under saline conditions.

### *c) Relevance of a homogeneously charged anchoring layer*

All other parameters being held constant (assembly in 0.15 M NaCl aqueous solution with pH fixed at 4.0), the relevance of functionalizing the quartz surface with an homogeneously charged layer to improve the sustainability of the Col/HA assembly was evaluated by pre-adsorbing positively-charged PEI on the substrate before initiating the LbL deposition (Figure 4.6). Injection of PEI is marked by the absence of equilibrium, even after 1 hour of circulation. Two adsorption regimes seem to occur consecutively as PEI first adsorbs very slowly, inducing a simultaneous slow increase of dissipation before a much faster adsorption rate is initiated, triggering an equally high and sudden increase in ΔD. It can be hypothesized that this is explained by the adsorption of branched PEI first under a flat conformation, leading to a low density of polymer chains tightly bound to the surface (Figure 4.6.b, step I) until a critical density of adsorbed chains is achieved where the chains reorganize themselves, extend towards the solution and give rise to a highly hydrated polymer brush (Figure 4.6.b, step II). Consecutive adsorption of HA saturates in about 50 min and shows a slight compaction of the film (decrease in ΔD). Similarly to previous assemblies, the first injection of Col is characterized by a fast increase in adsorbed mass (decrease in Δf) which is however difficult to stabilize, on the contrary to what was observed for previous assemblies under NaCl 0.15 M pH 4.0 (Figure 4.4). This might be due to the specificity of the film morphology, with PEI forming a brush and thus developing a high surface area available to

adsorption. Rinsing shows an increase in mass uptake of the Col monolayer, although surprisingly not correlated to an increase in dissipation. The frequency change reached after deposition of the PEI/HA/Col multilayer, ~ -267 Hz, is surprisingly similar to the frequency drop recorded for the Col/HA/Col film built at pH 4.0 whether in UPW (~ -216 Hz) or 0.15 M NaCl (~ -215 Hz), although PEI (Mw = 600,000-1,000,000 g $mol^{-1}$) is a much larger molecule than both Col and HA. Hence, pre-adsorbing PEI over the surface that is to be functionalized does not really give rise to thicker Col/HA LbL assemblies. Further adsorption of HA yields a fast but small frequency drop while the second circulation of Col leads first to a decrease in deposited mass (increase in Δf) which is overcompensated during the rinsing step, similarly to what was previously observed under saline conditions (Figure 4.4). This can potentially again be attributed to the formation of soluble Col-HA complexes, first depleting the surface in previously-adsorbed HA and water molecules before compensating the lost mass by adsorption of Col chains which become progressively swollen with water.

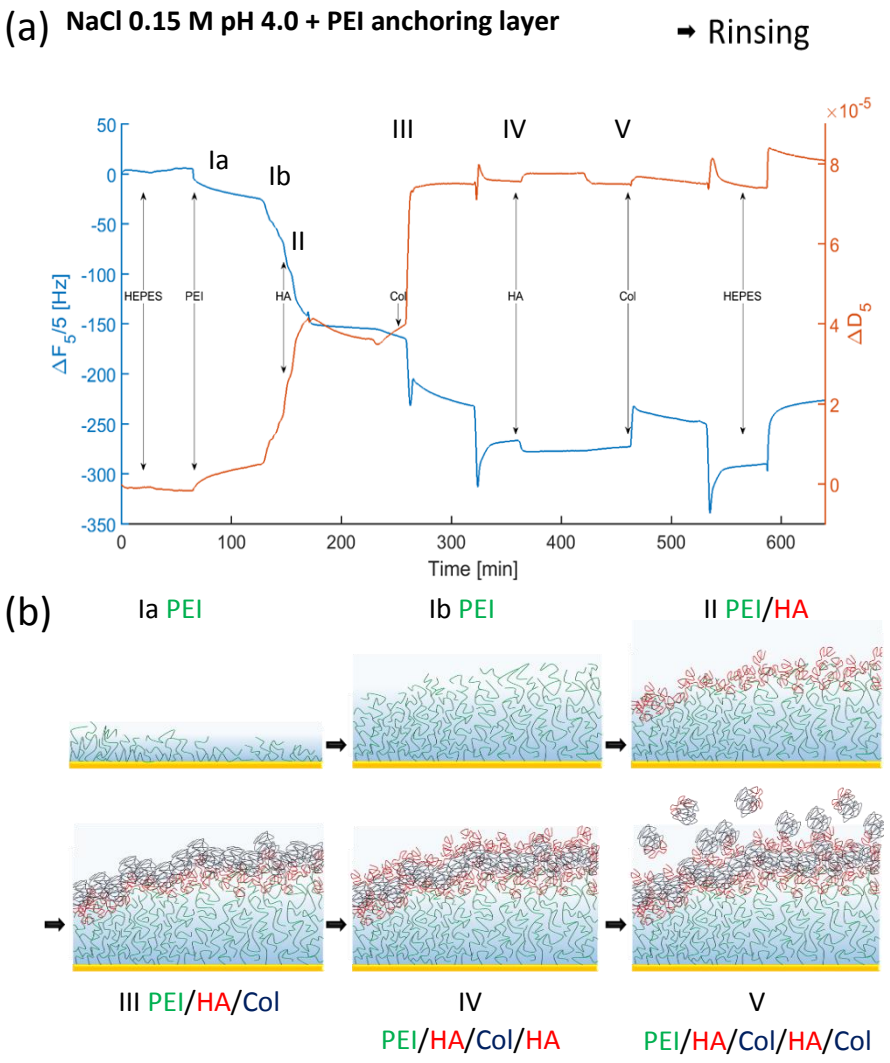


**Figure 4.6** *(a) Real time QCM-D monitoring of the frequency ($\Delta f_5/5$, left axis) and dissipation ($\Delta D_5$, right axis) shifts for the assembly of a PEI/(Col/HA)$_2$ film built with polymers dissolved in a 0.15 M NaCl aqueous solution adapted at pH 4.0. (b) Schematic interpretation of the adsorption sequence occurring at the crystal-liquid interface.*

## d) Overview of the assembly conditions

The calculated thickness of each adsorbed layer, computed using the Sauerbrey's equation (*see* ***Theoretical appendix 4.II***), under all probed conditions is summarized in Table 4.1.

**Table 4.1** *Thickness (in nm) for each polymer layer adsorbed on the QCM-D crystal as a function of the LbL conditions. Numerical thickness values were obtained by converting the QCM-D frequency shift data into adsorbed mass using the Sauerbrey's equation*.

| | Lbl conditions | Layer thickness (nm) | | | | | | | |
|---|---|---|---|---|---|---|---|---|---|
| | | PEI | Col I | HA I | Col II | HA II | Col III | HA III | Total |
| UPW | pH 4.0 | / | 19 | -6 | 29 | 6 | 14 | / | 82 |
| NaCl 0.15 M | No pH adjustment | / | 84 | 3 | 0 | -1 | 0 | -1 | 85 |
| | pH 4.0 | / | 36 | 3 | 1 | 1 | 1 | / | 40 |
| | pH 4.0 + PEI anchoring layer | 17 | 20 | 12 | 3 | 1 | / | / | 41 |

*a. The final rinsing step in HEPES buffer pH 7.4 being taken into account in the determination of the total thickness; this total value does not necessarily equate to the sum of each individual layer thickness*.

The thickest assembly is obtained under 0.15 M saline conditions without any pH adaptation step; although this thickness is to be almost solely attributed to the adsorption of the primal Col layer as a highly hydrated gel, as depicted in Figure 4.3.b. The assembly being discontinued after this first Col layer, the discussed conditions do not fulfil the need for a sustainable LbL process able to give rise to stable tubular or planar multilayers.

The second thickest assembly is obtained with the lowest ionic strength ($I = 10^{-4}$ M) and a pH value set at 4.0. The assembly process seems to be continuous and progressive in this case, except for the small discrepancy of the first HA layer, attributed to the formation of soluble Col-HA complexes. It is, however, rather surprising and counter-intuitive that the thickness of each individual polymer layer is greater in absence of salt than it is under 0.15 M NaCl. Indeed, the screening of the charges carried along the polymer backbones under saline conditions should favour their adsorption as more flexible chains, and hence thicker assemblies. This observation could be linked to a higher tendency to form Col-HA complexes under physiological conditions. Activation of the surface with a homogeneously positively-

charged PEI layer does not result in a thicker nor a more sustainable assembly, judging by the continuous decrease of the adsorbed mass per layer and the total thickness reached which are both similar in the presence or absence of PEI. That along with the potential cytotoxicity of PEI decided us to exclude PEI from further developments. Hence, the assembly of Col/HA multilayers under low (UPW, $I = 10^{-4}$ M) or physiological (NaCl 0.15 M, $I = 0.15$ M) ionic strength and a pH of 4.0 were the only conditions which were deemed satisfactory for the synthesis of stable biomimetic NTs and which were thus subjected to further exploration.

### *e) Assembly of NTs under optimal conditions*

The selected conditions were further compared while carrying out the LbL self-assembly of Col/HA biomolecules inside templates with cylindrical nanopores, subsequently dissolved in order to yield NTs (Figure 4.7).

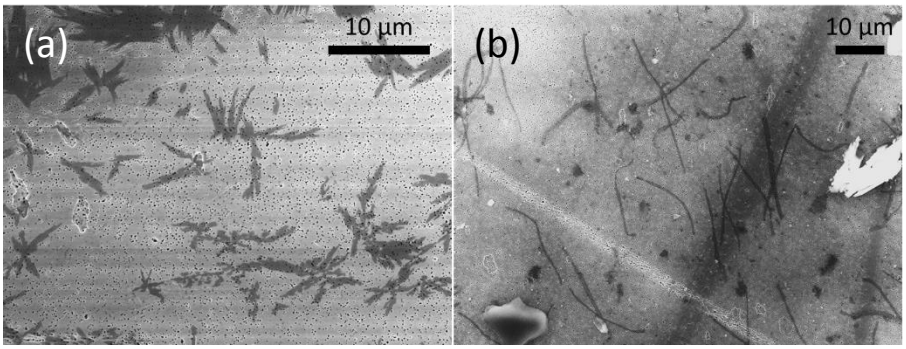


**Figure 4.7** *SEM pictures of $(Col/HA)_8$ NTs built via templated LbL self-assembly of biopolymers solubilized in (a) UPW with pH adjustment at 4.0 and (b) NaCl 0.15 M aqueous solution with pH adjustment at 4.0.*

Under low *I* conditions, no NT could be produced even after deposition of 8 bilayers of Col/HA molecules. The assembly process seems to give rise to polymer microsheets with no tubular morphology (Figure 4.7.a). On the contrary, conducting the same assembly under saline conditions (NaCl 0.15 M) yielded tubular nanostructures whose dimensions were in good agreement with the ones of their original template (length ~21 µm, diameter ~500 nm; Figure 4.7.b). Although QCM-D results (Table 4.1) seemed to point out that low *I* conditions would result in NTs with thicker multilayered walls, no tubular multilayer could be produced whatsoever. We hypothesize that this absence of any valid NT construction is to be related to the extended,

worm-like shape adopted by polymers under low ionic strength. The fully-extended length of collagen molecules being 300 nm, their diffusion along nanopores of 500 nm diameter might be drastically hindered (Figure 4.8). The very low amount of slowly diffusing molecules reaching the inside of the pores at each step of the LbL process might, in turn, considerably affect the synthesis of proper tubular walls, leading to the kind of objects observed in

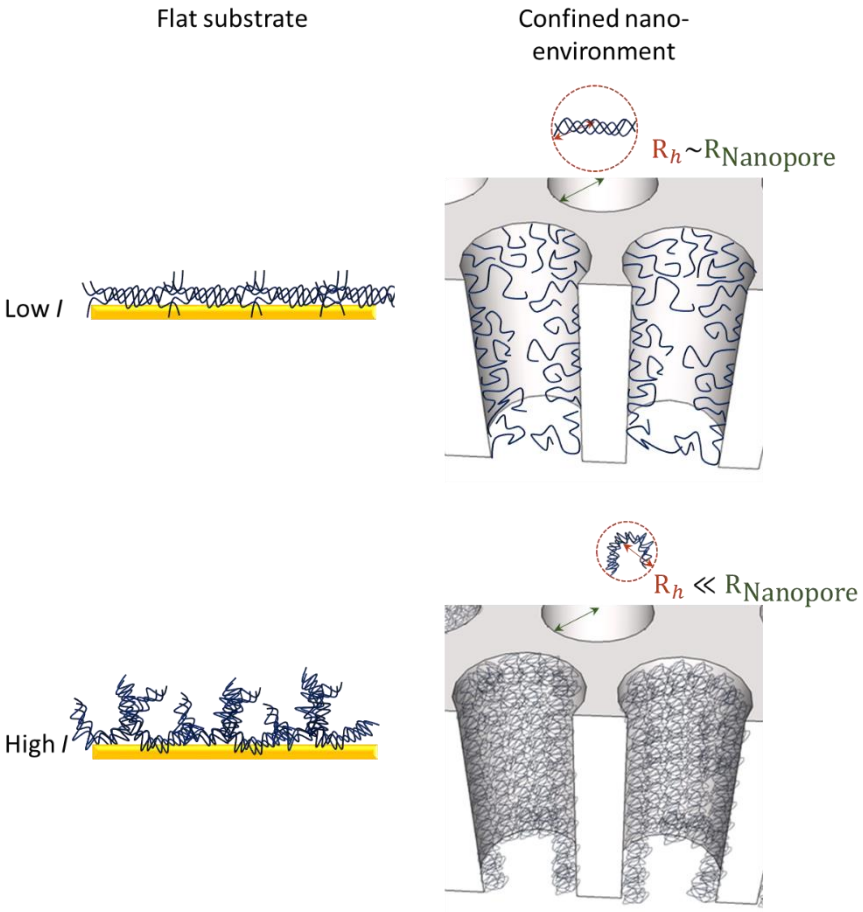


**Figure 4.8** *Scheme comparing the influence of ionic strength on the LbL self-assembly technique whether conducted over flat substrates or within nanoporous templates. Inside confined nano-environments, diffusion of polymers is limited by their hydrodynamic radius ($R_h$), which is itself influenced by the ionic strength.*

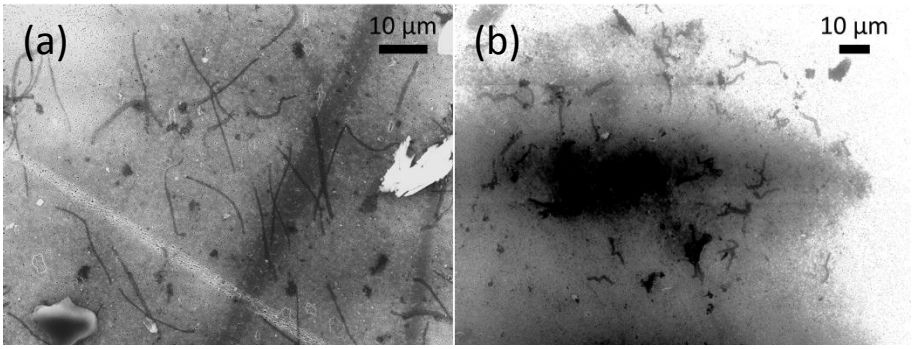


**Figure 4.9** *SEM pictures of (Col/HA)$_8$ NTs built via LbL self-assembly of biopolymers in NaCl 0.15 M aqueous solution pH 4.0 and subsequently chemically cross-linked (a) or not (b).*

figure 4.7.a. Optimal conditions for triggering the self-assembly of Col & HA biopolymers might thus differ depending on the substrate to be functionalized: low *I* conditions might be preferable when assembling the biomacromolecules over a flat substrate while high *I* would be required to enable the diffusion-limited assembly of polymers inside confined nano-environments (e.g., tubular nanopores).

QCM-D data showed that Col/HA assemblies built either in UPW or 0.15 M NaCl pH 4.0 were stable under physiological conditions (10 mM HEPES buffer, pH 7.4, NaCl 0.15 M) in the absence of any post-LbL cross-linking (Figure 4.4.a & 4.5.a). However, morphological analyses of resulting NTs highlighted that only EDC/S-NHS cross-linked NTs remained stable after dissolution of the PC template (Figure 4.9.a). Non cross-linked NTs (Figure 4.9.b) have the tendency to aggregate and are more tortuous than their covalently cross-linked counterparts. Dichloromethane used to selectively dissolve the PC template is probably responsible for damaging the NTs morphology. As a consequence, chemical cross-linking is proven useful to improve the cohesion of the polymer multilayers constitutive of the NT walls and hence will be routinely applied.

### 4.2.2 LbL assembly of nanostructured (bio)polymer interfaces

With a view to synthesize nanostructured biomimetic interfaces, the self-assembly of (Col/HA) multilayers was carried out within PC templates displaying intersected nanopores (detailed results regarding the design of such PC templates will be discussed in section 6.2.1).

*a) Biopolymer-based biointerfaces*

Building on the consecutive successes of the synthesis of fully biomimetic (Col/HA) NTs (Figure 4.9.a) and the design of a PC template (*see* section 6.2.1 ) with an optimal porous network, the self-assembly of the two biomacromolecules was initiated inside this optimized template (Figure 4.10).

Unfortunately, once released from its supporting template, the synthesized structure is observed to be completely collapsed. Even though tubular heads can be spotted (Figure 4.10.b-c), indicating that the structure is indeed composed of intersected NTs, the system as a whole shows a morphology similar to the one of a homogeneously flat polymer thin film rather than the expected self-supported porous nanostructure. It is hypothesized that this flat film results from the collapse of the nanotubular building blocks, as they fail to withstand the atmospheric pressure once released from their supporting template. It is further assumed that the collapse is ultimately the consequence of the low mechanical properties of the biopolymer partners involved in the assembly.

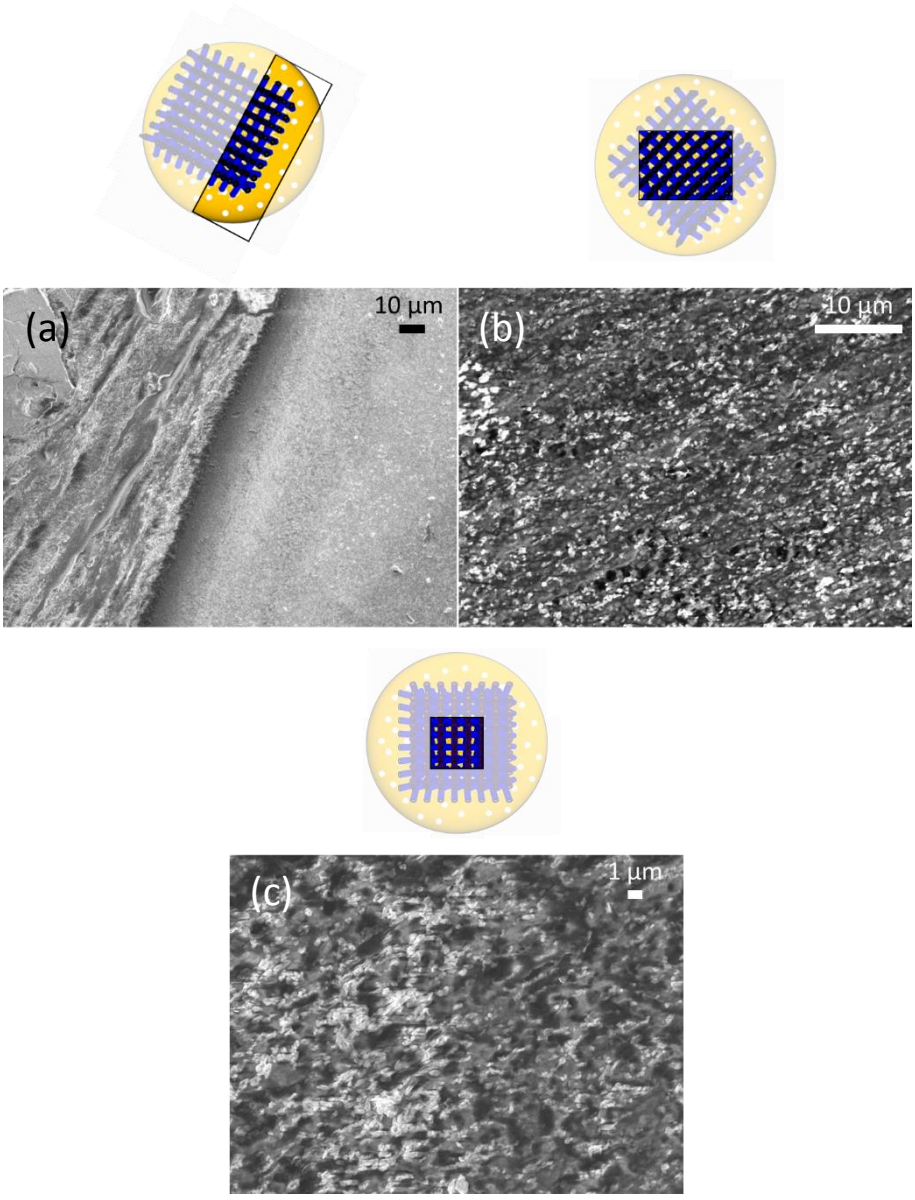


**Figure 4.10** *SEM pictures of a (Col/HA)$_8$ biointerface made of intersected NTs themselves fully composed of LbL-assembled Col and HA biopolymers. A flattened , collapsed polymer mat is obtained upon release from the template (white spots in figures (b) & (c) correspond to flattened NT heads).*

*b) Hybrid biointerfaces: synthetic core and biomimetic shell*

To test this hypothesis, a hybrid interface combining the biopolymers with stiffer PEs of synthetic origin (PAH and PSS) was produced (Figure 4.11). The synthesized hybrid system is composed of intersected NTs whose innermost layers are assembled from synthetic PEs (i.e., synthetic core: $(PAH/PSS)_6$) while their outermost layers still contain Col and HA (i.e., biopolymer shell: $(Col/HA)_3$).

The morphology of the resulting hybrid interface is quite similar to that of the system fully composed of biopolymers. Indeed, collapsed NTs are again observed (Figure 4.11.b) and seem to have merged into a relatively homogeneous polymer film with no visible porosity (Figure 4.11.c).

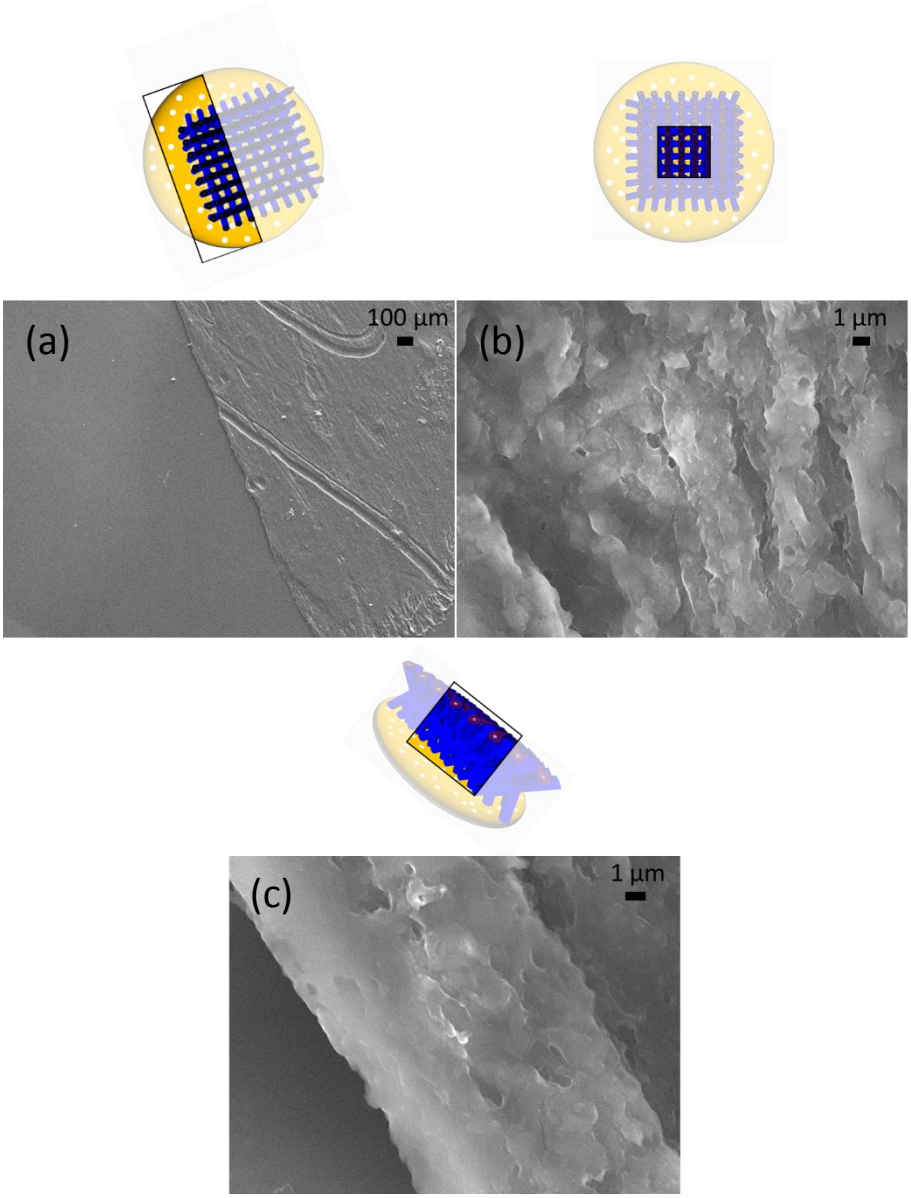


**Figure 4.11** *SEM pictures of a hybrid $(Col/HA)_3(PAH/PSS)_6$ interface made of intersected NTs themselves composed of a synthetic $(PAH/PSS)_6$ core and a biomimetic $(Col/HA)_3$ shell.*

*c) Synthetic PE-based interfaces*

Control systems entirely made of synthetic PEs (i.e., obtained through deposition of 6 PAH/PSS or 10 PAH-FITC/PSS bilayers) showed no better results (Figures 4.12 and 4.13, respectively), clearly establishing that the

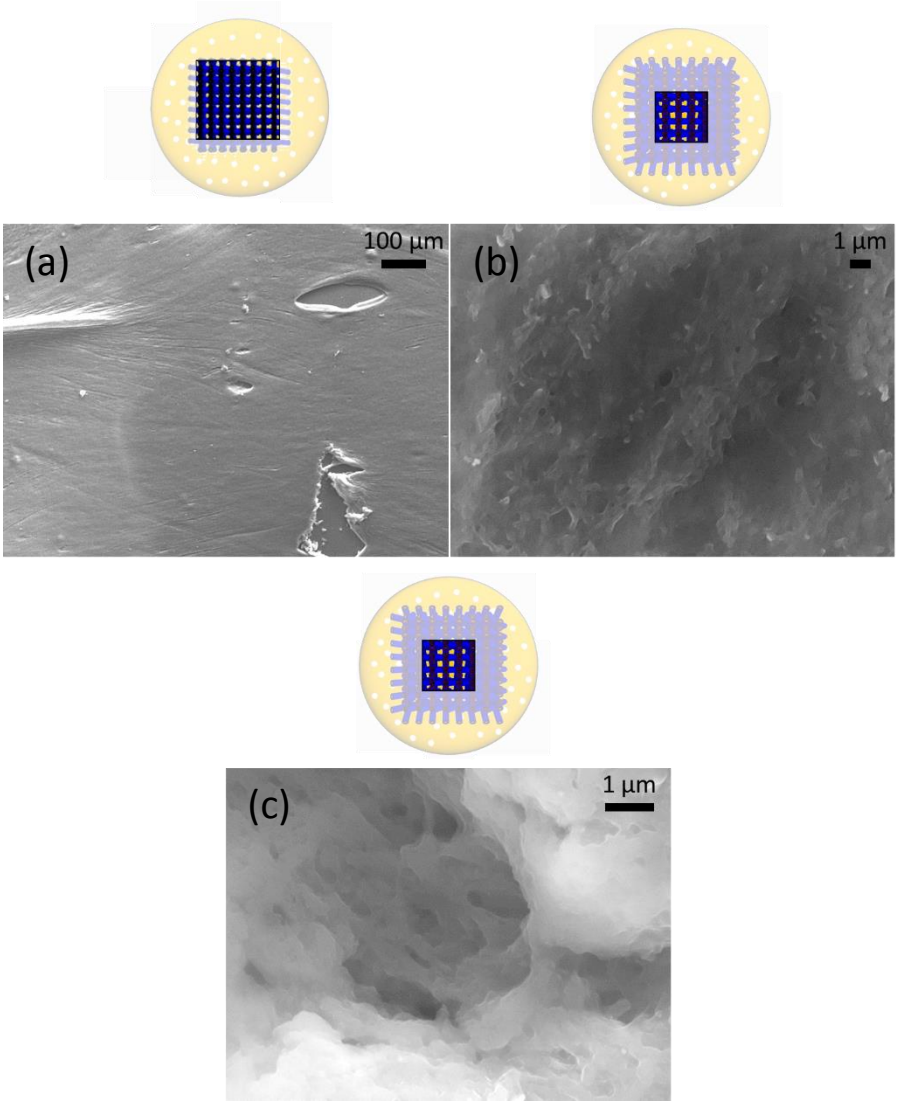


**Figure 4.12** *SEM pictures of a $(PAH/PSS)_6$ interface made of intersected NTs themselves fully composed of synthetic PEs*

ECM-derived polymers are not the only ones to be blamed for the poor mechanical properties of the structures, as synthetic PEs also seem to be lacking the adequate mechanical stiffness.

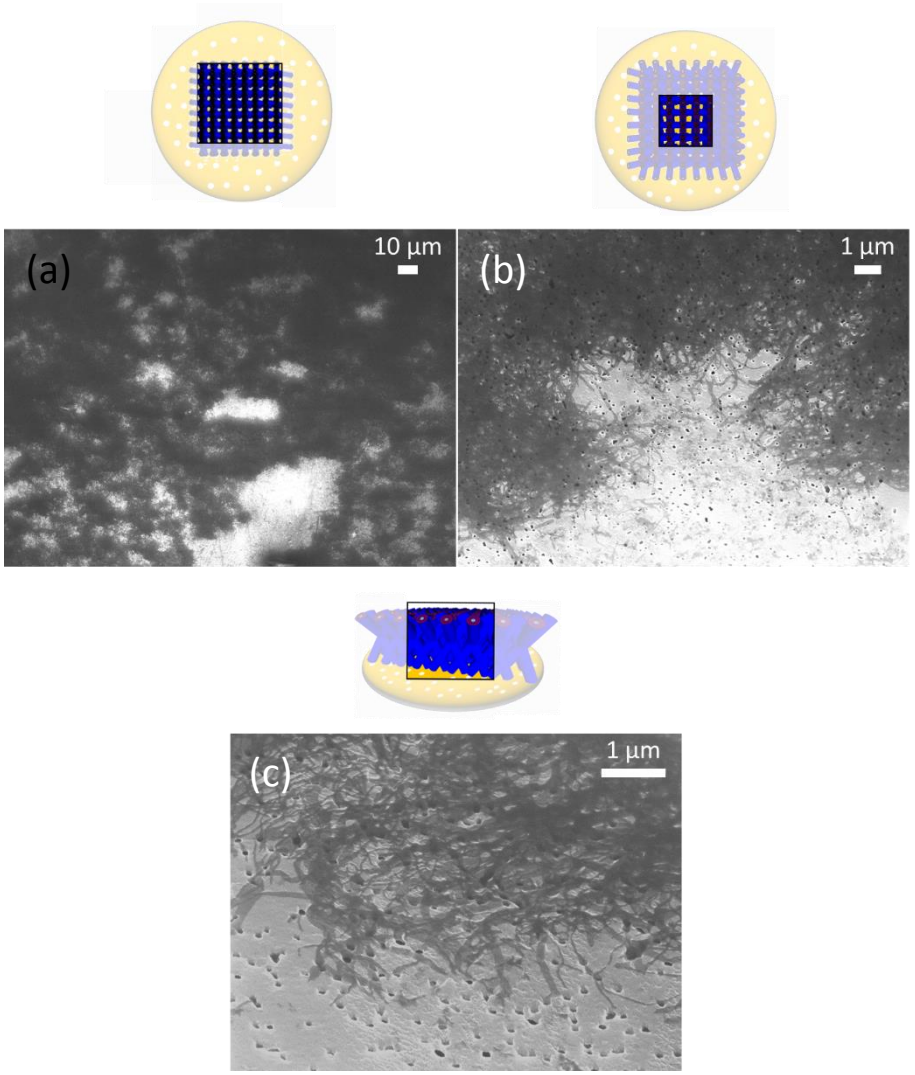


**Figure 4.13** *SEM pictures of a (PAH-FITC/PSS)$_{10}$ interface made of intersected NTs themselves fully composed of synthetic PEs*

## 4.3 Conclusions

Optimal conditions leading to the self-assembly of two ECM biomacromolecules, Col and HA, were identified. The assembly of a $(Col/HA)_{2.5}$ thin film is shown to proceed in a sustainable LbL fashion when conducted at pH 4.0, either in UPW or NaCl 0.15 M aqueous solution. The two-fold increase of the film thickness when built under low *I* (i.e., in UPW) in comparison with the medium *I* conditions (i.e., 0.15 M NaCl aqueous solution) is attributed to the adsorption of Col molecules under a flat, extended conformation in the absence of salt, leading to a high number of anchoring points to the substrate and a lesser tendency to form soluble complexes with HA molecules, which ultimately results in more homogeneous adsorbed layers. Col adopting a more flexible conformation in solutions of higher charge-screening capacities (i.e., medium to high *I*), the interactions it creates with the substrate are probably less numerous and strong, leading to a favoured tendency to create stronger interactions with diffusing HA molecules and leaving the interface, ultimately resulting in a depleted total adsorbed mass. The optimal conditions guiding the self-assembly of the two biopolymers are, however, evidenced to be substrate-dependent. While low *I* favours the adsorption of thicker or more homogeneous assemblies on flat substrates, it does not support the synthesis of tubular-shaped multilayers once the assembly is performed within nanoporous templates. On the contrary, medium to high *I* conditions seem to be favourable to the production of NTs, most probably due to the reduced hydrodynamic radius of the more flexible biopolymers under these conditions, which increases their diffusion rate down the nanopores. The biomimetic thin films are demonstrated to be stable under physiological conditions (HEPES buffer 10 mM pH 7.4, NaCl 0.15 M) without the need to resort to a cross-linking step. Such a cross-linking process, converting part of the electrostatic interactions between the LbL partners into strong covalent bonds, becomes however mandatory to guarantee the stability of the tubular multilayers upon dissolution of their supporting template. The pre-adsorption of an anchoring layer of PEI, a strong positively-charged PE, did not give rise to a thicker nor more sustained assembly and was thus discarded, knowing the potential cytotoxicity of PEI. Conducting the optimized assembly of the two biomolecules inside a custom-made PC

template displaying a network of intersected nanopores gives rise to fully biomimetic interfaces which are, however, lacking mechanical integrity and show a collapsed morphology once freed from their supporting template. This instability is to be attributed to the low stiffness intrinsic to the biopolymers and other commonly used PEs. Indeed, attempts at strengthening the construct via incorporation of a core of LbL-assembled synthetic (PAH/PSS) PEs in addition to the preliminary (Col/HA) multilayer did not succeed in considerably improving the mechanical stability of the construct. Other strategies, based on the inclusion of polymers of higher mechanical properties or on the addition of another phase in the engineered matrices will therefore be the focus of further research, with the goal to fulfil the requirement of a self-supported biomaterial opening the way to applications in the field of implantable technologies.

Despite their poor mechanical properties, the successful organization of two ECM compounds into supra-molecular architectures constitutes in itself a valuable innovation. It can be fairly assumed that the artificial matrices being entirely made of natural polymers having undergone little to no modification (the chemical cross-linking excepted), the intrinsic biocompatibility and bioactivity of the two macromolecules are preserved. Putative applications of the produced ECM-inspired interfaces could thus involve their use as a biomimetic coating of existing implants (e.g., to help the tissue integration of prostheses and other tissue-contacting devices) or lining of skin-contacting patches (e.g., artificial skin, wound dressings, wound repair solutions, etc.).

## Highlights of the chapter

- Experimental iep of Col in the range ]5;6[ in UPW and ]4;5[ in 0.15 M NaCl aqueous solution. IEP of HA < 3 in both cases
- LbL assembly of Col & HA into thin films on flat substrates optimized at pH 4.0 under low I (i.e., UPW). A wet thickness ~82 nm is obtained for a $(Col/HA)_{2.5}$ film built under these conditions.
- Chemical cross-linking compulsory to produce stable NTs able to withstand the dissolution of their supporting template in organic solvent
- LbL assembly of Col & HA into NTs optimized in 0.15 M NaCl pH 4.0 due to a shorter hydrodynamic radius under these conditions, easing their diffusion along the nanopores
- Successful production of biomimetic interfaces composed of intersected (Col/HA) NTs but further efforts are needed to synthesize self-supported systems

## 4.4 Experimental section

***Materials**:* Poly(fluorescein isothiocyanate allylamine hydrochloride) (PAH-FITC, $M_W$ ~ 15 kDa, monomer to dye ratio (PAH:FITC) of 50:1) and poly(allylamine hydrochloride) (PAH, $M_W$ ~ 15 kDa) were purchased from Sigma-Aldrich. Poly(sodium-p-styrenesulfonate) (PSS, $M_W$ ~ 70 kDa) was purchased from Acros. Dried sodium hyaluronate (HA, $M_W$ ~ 151-300 kDa) was purchased from Lifecore Biomedical. Type I collagen G from bovine calf skin (Col, 0.4% solution in 15 mmol $L^{-1}$ HCl, 4 $mg.mL^{-1}$) was purchased from Merck-Millipore. Individual NTs were synthesized within ion track-etched PC membranes with a thickness of 21 µm, displaying density of parallel pore equal to $4x10^7$ $pores.cm^{-2}$, and an average pore diameter of 500 nm. Interfaces of intersected NTs were synthesized through LbL assembly within PC templates with a thickness of 25 µm, showing a network of 300 nm diameter nanopores intersecting at a controlled angle of ~90°, with a density of $2.8x10^8$ $pores.cm^{-2}$. Nanoporous PC templates were kindly supplied by it4ip. Cross-linking agents, 1-(3-dimethylaminopropyl)-3-ethylcarbodiimide hydrochloride (EDC, 98+%) and *N*-hydroxysulfosuccinimide sodium salt (s-NHS, ≥98%) were purchased from Acros and Sigma-Aldrich, respectively. Sodium chloride (NaCl, ACS reagent, ≥99%) and hydrochloric acid solution (HCl, 0.1 N in aqueous solution) were purchased from Sigma-Aldrich. PET membranes, used for filtration purposes and as substrate for microscopical analysis, were supplied by it4ip and had an average pore diameter of 200 nm, a thickness of 23 µm and a pore density of $5.8x10^8$ $pores.cm^{-2}$.

***Monitoring of the electrophoretic mobility (EPM) of (bio)polymers**:* EPM measurements were carried out at 22 °C using a Malvern Zetasizer nanoZS (DTS1061, Malvern Instruments Ltd, UK). The results are presented as the mean and standard deviation of three to five replicates. The biopolymers HA and Col and PEI were solubilized either in ultrapure water or a 0.15 M NaCl aqueous solution, to reach a final concentration of 1 $mg.mL^{-1}$. The pH of the solutions and dispersion was subsequently adjusted using HCl 0.1 N or NaOH 0.1 N. The performance of the instrument was systematically verified (every six samples) using a zeta potential standard solution (Malvern, DTS1232).

***In-situ monitoring of the LbL assembly***: The capacity of the chosen biopolymers to interact with each other and self-assemble was monitored on reference substrates using quartz crystal microbalance with dissipation monitoring (QCM-D). The LbL construction was carried out on gold-coated quartz crystals [AT-cut 5MHz crystals coated with 100 nm Au, Q-Sense, Gothenburg (Sweden)]. Crystals were first cleaned in a piranha solution [$H_2O_2$ 30% (Prolabo, VWR, Leuven, Belgium)/$H_2SO_4$ 95% (Prolabo; VWR, Leuven, Belgium), 1:2 v/v] for 20 min, before being thoroughly rinsed with ultrapure water and dried under nitrogen flow. All measurements were performed in a Q-Sense E4 system (Gothenburg, Sweden) following the same protocol: resonance frequencies of the crystals were obtained under buffer for the different overtones, and the shifts of frequency (Δf) and of dissipation (ΔD) were both monitored as a function of time upon stepwise injection of each biopolymer and colloidal partner. The flow was set at 30 µL.min$^{-1}$ using a peristaltic pump, while the temperature was set at 25 °C. The solutions of either Col or HA were alternately injected in the system and allowed to adsorb on the crystals surface during 1 h. Each adsorption step was then followed by a rinsing step, conducted in the corresponding pH-adjusted solution for at least 30 min. Dissipation and frequency shifts recorded for the 5$^{th}$ overtone are displayed in this dissertation.

***Synthesis of biomimetic nanotubes****:* Col solutions were prepared at a final concentration of 1 mg.mL$^{-1}$ by diluting the stock solution in a 0.15 M NaCl aqueous solution or in UPW. When necessary, the pH of the resulting solution, initially measured to be around 2.56, was further adjusted (using NaOH 0.1 N). HA solutions were prepared at a final concentration of 1 mg.mL$^{-1}$ by dissolving the appropriate amount of weighed HA powder into a 0.15 M NaCl aqueous solution or UPW. When necessary, initial pH of the solution, measured at ~ 4.54 was further adjusted (using HCl 0.1 N). All solutions were freshly prepared and gently stirred for at least 20 min right before initiating the LbL assembly. The cross-linking solution was prepared, right before use, by adding EDC and s-NHS at a final concentration of 100 mg.mL$^{-1}$ and 11 mg.mL$^{-1}$ respectively, to a 0.15 M aqueous solution adjusted at pH 4.0. In order to trigger the self-assembly of biomimetic NTs, PC templates with parallel nanopores were successively dipped in a solution of Col for 2 h, then rinsed for 10 min in the construction medium (0.15 M NaCl aqueous solution adjusted at pH 4.0), prior to being immersed in a solution of HA for 30 min.

After the deposition of each polymer layer, the systems were decrusted by gently rubbing on both faces of the template a cell scraper wetter by the construction medium After the deposition of each biopolymer layer, both faces of the PC template were gently rubbed with a cell scraper wetted by the construction medium, so as to avoid the formation of a polymer crust which might clog the pores. This process of alternate dipping of the nanoporous template in solutions of Col and HA was most commonly cycled 8 times, so as to produce 8 bilayers of the Col/HA pair. The LbL deposition was carried out at 4 °C. Chemical cross-linking of selected samples was initiated right after completion of the LbL construction. For that purpose, multilayer-filled templates were immersed in the cross-linking solution [EDC 100 $mg.mL^{-1}$ & s-NHS 11 $mg.mL^{-1}$ in 0.15 M NaCl pH 4.0] and stored at 4 °C for at least 48 h, following an adaptation of the protocol of Picart *et al*.[1] Samples were then transferred into the construction medium (NaCl 0.15 M pH 4.0) and stored at 4 °C until further characterization.

***Templated LbL assembly of (PAH-(FITC)/PSS)$_n$ multilayers****:* PAH or PAH-FITC and PSS solutions were prepared by dissolving an appropriate amount of polymer into a 0.15 M NaCl aqueous solution to reach a final concentration of 1 mg/mL. The pH of the solutions was further adapted to 4.0 (pH similar to that of the Col and HA solutions) using HCl or NaOH 0.1 N. All solutions were prepared right before use and gently mixed for at least 20 minutes prior to being used.

(PAH-FITC/PSS)$_n$ or (PAH/PSS)$_n$ multilayers (where *n* represents a tunable number of bilayers) were deposited inside PC templates with intersected nanopores, using the LbL deposition by dipping process. The dipping time in all the polymer solutions (PAH-FITC or PAH and PSS) was fixed at 30 min, which is a convenient time for the diffusion of PEs and their adsorption in the form of a monolayer. After deposition of each polymer layer, the systems were decrusted by rubbing on both faces of the templates a cell scraper wetted by a NaCl 0.15 M pH 4.0 solution. The samples were then left to rinse in NaCl 0.15 M pH 4.0 for 5 minutes before initiating the construction of the next layer.

***Release of individual NTs.*** Individual nanotubes were first released from their PC template by dissolution of the templating membrane in dichloromethane ($CH_2Cl_2$, 99.8+% for analysis, stabilized with amylene, Acros

Organics). In practice, small cut-outs (~ 2-3 $mm^2$) in the PC membrane containing the self-assembled NTs were immersed in a test tube containing 5 mL of dichloromethane and left aside for 10 min, ensuring complete dissolution of PC. Prior to SEM analysis, the dispersion of NTs in $CH_2Cl_2$ was subsequently filtered over hydrophilic PET filters (200 nm pore size, pore density $5x10^8$ $pores.cm^{-2}$, thickness 23 µm, it4ip) prealably metallized, using a sputter coater (Cressington 208HR), with a chromium anchoring layer (3 nm) followed by a gold layer (20 nm). Metallized filters were introduced in the sample holder of a 5 mL syringe while the dispersion of NTs in dichloromethane was poured in the syringe and filtered. 5 mL of fresh dichloromethane were subsequently used to rinse the test tube and filtered through the device to maximize the NTs collection. The resulting NTs supported on metallized filters were left to dry overnight at room temperature before any further characterization.

***Release of polymer interfaces***. PET membranes were metallized with a supporting layer of chromium (3 nm) further coated by a gold layer (20 nm). PC templates in which the LbL assembly of nanostructured interfaces was conducted were deposited over metallized PET membranes. Large amounts of fresh dichloromethane (vol. ~ 30 mL) were then poured dropwise over the template until complete dissolution of PC was achieved. The released polymer interfaces supported over PET membranes were finally air-dried at room temperature for about 1h prior to microscopy analysis.

***SEM Observations***. The dimensions and morphology of the synthesized NTs were studied by scanning electron microscopy (SEM). SEM pictures were obtained using a thermal field emission scanning electron microscope (JSM-7600F, Jeol) operated at an acceleration voltage of 15 kV under SEM mode (maximum resolution of 1.0 nm using a secondary electron imaging detector).

# Theoretical appendix 4.I

## Electrophoretic mobility determination[2–7]

Electrophoretic mobility

The electrophoretic mobility of colloidal systems, that is to say their velocity in an electric field, is obtained by performing an electrophoresis experiment. The electrophoresis process consists in initiating the movement of charged particles through a liquid phase via application of an electric field and measuring their velocity using Laser Doppler Velocimetry (LDV). Briefly, a laser is used to illuminate the charged colloids dispersed in an electrolyte contained in a micro-electrophoresis cell across which an electric field is applied. While moving towards the electrode of charge opposite to the one of their surface, particles enter the laser beam and therefore cause a shift in the frequency of the scattered light. This frequency shift ($\Delta f$) is proportional to the particle speed, following the equation:

$$\Delta f = 2v\frac{\sin\left(\frac{\theta}{2}\right)}{\lambda} \qquad [Hz] \qquad (4.1)$$

where $v$ is the particle velocity, $\lambda$ is the laser wavelength and $\vartheta$ the scattering angle.

Once the velocity distribution of colloids is known, their electrophoretic mobility ($U_E$) can be easily computed as it is defined as the particle velocity under an applied electric field $E$ per unit of electric field strength:

$$U_E = \frac{v}{E} \qquad [m^2.V^{-1}.s^{-1}] \qquad (4.2)$$

If we consider a particle of charge $q$, dispersed in a liquid phase of viscosity $\eta$ and subjected to an electric field $E$, the electric force $F_e$ which applies to the particle and triggers its motion towards the oppositely-charged electrode is: $F_e = q.E$. [N] As the particle migrates through the liquid and towards the electrode, a frictional force $F_f$ appears which tends to counter the particle displacement (Figure 4.2):

$F_f = 6\pi\eta r v$ [N] (4.3)

where $\eta$ is the viscosity of the medium, $r$ is the hydrodynamic radius of the particle and $v_{stat}$ its speed. The particle thus accelerates until equilibrium is reached between these two opposing forces and a constant velocity is achieved, the expression of which is:

$F_e = q.E = F_f = 6\pi\eta r v_{stat}$ [N] (4.4)

$v_{stat} = \left(\frac{q}{6\pi\eta r}\right).E = U_E.E$ [$m.s^{-1}$] (4.5)

where $U_E = \frac{v}{E}$ is the electrophoretic mobility of the particle expressed in [$m^2V^{-1}s^{-1}$].

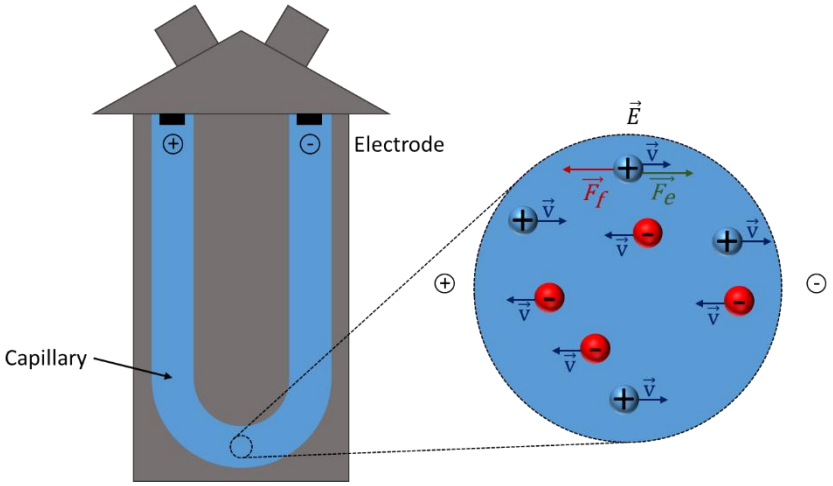


**Figure 4.2** *Schematic representation of a micro-electrophoresis cell showing the forces which apply to charged colloids upon introduction of an electric field. The application of an electric field triggers the emergence of an electric force ($\vec{F_e}$) which is applied on the charged particles and directed towards the electrode of opposite polarity. As a result, particles move towards this oppositely-charged electrode and their displacement is characterized by the velocity vector $\vec{v}$. While the particles migrate through the liquid, a frictional force( $\vec{F_f}$) is applied by the liquid on the particles, which tends to oppose their displacement.[Inspired from[8]].*

Electrical double-layer and ζ-potential

The net charge of a particle surface directly affects the distribution of ions in the electrolyte medium it is surrounded with, as counter ions (ions of opposite charge to that of the particle) tend to accumulate in direct vicinity of the particle surface (Figure 4.3). This ionic reorganization leads to the emergence of an electrical double layer around each particle. The inner part of this layer surrounding the particle is called the ***Stern layer*** and consists in ions which are strongly bound to the particle surface. The outer layer comprises ions which are less firmly attached to the particle surface and is therefore referred to as the ***diffuse layer***. When a particle moves through an electrolyte, both the ions of the Stern layer and part of the ions of the diffuse layer follow the movement. As such, the presence of a cloud of counterions tightly linked to the particle surface makes it difficult or even impossible to experimentally probe the electrical potential which exists at the particle surface ($\psi_s$). The notional boundary between ions that form a stable entity with the particle and thus travel with it and the ones which do not follow the particle displacement is located in the diffuse layer, nearby the external limit of the Stern layer, and is called the hydrodynamic shear or ***slipping plane***. The zeta potential (***ζ-potential***) is defined as the electric potential which exists at this boundary.

As it takes into account the formation of a counter-ion cloud around a particle in solution, the ζ-potential and its evolution with the pH of the dispersion is of prime importance for interface and colloid science. Unlike the surface potential of the particle ($\psi_s$), the ζ-potential is easily accessible experimentally and is thus the parameter of choice to characterize the polarity and magnitude of the superficial charge of the wetted colloid (i.e., the colloid-bound ions entity). The ζ-potential thus enables the prediction of the electrostatically-driven interactions which might occur between particles in liquid dispersion. Indeed, if all particles in solution have a large ζ-potential of same polarity, they will tend to repel each other. On the contrary, colloids having a weak ζ-potential or higher ζ-potentials of opposite charge will gather together and aggregate.

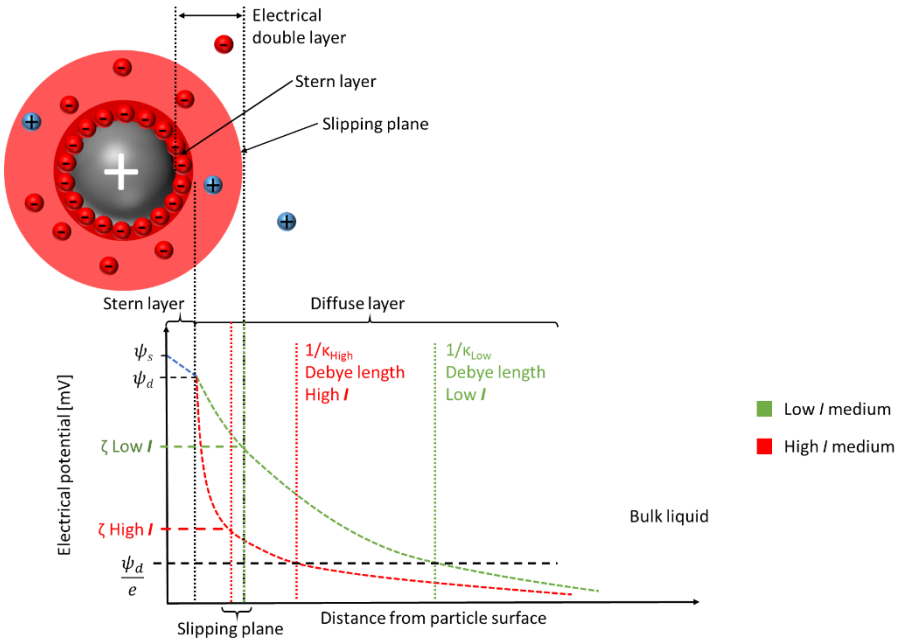


**Figure 4.3** *Schematic representation of the organization of ions around a charged particle dispersed in an electolyte, giving rise to an electrical double layer, along with the evolution of the electrical potential as a function of the distance from the particle surface. [Inspired from*[8]*].*

Link between ζ-potential and electrophoretic mobility

The ζ-potential of a colloid can be computed from its electrophoretic mobility ($U_E$), using Henry equation:

$$U_E = \frac{2\varepsilon\varepsilon_0\zeta f(\kappa a)}{3\eta} \qquad [m^2.V^{-1}.s^{-1}] \qquad (4.6)$$

where $\varepsilon$ is the relative dielectric constant of the medium, $\varepsilon_0$ is the dielectric constant of the vacuum, $\zeta$ is the ζ-potential, $\eta$ is the dynamic viscosity of the medium and $f(\kappa a)$ is Henry's function. The coefficient $f(\kappa a)$, where the dimensionless product $\kappa a$ describes the ratio of the particle radius ($a$) to the thickness of the electrical double layer which surrounds it (the Debye length, *i.e.* $\kappa^{-1}$), is often approximated by two values, corresponding to two limiting cases: $f(\kappa a) = 1.5$ (Helmholz-Smoluchowski approximation) or $f(\kappa a) = 1.0$ (Hückel approximation). The Smoluchowski model considers the case of

particles whose diameter is larger than the electrical double layer thickness ($\kappa a$ >> 1) and therefore only applies to fairly large particles ($a$ > 0.2 µm) dispersed in an electrolyte containing more than $10^{-3}$ M salt. The Smoluchowski expression is thus widely used for colloidal suspensions in aqueous medium. On the other hand, the Hückel approximation is more useful for non-aqueous applications, where nanosized particles ($a$ << 100 nm) are immersed in a low dielectric constant medium. In this situation, the particles are assumed to be much smaller than the electrical double layer extent ($\kappa.a$ << 1). When using the Smoluchowski approximation, the expression of $U_E$ becomes:

$$U_E = \frac{2\varepsilon\varepsilon_0\zeta 1.5}{3\eta} = \frac{\varepsilon\varepsilon_0\zeta}{\eta} \qquad [m^2.V^{-1}.s^{-1}] \qquad (4.7)$$

from which we can extract the expression of the ζ-potential as a function of the electrophoretic mobility ($U_E$):

$$\zeta = \frac{U_E\eta}{\varepsilon\varepsilon_0} \qquad [V] \qquad (4.8)$$

Strategic choices and assumptions

Under experimental circumstances, where particles of colloidal size are dispersed in solutions of moderate *I*, $\kappa.a$ often takes intermediate values and neither the Smoluchowski nor Hückel approximation is valid. As a corollary to this, the extraction of ζ-potentials from the experimental $U_E$ values becomes marked with considerable uncertainties. Attention is thus paid throughout this report to express electrophoretic data as mobilities, which are unambiguous experimental quantities.

In order to take into account, when appropriate, the presence of salt in the aqueous environment and the related evolution of its dielectric constant, the following expression was used[9]:

$$\mathrm{E} = \varepsilon_w + 2\bar{\delta}\mathrm{C} \qquad (4.9)$$

where $\mathcal{E}$ and $\mathcal{E}_W$ are the relative dielectric constant of the medium (containing salt) and of water, respectively. *C* is the concentration of salt in moles per liter and $\bar{\delta} = \frac{(\delta^+ + \delta^-)}{2}$, where $\delta^+$ and $\delta^-$ represent the contributions of the two

univalent ions constitutive of the salt. In the case of NaCl, estimation of these parameters gives[9,10] :

$$\delta^{+}_{Na^{+}} = -8 \pm 1 \text{ and } \delta^{-}_{Cl^{-}} = -3 \pm 1 \qquad (4.10)$$

using equations (4.9) and (4.10), the relative dielectric constant of the 0.15 M NaCl aqueous solution, as frequently used throughout our experiments, is found to be equal to 78.35.

The evolution of the dynamic viscosity $\eta$ of the medium as a function of the salt concentration is given by[11,12]:

$$\frac{\eta}{\eta_0} = 1 + A\sqrt{\mathrm{C}} + B\mathrm{C} + D\mathrm{C}^2 \qquad (4.11)$$

where $\eta_0$ = 8.90 x $10^{-4}$ Pa.s is the dynamic viscosity of water at 25°C while *A*, *B*, and *D* are constants. The constant *A* (equal to 0.0062 $M^{-1/2}$ for NaCl) originates from the Debye-Hückel theory[12] and was extracted from[11] ,while *B* (0.0614 $M^{-1}$ for NaCl) and *D* (0.0211 $M^{-2}$ for NaCl) are experimental values obtained from[11] .Injecting these constants into equation (4.11) leads to a dynamic viscosity of 9.0076.$10^{-4}$ Pa.s for a 0.15 M NaCl aqueous solution.

Debye length and ionic strength

The electrical potential decays almost exponentially as the distance from the surface of a charged particle increases towards the bulk of the liquid, which is embodied by the relation[5]:

$$\psi(\mathrm{x}) = \psi_d e^{(-\kappa \mathrm{x})} \qquad (4.12)$$

where $\psi(x)$ represents the electrical potential at a distance *x* from the particle surface, $\psi_d$ is the value of the electrical potential at the onset of the diffuse layer and $\kappa$the Debye-Hückel parameter (i.e., reciprocal of the Debye length $\kappa^{-1}$). $\kappa^{-1}$, the Debye length is defined by[2,5] :

$$\kappa^{-1} = \sqrt{\frac{\varepsilon\varepsilon_0 k_B T}{2N_A e^2 I}} \qquad [\mathrm{m}] \qquad (4.13)$$

with $\varepsilon$ being the relative dielectric constant of the medium, $\varepsilon_0$ the dielectric constant of the vacuum, $N_A$ Avogadro's number, *T* the absolute temperature,

*e* the elementary charge, $k_B$ the Boltzmann's constant, and *I* the ionic strength defined as:

$$I = \frac{1}{2}\sum_i z_i^2 \, c_i \qquad \text{[M]} \qquad (4.14)$$

where $z_i$ is the valence, and $c_i$ the molar concentration of ion *i*.

The Debye length ($\kappa^{-1}$) is a measure of how far the electrostatic effect of a charge carrier persists in a solution. With each Debye length, charges of the carrier are increasingly electrically screened. Indeed, if we inject $x = \kappa^{-1}$ in equation (4.12), it yields: $\psi(\kappa^{-1}) = \frac{\psi_d}{e}$. Hence, at a distance $\kappa^{-1}$ from the particle surface, the potential has fallen to a value 1/e (~ 1/2.72) of potential close to the particle surface, at the external limit of the Stern layer. For this reason, the distance $\kappa^{-1}$ is referred to as the thickness of the electrical double layer, although the region of varying potential extends to a distance of about $3\kappa^{-1}$ before the potential has decayed to about 2% of its value at the surface[4] . $\kappa^{-1}$ being inversely proportional to $\sqrt{I}$ (equation 4.13), increasing the ionic strength (*I*) causes a decrease in $\kappa^{-1}$ as a result of which the potential falls off more rapidly with distance. The electrostatic charges are thus screened within a shorter distance with increasing electrolyte concentration.

# Theoretical appendix 4.II

## *In situ* QCM-D monitoring of LbL self-assembly[13–21]

General principle

Quartz crystal microbalance (QCM or QCM-D) is a widely popular technique to monitor *in situ* changes in mass and viscosity of solvated interfaces. The working principle of QCM-D is based on the inverse piezoelectric effect, occurring in crystalline materials having certain symmetry properties, characterized by the generation of a mechanical deformation of the material upon application of a voltage (Figure 4.4). During QCM-D measurements, a quartz crystal is subjected to an oscillatory motion, triggered by alternating the voltage applied to the crystal. The frequency of the voltage alternation is chosen so as to match the resonance frequency of the crystal (or multiples of it, called overtones), in order to generate a standing wave inside the crystal. The AT-cut quartz crystals used in QCM vibrate in the so-called thickness-shear mode, where the two surfaces of the crystal move in an antiparallel fashion.

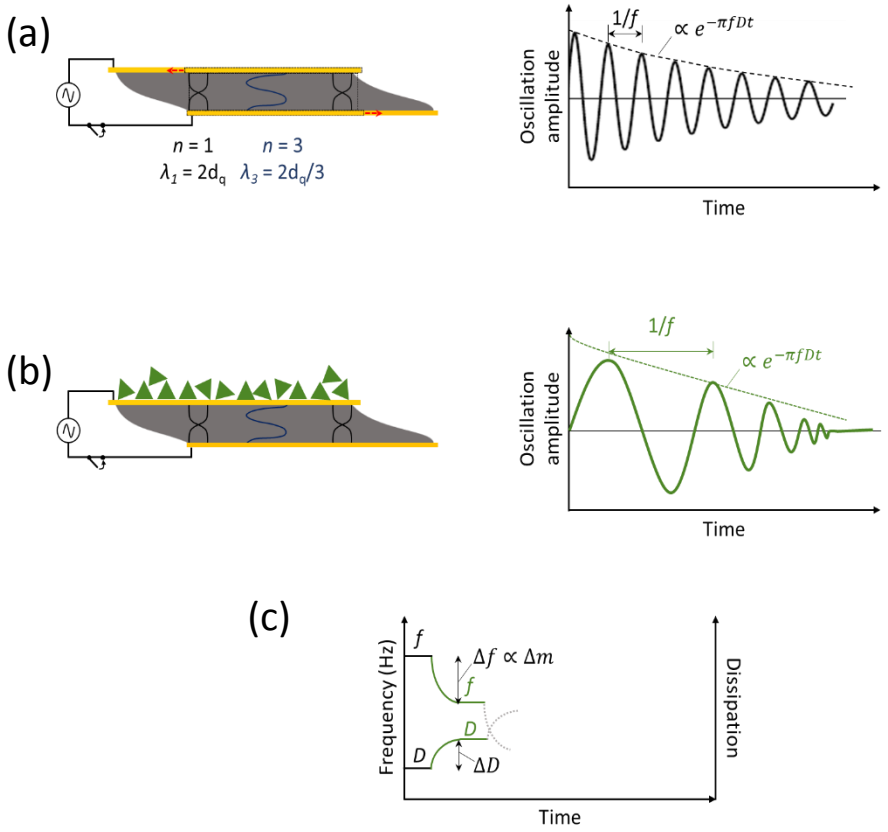


**Figure 4.4** *Principle of QCM-D. (A) Side view of an AT-cut quartz crystal. Application of an oscillatory voltage results in a cyclical deformation, where top and bottom surfaces of the crystal move tangentially in an antiparallel fashion. The fundamental frequency (n = 1, black waves at the edges of the crystal) and the third overtone (n = 3, blue wave in the middle) are depicted. The driving voltage is intermittently switched off so as to record the decay of the oscillation with time, allowing the extraction of the resonance frequency f and the energy dissipation D. (B) The adsorption of a substance on the crystal surface leads to a decrease of its oscillation frequency while the energy dissipation factor D is proportional to the decay rate of the oscillation. (C) Monitoring the change in resonance frequency and dissipation upon adsorption of a compound on the quartz surface enables the characterization of the mass and the viscoelastic properties of the adlayer, respectively.[Inspired from*[14]*].*

Relationship between changes in resonance frequency and adsorbed mass: derivation of Sauerbrey's equation

The condition for resonance to emerge in the AT-cut quartz crystal is that the induced standing wave has its anti-nodes located at the two opposite surfaces of the quartz crystal (i.e., maximum of the oscillation at the bottom face of the crystal and minimum at the top surface, or *vice-versa;* Figure 4.4.a), which translates into[20]:

$$\lambda_n = \frac{2d_q}{n} \qquad \text{[m]} \qquad (4.15)$$

where $\lambda_n$ is the wavelength of the standing wave of overtone *n* (odd number), and $d_q$ is the crystal thickness. The resonance frequency can then be stated as:

$$f_n = \frac{v_q}{\lambda_n} = n\frac{v_q}{2d_q} = nf_0 \qquad \text{[Hz]} \qquad (4.16)$$

where $f_n$ is the resonance frequency for overtone *n* (odd number), $v_q$ is the velocity of acoustic waves in quartz plate and $f_0$ is the fundamental resonance frequency ($f_0 = \frac{v_q}{2d_q}$).

Sauerbrey was the first to formulate, in 1959, a relationship between the resonance frequency of the oscillating quartz crystal and changes in mass adsorbed on its surface, paving the way for the use of QCM-D as a microgravimetric device[13] .When homogeneously distributed over the whole volume, the mass per unit surface of an object can be expressed as the product of its density and thickness. When considering a quartz crystal, it thus comes:

$$\frac{M_q}{A_q} = m_q = \rho_q . d_q \qquad \text{[kg.m}^{-2}\text{]} \qquad (4.17)$$

and $d_q = \frac{m_q}{\rho_q}$ [m] (4.18)

where $M_q$ is the total mass of the quartz crystal [kg], $A_q$ its active area [m$^2$], $m_q$ its areal mass [kg.m$^{-2}$], $d_q$ its thickness [m] and $\rho_q$ is the density of quartz

[kg.m$^{-3}$]. By replacing the expression of $d_q$ obtained in equation 4.18 into equation 4.16, the relationship between mass variation and frequency change, as discovered by Sauerbrey, appears:

$$f_n = n\frac{v_q}{2d_q} = n\frac{v_q\rho_q}{2m_q} \qquad \text{[Hz]} \qquad (4.19)$$

and, by differentiating the expression, it becomes:

$$\mathrm{d}f_n = -n.\frac{v_q\rho_q}{2m_q^2}.\mathrm{d}m_q = -\frac{f_n}{m_q}.\mathrm{d}m_q \qquad \text{[Hz]} \qquad (4.20)$$

The change in mass of the quartz crystal is thus linearly related to the change in its resonance frequency. Although initially developed and exclusively used for monitoring the thickness of thin and dense metal coatings deposited under vacuum or gas phase, equation 4.20 was further extended to the adsorption of any material (provided that certain conditions are satisfied) and to the liquid phase. In order to determine the mass of any compound adsorbed over the crystal, the Sauerbrey model (equation 4.20) is thus commonly used with the assumption that d$m_q$= d$m$ , which means that the change in added mass *dm* on the crystal originating from the adsorption of some material is treated as a direct variation of the mass of the quartz crystal itself *dm*$_q$. Measuring a variation of resonance frequency upon adsorption of a compound on the crystal surface can thus be directly related to the mass of the adsorbate, provided that the added material shares similarities with quartz and can be treated as an extension of the oscillating crystal itself. This assumption limits the applicability of the Sauerbrey equation to cases where the added mass is:

(i) small compared to the mass of the crystal ($\frac{\Delta f_n}{f_n} \ll 1$)
(ii) rigidly adsorbed on the crystal surface, with no slip or deformation imposed by the oscillating surface
(iii) evenly distributed over the crystal surface

It is generally accepted that these conditions are met and that the deposited film can be approximated as rigid and its areal mass extracted using the Sauerbrey equation when the ratio $\frac{\Delta D_n}{\left(\frac{-\Delta f_n}{n}\right)}$ is much lower than $4 \times 10^{-7}$ Hz$^{-1}$ for a 5 MHz crystal and if the variation in $\frac{\Delta f_n}{n}$ as a function of $n$

(overtone dispersion) is low[20] .On the contrary, if the deposited layer is soft, thick or not coupled to the surface, viscous and elastic contributions will be involved in the frequency change and Sauerbrey's assumption of a rigidly adsorbed mass will be violated. In particular, when dealing with the adsorption of highly hydrated films, behaving like viscous liquids or gels, the oscillatory motion of the crystal triggers the deformation of the film. As a result, frictional and viscous energy losses are induced due to the slipping of the film over the electrode and the oscillatory motion of the liquid and molecules trapped within the film, respectively. These energy dissipative phenomena are particularly important when the water content of the adsorbed film and its surface roughness (reinforcing the coupling with the bulk liquid at the film/liquid interface) are high. The dissipation factor *D* becomes prominent and data cannot be interpreted using the Sauerbrey equation anymore but, instead, a viscoelastic model such as the one developed by Voinova et al. should be used[19].

By allowing d → Δ, using Sauerbrey's approximation d$m_q$= d$m$ and replacing $m_q$ by its expression in equation 4.17, equation 4.20 becomes:

$$\mathrm{d}f = \Delta f = -\frac{f}{m_q}\Delta m = -\frac{f}{d_q\rho_q}\Delta m = -n\frac{f_0}{d_q\rho_q}\Delta m$$

since $f_0 = \frac{v_q}{2d_q}$, it comes $d_q = \frac{v_q}{2f_0}$

and $\Delta f = -n\frac{f_0}{v_q\rho_q}.2f_0.\Delta m = -n\frac{2f_0^2}{v_q\rho_q}\Delta m$ [Hz] (4.21)

The final expression of the Sauerbrey equation is then obtained after introduction of the Sauerbrey constant $C = \frac{v_q\rho_q}{2f_0^2}$ [kg.s.m$^{-2}$], which depends only on the fundamental resonance frequency $f_0$ and the material properties of the quartz crystal, into equation 4.21:

$$\Delta f = -n\frac{1}{C}\Delta m \text{ or } \Delta m = -C\frac{\Delta f}{n} \quad [\mathrm{kg.m^{-2}}] \quad (4.22)$$

for an AT-cut quartz crystal with a fundamental resonance frequency $f_0$ of 5 MHz, calculation of $C$ yields:

$$C = \frac{v_q \rho_q}{2 f_0^2} = \frac{3340 \times 2650}{2 \times (5.10^6)^2} = 1.7702 \times 10^{-7} \text{ [kg.m}^{-2}\text{.Hz}^{-1}\text{]}$$
$$= 17.702 \text{ [ng.cm}^{-2}\text{.Hz}^{-1}\text{]}$$

where $v_q = 3340$ m.s$^{-1}$ is the speed of an acoustic wave through a quartz plate, $\rho_q = 2650$ kg.m$^{-3}$ is the density of an AT-cut quartz crystal.

Energy dissipation factor (*D*)

The introduction by Rodahl et al. of the so-called "ring-down" method where the external driving voltage is intermittently switched off so as to allow the crystal oscillations to freely decay, enabled the quantification of the energy dissipation factor *D* and gave birth to QCM-D (quartz crystal microbalance with dissipation monitoring; Figure 4.4.a).[14] Indeed, given the piezoelectric property of quartz, the decaying mechanical oscillations give rise to a voltage which is recorded by two gold electrodes wrapping the quartz surface. The voltage over the crystal, U, decays as an exponentially damped sinusoidal (Figure 4.4.b):

$$U(t) = U_0 e^{-\frac{t}{\tau}} \sin(2\pi f t + \phi) \qquad (4.23)$$

where $\tau$ is the decay time constant and $\phi$ is the phase. The damping of the crystal oscillation, i.e., the dissipation factor D is given by:

$D = \frac{1}{\pi f \tau} = \frac{E_{dissipated}}{2\pi E_{stored}}$, where $E_{dissipated}$ is the energy dissipated during one period of oscillation and $E_{stored}$ is the energy stored in the oscillating system. Soft (viscous) films will dissipate more energy than solid (elastic) films and, as a consequence, the oscillation of the crystal will decay faster when functionalized with a soft film, leading to higher dissipation *D* values. Recording *D* yields valuable information regarding the viscoelastic properties of the adlayer. The advent of QCM-D thus enabled the measurement of two parameters per overtone: the resonance frequency $f_n$ and the dissipation $D_n$ (Figure 4.4.c).

Adsorbed mass estimate and assumptions

To help unravel the building mechanism of the diverse studied assemblies studied, changes in the resonance frequency recorded via QCM-

D were routinely translated into increments of adsorbed mass using the Sauerbrey equation, after careful evaluation of its applicability. Acceptance criteria include the fulfilment of the rigid and homogeneous adsorbed film condition, $\frac{\Delta D_n}{\left(\frac{-\Delta f_n}{n}\right)}$ << 4 x $10^{-7}$ $Hz^{-1}$ and $\frac{\Delta f_n}{n}$ ~ constant for all *n* (overtones), as well as the low thickness/mass status compared to the quartz crystal, $\frac{\Delta f_n}{f_n} \ll 1$.[20] All these conditions were fulfilled for most biofilms studied in this report. Moreover, even in borderline cases where the use of a viscoelastic model should be considered (such as the adsorption of highly hydrated proteins), it is common practise to use Sauerbrey's equation as first approximation as failure of the Sauerbrey model was quantified to be responsible for less than 10% of variation in the final results.[21]

The mass of each adsorbed compound per square centimetre of quartz surface is thus extracted using equation 4.22 and considering the fifth overtone (*n* = 5):

$$\Delta m = -C\frac{\Delta f}{5} \qquad [ng.cm^{-2}]$$

where $C = 17.702$ [$ng.cm^{-2}.Hz^{-1}$] for a 5 MHz quartz crystal. Assuming that the adsorbed mass is evenly distributed over the crystal surface, as should be the case when using Sauerbrey's approximation, the thickness of the adlayer *x* ($d_x$) is given by:

$$d_x = \frac{\Delta m_x}{\rho_x} \qquad [m] \qquad (4.24)$$

where $\rho_x$ is the density of the adlayer *x*. It is noteworthy to mention that the adsorbed mass obtained via QCM-D contains contributions from both the mass of molecules of compound *x* adsorbed on the surface and the mass of water molecules coupled to them. The mass determined through QCM-D is thus a wet mass and the polymers used in this study being highly hydrated, it is reasonable to use the density of water as an approximation in the computation of the adlayer thickness, so as to yield an average hydrodynamic thickness.

## 4.5 References

(1) Richert, L.; Boulmedais, F.; Lavalle, P.; Mutterer, J.; Ferreux, E.; Decher, G.; Schaaf, P.; Voegel, J.-C.; Picart, C. Improvement of Stability and Cell Adhesion Properties of Polyelectrolyte Multilayer Films by Chemical Cross-Linking. *Biomacromolecules* **2004**, *5* (2), 284–294. https://doi.org/10.1021/bm0342281.

(2) Elimelech, M.; Gregory, J.; Jia, X. *Particle Deposition and Aggregation Measurement, Modelling and Simulation*, 1st Editio.; Williams, R. A., Ed.; Elsevier: Owford, U.K., 1995. https://doi.org/10.1016/B978-0-7506-7024-1.X5000-6.

(3) Evans, D. F.; Wennerström, H. *The Colloidal Domain - Where Physics, Chemistry, Biology and Technology Meet*, 2nd Editio.; John Wiley: New York, USA, 1999.

(4) Hunter, R. J. *Zeta Potential in Colloidal Science*, 1st Editio.; Ottewill, R. H., Rowell, R. L., Eds.; Academic Press, 1988.

(5) Russel, W. B.; Saville, D. A.; Schowalter, W. R. *Colloidal Dispersions*; Cambridge University Press, 1989. https://doi.org/10.1017/CBO9780511608810.

(6) O'Brien, R. W.; White, L. R. Electrophoretic Mobility of a Spherical Colloidal Particle. *J. Chem. Soc. Faraday II* **1978**, *74*, 1607–1626.

(7) Shaw, D. J. *Electrophoresis*; Academic Press: London, England, 1969.

(8) Malvern technical booklet https://www.malvernpanalytical.com/fr/products/product-range/zetasizer-range/zetasizer-nano-range/zetasizer-nano-zs?creative=315711549994&keyword=&matchtype=b&network=g&device=c&gclid=Cj0KCQiA6IHwBRCJARIsALNjViVd2oSP8N5hmOGmz8h8YSrRTUk9LNl4iQVhwrKgFprzVAH7jo9WcmwaAoN4EALw_wcB (accessed Jun 20, 2019).

(9) Hasted, J. B.; Ritson, D. M.; Collie, C. H. Dielectric Properties of Aqueous Ionic Solutions. Parts I and II. *J. Chem. Phys.* **1948**, *16* (1), 1–21. https://doi.org/10.1063/1.1746645.

(10) Gavish, N.; Promislow, K. Dependence of the Dielectric Constant of Electrolyte Solutions on Ionic Concentration: A Microfield Approach. *Phys. Rev. E* **2016**, *94* (1), 012611. https://doi.org/10.1103/PhysRevE.94.012611.

(11) Oncsik, T.; Trefalt, G.; Borkovec, M.; Szilagyi, I. Specific Ion Effects on Particle Aggregation Induced by Monovalent Salts within the Hofmeister Series. *Langmuir* **2015**, *31* (13), 3799–3807. https://doi.org/10.1021/acs.langmuir.5b00225.

(12) Jenkins, H. D. B.; Marcus, Y. Viscosity B-Coefficients of Ions in Solution. *Chem. Rev.* **1995**, *95* (8), 2695–2724. https://doi.org/10.1021/cr00040a004.

(13) Sauerbrey, G. Verwendung von Schwingquarzen Zur Wägung Dünner Schichten Und Zur Mikrowägung. *Zeitschrift für Phys.* **1959**, *155* (2), 206–222. https://doi.org/10.1007/BF01337937.

(14) Dixon, M. C. Quartz Crystal Microbalance with Dissipation Monitoring: Enabling Real-Time Characterization of Biological Materials and Their Interactions. *J. Biomol. Tech.* **2008**, *19*, 151–158.

(15) Rodahl, M.; Höök, F.; Kasemo, B. QCM Operation in Liquids: An Explanation of Measured Variations in Frequency and Q Factor with Liquid Conductivity. *Anal. Chem.* **1996**, *68* (13), 2219–2227. https://doi.org/10.1021/ac951203m.

(16) Rodahl, M.; Höök, F.; Krozer, A.; Brzezinski, P.; Kasemo, B. Quartz Crystal Microbalance Setup for Frequency and Q -factor Measurements in Gaseous and Liquid Environments. *Rev. Sci. Instrum.* **1995**, *66* (7), 3924–3930. https://doi.org/10.1063/1.1145396.

(17) Rodahl, M.; Höök, F.; Fredriksson, C.; Keller, C. A.; Krozer, A.; Brzezinski, P.; Voinova, M.; Kasemo, B. Simultaneous Frequency and Dissipation Factor QCM Measurements of Biomolecular Adsorption and Cell Adhesion. *Faraday Discuss.* **1997**, *107*, 229–246. https://doi.org/10.1039/a703137h.

(18) Fant, C.; Sott, K.; Elwing, H.; Hook, F. Adsorption Behavior and Enzymatically or Chemically Induced Cross-linking of a Mussel Adhesive Protein. *Biofouling* **2000**, *16* (2–4), 119–132. https://doi.org/10.1080/08927010009378437.

(19) Voinova, M. V; Rodahl, M.; Jonson, M.; Kasemo, B. Viscoelastic Acoustic Response of Layered Polymer Films at Fluid-Solid Interfaces: Continuum Mechanics Approach. *Phys. Scr.* **1999**, *59* (5), 391–396. https://doi.org/10.1238/Physica.Regular.059a00391.

(20) Reviakine, I.; Johannsmann, D.; Richter, R. P. Hearing What You Cannot See and Visualizing What You Hear: Interpreting Quartz Crystal Microbalance Data from Solvated Interfaces. *Anal. Chem.* **2011**, *83* (23), 8838–8848. https://doi.org/10.1021/ac201778h.

(21) *Biomolecular Sensors*; Gizeli, E., Lowe, C., Eds.; CRC Press: London, England, 2002.

# Chapter 5

# Nanocomposite biointerfaces

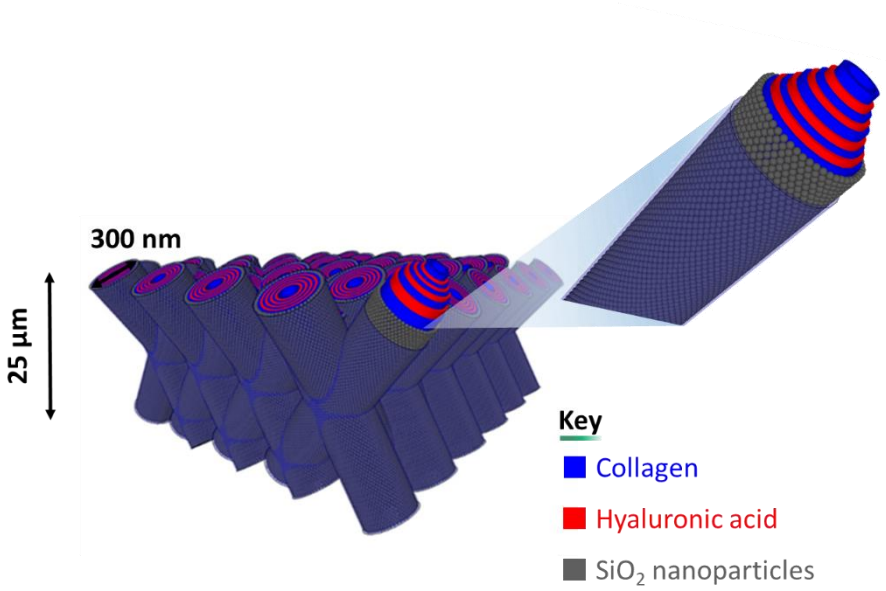


**Figure 5.1** *Schematic illustration of the nanocomposite biointerfaces synthesized as ECM mimics in the frame of this thesis. The nanostructured matrices are constituted of intersecting composite nanotubes, themselves composed of a multilayer of ECM-derived biopolymers and inorganic (i.e., silica) nanoparticles incorporated as strengthening phase.*

## Abstract

With the goal to synthesize a nanostructured biointerface, artificially recreating the ECM and its numerous roles as mechanical support and physicochemical guide for sustained cellular proliferation and differentiation as faithfully as possible, biomimetic matrices constituted of intersected nanotubes were built. In order to mimic the chemical composition and bioactive properties of the original ECM, collagen and hyaluronic acid were chosen as main components of the nanotubular building blocks. The self-assembly of the two biomacromolecules was successfully initiated and guided into intersected tubular-shaped nanoobjects relying on the template-assisted LbL deposition method. In an attempt to make up for the low

mechanical properties associated to biopolymers and improve the mechanical stiffness of the resulting construct, inorganic nanoparticles (ie., silica nanoparticles) were integrated in the multilayered nanotubes, yielding mechanically-stable composite biointerfaces. Mechanical stability of the nanocomposite tubes, blending in the biocompatibility of the (Col/HA) multilayer with the higher Young's modulus of the silica phase, was indeed shown to be increased compared to control unstiffened (Col/HA) nanotubes. AFM nanoindentation tests evidenced that the elastic modulus of the nanocomposite tubes was, on average, 38% higher than that of full biopolymer tubes, which translated into composite biointerfaces of higher mechanical integrity as compared to the collapsed morphology displayed by the unstiffened biopolymer interfaces. We envision these engineered nanocomposite matrices, sharing structural, compositional and mechanical similarities with the ECM of mineralized tissues (e.g., bone, tooth, etc.) to be useful as cell-educative biomaterials for tissue engineering and regenerative medicine strategies, although their fragility and the current impossibility to easily handle them manually and transfer them from one substrate to another might yet delay their actual applicability. Moreover, the composite matrices offering a high specific surface area developed both at the micro- (i.e., area of the tubular blocks) and nanoscale (i.e., area of the silica nanospheres) could be used as multifunctionalizable platforms for drug delivery, nanocatalysis or biosensing applications.

## 5.1 Strategy

The first strategy which was imagined to combine the requirements for bioactivity and mechanical integrity within the design of ECM-inspired biointerfaces relies on the synthesis of composite biomaterials. It was decided to produce such composite biomaterials via incorporation of a strengthening agent, in the form of silica ($SiO_2$) NPs, inside multilayered NTs composed of biopolymers. The parameters leading to the successful integration of silica NPs during the LbL assembly of polymers into nanoporous templates thus needed to be optimized.

Selection of these optimal parameters was the subject of an exploratory phase where the incorporation of silica colloids was conducted at various stages along the LbL assembly of NTs made of well-known synthetic polyelectrolytes (PEs) (Figure 5.2). Completion of this step was achieved using a trial-and-error process where the assembly of two oppositely-charged PEs, poly(allylamine hydrochloride) (PAH) or its fluorescent-tagged counterpart, PAH-FITC, and poly(acrylic acid) (PAA) was initiated inside nanoporous PC templates before incorporating silica NPs, under different circumstances, along the growing multilayer. Among the tested parameters are the concentration of the colloidal dispersion to be diffused through the NTs, their means of incorporation (passive diffusion or filtration), the location of their infiltration (inner versus outer layers of the NTs) and the number of incorporation steps to be carried out. The influence of these parameters on the successful production of mechanically-stable composite NTs was evaluated by assessing the morphology of the resulting NTs via scanning electron microscopy (section S.I.5.1).

In a second phase, the optimized parameters found for the incorporation of inorganic particles in synthetic NTs are extended to the case of biopolymer NTs, so as to yield nanocomposite biomimetic tubes (Figure 5.3.b) and biointerfaces made thereof (Figure 5.3.a).

The synthesized nanocomposite biointerfaces are imaged by SEM and their total content in protein (Col) is further quantified using the µBCA colorimetric assay (*see* ***Theoretical appendix 5.V***) in a way to determine the mass of Col incorporated per step of the LbL assembly. Mechanical properties of the elementary building blocks of the structures, that is to say the composite biomimetic NTs, are further evaluated by determining their elastic modulus via AFM nanoindentation tests (*see* ***Theoretical appendix 5.VI.A***) and by extracting morphology-based indexes from their microscopic observation (*see* ***Theoretical appendix 5.VI.B***).

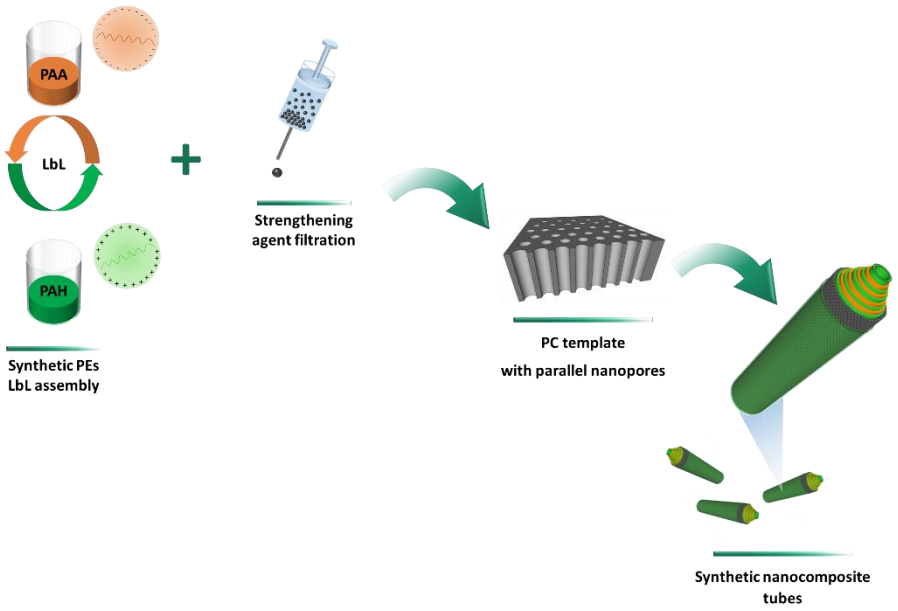


**Figure 5.2** Schematic illustration of the first step of the strategy aiming at the production of nanocomposite biointerfaces: the parameters relevant to the incorporation of silica NPs inside a growing multilayer are first optimized in the case of individual NTs made of synthetic PEs.

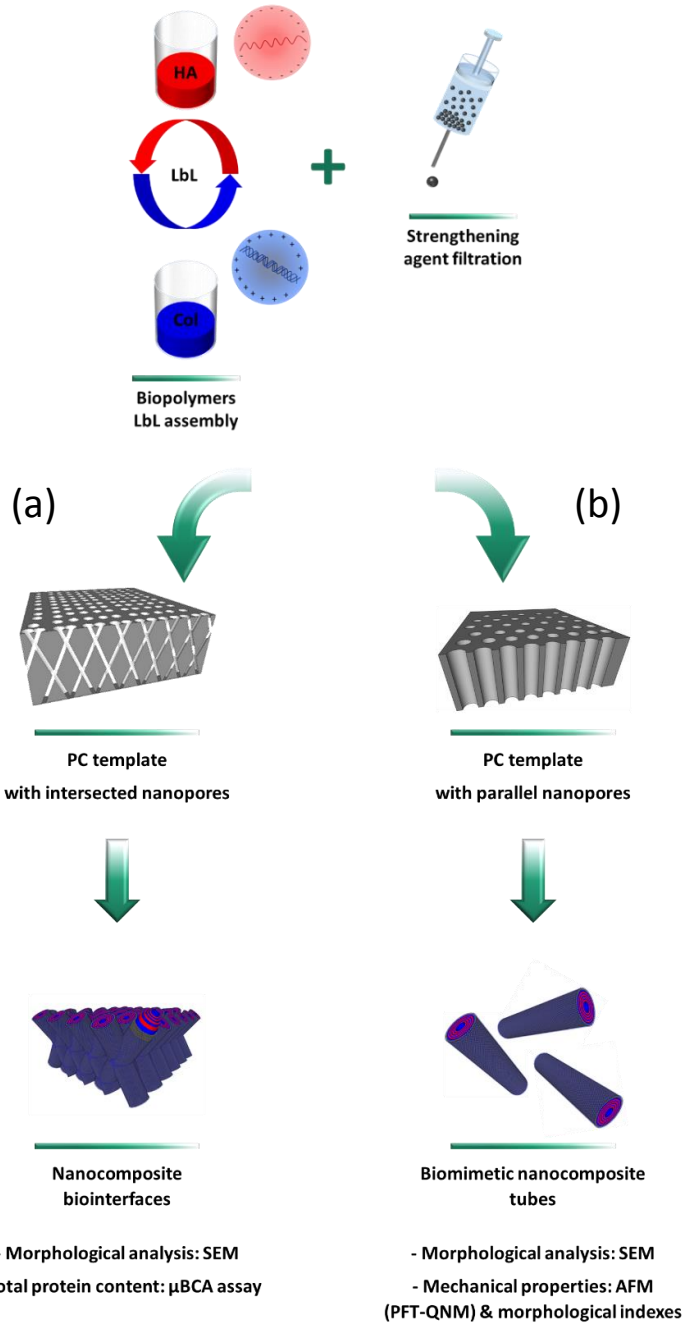


**Figure 5.3** Schematic illustration of the second step of the strategy aiming at the production of nanocomposite biointerfaces along with the ensuing characterization techniques.

## 5.2 Results and discussion

### 5.2.1 LbL assembly of nanocomposite biointerfaces

After careful optimization of the assembly conditions leading to mechanically-stable NTs blending stiff inorganic NPs and highly flexible polymers of synthetic nature (the detailed results of this exploratory phase is presented in section S.I.5.1), the incorporation of silica NPs within biopolymer-based NTs was investigated.

The electrophoretic mobility of colloidal silica as a function of pH was monitored for two different ionic strengths: ultrapure water ($I$ = $10^{-7}$ M) versus a 150 mM NaCl aqueous solution ($I$ = 0.15 M) (Figure 5.4). As expected, the superficial oxide layer of $SiO_2$ particles entails a negatively-charged surface under all probed pH conditions. When brought in contact with Col molecules, globally positively-charged at pH 4 (Figure 4.2), the negatively-charged colloids are expected to electrostatically interact with the biomacromolecule and therefore be incorporated in the (Col/HA) self-assembly as a counterpart to Col.

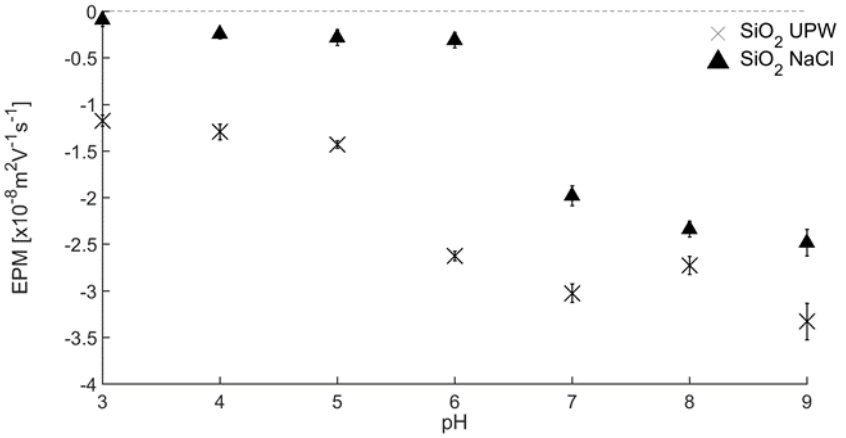


**Figure 5.4** *Evolution of the electrophoretic mobility of silica NPs as a function of pH and ionic strength: silica colloids dispersed in ultrapure water (I = $10^{-7}$ M, cross) or in 0.15 M NaCl aqueous solution (I = 0.15 M, triangle).*

The introduction of NaCl in the medium is responsible for a drop in mobility and the ζ-potential of the particles. The higher *I* of the salt solution imparts a higher charge-screening efficiency to the medium, as depicted by the drastic reduction of the Debye length from ~ 972.6 nm in ultrapure water to ~ 0.8 nm in the 0.15 M NaCl solution (equation 4.13, Th.A.4.I). As a consequence, the ζ-potential of the silicon dioxide NPs drops from -16.3 mV in water to -3.2 mV in 0.15 M NaCl. In order to maximize the electrostatic interactions between $SiO_2$ and the positively-charged Col macromolecules as well as avoid flocculation of the colloids, care has been taken to disperse silica particles in UPW with no added salt for all assemblies.

The ability of Col, HA and $SiO_2$ NPs to self-assemble into stable multilayers was further evaluated *in situ* using QCM-D. The frequency $\Delta f$ and dissipation $\Delta D$ shifts recorded for the fifth overtone as a function of time, characterizing the adsorption kinetics of the assembly partners, are presented in Figure 5.5.a. The extracted parameters $-\Delta f_5/5$, proportional to the wet mass adsorbed on the crystal surface (as explained in Th.A.4.2) and $\Delta D_5/(-\Delta f_5/5)$, related to the viscoelastic properties of the film, are displayed in Figure 5.5.b and 5.5.c. Circulation of the first Col solution within the QCM system is characterized by an increase of $-\Delta f/n$ and a sharp rise in the dissipation level, suggesting that Col molecules do adsorb on the crystal surface in a highly hydrated fashion, giving rise to a soft and viscous adlayer, dissipating a high amount of energy. An adsorption plateau is reached after less than 20 min, indicating that the crystal surface has probably been saturated with a Col monolayer. In contrast, the dissipation continues to slightly increase until rinsing, suggesting that the protein monolayer swells with water.

The change in $-\Delta f_5/5$ upon Col adsorption is 181.4 Hz, which translates into an areal adsorbed mass of 3211 $ng.cm^{-2}$ using the Sauerbrey equation (4.22, Th.A.4.II) and a wet thickness of ~32.1 nm (equation 4.24, Th.A.4.II). The fibrillar morphology of Col can be approximated, in its fully extended state, as a cylinder of 300 nm length and 1.5 nm diameter. Hence we can fairly assume that the 32 nm thickness is due to Col adsorbing on the gold-metallized quartz crystal under a flexible end-on conformation, with part of its peptide backbone protruding away in the solution (Figure 6.20.I). The

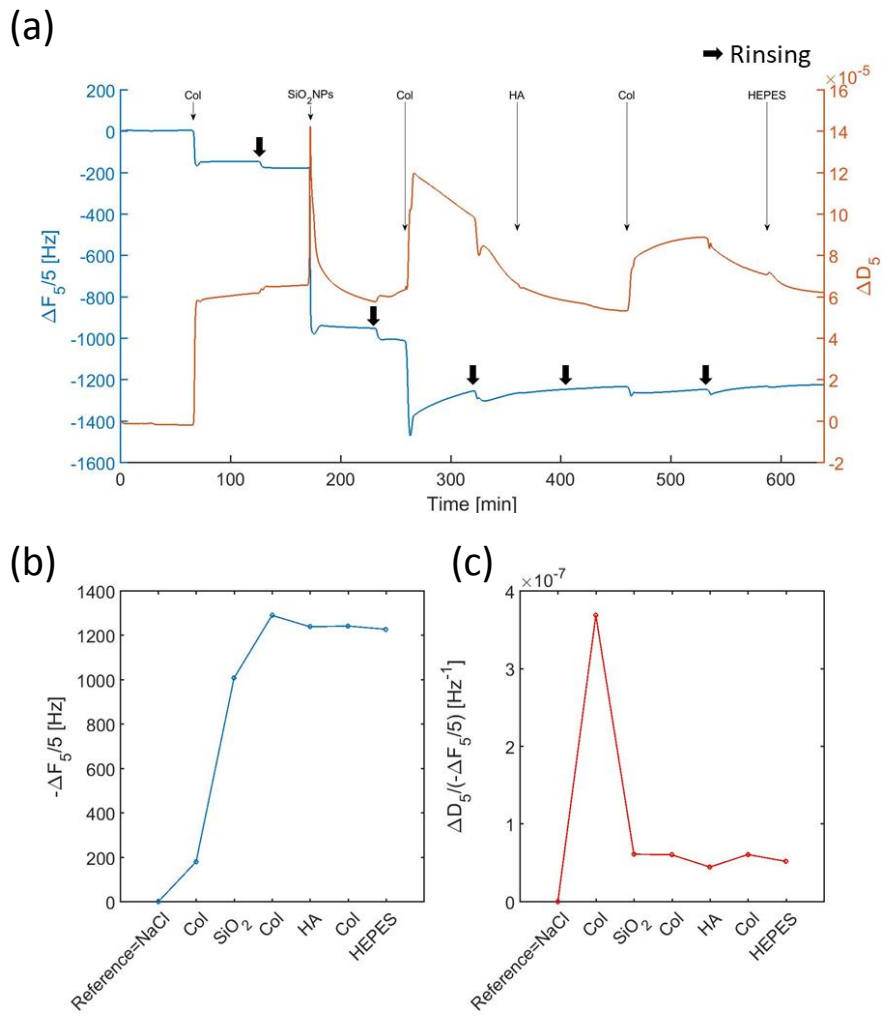


**Figure 5.5** *(a) Real time QCM-D monitoring of the frequency ($\Delta f_5/5$, left axis) and dissipation ($\Delta D_5$, right axis) shifts for the assembly of a $(Col/SiO_2)_1(Col/HA)_{1.5}$ film in a NaCl 0.15 M aqueous solution pH 4.0 (except for $SiO_2$ NPs which were kept in suspension in UPW pH 4.0). Cumulated (b) $-\Delta f_5/5$ (proportional to the adsorbed wet mass) and (c) $\Delta D_5/(-\Delta f_5/5)$ extracted from the construction kinetics of the $(Col/SiO_2)_1(Col/HA)_{1.5}$ film.*

introduction of colloidal silica over the pre-adsorbed Col layer is characterized by a fast and huge drop in both frequency and dissipation

factors, attesting to the adsorption of the NPs as a rigid layer compacting the protein film and expelling water (Figure 5.6.II). The adsorption of $SiO_2$ colloids is responsible for a frequency shift *($-\Delta f_5/5$)* of 827.7 Hz, yielding an adsorbed mass as high as 14652 ng.cm$^{-2}$. Injecting the density of silica (2.334 g.cm$^{-3}$) in equation 4.24 (Th.A.4.II) results in a thickness of ~ 62.8 nm, which is equivalent to about a double and a half layer of silica NPs (Ø ~ 25 nm).

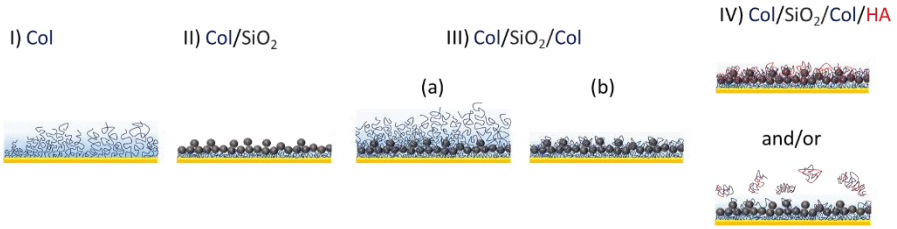


**Figure 5.6** *Schematic interpretation of the QCM-D data recorded in Figure 5.5. A) Col molecules first adsorb in an extended conformation, trapping a high amount of water as evidenced by the concomitant increase in -Δf and dissipation parameters. II) The adsorption of silicon dioxide colloids expels a lot of water from the interface and leads to a compaction of the film, as evidence by simultaneous increase in -Δf and decrease in ΔD. III) Col adsorbs in large quantities as the interfacial area available to adsorption has increased following deposition of silica colloids (IIIa). A certain reorganization of the film occurs after Col adsorption as the drop in ΔD suggests a compaction of the film (IIIb). IV) The absence of any significant variation of -Δf after injection of HA, combined with the slow but steady dissipation decrease makes it difficult to conclude whether HA tightly adsorbs to Col molecules on the silica NPs surface and displaces water molecules or rather form soluble complexes with Col molecules which are released towards the bulk liquid.*

The sedimentation rate of the silica colloids in the QCM-D chamber is determined to be ~4.55 10$^{-10}$ m.s$^{-1}$ by modelling the system as spheres free falling down a column of stationary liquid and using the Stoke's law (*see **Theoretical appendix 5.I***). The corresponding sedimentation time of 25 nm diameter silica NPs is computed to be 1.83 10$^3$ h to fall down a distance as small as 3 mm. The flow speed through the QCM tubing, $v_{flow}$, assumed to be equal to the horizontal speed at which the particles cross the crystal surface is computed to be 6.37 10$^{-4}$ m.s$^{-1}$. The horizontal velocity of the colloids being much higher than their vertical sedimentation speed, the

majority of the NPs should be expelled from the QCM chamber before passively reaching its bottom surface. This leads to the conclusion that the huge frequency drop associated with $SiO_2$ NPs adsorption in less than 20 min time cannot be explained by the simple passive sedimentation of particles but instead is the result of an active phenomenon, such as the electroattractive forces exerted by the positively-charged Col molecules. What is true for a 25 nm particle with a much higher density than water is even more so for light biomacromolecules ($\rho_{proteins} \sim 1350\ \mathrm{kg.m^3}$) whose larger dimension is below 300 nm. Hence, it is to be excluded that the large and fast frequency drops are due to passive sedimentation of the assembly partners.

The second circulation of the Col solution is marked by a much deeper frequency shift than the first adsorption step ($-\Delta f_5/5$ = 282.2 Hz for the second Col adsorption step compared to 181.4 Hz for the first one), translating into a higher adsorbed mass using equation 4.22 (Th.A.4.II) (4996 $ng.cm^{-2}$ as compared to 3211 $ng.cm^{-2}$ for the first Col monolayer) and higher thickness of 50.0 nm (~ 32.1 nm for the first layer) using equation 4.24 (Th.A.4.II). The higher Col mass adsorbed is most probably due to the prior adsorption of silica colloids covering the crystal surface and offering a much higher surface area for the adsorption of Col. It is thus likely that the density of adsorbed Col molecules (number of Col molecules adsorbed per square centimeter) does not change but, instead, the surface available to Col adsorption does increase a lot after deposition of colloidal particles, leading to a higher total amount of Col present at the interface (Figure 5.6.IIIa). Hence, the hydrodynamic thickness measured in this case does not have much relevance given that it is computed assuming a constant interfacial area (i.e., the area of the quartz crystal surface) available for adsorption, which clearly is not the case after adsorption of $SiO_2$ colloids. Assuming a packing density of 1 and considering that only half of the total surface developed by each particle (i.e., the face of the particle exposed to the bulk liquid phase) is available to the adsorption of species in solution, one can compute the effective area developed by a monolayer of close-packed 25 nm diameter silica nanospheres to be 1.57 $cm^2$ per $cm^2$ of quartz substrate (*see* Th.A.5.II). If we divide the areal mass of Col adsorbed after deposition of the silica NPs, 4996 $ng.cm^{-2}$, by this corrective factor of 1.57 allowing for the

increase of surface area upon $SiO_2$ adsorption to be taken into account, it yields:

$\frac{4996\ \mathrm{ng.cm^{-2}}}{1.57} = 3182\ \mathrm{ng.cm^2}$. This value being very close to the areal mass of Col adsorbed before silica deposition (3211 ng.cm$^{-2}$), it further evidences that the increase in deposited Col mass is to be fully attributed to the sudden rise in available surface area.

The adsorption of Col molecules saturates after less than 20 minutes (indicating that the surface of $SiO_2$ particles is fully covered) but the *Δf* signal then steadily increases until rinsing, just like the *ΔD* peaks rapidly before decreasing steadily after rinsing and reaching a value similar to the one obtained after $SiO_2$ adsorption. This sequence of events can be interpreted as the adsorption of Col first as a highly hydrated layer (Figure 5.6.IIIa) which then reorganizes, probably by interacting with more adsorption sites on the silica colloids and adsorbing in a more extended conformation (Figure 5.6.IIIb), perhaps bridging NPs together and hence expelling water from the film.

After these three first adsorption steps, the system does not evolve much: $-\Delta f_5/5$ stays almost constant or slightly decreases after introduction of HA, whereas *ΔD* first decreases after injection of HA, increases again when a Col solution is circulated but then stabilizes back to its initial value when rinsing occurs. It is difficult to determine whether the absence of variation in the resonance frequency is due to a saturation of the system after adsorption of the first three layers or to a massive loss of water from the film, compensated by the adsorption of biopolymers. The fact that the dissipation parameter keeps on evolving after introduction of each specie leads us to the statement that the equilibrium reached is dynamic. Indeed, when HA is injected in the system, *ΔD* decreases which might be either the sign of the incorporation of HA in the Col/$SiO_2$ film as a replacement for water molecules, triggering the compaction and rigidification of the film or rather the sign of the formation of soluble Col/HA complexes leaving the interface (Figure 5.6.IV), as highlighted previously for d-Col/PSS[1] and d-Col/Fn[2] assemblies. More unsettling is the gain in *ΔD* decoupled from any significant variation in Δf after addition of the third and last Col solution, which seems to point towards the deposition of Col as a hydrated adlayer which the saturating balance fails to detect.

Although it is blatant that the assembly proceeds gradually, in a layer-by-layer fashion from the first Col monolayer to the second one, both sandwiching a colloidal interlayer, it is impossible to clearly state at this point whether HA takes part in this LbL assembly or not and whether the assembly stops in its early stages or keeps on progressing sustainably while being unnoticed due to saturation of the device. A comprehensive summary of the adsorption events recorded by QCM-D is provided in Table 5.1.

**Table 5.1** *Summary of the frequency shifts ($-\Delta f_5/5$) recorded during the QCM-D monitoring of the $(Col/SiO_2)_1(Col/HA)_{1.5}$ buildup and the corresponding adsorbed areal mass and wet thickness values, computed using Sauerbrey's equation*

| Layer | Medium | $-\Delta f_5/5$ (Hz) | Adsorbed areal mass ($ng.cm^{-2}$) | Thickness of wet layer (nm) |
|---|---|---|---|---|
| **Col1** | NaCl 0.15 M pH 4 | 181 | 3211 | 32 |
| **$SiO_2$ NPs** | UPW pH 4 | 828 | 14652 | 63 |
| **Col2** | NaCl 0.15 M pH 4 | 282 | 4996 | 50 |
| **HA1** | NaCl 0.15 M pH 4 | -52 | -913 | -9 |
| **Col3** | NaCl 0.15 M pH 4 | 3 | 63 | 1 |
| **Rinsing** | HEPES 10 mM pH 7.4 NaCl 0.15 M | -15 | -257 | -3 |

Templating this composite assembly within PC membranes with parallel nanopores enabled the production of individual composite NTs (Figure 5.7.c-f). Compared to the fully biomimetic (Col/HA) NTs (Figure 5.7.a-b) which present a flattened and winding conformation, the tubes with filtered colloids (Figure 5.7. c-f) show a more homogeneous morphology and a greater thickness and thus appear to be less affected by the template dissolution and NTs collection processes. Adding inorganic colloids to the polymer multilayer thus seems to have a beneficial effect on the mechanical stability of the NTs. The successful incorporation of silica particles inside the tubular multilayer can be visually demonstrated when observing the NTs at high magnification as they clearly appear to be filled with nanosized colloids (Figure 5.7.d,f).

The analysis of the chemical composition of individual composite NTs via TEM-EDX further corroborates the presence of silica colloids within the NTs, as the characteristic X-ray of the Si element appears as the predominant signal of the spectrum (Figure 5.8). The presence of carbon, oxygen and nitrogen is attributed to the Col and HA biomolecules which are the major organic constituents of the NTs while the Cu and Zn elements come from the

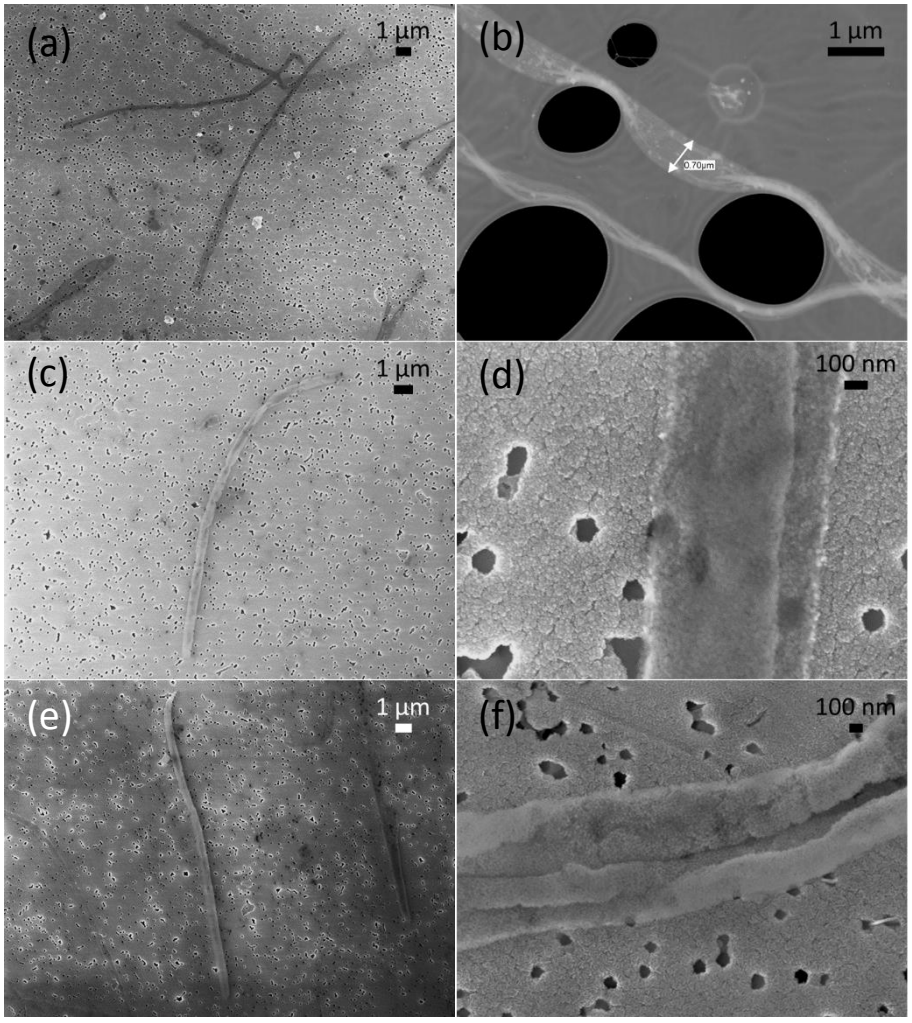


**Figure 5.7** *SEM (a,c-f) and STEM (b) pictures of individual biomimetic NTs composed of: (a-b) an ECM-like $(Col/HA)_8$ multilayer with no added $SiO_2$ NPs, (c-d) a composite $(Col/SiO_2)_1(Col/HA)_7$ multilayer displaying $SiO_2$ NPs in their outermost bilayer and (e-f) a composite $(Col/HA)_6(Col/SiO_2)_1(Col/HA)_1$ multilayer displaying $SiO_2$ NPs in one of their innermost bilayers.*

copper grid (presenting some zinc impurities) used as substrate for TEM analysis. Similarly to what was previously undertaken on NTs of synthetic polymers (section S.I.5.1), nanocomposite tubes with silica colloids incorporated either in one of their outermost (Figure 5.7.c-d) or one of their innermost (Figure 5.8.e-f) bilayers were produced. Both systems

reproducibly yielded NTs with preserved integrity and no distinction could be made visually between them in terms of mechanical stability.

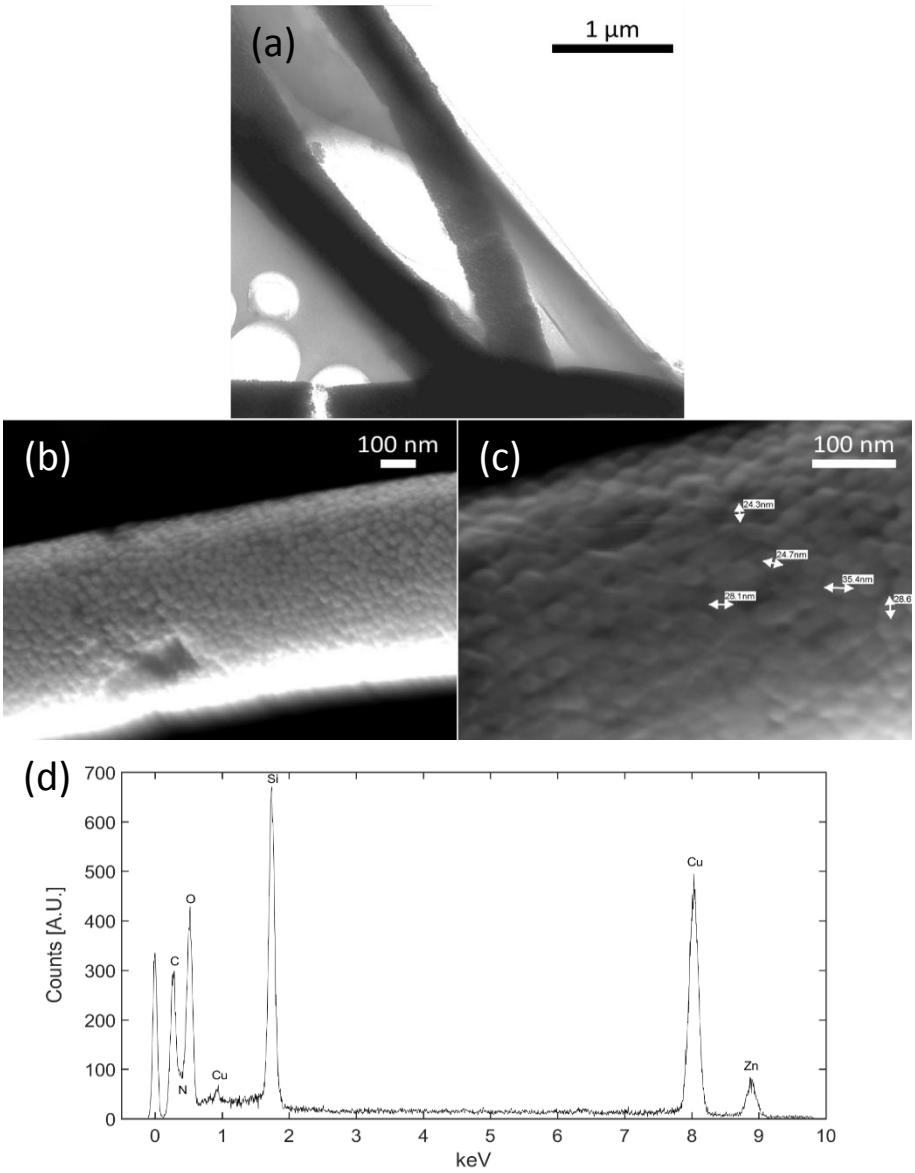


**Figure 5.8** *EDX analysis of $(Col/SiO_2)_1(Col/HA)_7$ individual NTs: (a)-(c): TEM pictures showing the analysed composite NTs at increasing magnification from (a) to (c). (d) EDX spectrum recorded over a portion of a composite NT. All identified peaks correspond to Kα X-rays of the elements entering in the composition of the NT, except for the peaks at ~0.95 and ~8.05 KeV which relate to the Lα and Kα X-rays of Cu and the Kα X-ray at ~8.64 KeV attributed to Zn; both of these elements being the constituents of the TEM grid.*

Once templated inside the custom-made PC membrane with intersected nanopores, the Col/HA assembly strengthened with inorganic colloids gives rise to 3D matrices with a well-ordered structure down to the nanoscale, as the nanotubular elements intersect in a controlled pattern (Figures 5.9 & 5.10). Intersections between NTs occurring at a fixed angle, they generate a grid-like pattern clearly visible when observing the structure from above (Figure 5.10.b) or sideways (Figures 6.9.b, 6.10.c). The successful incorporation of silica NPs in the outermost layer of the tubular building blocks is clearly visible when zooming in on the edges of the network, as they feature a characteristically rough surface (Figure 5.9.d).

In sharp contrast to the "collapsed film" morphology of the systems made solely of (bio)polymer materials (Figures 4.10-4.13), the composite structures clearly show a third dimension of appreciable size as the sides of the artificial matrix do show a well-organized palisade of self-supported NTs with a height close to that of the templating membrane (i.e., ~25 μm) (Figures 5.9.c & 5.10.c). Hence, the infiltration of $SiO_2$ colloids clearly reinforces the mechanical properties of the highly flexible polymer materials and improves the capability of the multilayered NTs to support their own weight and withstand the atmospheric pressure, leading to the creation of nanostructured composite biointerfaces with structural integrity.

In order to elucidate whether the LbL assembly of the composite multilayers stops after the deposition of the second layer of Col as hinted at by the QCM-D results (Figure 5.5) or keeps on evolving, the LbL process was alternatively stopped after the construction of either 2 (Figure 5.9) or 7 (Figure 5.10) (Col/HA) bilayers, besides the first (Col/$SiO_2$) one.

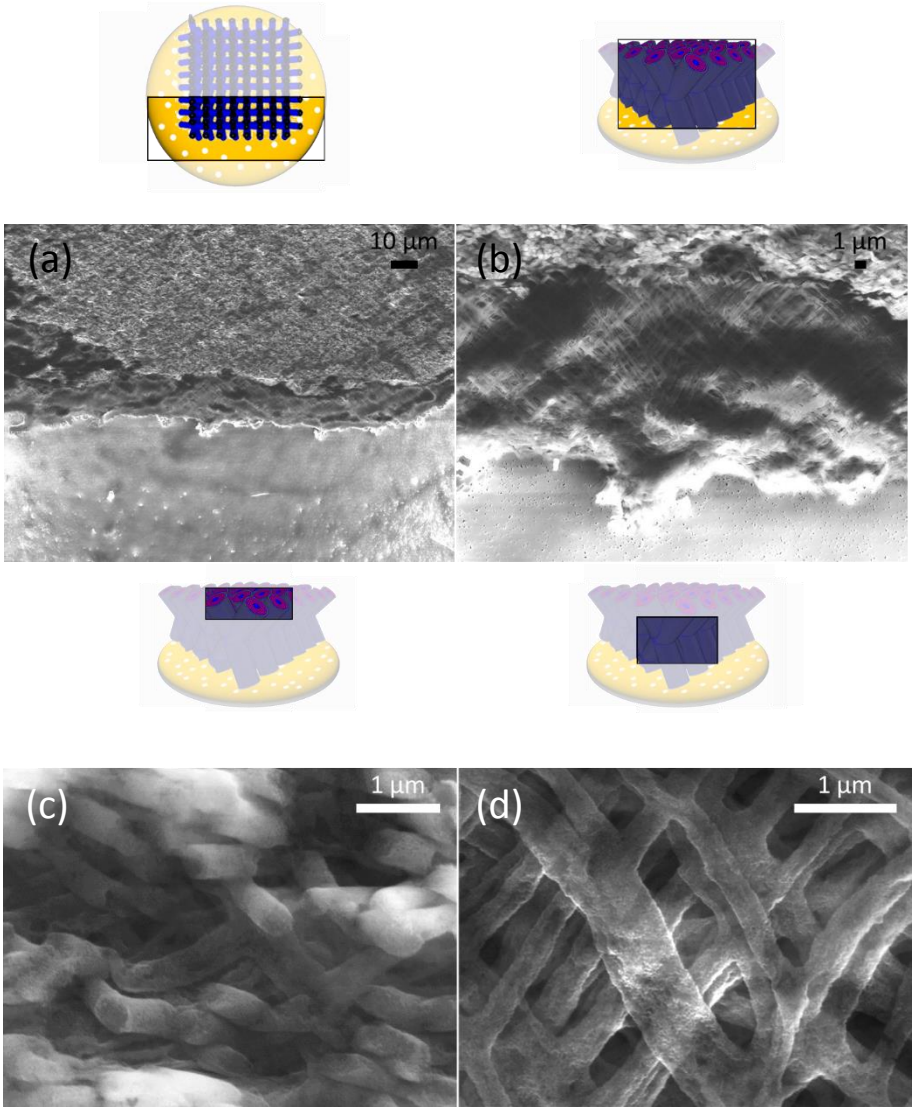


**Figure 5.9** *SEM pictures of a nanocomposite biointerface made of intersected NTs themselves composed of a composite* $(Col/SiO_2)_1(Col/HA)_2$ *multilayer combining the bioactivity of the ECM-derived biopolymers Col & HA with the mechanical stiffness of* $SiO_2$ *NPs used as strengthening agent. (a) Low magnification view of one side of the biointerface; (b) medium magnification view of one side of the biointerface, clearly showing intersected NTs of ~25 µm length; (c) high magnification view of a portion of the top surface of the biointerface, showing tubular heads and (d) high magnification view of the side of the biointerface, showing the rough surface of intersected NTs.*

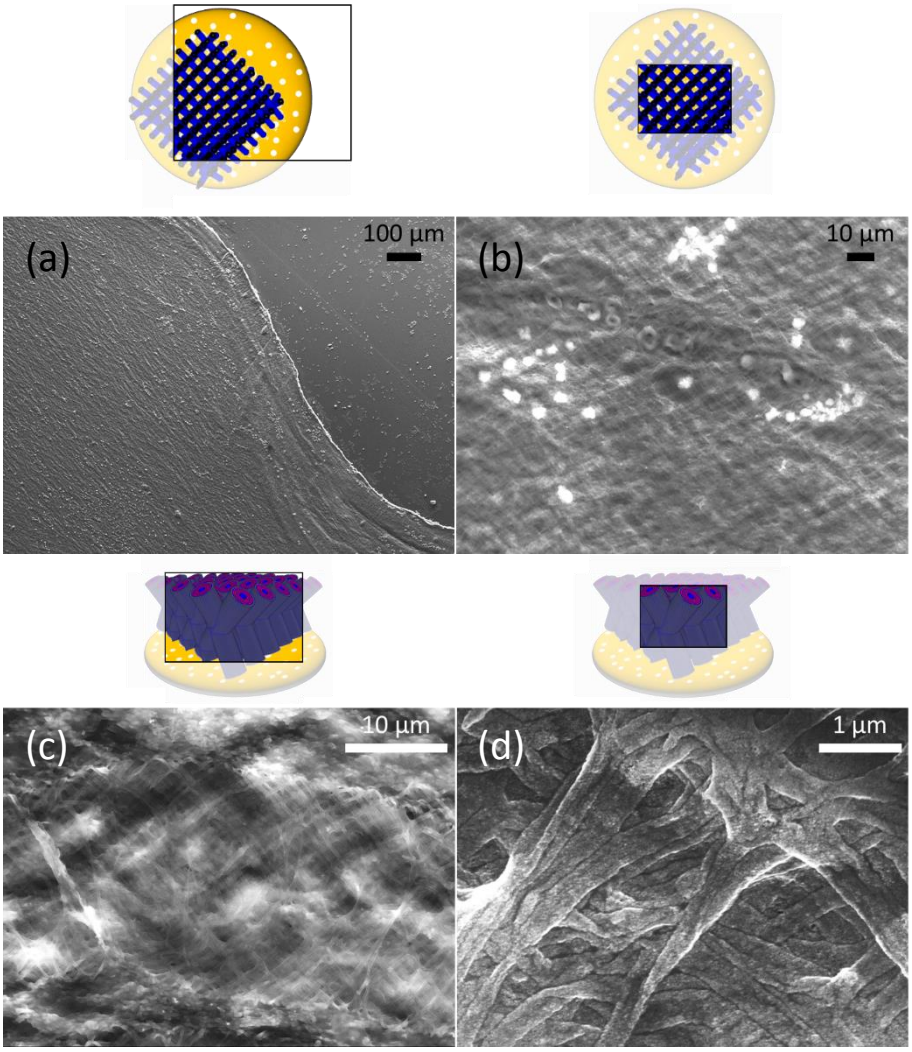


**Figure 5.10** *SEM pictures of a nanocomposite biointerface made of intersected NTs themselves composed of a composite* $(Col/SiO_2)_1(Col/HA)_7$ *multilayer combining the bioactivity of the ECM-derived biopolymers Col & HA with the mechanical stiffness of* $SiO_2$ *NPs used as strengthening agent and incorporated inside the outermost bilayer. (a) Low magnification view of one side of the biointerface; (b) medium magnification view of one portion of the top surface of the biointerface; (c) medium magnification view of one side of the biointerface and (d) high magnification view of one side of the biointerface.*

No clear distinction could be made visually between the two systems in terms of morphology, which adds further weight to the idea that the layer build-up runs out after the preliminary Col/$SiO_2$/Col steps.

In order to examine this question in a more quantitative way, the total protein content (i.e., the total amount of Col) present in the composite biointerfaces as a function of the number of assembled (Col/HA) bilayers was determined using the µBCA assay (*see* Theoretical appendix 5.V for details on the method) (Figure 5.11). As can be seen from Figure 5.11, the amount of Col effectively incorporated in the biointerface containing 7 bilayers is unambiguously greater than the Col content found in the 3-bilayer system and even more than that of the one-bilayer structure. These findings suggest that the diffusion of Col macromolecules down the nanopores and their incorporation inside the growing tubular multilayer is actually effective up to, at least, the $7^{th}$ dipping cycle. Hence, the LbL assembly of (Col/HA) bilayers doubtlessly continue to grow past the second deposited layer of Col. A corollary to this is that, although no technique could be successfully undertaken to selectively detect and quantify the amount of HA present in the NTs, HA necessarily takes part in the assembly as the multilayer would not be able to grow past the preliminary Col/$SiO_2$/Col layers without the incorporation of a negatively-charged counterpart to Col. However, although the assembly of the Col and HA partners is effective up to at least 7 bilayers, the ensuing intersected nanostructures do not seem to benefit much from the deposition of a high number of (Col/HA) bilayers, as highlighted by the similarity of Figures 5.9 and 5.10. Indeed, the morphology and mechanical stability of the structures do not seem to evolve past the second (Col/HA) bilayer. Consequently, the mechanical properties of the resulting nanostructures are rather independent of the number of biopolymer layers built but are, on the other hand, drastically enhanced by the incorporation of inorganic colloids.

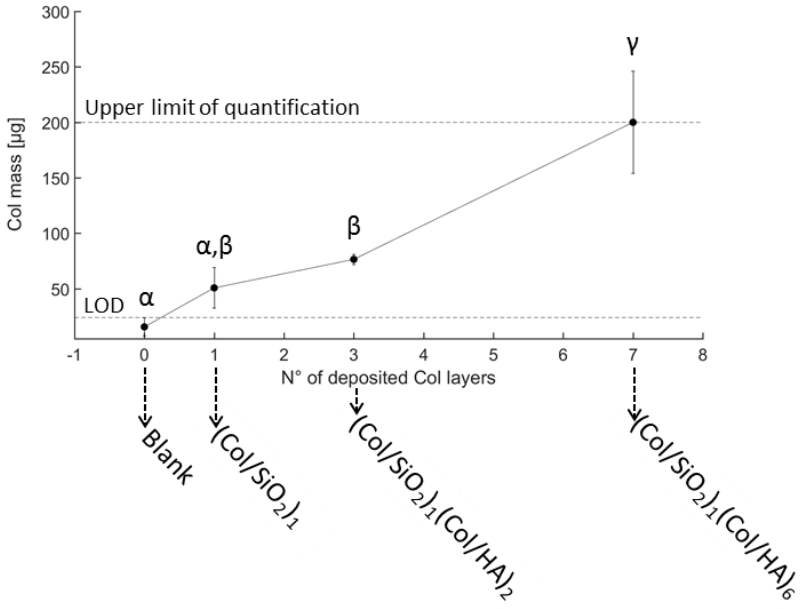


**Figure 5.11** *Dry mass of Col (µg) contained, as determined via µBCA assay, within the nanocomposite biointerfaces as a function of the number of (Col/HA) bilayers deposited. The solid line connecting individual data points is added as a guide to the eye. The black dashed line represents the upper limit of quantification of the test, as experimentally determined (maximum concentration: 100 µg/mL, equivalent to a total mass of 200 µg protein in a 2 mL sample). Error bars represent standard deviation (n=3). Bars topped with different Greek letters indicate significant difference (p-value < 0.05 as computed via consecutive Welch's ANOVA and Games-Howell post hoc tests). Limit of detection, LOD, was experimentally determined to be 24.1 µg. Upper limit of quantification was experimentally determined to be 200 µg.*

A comparison between the mass of Col incorporated in flat thin films (derived from QCM-D measurements) and that integrated in 3D nanostructures (quantified via µBCA assay) can be drawn, provided that the µBCA data are first converted into areal mass by dividing the mass of Col adsorbed by the superficial area developed by the 3D interface. The total surface area of the produced biointerfaces can be obtained from the computation of the lateral area developed by the porous network of the template from which they issue, equal to 0.0103 $m^2$ (*see* Th.A.5.III).

Dividing the values obtained from the µBCA test plotted in Figure 5.11 by the superficial area of the custom-made biointerface (0.0103 $m^2$) enables the comparison between the mass of Col incorporated in flat multilayered thin films (QCM-D data) and inside nanotubular thin films (µBCA data) (Table 5.2).

**Table 5.2** *Comparison between the cumulated areal mass and cumulated thickness of the Col layer(s) incorporated in flat multilayered thin films (QCM-D data) or inside nanocomposite biointerfaces (µBCA data).*

| N° of deposited Col layer(s) | Cumulated areal mass ($ng.cm^{-2}$) | | Cumulated thickness (nm) | |
|---|---|---|---|---|
| | QCM-D | µBCA | QCM-D | µBCA |
| **1** | 3211 | 493 | 32 | 5 |
| **2** | 8207 | / | 82 | / |
| **3** | 8267 | 743 | 83 | 7 |
| **7** | / | 1942 | / | 19 |

It is striking to observe that the amount of Col adsorbed per square centimeter of 3D biointerface is much lower than the amount of Col adsorbed per square centimeter of quartz crystal. Considering that the superficial area developed by the intersected NTs constituting the biointerface (~103 $cm^2$) is much higher than that of a quartz crystal (~1 $cm^2$), this difference might be explained by the fact that the conformation adopted by the biomolecules upon their adsorption might differ in the two cases. Under a regime of high molecular concentration (1 mg/mL) combined with a low surface area available to adsorption and in the absence of any major diffusion limitation other than the previously-adsorbed molecules such as is the case for a quartz crystal in a QCM-D chamber, the macromolecules probably adsorb in a highly flexible conformation, favouring the adsorption of a higher number of molecules per unit space and hence the formation of thicker layers. On the contrary, when adsorbing along the pore walls of a nanostructured template and even though the molecular concentration is equally high (1 mg/mL), the biomolecules have to face both a diffusion barrier (i.e., the bottleneck that the nanopore represents) and an extremely high surface area available to adsorption. Under these circumstances, the biomacromolecules might adsorb under an extended conformation, maximizing the number of interaction sites with the surface and thus leading to the adsorption of fewer molecules per unit surface and to flatter layers. Additionally, it is noteworthy to mention that while the QCM-D technique is

non-specific and reports the wet mass (i.e., protein layers + the water they contain) adsorbed on the crystal surface, the µBCA assay is specific to proteins and therefore reports their total dry mass, which should be one of the reasons why the computed values are lower than those measured via QCM-D. In this regard, determining the dry thickness of composite thin films built on flat substrates via ellipsometry and comparing the values to the wet thicknesses derived from QCM-D would be helpful to estimate the water content of the films. However, attempts at determining the dry thickness of thin films built on silicon wafers were not successful, as the ellipsometry measurements undertaken were found to be poorly reproducible. Indeed, no model could satisfactorily fit the data. This might be due to the composite nature of the film leading to a drastic change of the refractive index over a few nm distance, as well as to a high roughness and/or low homogeneity of the film. Besides the estimation of a hydration degree, the dry thickness is of limited relevance in the framework of this thesis as the engineered biointerfaces will eventually be brought in contact with cells under physiological conditions (i.e., aqueous environment), a situation where the thickness of the ECM-derived multilayer will better be reflected by the QCM-D measurements as these are carried out under wet conditions.

### 5.2.2 Mechanical properties of composite NTs

The mechanical properties of the biopolymer and biopolymer/silica composite NTs were experimentally evaluated and compared so as to assess objectively whether silica colloids effectively improve the stiffness of the multilayered NTs.

The first criteria used to evaluate the mechanical properties of individual NTs are the so-called "morphological indices", referred to as such given that they enable numerical estimates to be derived from the microscopic observations of the tubes (*see* section Th.A.VI.B). The first of these parameters, the rigidity index, $\frac{{R_{EE}}^2}{L^2}$ is an estimate of how tortuous a tube is, as it compares its end-to-end distance ($R_{EE}$, measured as the shortest segment connecting the two extremities of a NT) with its contour length ($L$, taken as the sum of the lengths of $n$ segments, with $n$ tending to infinity, drawn along the middle of a NT, perpendicular to its main axis, from one end to the other) (Figure 5.12).

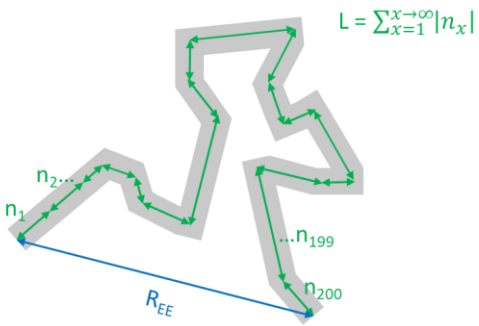


**Figure 5.12** *Schematic illustration of the end-to-end distance, REE, and contour length, L, along with the method used to measure them*

Stiff NTs being made out of rigid materials are expected to form less meanders, their contour length will consequently be similar to their end-to-end distance and they will thus exhibit a rigidity index close to 1. On the other end, highly flexible, low stiffness NTs will adopt a more winding morphology

and their contour length, following each of their curves, will therefore be much greater than their end-to-end distance, leaving a rigidity index strictly inferior to 1. The rigidity index being, above all, a measure of the tortuosity of NTs can thus be further apprehended as an estimate of the stiffness or rigidity of a NT. Figure 5.13 shows the distribution of the rigidity indices measured for 3 populations of NTs: fully biomimetic $(Col/HA)_8$ NTs and composite NTs containing silica NPs either in their outermost bilayer, $(Col/SiO_2)_1(Col/HA)_7$ or inside one of their innermost bilayers, $(Col/HA)_6(Col/SiO_2)_1/(Col/HA)_1$. No difference of statistical significance can be found between the median index of the NTs with $SiO_2$ in their external bilayer and that of NTs containing no particles. The median rigidity index of NTs with internal particles is, on the contrary, much closer to 1 (median = 0.98) and significantly different from that of native $(Col/HA)_8$ tubes.

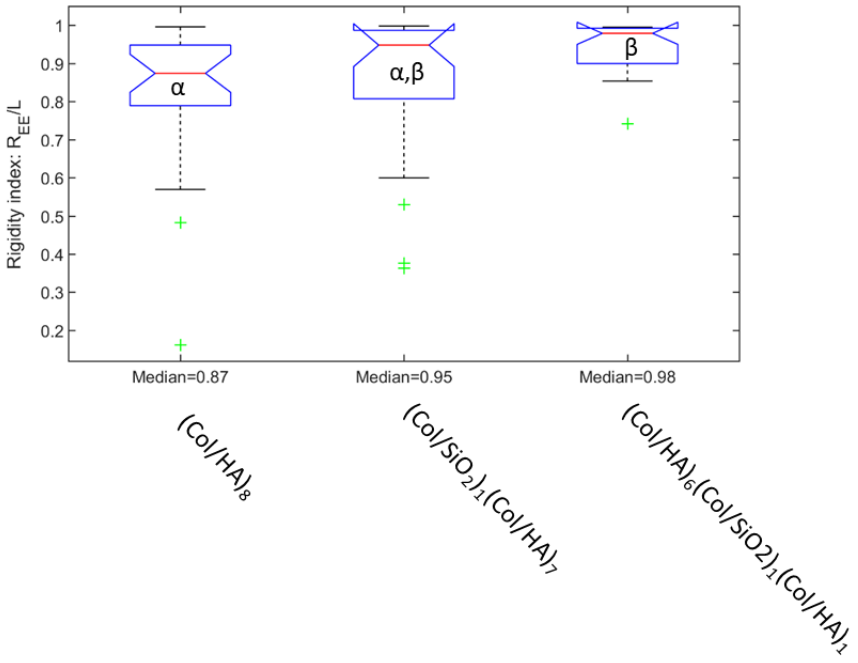


**Figure 5.13** *Notched boxplot presenting the full distribution of the rigidity indices, $\frac{{R_{EE}}^2}{L^2}$, computed for different populations of individual NTs based on microscopy images: $(Col/HA)_8$ NTs containing no silica NPs, $(Col/SiO_2)_1(Col/HA)_7$ NTs containing silica NPs in their outermost bilayer and $(Col/HA)_6(Col/SiO_2)_1(Col/HA)_1$ NTs with silica NPs in one of their innermost bilayers. The red line displays the median of each population (N=25), the length of the whiskers represent 1.5 x interquartile range (IQR), the width of the notches represent the 95% confidence interval on the median while outliers are represented by the green '+' signs. Bars topped with different Greek letters indicate significant difference of the mean (p-value < 0.05 as computed via consecutive Welch's ANOVA and Games-Howell post hoc test).*

When looking at the full set of data, one can distinguish that the median value (represented by the red line) substantially increases towards 1 when silica NPs are incorporated in the tubes and, more importantly, the dispersion of data is reduced. Outliers (symbolized by green '+' signs) are indeed less numerous and the length of whiskers (depicting the 1.5 x IQR length) is decreased. The absence of any overlap in the boxplot notches between the native biopolymer NTs and those incorporating silica in their internal layers indicate with 95% confidence that the medians of these two populations differ. The broad spread of data around the mean and median

values of ECM-like $(Col/HA)_8$ NTs can be ascribed to the fact that these tubes being composed only of highly flexible materials, the conformation they adopt upon collection on a substrate is totally random. Some might immobilize in a straight shape and some might present countless meanders, the probability of adopting any particular shape being equal. The successful incorporation of inorganic colloids in the NTs might thus be reflected in a less random distribution of their shape, as clearly evidenced by the reduced scatter of the rigidity index values upon addition of $SiO_2$ particles. Conducting the Levene's test for equality of variances on the data further demonstrates that the variances of the three NT populations differ. It is thus reasonable to state that the incorporation of silica NPs inside biopolymer-based NTs leads to both an homogenization and a raise of the stiffness modulus of the NTs.

The second morphological index, the flattening index $\frac{D_{NT}}{D_{Pore}}$, is obtained by taking the ratio between the average diameter of the NTs measured after filtration and the average diameter of the template nanopores in which the tubes were synthesized ($D_{Pore} = 521.4 \pm 66.8\ nm$, *N* = 190). The definition of this parameter is based on the observation that NTs tend to flatten once they are freed from their supporting template and collected over a substrate by filtration. NTs made of stiff, rigid materials will tend to deform less upon application of a pressure and show a lesser tendency to flatten compared to NTs composed of soft, flexible materials. Consequently, the diameter of stiff NTs will be less impacted by the filtration process and its value will be close to that of the template nanopores, leading to a flattening index close to ~ 1. On the contrary, the diameter of soft NTs will be greatly affected by the collection process and will tend to show increased values (compared to that of the template pores), which will result in a flattening index higher than 1. The flattening index might thus be used as an estimate of the stiffness of a population of NTs. The full distribution of the flattening index data recorded for the three nanotubular samples are summarized in Figure 5.14. The same observations can be made regarding this flattening index as those which were made about the rigidity index. Although no statistically significant difference can be highlighted between the medians of the three groups, their data dispersion is indeed different and tends to narrow down in the presence of colloids. Moreover, the same trend of a narrower distribution centered around a value close to 1 is found for both indices in the case of the composite tubes containing silica particles in their internal structure. Hence,

the straightest tubes are also the less flattened after filtration and probably the stiffest ones.

AFM and, more specifically, its PFT-QNM mode provides a more direct approach to undisputably determine the intrinsic mechanical stiffness of the synthesized NTs in a quantitative manner (*see* Th.A.5.VI.A). The nanometer-sized tip of the AFM cantilever can indeed enter in direct contact with the NTs surface and indent it to record its ability to elastically relax against the applied force. The compilation of these tip-sample interactions along the

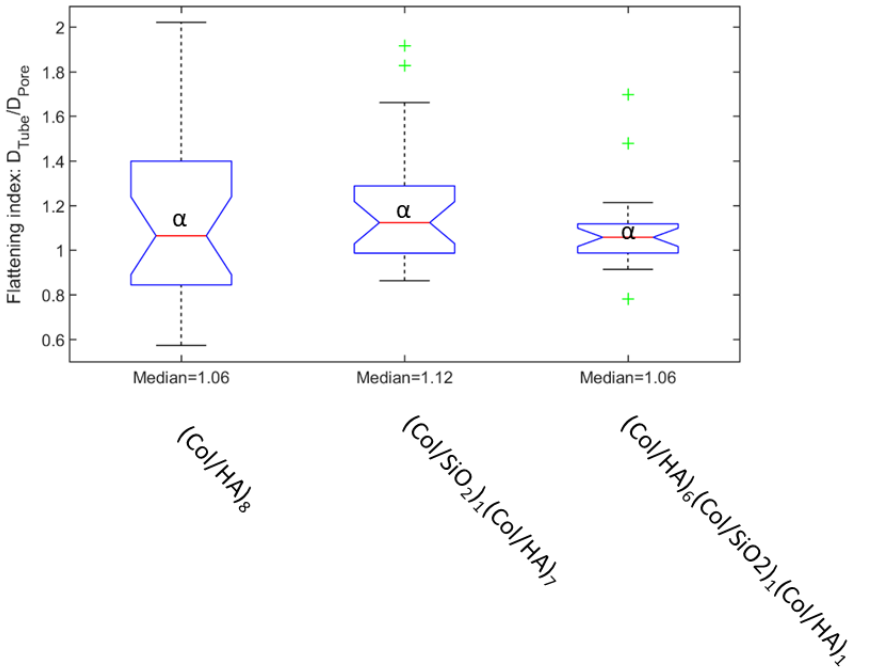


**Figure 5.14.** *Notched boxplot presenting the full distribution of the flattening indices,* $\frac{D_{Tube}}{D_{Pore}}$*, computed for different populations of individual NTs based on microscopy images: (Col/HA)₈ NTs containing no silica NPs, (Col/SiO₂)₁(Col/HA)₇ NTs containing silica NPs in their outermost bilayer and (Col/HA)₆(Col/SiO₂)₁(Col/HA)₁ NTs with silica NPs in one of their innermost bilayers. The red line displays the median of each population (N=25), the length of the whiskers represent 1.5 x interquartile range (IQR), the width of the notches represent the 95% confidence interval on the median while outliers are represented by the green '+' signs. Bars topped with different Greek letters indicate significant difference of the mean (p-value < 0.05 as computed via consecutive Welch's ANOVA and Games-Howell post hoc test).*

complete indentation-withdrawal cycle of the AFM probe generates force versus distance curves whose collection along the whole NTs length can in turn provide a comprehensive overview of the NTs elastic properties at the nanoscale. The NTs whose mechanical properties are explored in the frame of this thesis being supported over a PET filter, a relative elasticity modulus is reported which takes into account the potential influence of the underlying substrate on the stiffness values measured along the NTs. The Young's modulus of the PET foil used by it4ip to produce the filtration membranes being 4 GPa (as announced by the manufacturer's product datasheets), this value was used as an internal standard. During the offline treatment of the collected force/distance curves to extract the mechanical properties of interest, the value of the tip radius of curvature (*R*) was indeed tuned so as to find an average Young's modulus of ~4 GPa on the PET phase of each sample. The *R* value obtained for the PET phase was then kept constant when extracting the moduli of the NT phase, in a way to limit the systematic error.

The distribution of the relative modulus, $\frac{E_{NT}}{E_{PET}}$, of the three types of NTs synthesized, extracted from the nanoindentation tests is presented in Figure 5.15. Representative pictures of the NTs as recorded by the topography channel of AFM are displayed in S.I. (*see* S.I.5.2). Conduction of consecutive Welch's ANOVA and Games-Howell post hoc statistical analyses demonstrates that both the mean and median of the relative modulus of silica-strengthened NTs do differ from those of the native (Col/HA) NTs. By contrast, no difference can be highlighted between the two composite systems. Therefore, it can be fairly concluded that the addition of inorganic colloids within the assembly of NTs based on ECM-derived biopolymers do significantly increase the stiffness of the resulting NTs, although the location of these NPs (i.e., within the most external or internal layers) do not further influence their mechanical properties. Assuming an average Young's modulus of 4 GPa for the supporting PET substrate (as announced by the manufacturer), a numerical value of ~4.5 and ~6.2 can be estimated for the Young's modulus of the biopolymer-based and composite NTs, respectively. One has to keep in mind that these numerical values should only be considered with caution given that the influence of the underlying PET substrate on the modulus measured on the NTs cannot be totally ruled out, even if all the values were averaged by the modulus found for the PET phase. Only the relative modulus is thus deemed accurate.

Comparing the data distribution of the AFM indentation tests (Figure 5.15) with that of the morphological indices (Figure 5.13 & 5.14), one can argue that an inverse trend is observed: while the dispersion of the data set is reduced upon infiltration of ceramic particles in the case of morphological indices, it increases in the case of AFM experiments. Although this might appear surprising at first, this observation might be accounted for by the fact that while morphological indices gauge the complete NT at the microscale, the AFM probes the NT properties at the nanoscale. Hence, larger discrepancies are observed when testing composite NTs via AFM because the measured modulus will drastically vary depending on whether the probe lands on a ceramic-rich zone or a biopolymer-rich zone of the same NT.

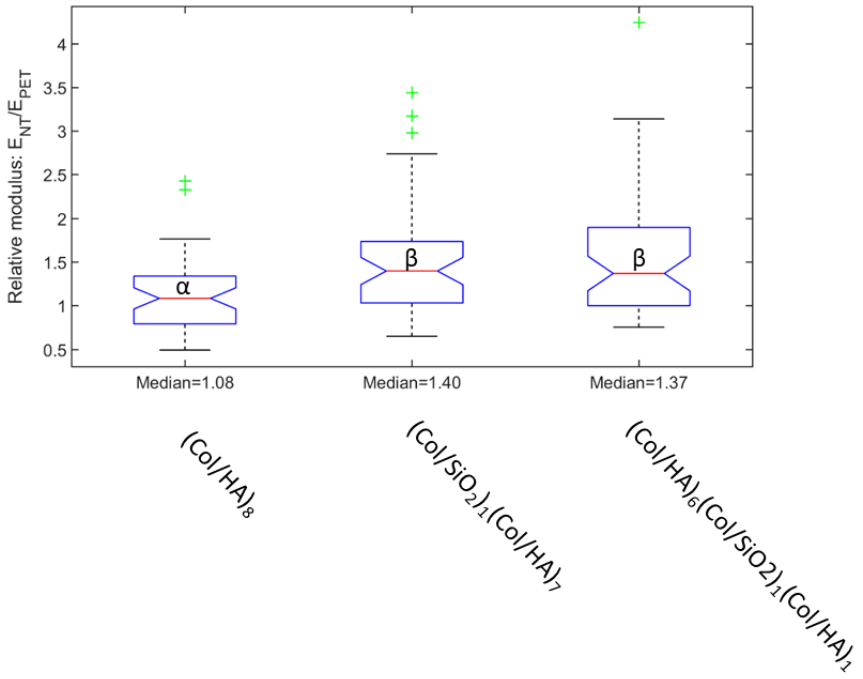


**Figure 5.15** *Notched boxplot presenting the full distribution of the relative modulus, $\frac{E_{NT}}{E_{PET}}$, computed for different populations of individual NTs based on AFM force-distance curves: $(Col/HA)_8$ NTs containing no silica NPs, $(Col/SiO_2)_1(Col/HA)_7$ NTs containing silica NPs in their outermost bilayer and $(Col/HA)_6(Col/SiO_2)_1(Col/HA)_1$ NTs with silica NPs in one of their innermost bilayers. The red line displays the median of each population (N=50)., the length of the whiskers represent 1.5 x interquartile range (IQR), the width of the notches represent the 95% confidence interval on the median while outliers are represented by the green '+' signs. Bars topped with different Greek letters indicate significant difference of the mean (p-value < 0.05 as computed via consecutive Welch's ANOVA and Games-Howell post hoc test).*

### 5.2.3 Towards biomineralized ECM-like interfaces

The nanocomposite biointerfaces synthesized in this work share many similarities with the native ECM of bone as bone is itself a natural biocomposite material[3,4], composed of a soft organic phase (mainly Col) mineralized with hard inorganic crystals (i.e., carbonated hydroxyapatite nanocrystals, of chemical formula $Ca_{10}(PO_4)_6(OH)_2$).[4,5] Hydroxyapatite (HyAp) crystals thus play the role of stiffening agent in the bone matrix, in a manner similar to how colloidal silica particles stiffen the biomimetic multilayers in our systems. In order to further increase the bio-mimicry of the synthesized matrices, it would be highly advantageous to substitute the bioinert $SiO_2$ NPs with bioactive HyAp crystals. In addition to its role of mechanical support, HyAp has indeed been documented to be osteoinductive (i.e., meaning that it has the ability to promote the differentiation of osteogenic progenitor cells into mature bone-forming cells).[6,7] *In vitro*, the synthesis of HyAp crystals is mainly achieved through the co-precipitation of calcium ions with inorganic phosphate ions under alkaline conditions.[8–11] Another approach involves the maturation of the substrate to be functionalized with HyAp within simulated body fluid (SBF; solution whose ionic composition is close to that of human blood plasma, with the purpose to mimic the native bone-forming environment).[12–14] A biomimetic method of interest, yet only scarcely reported in the literature, consists in taking advantage of enzymes whose natural purpose is to produce inorganic phosphate. Alkaline phosphatase (ALP) is one of these enzymes and is present in different tissues (e.g., bone, liver, kidney, intestinal mucosa, etc.) where it is embedded in the external face of the cell membrane.[15–17] ALP is actually the main enzyme responsible for the mineralization of the Col phase in bone tissue. It catalyzes dephosphorylation reactions under alkaline conditions and generates an alcohol and an inorganic phosphate, according to the following chemical equation[18,19]:

$$R\text{-}PO_4^{2-} + H_2O \rightarrow R\text{-}OH + HPO_4^{2-}$$

The produced phosphate ions can further precipitate with calcium ions to yield HyAp crystals.

*a) Functionalization of nanostructured interfaces via chemical precipitation of calcium phosphate (CaP) particles*

According to a protocol reported by Ngiam *et al.*, HyAp nanocrystals can be nucleated on a chosen interface by alternately dipping it into a solution of calcium ions (0.5 M $CaCl_2$, pH 7.2) and of phosphate ions (0.3 M $Na_2HPO_4$, pH 8.96).[20,21] The authors thoroughly analysed the mineral phase obtained through this alternate dipping process and concluded that it consisted in bone-like apatite. Given the strong alkaline conditions required for the synthesis of HyAp under this approach, attempts to use it to nucleate HyAp within (HA/Col) during their LbL assembly were unsuccessful. Indeed, the synthesized HyAp was found to largely dissolve once brought under conditions compatible with the LbL assembly of (HA/Col) (i.e., pH 4) whereas attempts at conducting the LbL assembly of (HA/Col) under alkaline conditions equally failed (data not shown). Replacing the silica particles in their role as strengthening agent was thus impossible using this strategy. However, it was possible to use this alternate dipping approach to functionalize the surface of chemically cross-linked systems, such as the composite biointerfaces produced in this chapter or biofunctionalized PPy frameworks (Figure 5.16). Figure 5.17 displays an example of such a PPy framework functionalized with chemically precipitated HyAp crystals.

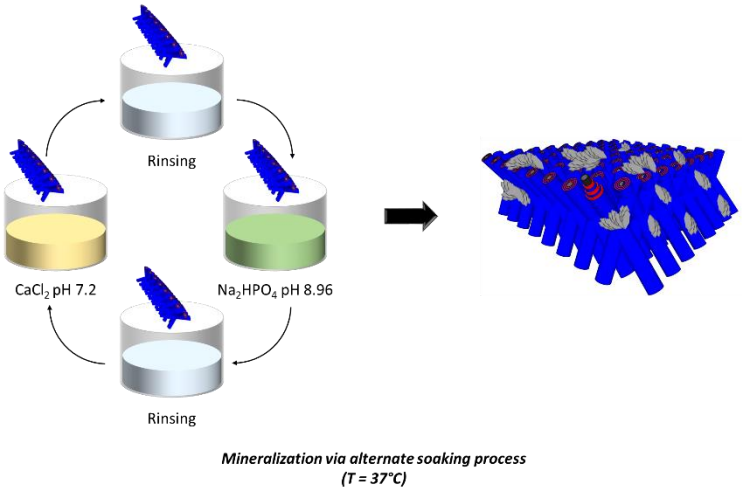


**Figure 5.16** *Schematic illustration of the alternate soaking process used to precipitate HyAp particles on the surface of biointerfaces.*

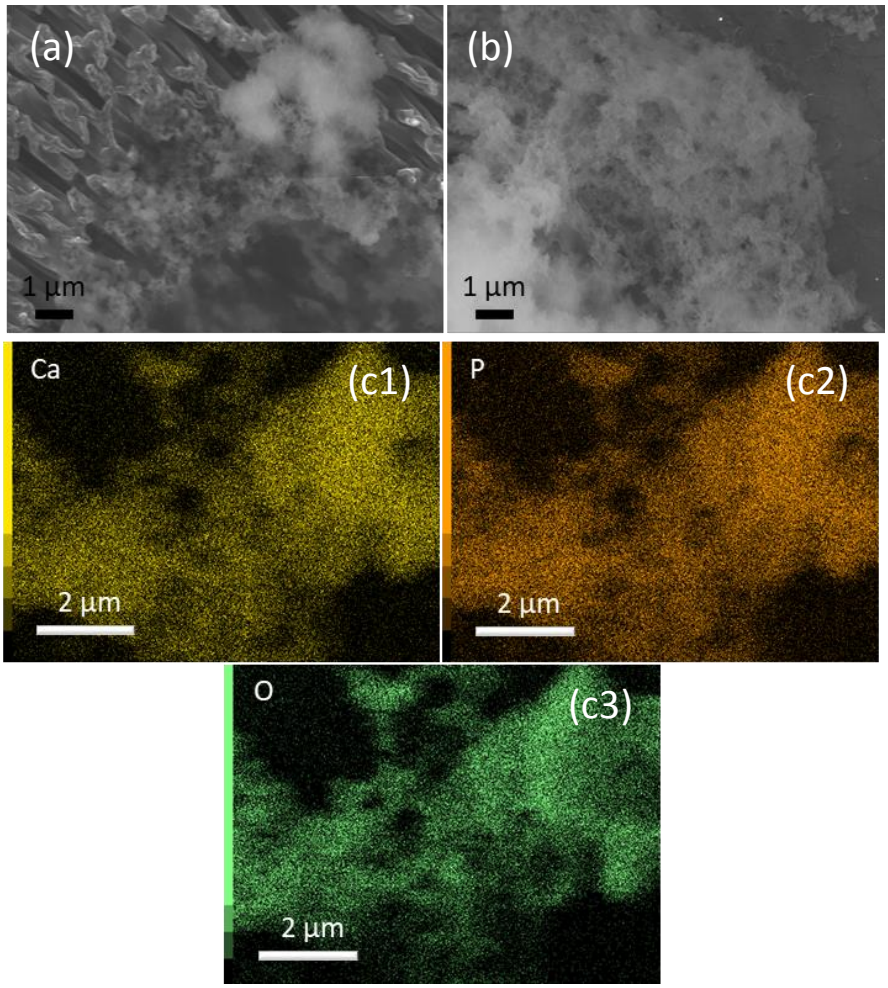


**Figure 5.17** *(a) SEM pictures showing the surface of a PPy framework functionalized with HyAp crystals following the alternate dipping method. (b) Image showing an aggregate of HyAp particles with a characteristic platelet morphology. (c) EDX mapping of an HyAp aggregate showing the signal of (c1) calcium, (c2) phosphore and (c3) oxygen.*

## *b) Biomineralized ECM-like nanocomposite interfaces*

Within the frame of her thesis, E. Colaço *et al*.[22] evidenced that the isoelectric point of ALP being around 5, it was possible to immobilize it into multilayered assemblies in combination with a polycation under alkaline conditions, while preserving its activity. Once provided with an adequate substrate (such as α-glycerophosphate), a source of calcium ions and brought under conditions favoring its optimum activity (i.e., alkaline pH in the range 7-9 and physiological temperature), ALP can nucleate HyAp crystals *in situ* and thus mineralize the supramolecular architecture, in a process much similar to that occurring naturally *in vivo* (in bone tissue, for instance). Templating the ALP/PAH assembly inside PC templates with intersected nanopores , gave rise to highly mineralized nanocomposite interfaces, clearly displaying HyAp nanocrystals with a platelet morphology (Figures 5.18 & 5.19).

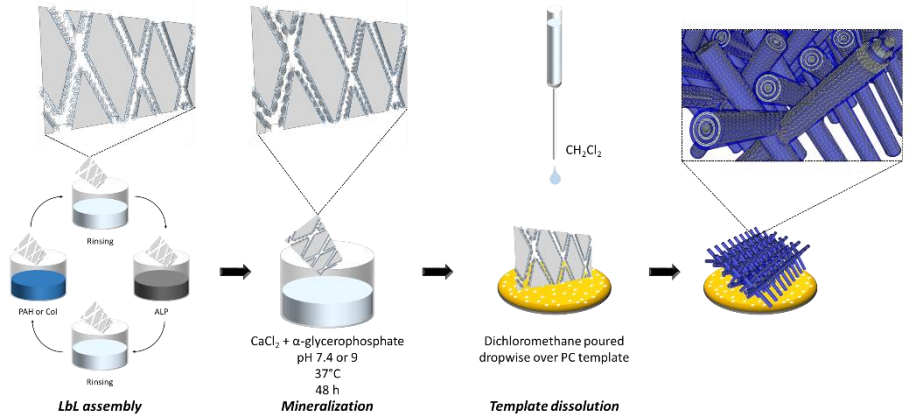


**Figure 5.18** *Schematic illustration of the biomineralization process used to nucleate HyAp nanocrystals within a templated polymeric multilayer. The ALP enzyme is first introduced as a component of the LbL assembly. The resulting templated multilayer is then incubated in a mineralization solution at 37°C for 48 h. The template is finally dissolved using dichloromethane, revealing a biomimetic HyAp/(bio)polymer interface.*

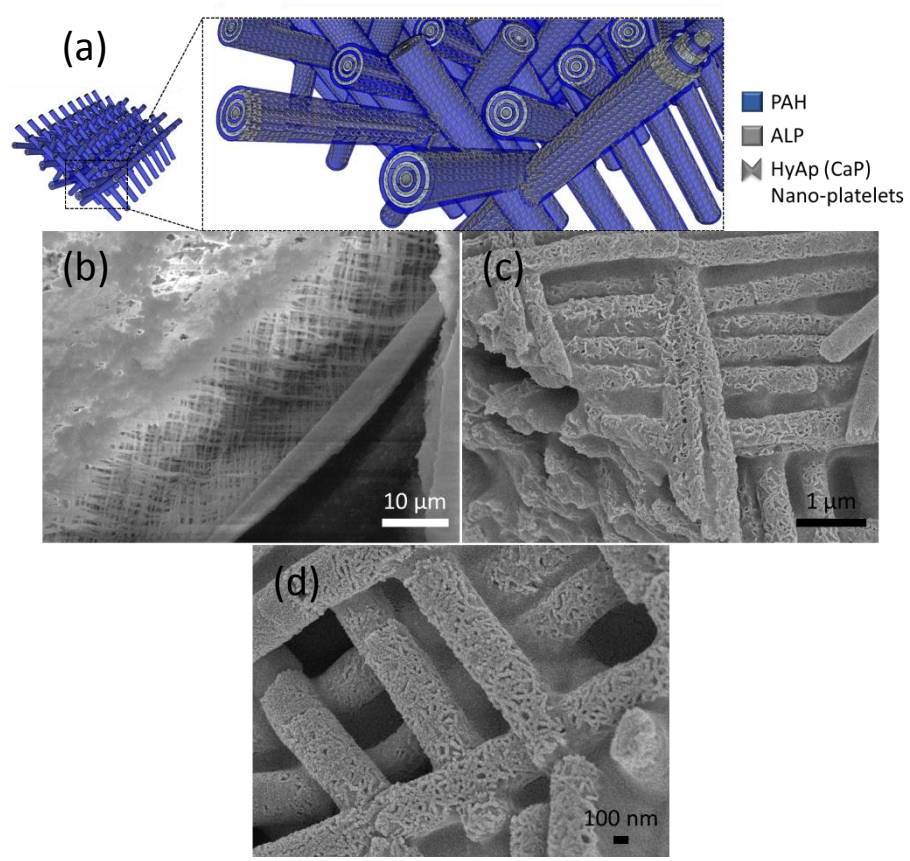


**Figure 5.19** *Biomineralized network of intersected $(PAH/ALP)_5$ NTs: (a) schematic illustration. (b, c, d) SEM images at increasing magnification of the template-freed biomineralized interfaces: lateral view of the network, showing numerous intersections between NTs (b); medium magnification picture of the network edge (c); high magnification picture of the HyAp/CaP platelets constituting the NTs (d).*

In order to further increase the biomimicry of these biomineralized systems, we managed to self-assemble Col and ALP, alternating the deposition pH between 4 (when depositing Col) and 9 (when depositing ALP), which resulted in fully biomimetic composite interfaces (Figure 5.20). Due to their high content in ceramic, both systems displayed in Figures 5.19 & 5.20 are, however, highly brittle.

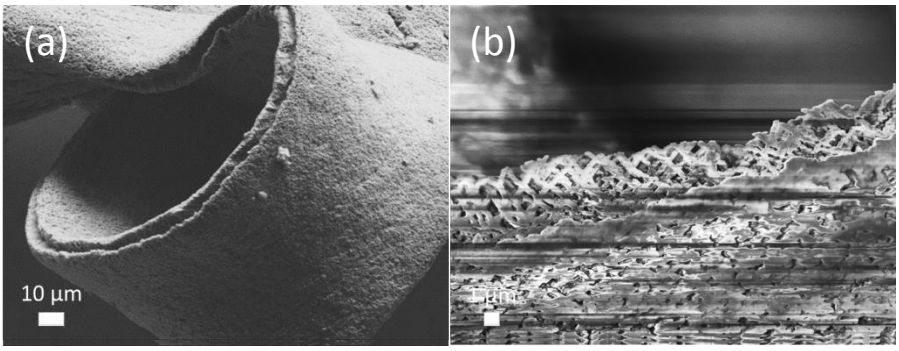


**Figure 5.20** SEM pictures of fully biomimetic $(Col/ALP)_5$ nanocomposite interfaces

## 5.3 Conclusions

Silica nanocolloids are evidenced to be incorporated in LbL assemblies as a negatively-charged counterpart to Col molecules via electrostatically-enhanced sedimentation. The resulting $(Col/SiO_2)_1$ $(Col/HA)_x$ composite assembly is demonstrated to proceed gradually until, at least, the 7$^{th}$ (Col/HA) bilayer and can be alternatively templated within PC membranes with parallel or intersected nanopores to produce composite NTs or biointerfaces, respectively.

The filtration of silica NPs within biopolymer-based NTs clearly compensates for the weak mechanical properties of the highly flexible polymer materials and creates composite NTs and biointerfaces made thereof which are less impacted by the template dissolution and collection processes, therefore yielding nanostructures of improved mechanical stability. This is confirmed both by the visual observation of more robust composite tubes and interfaces as compared to the unorganized entanglement of polymer threads imaged in the absence of the silica phase and by the homogenization of the tubes morphology after $SiO_2$ incorporation as gathered by the narrowing spread of the data obtained for both morphological indices. Furthermore, the elasticity modulus of composite NTs, as measured via AFM nanoindentation, is unambiguously 38% higher than that of native ECM-derived $(Col/HA)_8$ NTs.

Well-ordered nanocomposite biointerfaces of ~25 µm height could be reproducibly produced. The number of biopolymer (Col/HA) layers built past the preliminary $(Col/SiO_2)_1/(Col/HA)_2$ multilayer has little to no effect on the mechanical properties of the resulting NTs, as highlighted by the similarity between the $(Col/SiO_2)_1(Col/HA)_2$ and $(Col/SiO_2)_1(Col/HA)_7$ biointerfaces. Hence, the stacking of a high number of polymer layers is not sufficient to impart enhanced mechanical stability to the NTs and the resulting effect, if any, is by no means comparable to the beneficial effect of adding a silica phase. Similarly, microscopic observations and mechanical properties estimates evidenced that the location of the colloids within the ECM-derived NTs, inside either the innermost or outermost layers, does not influence the stiffness of the resulting nanostructures.

Although the engineered nanocomposite biointerfaces do share similarities with the ECM of mineralized tissues, such as bone and tooth, and feature as well a wide range of potentially tunable properties whose effect on cellular behaviour would be thrilling to investigate, the nanostructures are yet too fragile to be easily detached from the supporting substrate upon which they are laid once freed from the PC template. Among the set of tunable cues displayed by the synthesized artificial matrices and most likely to influence cell fate, we can cite: the mechanical properties which could potentially be varied by fine-tuning the concentration and number of layers of $SiO_2$ NPs incorporated; the chemical composition of the nanotubular blocks as another pair of ECM-derived biopolymers could be used as starting materials; the average diameter of the intersected NTs, leading to a variation of the nanotopography presented to the hosted cells and, finally, the nature of the valuable cargo (e.g., growth factors, cytokines, etc.) which could potentially be incorporated within the NTs either via passive diffusion or filtration through the NTs internal cavity or via preliminary incubation with silica colloids and adsorption on their surface.

The composite structures are not self-supported and, consequently, the influence of the underlying substrate could not be totally ruled out in the event of cellular tests. Moreover, if the engineered matrices would have to be detached from their substrate only to be laid over another support better suited for cellular assays, the integrity and homogeneity of the nanotube arrays could not be guaranteed which would further negatively impact the conclusions of the cellular investigations. Given that they do not fulfil the requirement of an easy to handle, self-supported biomaterial, the ability of

the composite ECM-like matrices to sustain cellular adhesion, proliferation and differentiation was not investigated further in this thesis.

Even though the foreseen applications in tissue engineering and regenerative medicine might be out of reach at this point, the engineered artificial matrices still offer outstanding opportunities as multifunctionalizable nanostructured platforms bridging the gap between mechanical stability and preservation of the bioactivity of native biomacromolecules. The tremendously high specific surface area of these matrices, developed both at the microscale by the well-ordered array of intersected NTs they are made of and at the nanoscale, by the high amount of silica colloids contained in each tubular building block, could be taken advantage of in the following applications:

- Provided that $SiO_2$ NPs are proven biocompatible, they could be pre-incubated with valuable drugs, so as to create complexes, before being integrated in the LbL assembly of the nanotube arrays which could then be used as implantable or skin-contacting drug-delivery platforms with a high exchange surface area.
- Similarly, functionalizing the colloids with proteins known to bind a specific ligand with high affinity (i.e., enzymes, antibodies, etc.) and finding a way to translate the binding event into a detectable signal (e.g., an electrical signal) could lead to opportunities of using the synthesized frameworks as biosensing devices with high sensitivity. Such interfaces could also be used *in vitro* as highly sensitive membranes for immunoassays (e.g., ELISA, etc.).
- Usage of the composite nanostructures as nanocatalytic platforms enabling the high-throughput transformation of pollutants or the synthesis of products of high added value could also be considered, provided that the colloidal inorganic phase is adequately functionalized.

## Highlights of the chapter

- Electrostatically driven LbL assembly of nanocomposite $(Col/SiO_2)_1(Col/HA)_2$ biointerfaces of ~25 μm height with preserved integrity as compared to full (bio)polymer interfaces
- Elasticity modulus of composite NTs ~38 % higher than that of native ECM-derived $(Col/HA)_8$ NTs
- Mechanical properties of the nanostructures apparently independent of the location of the silica phase within the biopolymer multilayer
- Mechanical properties of the nanostructures apparently independent of the number of $(Col/HA)_x$ layers built past the $(Col/SiO_2)_1(Col/HA)_2$ assembly
- Sucessful synthesis of LbL-assembled enzyme-based NTs (i.e., ALP/PAH or Col/ALP) followed by *in situ* biomineralization of HyAp nanocristals, leading to bone ECM-like biointerfaces

## 5.4 Experimental section

***Materials:*** ion track-etched PC membranes with a thickness of 21 µm, a pore density of $4x10^7$ pores.cm$^{-2}$, and an average pore diameter of 500 nm were used as template for the fabrication of individual NTs. Interfaces of intersected NTs were synthesized through LbL assembly within PC templates with a thickness of 25 µm, showing a network of 300 nm diameter nanopores intersecting at a controlled angle of ~90°, with a density of $2.8x10^8$ pores.cm$^{-2}$. Nanoporous PC templates were kindly supplied by it4ip. Dried sodium hyaluronate (HA, $M_W$ ~ 151-300 kDa) was purchased from Lifecore Biomedical. Type I collagen G from bovine calf skin (Col, 0.4% solution in 15 mmol $L^{-1}$ HCl, 4 mg.mL$^{-1}$) was purchased from Merck-Millipore. Cross-linking agents, 1-(3-dimethylaminopropyl)-3-ethylcarbodiimide hydrochloride (EDC, 98+%) and *N*-hydroxysulfosuccinimide sodium salt (s-NHS, ≥98%) were purchased from Acros and Sigma-Aldrich, respectively. Sodium chloride (NaCl, ACS reagent, ≥99%) and hydrochloric acid solution (HCl, 0.1 N in aqueous solution) were purchased from Sigma-Aldrich, while sodium hydroxide solution (NaOH, 0.1 N in aqueous solution) was bought from VWR. Poly(allylamine hydrochloride) (PAH, $M_W$ ~ 15 kDa), α-Glycerol phosphate magnesium salt hydrate (~ 85%) and alkaline phosphatase from bovine intestinal mucosa (ALP, ≥ 10 U/mg) were bought from Sigma-Aldrich. Sodium phosphate, dibasic ($Na_2HPO_4$) (~98%) was purchased from Acros. Spherical silica colloids ($SiO_2$ NPs, LUDOX® TM-50 colloidal silica 50 wt.% suspension in $H_2O$, average diameter ~ 25 nm) were bought from Sigma-Aldrich. PET membranes, used for filtration purposes and as substrate for microscopical analysis, were supplied by it4ip and had an average pore diameter of 200 nm, a thickness of 23 µm and a pore density of $5.8x10^8$ pores.cm$^{-2}$.

***Monitoring of the electrophoretic mobility (EPM) of (bio)polymers and colloids:*** EPM measurements were carried out at 22 °C using a Malvern Zetasizer nanoZS (DTS1061, Malvern Instruments Ltd, UK). The results are presented as the mean and standard deviation of three to five replicates. The biopolymers HA and Col and the $SiO_2$ NPs were respectively solubilized and dispersed in ultrapure water or a 0.15 M NaCl aqueous solution, to reach a final concentration of 1 mg.mL$^{-1}$ (for the biopolymers) and 1 wt% (for the

NPs). The pH of the solutions and dispersion was subsequently adjusted using HCl 0.1 N or NaOH 0.1 N. The performance of the instrument was systematically verified (every six samples) using a zeta potential standard solution (Malvern, DTS1232).

***In-situ monitoring of the nanocomposite LbL assembly*:** The capacity of the chosen biopolymers and colloids to interact with each other and self-assemble was monitored on reference substrates using quartz crystal microbalance with dissipation monitoring (QCM-D). The LbL construction was carried out on gold-coated quartz crystals [AT-cut 5MHz crystals coated with 100 nm Au, Q-Sense, Gothenburg (Sweden)]. Crystals were first cleaned in a piranha solution [$H_2O_2$ 30% (Prolabo, VWR, Leuven, Belgium)/$H_2SO_4$ 95% (Prolabo; VWR, Leuven, Belgium), 1:2 v/v] for 20 min, before being thoroughly rinsed with ultrapure water and dried under nitrogen flow. All measurements were performed in a Q-Sense E4 system (Gothenburg, Sweden) following the same protocol: resonance frequencies of the crystals were obtained under buffer for the different overtones, and the shifts of frequency (Δf) and of dissipation (ΔD) were both monitored as a function of time upon stepwise injection of each biopolymer and colloidal partner. The flow was set at 30 $\mu L.min^{-1}$ using a peristaltic pump, while the temperature was set at 25 °C. The solutions of either Col, HA, or the colloidal dispersion of $SiO_2$ were alternately injected in the system and allowed to adsorb on the crystals surface during 1 h. Each adsorption step was then followed by a rinsing step, conducted in the corresponding pH-adjusted solution for at least 30 min. Dissipation and frequency shifts recorded for the $5^{th}$ overtone are displayed in this dissertation.

***Synthesis of biomimetic nanocomposite interfaces:*** Col solutions were prepared at a final concentration of 1 $mg.mL^{-1}$ by diluting the stock solution in a 0.15 M NaCl aqueous solution. The pH of the resulting solution, initially measured to be around 2.56, was further adjusted at 4.0 (using NaOH 0.1 N). HA solutions were prepared by dissolving the appropriate amount of weighed HA powder into a 0.15 M NaCl aqueous solution. Initial pH of the solution, measured at ~ 4.54 was further adjusted at 4.0 (using HCl 0.1 N). Colloidal silica dispersion, initially 50 wt% in pH 9 buffer, was diluted to 1 wt% by simple mixing of 1 mL of stock dispersion (50 wt%) with an appropriate mass of ultrapure water and further adjusted at pH 4.0. All solutions were freshly prepared and gently stirred for at least 20 min right before initiating the LbL assembly. The cross-linking solution was prepared, right before use,

by adding EDC and s-NHS at a final concentration of 100 $mg.mL^{-1}$ and 11 $mg.mL^{-1}$ respectively, to a 0.15 M aqueous solution adjusted at pH 4.0. In order to trigger the self-assembly of composite NTs, PC templates with either parallel or intersected nanopores were successively dipped in a solution of Col for 2 h, then rinsed for 10 min in the construction medium (0.15 M NaCl aqueous solution adjusted at pH 4.0), prior to being immersed in a solution of HA for 30 min. This process of alternate dipping of the nanoporous template in solutions of Col and HA was most commonly cycled 7 times, so as to produce 7 bilayers of the Col/HA pair. Incorporation of silica NPs in various locations of the tubular multilayer, either as one of the innermost or as one of the outermost layers, was accomplished by manual filtration of a small volume (most commonly 5 mL) of silica dispersion through the templated multilayer, using a glass syringe. Filtration of silica colloids was always carried out as counterpart to a previously-adsorbed Col layer, as the superficial negatively-charged oxide layer of silicon dioxide NPs was expected to electrostatically interact with collagen molecules, positively-charged under the studied conditions. The LbL deposition was carried out at 4 °C. Right after completion of the LbL construction, multilayer-filled templates were immersed in the cross-linking solution [EDC 100 $mg.mL^{-1}$ & s-NHS 11 $mg.mL^{-1}$ in 0.15 M NaCl pH 4.0] and stored at 4 °C for at least 48 h, following an adaptation of the protocol of Picart *et al*.[23-28] Samples were then transferred into the construction medium (NaCl 0.15 M pH 4.0) and stored at 4 °C until further characterization.

***Synthesis of intersected (PAH/ALP) interfaces and mineralization.*** PAH solutions were prepared at a final concentration of 1 $mg.mL^{-1}$ in UPW and further adapted to pH 7.4 or 9. ALP solutions were prepared at a final concentration of 0.1 $mg.mL^{-1}$ in UPW and further adjusted at pH 7.4 or 9. The mineralization solution was prepared by dissolving $CaCl_2$ and α-glycerophosphate into UPW to reach a respective final concentration of 11.4 mM and 6.8 mM. The pH of the mineralization solution was further adapted at 7.4 or 9. All solutions were freshly prepared and gently stirred for at least 20 min right before initiating the LbL assembly. The LbL assembly was carried out by alternately dipping the PC template into a solution of PAH for 30 min, rinsing twice for 2 min each in UPW pH 7.4 or 9, and then dipping the PC template into the ALP solution for 30 min. This process of alternate dipping was cycled five times so as to create 5 (PAH/ALP) bilayers. After each step of

incubation within a polymer solution, both faces of the template were gently rubbed with a cell scraper wetted by the construction medium, so as to prevent the formation of a polymer crust plugging the nanopores. The mineralization phase was initiated by immersion of the template containing the LbL-assembled NTs into the mineralization solution heated at 37°C. The mineralization reaction was left to proceed for 48 h under mild agitation in a water bath at 37°C. After completion of the mineralization phase, both faces of the samples were thoroughly decrusted and rinsed with UPW pH 7.4 or 9.

***Synthesis of intersected (Col/ALP) biointerfaces and mineralization.*** Col solutions were prepared at a final concentration of 1 $mg.mL^{-1}$ in 0.15 M NaCl aqueous solutions and further adapted to pH 4. ALP solutions were prepared at a final concentration of 0.1 $mg.mL^{-1}$ in UPW and further adjusted at pH 9. The mineralization solution was prepared by dissolving $CaCl_2$ and α-glycerophosphate into UPW to reach a respective final concentration of 11.4 mM and 6.8 mM. The pH of the mineralization solution was further adapted at 9. All solutions were freshly prepared and gently stirred for at least 20 min right before initiating the LbL assembly. The LbL assembly was carried out by alternately dipping the PC template into a solution of Col for 2 hours, rinsing twice for 2 min each in UPW pH 4, and then dipping the PC template into the ALP solution for 30 min. This process of alternate dipping was cycled five times so as to create 5 (Col/ALP) bilayers. After each step of incubation within a polymer solution, both faces of the template were gently rubbed with a cell scraper wetted by the construction medium, so as to prevent the formation of a polymer crust plugging the nanopores. Chemical cross-linking of the multilayers was initiated right after completion of the LbL construction. For that purpose, multilayer-filled templates were immersed in the cross-linking solution [EDC 100 $mg.mL^{-1}$ & s-NHS 11 $mg.mL^{-1}$ in 0.15 M NaCl pH 4.0] and stored at 4°C for at least 48 h, following an adaptation of the protocol of Picart et al.[23]Samples were abundantly rinsed in UPW before initiating the mineralization reaction.The mineralization phase was initiated by immersion of the template containing the LbL-assembled NTs into the mineralization solution heated at 37°C. The mineralization reaction was left to proceed for 48 h under mild agitation in a water bath at 37°C. After completion of the mineralization phase, both faces of the samples were thoroughly decrusted and rinsed with UPW pH 9.

***Sample preparation for structural analyses*:** Individual composite nanotubes were first released from their PC template by dissolution of the templating

membrane in dichloromethane ($CH_2Cl_2$, 99.8+% for analysis, stabilized with amylene, Acros Organics). In practice, small cut-outs (~ 2-3 $mm^2$) in the PC membrane containing the self-assembled NTs were immersed in a test tube containing 5 mL of dichloromethane and left aside for 10 min, ensuring complete dissolution of PC.

Prior to SEM analysis, the dispersion of NTs in $CH_2Cl_2$ was subsequently filtered over hydrophilic PET filters (200 nm pore size, pore density $5x10^8$ $pores.cm^{-2}$, thickness 23 µm, it4ip) prealably metallized, using a sputter coater (Cressington 208HR), with a chromium anchoring layer (3 nm) followed by a gold layer (20 nm). Metallized filters were introduced in the sample holder of a 5 mL syringe while the dispersion of NTs in dichloromethane was poured in the syringe and filtered. 5 mL of fresh dichloromethane were subsequently used to rinse the test tube and filtered through the device to maximize the NTs collection. The resulting NTs supported on metallized filters were left to dry overnight at room temperature before any further characterization.

Filtration of individual composite NTs prior to AFM analysis followed the same protocol, except that virgin PET membranes were used instead of metallized ones.

In anticipation of STEM and TEM analysis, the suspension of NTs in dichloromethane collected upon template dissolution was gently dropped on TEM grids consisting of a carbon film supported on a copper mesh grid (Agar Scientific Ltd).

Interfaces of intersected composite NTs were released from their template by placing the latter atop metallized PET filters before pouring large amounts of fresh dichloromethane (Vol. ~ 30 mL) dropwise over their surface until achieving complete dissolution of the PC.

***SEM and STEM observations*****:** The dimensions and morphology of the synthesized NTs and biointerfaces were studied by scanning electron microscopy (SEM) and scanning transmission electron microscopy (STEM).

STEM pictures were obtained using a thermal field emission scanning electron microscope (JSM-7600F, Jeol) operated at an acceleration voltage

of 30 kV under STEM mode (maximum resolution of 0.8 nm, making use of a TED detector).

SEM pictures were obtained using the same microscope operated at an acceleration voltage of 15 kV under SEM mode (maximum resolution of 1.0 nm using a secondary electron imaging detector).

***TEM observations and energy dispersive X-ray spectroscopy (EDX):*** TEM pictures were obtained using a LEO 922 transmission electron microscope (Carl Zeiss SMT Inc.) operating at 200 kV. EDX experiments were carried out with the LEO 922 TEM equipped with an INCA x-sight detector (Oxford Instruments).

***Adsorbed protein mass quantification:*** The total protein content of the nanocomposite interfaces was quantified using a Micro BCA™ Protein Assay Kit (Thermo Scientific). This kit allows dilute protein concentrations (0.5-20 µg/mL) to be determined, relying on the colorimetric detection of cuprous ions ($Cu^{+}$), produced through the reduction of $Cu^{2+}$ ions by proteins under alkaline conditions. Briefly, the kit protocol was adapted as follows: the composite samples supported on virgin PET filters were first immersed in test tubes filled with 1 mL of pH 11.25 buffer (MA reagent of Micro BCA™ kit, Thermo Scientific. Probable composition [Ref.4.7.a]: aqueous solution of 8% $Na_2CO_3.H_2O$, 1.6% NaOH, 1.6% $Na_2$ tartrate and sufficient $NaHCO_3$ to adjust the pH to 11.25) containing 1% v/v sodium dodecyl sulfate (SDS), thoroughly vortexed and incubated for 2 h at 60 °C in a water bath, so as to trigger the deconstruction of the Col/HA multilayer and the solubilisation of the Col protein. After solubilisation of the multilayer compounds, 1 mL of working reagent was added to each tube, which was consecutively vortexed and incubated 1 h at 60 °C. The working reagent itself was freshly prepared by mixing a bicinchoninic acid (BCA) solution (MB reagent of Micro BCA™ kit, Thermo Scientific. Probable composition [Ref.4.7.a]: 4% BCA-$Na_2$ in deionized water) playing the role of detection reagent for $Cu^{+1}$, with an alkaline buffer (reagent MA), a $Cu^{2+}$ solution (MC reagent of Micro BCA™ kit, Thermo Scientific. Probable composition [Ref.4.7.a]: aqueous solution of 4% $CuSO_4.5H_2O$) and SDS in the proportions 50/47/2/1 % v/v. After 1 h of reaction, the tubes were cooled to room temperature, and thoroughly vortexed before 1 mL of each sample-specific tube was transferred to a cuvette whose absorbance was read at 562 nm using a UV/Vis. Spectrophotometer. Collagen standards with a concentration ranging from

3.125 µg/mL to 100 µg/mL were prepared by successive dilution of a Col stock solution (4 mg/mL) in a 1% v/v SDS solution in the kit pH 12 buffer. A standard curve, relating each standard absorption at 562 nm to its known Col content, was finally plotted and used to infer the Col content of the composite samples. The absorbance of a virgin PET membrane, containing no protein and incubated in the working reagent, was used as blank and substracted from the 562 nm reading of all other samples. All samples absorbance was measured within 10 min.

***Morphological indices computation:*** The rigidity $\frac{R_{EE}}{L}$, and flattening $\frac{D_{NT}}{D_{Pore}}$, indices were computed based on SEM pictures of, at least, 25 individual NTs (N = 25) for each type of sample ((Col/HA)$_8$, (Col/SiO$_2$)$_1$(Col/HA)$_7$ and (Col/HA)$_6$(Col/SiO$_2$)$_1$(Col/HA)$_1$ NTs). The rigidity index of each individual NT, $\frac{R_{EE}}{L}$, is computed as the ratio between the end-to-end distance of the NT ($R_{EE}$, defined as the length of the shortest segment joining the two opposite ends of the NT) and the contour length of the NT (*L*, computed as the sum of the lengths of *n* individual segments, with *n* tending to infinity, drawn along the middle of a NT, perpendicular to its main axis, from one end to the other). The flattening index of each individual NT, $\frac{D_{NT}}{D_{Pore}}$, is itself computed as the ratio between the diameter of the NT ($D_{NT}$) and the diameter of the template pores in which they were grown ($D_{Pore} = 521.4 \pm 66.8\ nm$, N = 190).

***AFM force-distance spectroscopy and nanomechanical property mapping:*** Elastic modulus of composite NTs was estimated using the Peak Force Tapping Quantitative Nanomechanical Mapping (PFT-QNM) AFM mode equipped on a Bruker Dimension-Icon system. TESPA probes from Bruker were used for all measurements. The calibration process was carried out as follows: the spring constant (k) for each probe was determined via thermal tuning (25.9777 N/m). The deflection sensitivity (82.31 nm/V) was obtained by imaging a silicon wafer, while the Sync. Distance QNM (81 nm) and the PFT amplitude were calibrated on a sapphire reference sample, all reference samples being provided by Bruker. A relative calibration method was used to determine the radius of curvature (*R*) of the tip apex. In practice, the tip radius parameter was adapted so as to measure an elastic modulus ~ 2.7 GPa for a reference polystyrene (PS) sample, while the sample deformation was kept to a value of about 3-4 nm when indenting the PS reference. The

obtained tip radius can then be kept constant when imaging the samples of interest, provided the deformation of the sample is kept constant at ~ 3-4 nm via adaptation of the PeakForce setpoint. The calibrated parameters were kept constant for further mapping along the samples surface. Force-distance curves were systematically recorded on areas of interest along each sample, and later treated using the Nanoscope and Igor softwares to estimate the sample's Young modulus. The Young's modulus of the PET foil used by *it4ip* to synthesize the filtration membranes being announced at 4 GPa (manufacturer's datasheets, Lumirror 40.60 PET foil, Hirosugi-Keiki Co., Ltd), this reference was used as an internal standard in a way to further limit the systematic error. In practice, during the offline treatment of the force curves recorded along the NT samples, the value of the tip radius of curvature (*R*) which is a parameter calibrated using a relative method was varied so as to obtain an average Young's modulus equal to ~4 GPa on the PET phase of each sample. The *R* value determined for the PET phase was then kept constant while treating the curves recorded along the NTs.

***Statistical analyses:*** The full distribution of both morphological indices and of the relative modulus is presented as a boxplot in Figures 5.13, 5.14 & 5.15. The central red line within the box corresponds to the median of the population, while the bottom and top edges of the box indicate the 25$^{th}$ (first quartile, $Q_1$) and 75$^{th}$ (third quartile, $Q_3$) percentile of the data, respectively. The length of the whiskers is defined as 1.5 x IQR (interquartile range, difference between the 75$^{th}$ and 25$^{th}$ percentiles, IQR = $Q_3$ - $Q_1$). The bottom whisker thus extends from the bottom edge of the box ($Q_1$, 25$^{th}$ percentile) down to the $Q_1$ - 1.5 x ($Q_3$ - $Q_1$) value, while the top whisker extends from the top edge of the box ($Q_3$, 75$^{th}$ percentile) up to the $Q_3$ + 1.5 x ($Q_3$-$Q_1$) value. Data points superior or inferior to these limits are displayed as outliers (green '+' signs). The notches around the median value illustrate the limits of the 95% confidence interval around the median, computed as: $median \pm 1.57 \times \frac{(Q_3-Q_1)}{\sqrt{N}}$, where *N* is the number of data points. The absence of any overlap between the notches of two boxes evidences a statistically significant difference between the medians of the two populations.

***Chemical precipitation of CaP particles via alternate dipping.*** A 0.5 M $CaCl_2$ aqueous solution was prepared and adapted at pH 7.2. A 0.3 M $Na_2HPO_4$ aqueous solution was prepared and adapted at pH 8.96. Both solutions were thoroughly mixed and incubated at 37°C in a water bath. The interface to be

functionalized with CaP particles was alternately dipped in the 0.5 M $CaCl_2$ solution for 30 min, rinsed in UPW for 10 min and then immersed in the 0.3M $Na_2HPO_4$ solution for 30 min. This sequence constituted one cycle which was repeated 3 times for each sample. The whole process was carried out under mild agitation at 37°C.

# Supporting information 5

## S.I.5.1 LbL assembly of polymer/ceramic composite NTs

A set of identified key parameters were first screened regarding their influence on the successful production of mechanically strengthened NTs based on synthetic PEs and incorporating silica NPs as toughening agent. The morphology of synthetic NTs built with a varying concentration of $SiO_2$ NPs, incorporated either via passive (i.e., dipping) or forced (i.e., filtration) diffusion, whether in the innermost or outermost layers of the tubular multilayer and subsequently chemically cross-linked or not, was investigated by SEM and STEM and visually compared.

The basic system consisting of unstiffened NTs fully composed of synthetic PEs is shown in Figure S5.1 as a means of visual control.

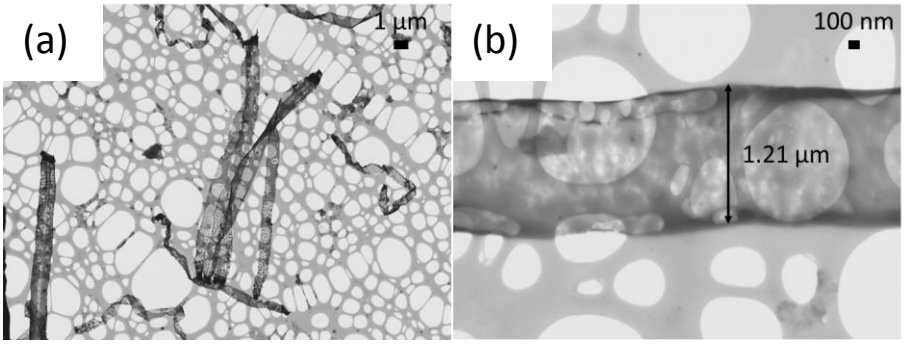


**Figure S5.1** *STEM pictures of synthetic $(PAH\text{-}FITC/PAA)_6$ NTs at low magnification (a), and high magnification (b).*

### *a) The importance of chemical cross-linking*

The insertion of a chemical cross-linking step at the end of the LbL self-assembly was discovered to be of prime importance to guarantee the mechanical integrity of the composite NTs upon dissolution of their supporting template and subsequent filtration. The non cross-linked NTs

(Figure S5.2.a-d) do not withstand the sum of forces applied to their surface after being collected from the template, among which are the positive pressure applied during the filtration step and the negative pressure exerted throughout imaging processes. As a result, the pictures captured show a ruptured morphology, with silica nanospheres ejected out of the broken tubular walls. On the contrary, cross-linked systems show walls with preserved integrity, efficiently retaining silica colloids within the assembly. Comparing native polymer NTs (Figure S5.1) with composite NTs (Figure S5.2), the successful incorporation of $SiO_2$ particles in the outermost layer of the latter is visually demonstrated, as the NTs surface appears to be fully decorated with colloids, yielding a granular texture. The integration of inorganic colloids in the multilayer is visibly effective at enhancing the stiffness of the NTs, to the point where NTs become so rigid that they tend to be brittle. The observation of multiple pieces of broken-down NTs is a sign of that brittleness. An effect directly related to the concentration of toughening colloids incorporated within the multilayer, another key parameter which has to be finely tuned, as will be discussed later. All other variables (colloid concentration, incorporation method, location of colloids, etc.) being held constant, chemical cross-linking thus helps preserving the mechanical stability of composite NTs. Being a step in the right direction of strong, self-supported NTs, chemical cross-linking will be systematically carried out on all succeeding samples, unless otherwise stated.

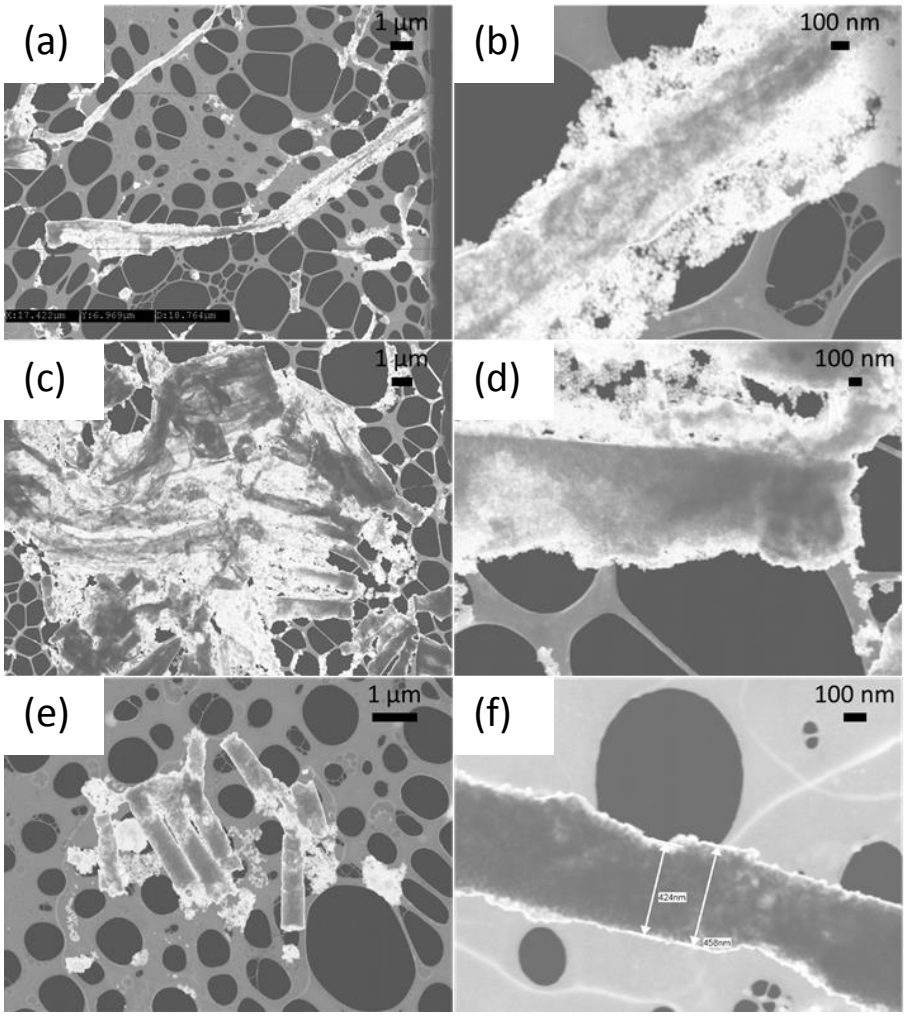


**Figure S5.2** *STEM pictures of non cross-linked synthetic NTs : $(SiO_2^{9.27\%dipping}$-PAH-FITC/PAA)$_3$(PAH/PAA)$_3$ (a, b), (PAH/PAA)$_3$($SiO_2^{9.27\%dipping}$-PAH-FITC/PAA)$_2$(PAH/PAA)$_1$ (c, d) and cross-linked synthetic NTs: ($SiO_2^{9.27\%dipping}$-PAH-FITC/PAA)$_3$(PAH/PAA)$_3$ (e, f). (left) low magnification, (right) high magnification.*

*b) Colloids incorporation method: passive versus forced diffusion*

Two different methods were investigated to efficiently infiltrate silica colloids and homogeneously distribute them within the growing multilayer. Passive diffusion consists in simply dipping the templated NTs in a colloidal suspension and allowing the NPs to slowly diffuse within the template nanopores owing to capillary forces, sedimentation and electrostatic interactions. On the other hand, filtration of the colloidal dispersion through the template pores was applied to some samples, as a way to speed up the diffusion process by applying a positive pressure. For a higher silica content, NTs obtained via passive diffusion show a much more tortuous morphology (Figure S5.3.a) than NTs containing a lower amount of filtered silica particles (Figure S5.3.c). When investigating the central lumen of NTs at high magnification, $SiO_2$ nanospheres are found to be less evenly distributed along the tube diameter for NTs obtained via dipping (Figure S5.3.b). Vacancies containing no silica particles can be found in some parts of the tubes, leading to a lower stiffness and more twisted morphology. Moreover, a lower packing density of colloidal spheres is also visible for NTs obtained via the passive diffusion process, even though a higher concentration of silica was engaged ($SiO_2$ 2.76 wt% and 1 wt% for dipping and filtration NTs,

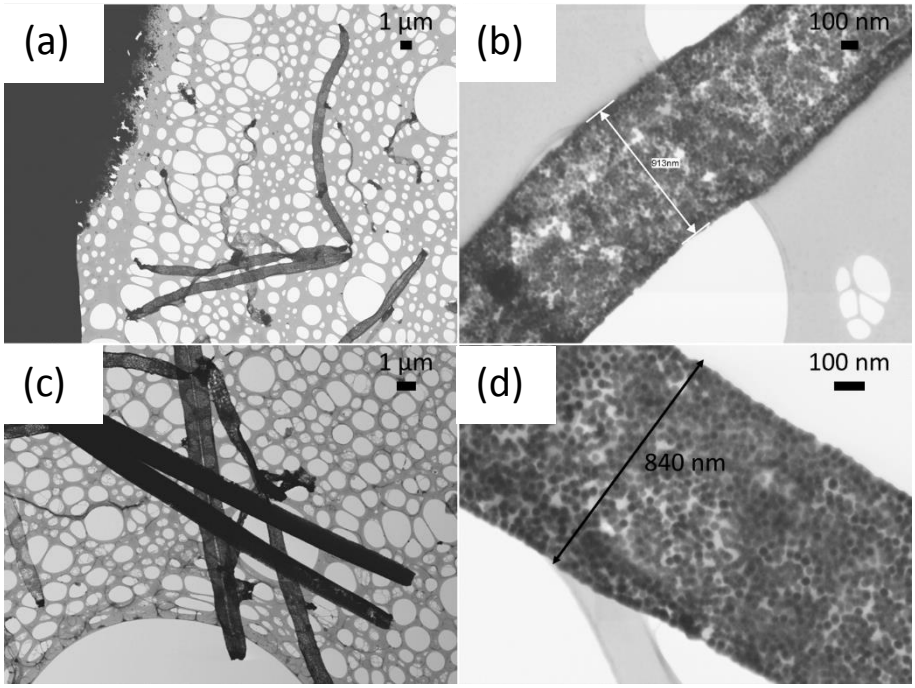


**Figure S5.3** *STEM pictures of synthetic NTs stiffened by the addition of silica colloids, incorporated by dipping: $(PAH\text{-}FITC/PAA)_{3.5}/SiO_2^{2.76\%dipping}/(PAH\text{-}FITC/PAA)_2$ (a, b), or by filtration: $(PAH\text{-}FITC/PAA)_{3.5}/SiO_2^{1\%filtration}/(PAH\text{-}FITC/PAA)_2$ (c, d). (left) low magnification, (right) high magnification.*

respectively). The filtration process was therefore deemed more satisfactory and used throughout further developments, unless otherwise stated.

### *c) Concentration of the colloidal dispersion*

While keeping other parameters constant, the concentration of the colloidal dispersion filtered within the multilayer was varied between 0.1, 1, 1.25 and 2.76 wt%. When incorporating colloidal particles in the outermost layer of synthetic NTs, the silica content of the 0.1 wt% dispersion is clearly too low to ensure proper stiffening of the resulting composite tubes. Indeed, many of the produced tubes show a sinuous morphology (Figure S5.4.a) which is directly related to the low amount of $SiO_2$ present within their structure. Only the endpoints of the tubes contain a homogeneous distribution of colloids and are consequently efficiently rigidified (Figure S5.4.b), while their central portion clearly displays fewer NPs and more widely scattered (Figure S5.4.c). NTs built via filtration of the 1 wt% silica

suspension, on the contrary, show a highly homogeneous distribution of NPs along their whole length (Figure S5.4.d-e). Consequently, the latter NTs are more efficiently stiffened and no curvy NT is observed. The higher stiffness of the NTs built from a 1wt% silica dispersion compared to the 0.1 wt% dispersion is equally noticeable when comparing composite NTs incorporating $SiO_2$ colloids within a deeper layer (0.1wt%, Figure S5.5.a-b and 1 wt%, Figure S5.5.c-d). The density of NPs incorporated within the tubes when using a 2.76 wt% colloid suspension is even higher, resulting in highly stiff but brittle NTs. Many small pieces of straight but broken NTs are indeed observed (Figure S5.4.f-g), demonstrating that the NTs are too rigid to withstand the collection process without breaking down into pieces. The 2.76 wt% silica NPs concentration is thus deemed too extreme to yield mechanically stable NTs. On the other hand, the 0.1 wt% concentration is too low to ensure proper stiffening of the NTs and the 1 wt% concentration was therefore selected as optimal colloidal concentration for further experiments.

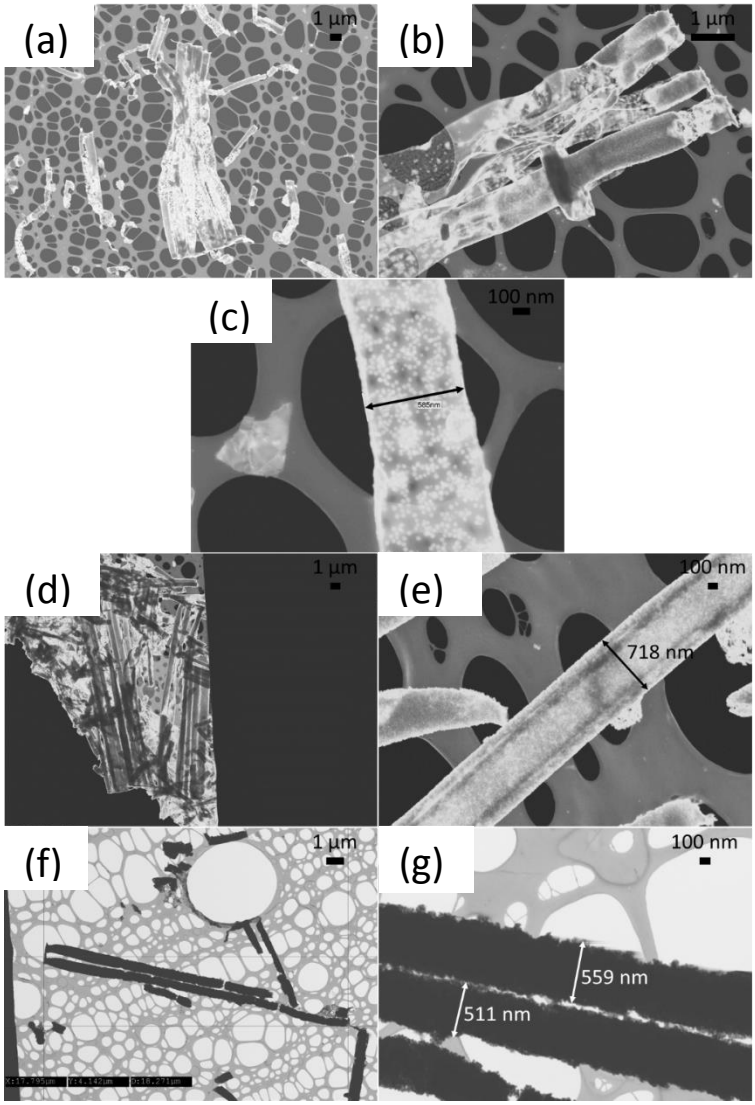


**Figure S5.4** *STEM pictures of composite NTs stiffened by the filtration of silica particles at a concentration of 0.1 wt%: $(SiO_2^{0.1\%filtration}$-PAH-FITC/PAA$)_1$ (PAH/PAA$)_5$ (a, b, c), 1 wt%: $(SiO_2^{1\%filtration}$-PAH-FITC/PAA$)_1$(PAH/PAA$)_5$ (d, e) or 2.76 wt%: $(SiO_2^{2.76\%filtration}$-PAH-FITC/PAA$)_1$(PAH-FITC/PAA$)_5$ (f, g). (left) low magnification, (right & center) high magnification.*

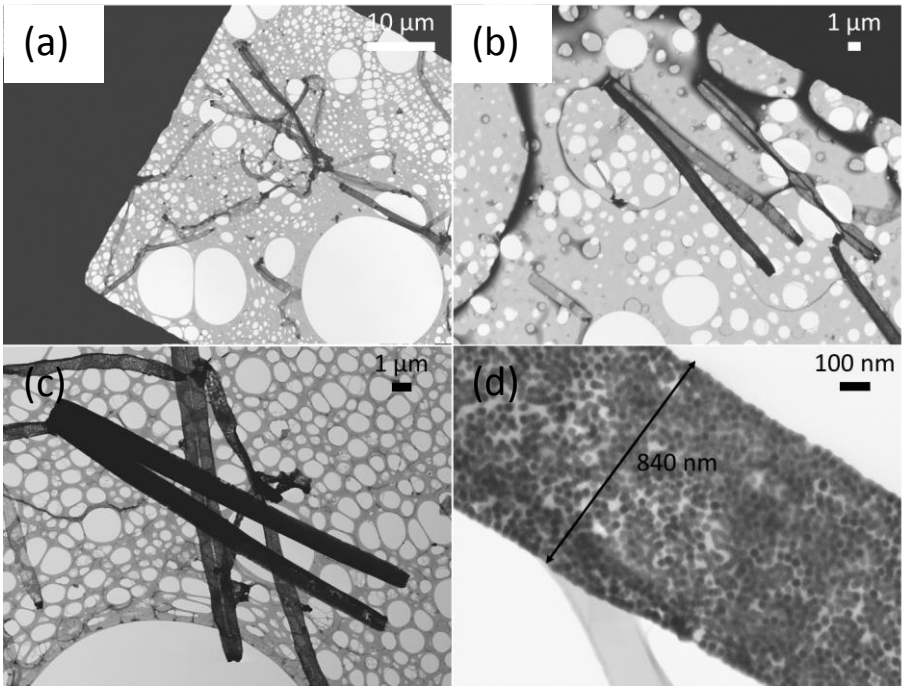


**Figure S5.5** *STEM pictures of composite NTs stiffened by the filtration of silica particles at a concentration of 0.1 wt%: (PAH-FITC/PAA)$_{3.5}$/SiO$_2^{0.1\%filtration}$/(PAH-FITC/PAA)$_2$ (a, b) or 1 wt%: (PAH-FITC/PAA)$_{3.5}$/SiO$_2^{1\%filtration}$/(PAH-FITC/PAA)$_2$ (c, d). (left) low magnification, (right) high magnification.*

### *d) Location of the colloids within the polymer multilayer*

Depending on when the incorporation of silica nanospheres is carried out during the NTs synthesis process, they can be either integrated in the most superficial layer of the NTs or rather in one of their innermost layers. Two distinct morphologies arise from this possibility of choosing the colloids location within the tubes. When added to the outermost layer of the multi-layered NTs, the surface of the latter shows a rough, granular texture (Figure S5.6.a-c). On the contrary, adding the particles to a deeper layer of the NTs gives rise to a smooth outer surface under which appear the particles (Figure S5.6. d-e). No major difference in the mechanical properties of the two different systems could be identified. Composite NTs incorporating silica NPs

as strengthening agents either in their outermost or innermost layers could thus be alternatively produced.

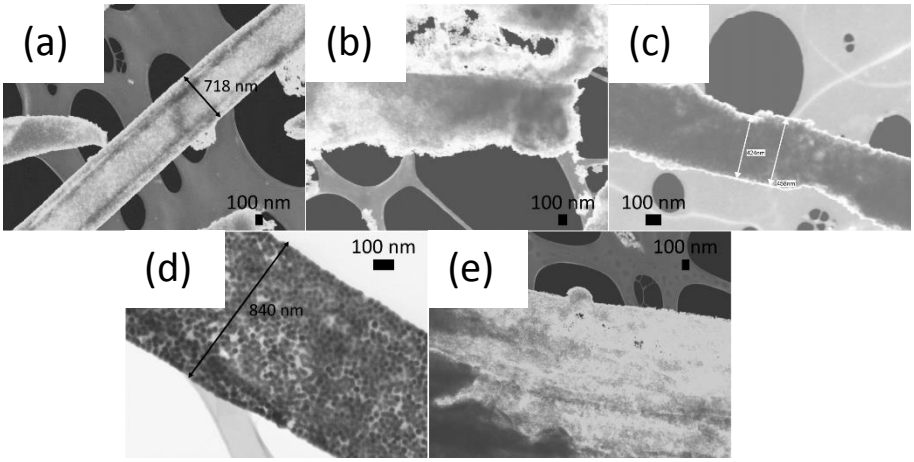


**Figure S5.6** *STEM pictures of composite NTs stiffened by the incorporation of silica particles within their outermost layer : ($SiO_2^{1\%filtration}$-PAH-FITC/PAA)$_1$(PAH-FITC/PAA)$_5$ (a), ($SiO_2^{9.27\%dipping}$-PAH-FITC/PAA)$_3$(PAH/PAA)$_3$ (non cross-linked, b), ($SiO_2^{9.27\%dipping}$-PAH-FITC/PAA)$_3$(PAH/PAA)$_3$ (c) or into one of their innermost layers: (PAH-FITC/PAA)$_{3.5}$/$SiO_2^{1\%filtration}$/(PAH-FITC/PAA)$_2$ (d), (PAH/PAA)$_3$($SiO_2^{9.27\%dipping}$-PAH-FITC/PAA)$_2$(PAH/PAA)$_1$ (e).*

### *e) Number of colloid layers incorporated in the NTs*

The possibility of incorporating more than a single layer of inorganic particles in order to better improve the stiffness of the composite NTs was evaluated. One or three cycles of passive diffusion of silica NPs were therefore carried out (Figure S5.7.a-b and c-d, respectively). As can be seen from Figure S5.7, no difference is observed between the systems incorporating one or three $SiO_2$ layers. Indeed, as both systems were produced by simple passive diffusion of NPs, resulting NTs equally show a low density of incorporated particles, especially in their central portion, no matter whether one or three cycles of silica diffusion took place. Filtration was excluded in order to avoid repeatedly applying a high pressure, which might have damaged previously adsorbed layers.

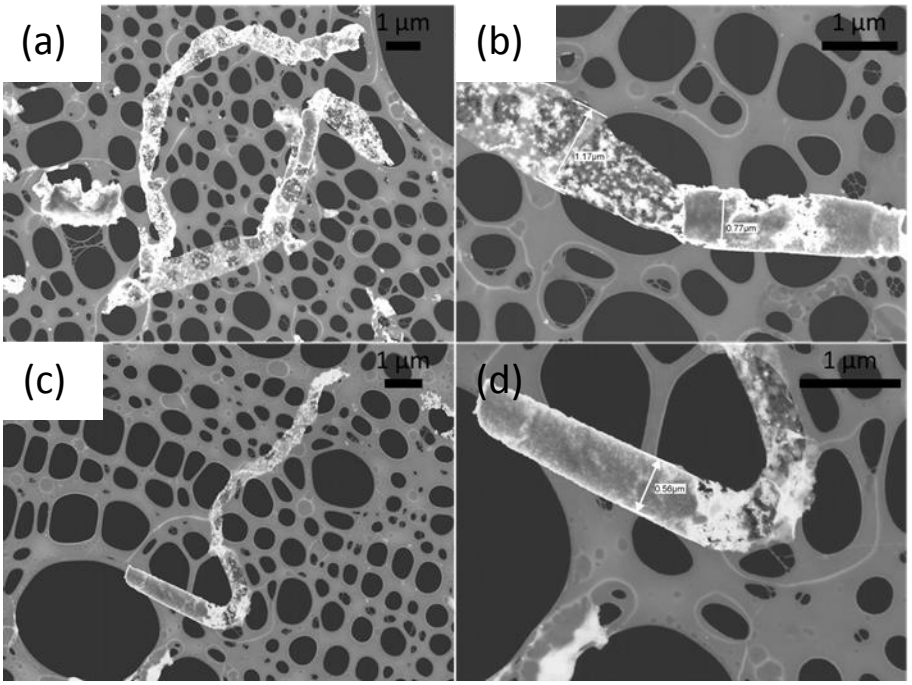


**Figure S5.7** *STEM pictures of composite NTs stiffened either via a single cycle of silica NPs diffusion: $(SiO_2^{1.25\%dipping}\text{-PAH-FITC/PAA})_1(\text{PAH-FITC/PAA})_5$ (a, b) or via three cycles of silica NPs diffusion: $(SiO_2^{1.25\%dipping}\text{-PAH-FITC/PAA})_3(\text{PAH-FITC/PAA})_3$.*

The apparent independence of the NTs mechanical performances from the number of incorporated $SiO_2$ layers might indicate that the adsorption of a single layer of NPs is sufficient to clog the template nanopores and prevent further diffusion of any other constituent. Such clogging of the pores might especially happen due to the fact that NPs tend to aggregate at the extremities of the NTs (Figure S5.7.b,d), which might result in the formation of a plug. At this point, it is therefore unknown whether polymers can still diffuse in the nanopores and adsorb on their surface after deposition of the $SiO_2$ strengthening layer and whether it is thus useful or not to pursue the LbL assembly after the incorporation of NPs.

## *f) Concluding remarks*

The set of optimal parameters for the successful production of NTs incorporating silica NPs as toughening agent, resulting from our exploratory study on synthetic PE-based NTs, are summarized in Table S5.1 and will be used for further developments.

**Table S5.1** *Summary of optimized parameters (in bold) for the synthesis of composite NTs incorporating $SiO_2$ NPs as strengthening agent.*

| | | **Optimal parameters** |
|---|---|---|
| **Colloidal dispersion** | Incorporation method | Passive diffusion VS **Filtration** |
| | Concentration | 0.1 wt%, **1 wt%**, 1.25 wt%, 2.76 wt%, 9.27 wt% |
| **Location of the colloids within the multilayer** | | **Outermost** vs **Inner layers** |
| **N° of colloid incorporation cycles** | | **1** vs 3 |
| **LbL post-treatment** | | **Chemical cross-linking** |

*g) Experimental section*

***Materials**:* Poly(acrylic acid) (PAA, $M_W$ ~ 100 kDa, 35 wt.% in $H_2O$), poly(fluorescein isothiocyanate allylamine hydrochloride) (PAH-FITC, $M_W$ ~ 15 kDa, monomer to dye ratio (PAH:FITC) of 50:1) and poly(allylamine hydrochloride) (PAH, $M_W$ ~ 15 kDa) were purchased from Sigma-Aldrich. Poly(sodium-p-styrenesulfonate) (PSS, $M_W$ ~ 70 kDa) was purchased from Acros. Spherical silica colloids ($SiO_2$ NPs, LUDOX® TM-50 colloidal silica 50 wt.% suspension in $H_2O$, average diameter ~ 25 nm) were bought from Sigma-Aldrich. Characteristics of the PC templates used to produce individual nanotubes were as follows: the average pore diameter was 500 nm, while the average porosity was $4.10^7$ pores.cm$^{-2}$ and the template thickness, 21 µm. Nanoporous PC templates were kindly supplied by *it4ip*. Cross-linking agents, 1-(3-dimethylaminopropyl)-3-ethylcarbodiimide hydrochloride (EDC, 98+%) and *N*-hydroxysulfosuccinimide sodium salt (s-NHS, ≥98%) were purchased from Acros and Sigma-Aldrich, respectively. Sodium chloride (NaCl, ACS reagent, ≥99%) and hydrochloric acid solution (HCl, 0.1 N in aqueous solution) were purchased from Sigma-Aldrich. PET membranes, used for filtration purposes and as substrate for microscopical analysis, were supplied by it4ip and had an average pore diameter of 200 nm, a thickness of 23 µm and a pore density of $5.8x10^8$ pores.cm$^{-2}$.

***Synthesis of composite nanotubes based on synthetic PEs**:* PAH-FITC and PAA solutions were prepared by dissolving an appropriate amount of polymer into MES buffer (100 mM, pH 5.5) to reach a final concentration of 1 mg/mL. The same procedure was applied to prepare solutions of PSS and PAH. MES buffer (100 mM, pH 5.5) was preferred to acetate buffer in order to ensure a high density of charges on both polymer backbones, while avoiding at the same time the presence of free carboxylic acid groups in solution which might potentially interfere with the proper cross-linking of the NTs by playing the role of reactive sites for the EDC/s-NHS coupling. The commercial dispersion of colloidal silica was abundantly diluted in UPW until reaching the desired NPs mass fraction. The pH of the dispersion was further adapted from ~9 to 5.5 (pH similar to the MES buffer used to solubilize the

polymers) using HCl 0.1 N. All solutions were prepared right before use and gently mixed for at least 20 minutes prior to being used.

$(PAH\text{-}FITC/PAA)_n$ or $(PAH/PSS)_n$ multilayers (where *n* represents a tunable number of bilayers) were deposited as starting materials inside PC templates featuring simple, parallel nanopores, using the LbL deposition by dipping process. The dipping time in all the polymer solutions (PAH-FITC and PAA or PAH and PSS) was fixed at 30 min, which is a convenient time for the diffusion of PEs and their adsorption in the form of a monolayer. After deposition of each polymer layer, the systems were decrusted by rubbing on both of their faces, a cell scraper wetted by MES buffer. The samples were then left to rinse in MES buffer for 5 minutes before initiating the construction of the next layer.

In order to improve the mechanical properties of the constructed synthetic multilayers, silica NPs were incorporated inside these constructs in a location which could vary from a sample to another (i.e., NPs were integrated either in one of the outermost or one of the innermost layers). Whenever silica NPs had to be integrated after a polycation layer and therefore had to play the role of polyanion, we simply relied on the superficial oxide layer characteristic of silicon to ensure a proper density of negative charges. On the other hand, whenever silicon dioxide NPs had to be incorporated as a polycation, they were first pre-incubated in the presence of a polycation (either PAH-FITC or PAH), which is thought to adsorb on the particle surface thanks to electrostatic interactions with the superficial native oxide layer. In practice, an adequate amount of polycation (PAH-FITC or PAH) was dissolved in a corresponding volume of colloidal dispersion (prealably diluted to reach the targeted mass fraction in silica NPs) to reach a final concentration in polymer equal to 1 mg/mL. The resulting polycation-enriched dispersion was then gently mixed for at least 1 h in order to promote adsorption of the polycation on the particles surface.

The stiffening agents which constitute silica NPs were integrated in the desired layer of the synthetic NTs relying either on simple or forced diffusion. For that purpose, the PC template filled with synthetic NTs was respectively simply dipped in the (un)modified colloidal silica dispersion (dipping time set a minimum 1 h) or the dispersion was filtered through the template (filtration volume: 1 to 3 mL). After filtration of the particles, the samples were left aside in MES buffer (100 mM pH 5.5) for at least 30 min to ensure proper

diffusion and repartition of the NPs along the length of the tubular multilayer. Both faces of each sample were then decrusted using a cell scraper wetted by MES buffer. In cases where silicon dioxide NPs had to be integrated in one of the outermost layers of the tubes, the LbL deposition was simply re-initiated as previously described, after completion of the ceramic particles incorporation step.

When deemed necessary, chemical cross-linking of selected samples was initiated right after completion of the LbL construction. For that purpose, multilayer-filled templates were immersed in the cross-linking solution [EDC 100 $mg.mL^{-1}$ & s-NHS 11 $mg.mL^{-1}$ in 0.15 M NaCl pH 4.0] and stored at 4 °C for at least 48 h, following an adaptation of the protocol of Picart *et al*.[23-28] Samples were then transferred into the construction medium (MES buffer) and stored at 4 °C until further characterization.

***Sample preparation for structural analyses***: Individual nanotubes were first released from their PC template by dissolution of the templating membrane in dichloromethane ($CH_2Cl_2$, 99.8+% for analysis, stabilized with amylene, Acros Organics). In practice, small cut-outs (~ 2-3 $mm^2$) in the PC membrane containing the self-assembled NTs were immersed in a test tube containing 5 mL of dichloromethane and left aside for 10 min, ensuring complete dissolution of PC.

Prior to SEM analysis, the dispersion of NTs in $CH_2Cl_2$ was subsequently filtered over hydrophilic PET filters (200 nm pore size, pore density $5x10^8$ $pores.cm^{-2}$, thickness 23 µm, it4ip) prealably metallized, using a sputter coater (Cressington 208HR), with a chromium anchoring layer (3 nm) followed by a gold layer (20 nm). Metallized filters were introduced in the sample holder of a 5 mL syringe while the dispersion of NTs in dichloromethane was poured in the syringe and filtered. 5 mL of fresh dichloromethane were subsequently used to rinse the test tube and filtered through the device to maximize the NTs collection. The resulting NTs supported on metallized filters were left to dry overnight at room temperature before any further characterization.

In anticipation of STEM and TEM analysis, the suspension of NTs in dichloromethane collected upon template dissolution was gently dropped on

TEM grids consisting of a carbon film supported on a copper mesh grid (Agar Scientific Ltd).

***SEM & STEM observations***: The dimensions and morphology of the synthesized NTs were studied by scanning electron microscopy (SEM).

SEM pictures were obtained using a thermal field emission scanning electron microscope (JSM-7600F, Jeol) operated at an acceleration voltage of 15 kV under SEM mode (maximum resolution of 1.0 nm using a secondary electron imaging detector).

STEM pictures were obtained using the same microscope operated at an acceleration voltage of 30 kV under STEM mode (maximum resolution of 0.8 nm, making use of a TED detector).

## S.I.5.2 AFM topographical maps of biomimetic (Col/HA) NTs

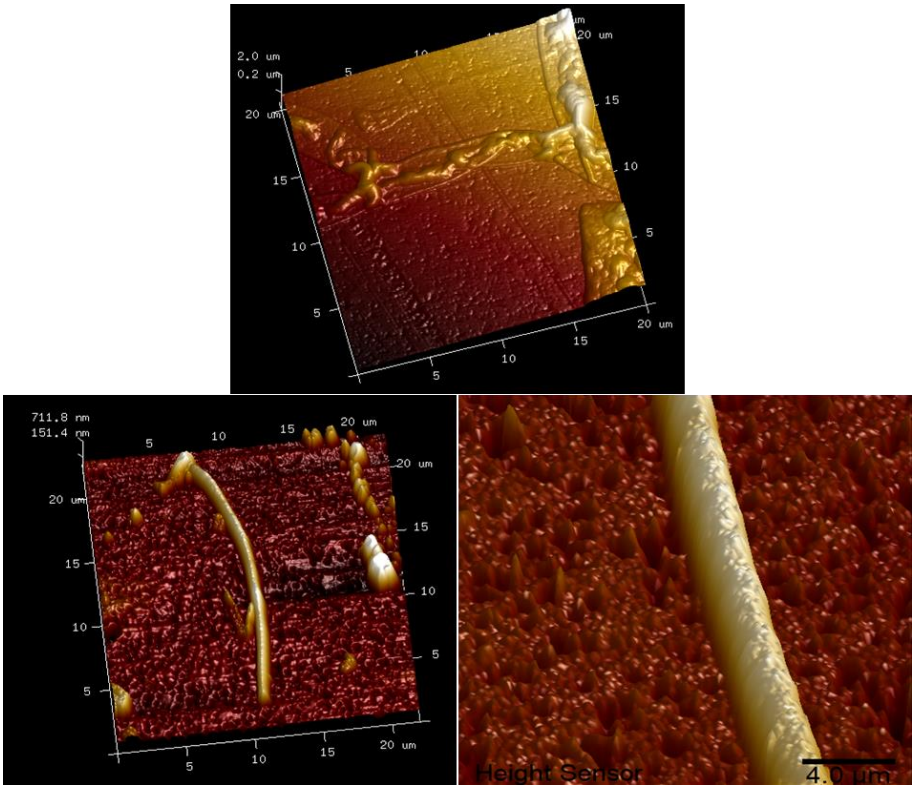


**Figure S5.8** *AFM pictures (topography channel) of (a) $(Col/HA)_8$ NTs and (b) $(Col/SiO_2)_1(Col/HA)_7$ NTs, supported over a PET filtration membrane. (c) High magnification view of (b).*

# Theoretical appendix 5.I

## Computation of the sedimentation rate, $v_s$, of a 25-nm diameter silica colloid in a QCM-D chamber

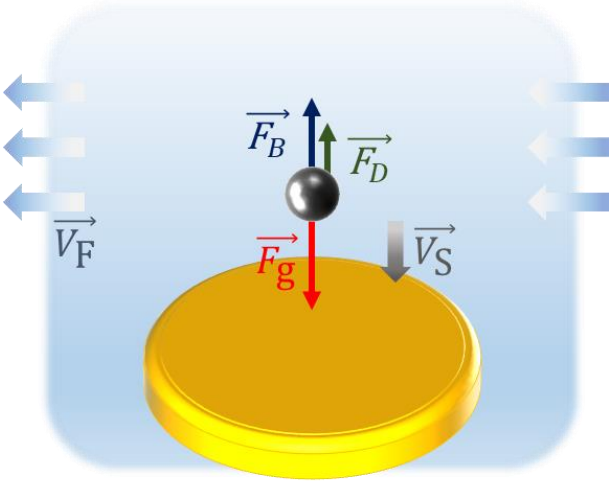


**Figure Th.A.5.I** *Schematic representation of the forces which apply along the vertical direction on a particle sedimenting down the QCM-D chamber.* $\overrightarrow{V_F}$ *is the velocity of the flow through the QCM device,* $\overrightarrow{V_S}$ *the sedimentation rate,* $\overrightarrow{F_g}$ *is the weight of the particle,* $\overrightarrow{F_B}$ *is the generated buoyant force and* $\overrightarrow{F_D}$ *the friction force.*

A rapid overview of the forces which apply on a sedimenting particle in the vertical direction shows that its movement is governed by the balance between the gravitational force (weight of the particle, $\overrightarrow{F_g}$) attracting the particle down the liquid column and the buoyant ($\overrightarrow{F_B}$) and frictional (drag force, $\overrightarrow{F_D}$) forces which both tend to oppose this movement.

The weight of the silica NP is given by:

$$\overrightarrow{F_g} = m_{particle} \times g = \rho_{SiO_2} \times V_{particle} \times g \qquad (5.1)$$

where $g$ is the gravitational acceleration (9.81 m.s$^{-2}$), $\rho_{SiO_2}$ the density of silica (2334 kg.m$^{-3}$), $m_{particle}$ is the mass of one $SiO_2$ NP and $V_{particle}$ its volume.

The buoyant force is equivalent to the weight of water displaced by the particle:

$$\overrightarrow{F_B} = m_{water} \times g = \rho_{water} \times V_{particle} \times g \quad (5.2)$$

where $\rho_{water}$ is the density of water (997 kg.m$^{-3}$).

The drag force exerted on a spherical object with a small Reynolds number (Re < 1[3]) moving through a viscous fluid is given by Stokes' law:

$$\overrightarrow{F_D} = 6\pi\eta R_{particle} v_s \quad (5.3)$$

where $\eta$ is the dynamic viscosity of the fluid ($10^{-3}$ Pa.S for water at 20°C), $R_{particle}$ is the radius of the particle and $v_s$ is the flow velocity relative to the object (i.e., the sedimentation velocity of the particle in this case). The sedimentation rate ($v_s$) becomes constant when an equilibrium is reached between these forces, i.e. when their sum equals to 0. Hence, it comes:

$$\overrightarrow{F_{\mathrm{g}}} - \overrightarrow{F_{\mathrm{B}}} - \overrightarrow{F_{\mathrm{D}}} = 0 \quad (5.4)$$

Which gives:

[3] The Reynolds number is computed as follows:

$$Re = \frac{\rho \times v_{flow} \times \emptyset_{NP}}{\eta} = \frac{1000 \times 7.07 \times 10^{-5} \times 25 \times 10^{-9}}{10^{-3}} = 1.77 \times 10^{-6}$$

$$\rho_{particle} V_{particle} g - \rho_{water} V_{particle} g - 6\pi\eta R_{particle} v_s = 0$$

Or, equivalently:

$$6\pi\eta R_{particle} v_s = \left(\rho_{particle} - \rho_{water}\right) \times V_{particle} \times g \qquad (5.5)$$

and, the volume of a spherical particle being $\frac{4}{3}\pi R_{particle}^3$, it yields:

$$v_s = \frac{\left(\rho_{particle} - \rho_{water}\right) \times 2R_{particle}^2 \times g}{9\eta}$$
$$= \frac{(2334 - 997) \times 2 \times (12.5 \times 10^{-9})^2 \times 9.81}{9 \times 10^{-3}}$$
$$= 4.55 \times 10^{-10}\ \mathrm{m.s^{-1}}$$

The sedimentation rate of 25 nm diameter silica colloids is thus ~ 4.55 $10^{-10}$ m.s$^{-1}$, resulting in a sedimentation time of 1.83 $10^3$ h to fall down a distance as small as 3 mm ($T_{sedimentation} = \frac{3.10^{-3}}{v_s}$).

Calculating the flow speed through the QCM tubing, which is assumed to be also the horizontal speed at which the particles cross the crystal surface, we get: $v_{flow} = \frac{Q}{S_{tube}} = \frac{30\times10^{-6}\times10^{-3}}{\pi R_{tube}^2\times60} = 6.37 \times 10^{-4}\mathrm{m.s^{-1}}$, where $Q$ is the flow rate ($Q = 30$ µL.min$^{-1}$) and $S_{tube}$ is the tubing section ($S_{tube} = \pi R_{tube}^2 = \pi \times (0.5 \times 10^{-3})^2$, assuming a QCM tubing of 1 mm diameter).

# Theoretical appendix 5.II

## Computation of the active area developed by a close-packed monolayer of 25-nm diameter silica colloids

The maximum number of spheres of 25 nm diameter which can be aligned on a 1 cm segment is given by: $\frac{1 \times 10^7\ [\text{nm}]}{25\ [\text{nm}]} = 400{,}000\ \text{NPs}$. Thus, the number of particles contained in a monolayer adsorbed on a 1 $cm^2$ surface unit of the quartz crystal is: $(400{,}000)^2 = 1.6 \times 10^{11}\ SiO_2\ \text{NPs}$. If we consider that only half of the total surface developed by each particle (i.e., the face of the particle exposed to the liquid phase) is available to the adsorption of species in solution, the area available for adsorption phenomena per square centimeter of crystal after silica deposition is:

$$\frac{\text{surface area of 1 silica NP}}{2} \times \frac{\text{Number of silica NP}}{\text{cm}^2\ \text{of substrate}}$$

$$= \frac{4 \times \pi \times \left(\frac{25 \times 10^{-9}}{2}\right)^2}{2} \times 1.6 \times 10^{11} = \frac{1.57 \times 10^{-4}\ \text{m}^2}{\text{cm}^2\ \text{of substrate}} = \frac{1.57\ \text{cm}^2}{\text{cm}^2\ \text{of substrate}}.$$

The area developed by silica NPs adsorbed on 1 $cm^2$ of quartz crystal is thus equal to 1.57 $cm^2$

# Theoretical appendix 5.III

## Computation of the superficial area developed by a 14-mm diameter sample of PC template with intersected pores of 300-nm diameter

The lateral area of a 300-nm tube of 25 µm height is given by:

$$2\pi \times r_{tube} \times h_{tube} = 2\pi \times \left(\frac{300.10^{-9}}{2}\right) \times 25 \times 10^{-6}$$

$= 2.36 \times 10^{-11}$ [m²]

where $r_{tube}$ and $h_{tube}$ are respectively the radius and height of the NT.

The porosity of the template being 2.83 $10^8$ pores.cm$^{-2}$ (= 2.83 $10^{12}$ pores.m$^{-2}$), the total number of pores on a circular piece of template of 14 mm diameter (i.e., the piece of template used to produce the biointerfaces) is:

$$Pore\ density\ \left[\frac{\#\ pores}{m^2 template}\right] \times Area\ of\ template\ [m^2]$$

$$= 2.83 \times 10^{12} \times \pi \times \left(\frac{14 \times 10^{-3}}{2}\right)^2$$

$$= 4.3564 \times 10^8\ \left[\frac{\#\ pores}{piece\ of\ 14\ mm\ diameter\ template}\right]$$

The total superficial area developed by a biointerface issued from this Ø14 mm piece of template is thus:

$$lateral\ area\ of\ one\ NT \times \frac{\#\ pores}{piece\ of\ 14\ mm\ diameter\ template}$$

$$= 2.36 \times 10^{-11} \times 4.36 \times 10^8 = 0.0103\ [m^2]$$

# Theoretical appendix 5.IV

## Computation of the superficial area developed by a 14-mm diameter sample of PC template with intersected pores of 40-nm diameter

The lateral area of a 40-nm tube of 25 µm height is given by:

$$2\pi \times r_{tube} \times h_{tube} = 2\pi \times \left(\frac{40.10^{-9}}{2}\right) \times 25 \times 10^{-6}$$

$= 3.142 \times 10^{-12}$ [m²]

where $r_{tube}$ and $h_{tube}$ are respectively the radius and height of the NT.

The porosity of the template being 1.2 $10^{10}$ pores.cm$^{-2}$ (= 1.2 $10^{14}$ pores.m$^{-2}$), the total number of pores on a circular piece of template of 14 mm diameter (i.e., the piece of template used to produce the biointerfaces) is:

$$Pore\ density\ \left[\frac{\#\ pores}{m^2 template}\right] \times Area\ of\ template\ [m^2]$$

$$= 1.2 \times 10^{14} \times \pi \times \left(\frac{14 \times 10^{-3}}{2}\right)^2$$

$$= 1.847 \times 10^{10}\ \left[\frac{\#\ pores}{piece\ of\ 14\ mm\ diameter\ template}\right]$$

The total superficial area developed by a biointerface issued from this Ø14 mm piece of template is thus:

$$lateral\ area\ of\ one\ NT \times \frac{\#\ pores}{piece\ of\ 14\ mm\ diameter\ template}$$

$$= 3.142 \times 10^{-12} \times 1.847 \times 10^{10} = 0.0580\ [m^2]$$

# Theoretical appendix 5.V

## Quantification of total protein content: colorimetric BCA test[24–27]

The bicinchoninic acid (BCA) test is a quantitative protein assay based on the chelation of cupric ions ($Cu^{2+}$) by proteins in an alkaline environment (i.e., the biuret reaction) coupled to a colorimetric detection of the resulting cuprous ($Cu^{1+}$) ions, in a similar process as the Lowry assay. Peptides containing at least three amino acid residues brought in an alkaline environment containing $Cu^{2+}$ and sodium potassium tartrate react according to the "Biuret reaction", whereby lone pairs of electrons from the nitrogen atoms involved in peptide bonds create coordination bonds with a cupric ion, resulting in a colored tri- or tetra-dentate coordination complex[28,29] (Figure S5.10). In a secondary reaction, the cupric ion ($Cu^{2+}$) is reduced to its cuprous form ($Cu^{1+}$) and the peptide bond is oxidized. Both BCA and Lowry methods then involve the colorimetric detection of the resulting cuprous cation. The Lowry protein assay[30,31] relies on the nonspecific transfer of electrons between $Cu^{1+}$, which is oxidized back to $Cu^{2+}$ in the process, and the Folin-Ciocalteu reagent (mixture of phosphomolybdate and phosphotungstate) whose reduction produces the intense blue-colored Mo (IV) (Figure S5.10.c). The BCA assay, on the other hand, uses bicinchoninic acid sodium salt as chromophore which forms a highly specific 2:1 purple complex with $Cu^{+}$ (Figure S5.10.b). This BCA/copper complex is water-soluble and exhibits a strong linear absorbance at 562 nm with increasing protein concentrations. Establishment of a calibration curve displaying the absorbance intensity at 562 nm as a function of the concentration of the protein of interest thus enables the quantification of the protein content of unknown samples.

Smith *et al.*, who introduced the BCA method in 1985 postulated that the total color yield (i.e., $Cu^{+}$ formation) is actually the result of, at least, two contributions: (i) the direct reduction of $Cu^{2+}$ into $Cu^{+}$ by the readily oxidizable amino acid residues tyrosine, cysteine/cystine and tryptophan. This first contributory mechanism is considered to be temperature independent and is responsible for slight protein-to-protein variations in the results, given that the proportion of these 3 amino acids differs from one protein to another and (ii) the reduction of copper by the peptide bonds present in the protein backbone following the biuret reaction, which is

temperature dependent and represents the major contribution to the color development of the BCA assay.

Incubation of proteins with the BCA reagent is thus preferably conducted at 60°C, in order to reduce the protein-to-protein deviations. Although the BCA technique shows less dependence on the protein sequence compared to Bradford[32] or Lowry assays, it is common practice to record an independent calibration curve for each protein of interest, so as to further

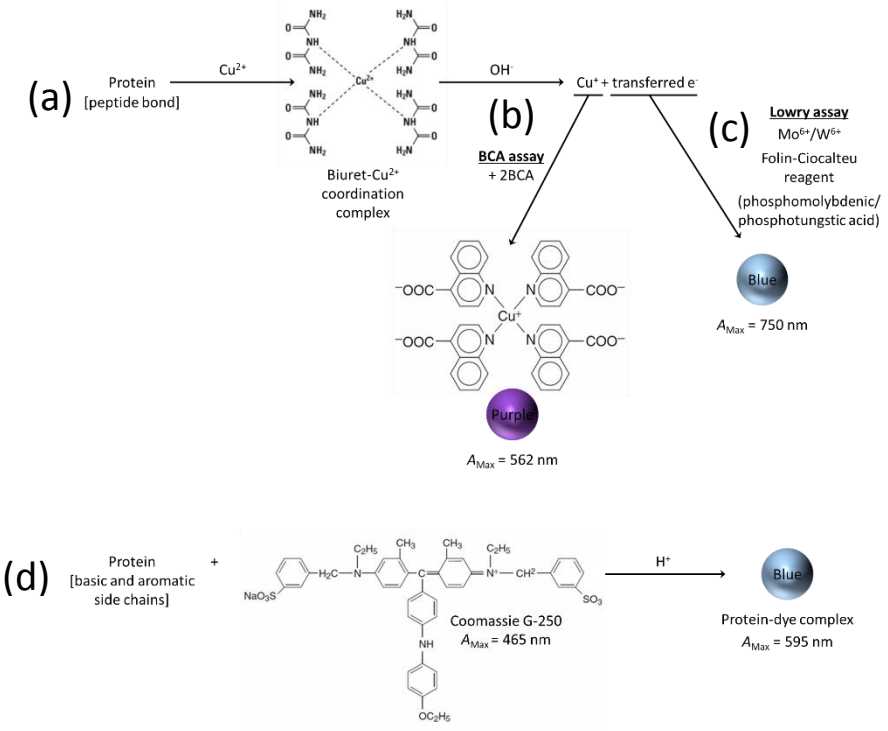


**Figure S5.10** *Overview of most popular colorimetric protein quantification assays : (a) the biuret reaction yielding a peptide-$Cu^{2+}$ complex [a biuret-$Cu^{2+}$ complex is presented for the sake of simplicity but the reaction proceeds in the same way when peptide bonds of proteins are involved] is the working principle of copper-based protein assays such as the BCA assay (b) which detects the resulting $Cu^{+}$ via formation of a colored complex with 2 BCA molecules and the Lowry method (c) which involves the reduction of the Folin-Ciocalteu reagent, producing an intense blue color. (d) The dye-based Bradford assay relying on the binding of the Coomassie dye to the protein backbone, enabling direct detection of a blue-colored complex (adapted from [29-32].).*

limit this variation. An example of such a calibration curve, relating the protein content of a sample to its absorbance at 562 nm, obtained for the Col protein in the frame of this thesis is displayed in Figure S5.11

The BCA assay has become the favoured method for colorimetric quantification of total protein amount due to its high sensitivity (detection of protein concentrations ranging from $5.10^{-4}$ to 2 mg/mL sample, as compared to $5.10^{-3}$-2 mg/mL sample for the Lowry method), the increased stability of its chromophore as well as its higher tolerance towards substances known to interfere with classical Lowry and Bradford protocols (such as non-ionic surfactants, compatible with BCA at concentrations up to 5% and common buffer salts). The list of known interferents in the BCA protocol include glucose, mercaptoethanol and dithiothreitol which elicit a strong absorbance at 562 nm when combined with the BCA working reagent, as well as ammonium sulfate and certain ampholytes which, on the contrary, attenuate the color development and shift the wavelength of the response. Generally speaking, any substance reducing copper will produce color in the BCA assay and lead to an overestimation of the protein content, while any reagent able to chelate the copper will also interfere by disturbing the color development and lead to an underestimation of the protein amount.

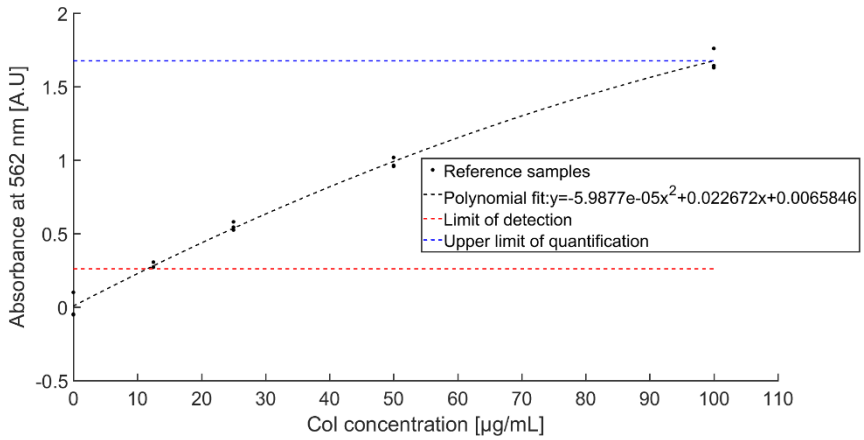


**Figure S5.11** *Calibration curve (black dashed line) relating the absorbance recorded at 562 nm with the concentration (in µg/mL) in Col of various reference samples incubated with the µBCA assay. The calibration curve is obtained by quadratic least squares regression of the reference data points (black dots). The limit of detection (dashed red line) is computed as 3 times the standard deviation of the blank while the upper limit of quantification (dashed blue line) depicts the upper limit of the linear working range of the µBCA kit (100 µg/mL).*

# Theoretical appendix 5.VI

## Evaluation of the mechanical properties of composite NTs

### A) Atomic force microscopy (AFM) with Peak-force tapping and quantitative nanomechanical mapping (PFT-QNM).[33–42]

AFM general principle

The basic working principle of AFM entails the scanning of a surface with a micro-probe in order to gather information relative to the topography and other local surface properties of the sample at the nanoscale. As the sample surface is approached from the nanometric AFM tip thanks to a piezoelectric scanner, the tip is subjected to a set of attractive and repulsive inter-atomic forces which are exerted between its apex (radius of curvature ~10 nm) and the sample surface. These tip-sample interactions trigger the bending of the AFM cantilever on the extremity of which is integrated the sharp tip. The cantilever deflections are translated into an optical signal as a laser beam is reflected on top of the cantilever and directed towards a position-sensitive photodiode (Figure S5.11). Hence, any modification of the cantilever bending degree triggers a displacement of the reflected laser beam on the photodiode, which then converts the received optical signals into electrical ones. A built-in software then finally translates these signals into displacement values.

Peak-force tapping (PFT) mode

While for the most classical contact mode, the AFM probe is static and in constant contact with the sampled surface, more recent dynamic modes have been developed where the probe is made to oscillate at some distance away from the substrate without ever touching it (non-contact mode) or only periodically (intermittent-contact mode or TappingMode™).The major advantage of such dynamic modes is the reduction of the lateral frictional forces which are generated in the contact mode, when the cantilever drags

over the surface. Hence, dynamic modes are favoured for the characterization of delicate polymeric and biological samples.

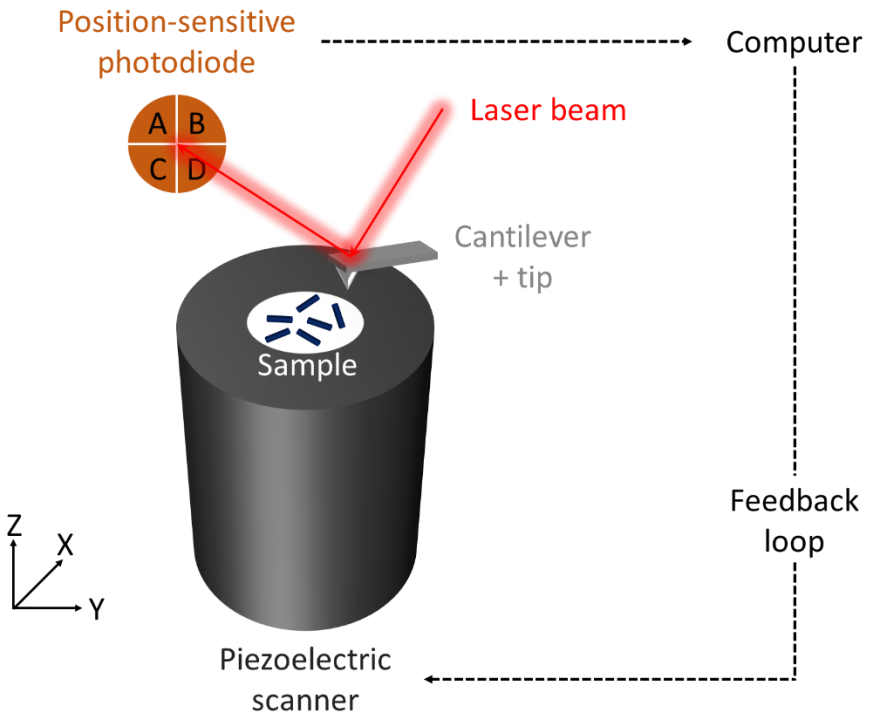


**Figure S5.11** *Schematic illustration of Atomic Force Microscopy (AFM) working principle. The sample of interest is fixed on a piezoelectric scanner and approached from the cantilever at the extremity of which is integrated a nanometric tip. The sample surface is scanned by this probing tip which is, as a result, subjected to a set of attractive and repulsive forces generating a deflection of the cantilever. Any deflection of the cantilever is tracked thanks to an optical detection system, based on the reflection of a laser beam on top of the cantilever surface and towards a position-sensitive photodiode. The movements of the cantilever are analyzed in real time by a computer which consequently adapts the scanner position so as to keep a setpoint parameter constant (feedback loop) [Adapted from[38]].*

The peak-force tapping mode (PFT) is an intermittent-contact AFM mode where the probe oscillates vertically at frequencies lower than its resonance frequency and the tip-sample distance is adapted so that the

maximum force applied when indenting the sample reaches a constant setpoint value during each tapping cycle (i.e., the maximum applied force is the feedback parameter used to adapt the z position of the piezoelectric table on which lies the sample) (Figure S5.12.a). The ability to control the applied force is at the core of the PFT mode and, in addition to preserving the native surface morphology, it enables the monitoring of load-dependent mechanical properties of the studied surface such as adhesion force, elastic modulus and energy dissipation. Indeed, as these mechanical parameters depend on the depth of indentation; fixing the applied force at a given setpoint ensures that the probed depth remains constant while scanning different locations of the sample surface and thus yields reliable measurements of the surface mechanical properties.

Force versus separation curves

The determination of these mechanical properties is based on the recording of a set of force versus time curves along each tapping cycle (Figure S5.12.b). Given that the tip-sample separation is recorded by the software for each position, the force versus time curses are converted to force versus tip-sample distance (f-d) curves (Figure S5.12.c). These f-d curves can be reasonably characterized by a restricted number of points of critical importance: as the tip approaches the surface starting from rest position (point A), the long-range (van der Waals) attractive forces start to act on the tip and once the intensity of the force dominates over the spring constant $k$ of the cantilever, it snaps into contact ($F_{a,VdW}$, point B). Once the contact with the surface has been established, short-range repulsive forces (Pauli interactions or contact forces) come into play and cause the cantilever to deflect away from the surface. By increasing the force applied by the probe on the sample, it can be indented until reaching the maximum setpoint force ($F_{r,max}$ or peak force, point C). Then, as the tip is being retracted from the surface, the cycle is reversed and once the force exerted by the cantilever surpass the adhesion force between the tip and the sample ($F_{a,max}$), it jumps out of contact (point D) before reaching back the equilibrium distance (point A). An example of such a force versus tip-sample separation curve (f-d curve), recorded on a composite NT in the frame of this thesis is displayed in Figure S5.13.

In addition to the qualitative insights provided by the shape of the f-d curves, quantitative values for different surface mechanical properties like hardness and elastic modulus can be extracted in real time from the force curves by analysing them with suitable models of contact mechanics. The fast

recording of a large set of force curves in each point of the probed surface and their fitting with appropriate models enables the real time mapping of the surface mechanical properties.

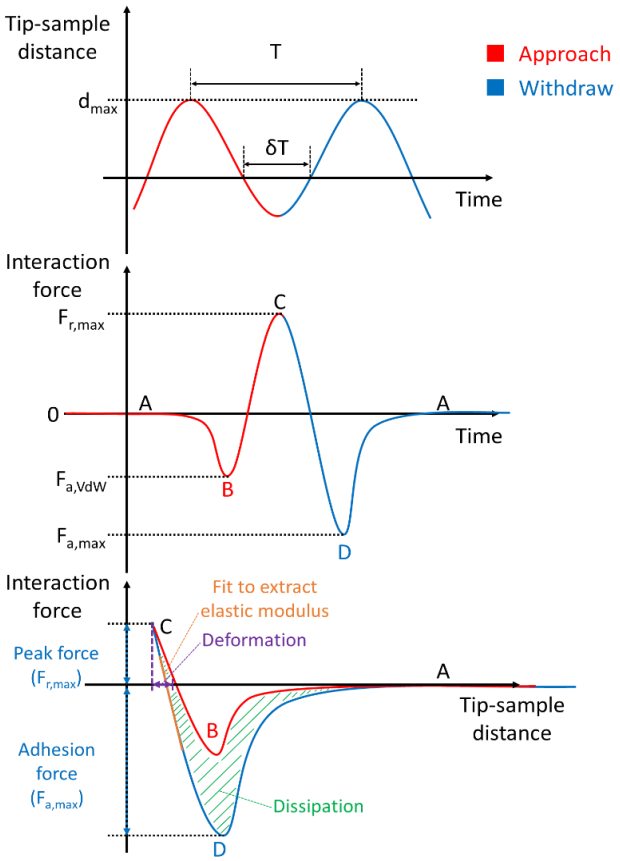


**Figure S5.12** *(a) Trajectory of the tip in Peak-Force Tapping mode, showing the period of a tapping cycle (T), the indentation time (δT) when the probe digs into the sample surface and the maximum tip-sample distance ($d_{max}$). (b) Tip-sample interaction forces as applied to the tip during one tapping cycle (T): the van der Waals attraction force at contact ($F_{a,VdW}$), the maximum repulsive force (peak force) at maximum indentation depth ($F_{r,max}$) and the adhesion force (attractive for the tip) at pull-out ($F_{a,max}$). Knowing the tip-sample position (as it equates to the addition of the Z position of the piezoelectric scanner to the cantilever deflection) at each point of the tapping cycle, the force versus time curve obtained in (b) is converted by the software in force versus tip-sample separation curve (c). This force vs. separation curve is used to extract in real time several mechanical parameters of the studied surface: adhesion force, maximum indentation force, elastic modulus (by fitting the retract curve with an appropriate contact mechanics model), deformation and dissipation. [Adapted from*[39,41]*].*

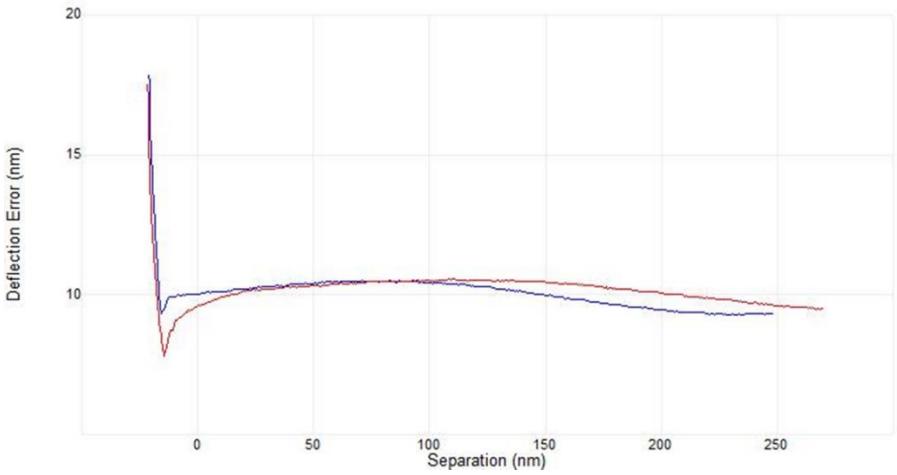


**Figure S5.13** *Example of a force versus tip-sample separation (f-d) curve recorded on a composite NT*

Procedure for the determination of a relative elastic modulus

Elastic modulus of composite and native biomimetic NTs was estimated using the Peak Force Tapping Quantitative Nanomechanical Mapping (PFT-QNM) AFM mode equipped on a Bruker Dimension-Icon system. TESPA probes from Bruker were used for all measurements. The probes and their intrinsic spring constant (*k*) should be carefully chosen when mapping the nanomechanical properties of samples showing local heterogeneities in elastic modulus, such as composites. Indeed, if the spring constant of the probe is too low, the cantilever will deflect too easily at a given force without sufficiently indenting the sample surface. On the contrary, if a very hard probe is selected, it will barely deflect at equivalent forces and will end up damaging the sample. Standard TESPA probes having an axial spring constant in the range 20-50 N/m were thus selected for our applications, as they offer a good compromise between cantilever deflection and penetration depth, yielding a detectable signal and a good probe sensitivity.

The calibration process was carried out as follows: the spring constant (*k*) for each probe was determined via thermal tuning (25.9777 N/m). The deflection sensitivity (82.31 nm/V) was obtained by imaging a silicon wafer, while the Sync. Distance QNM (81 nm) and the PFT amplitude were

calibrated on a sapphire reference sample, all reference samples being provided by Bruker. A relative calibration method was used to determine the radius of curvature (*R*) of the tip apex. In practice, the tip radius parameter was adapted so as to measure an elastic modulus ~ 2.7 GPa for a reference polystyrene (PS) sample, while the sample deformation was kept to a value of about 3-4 nm when indenting the PS reference. The obtained tip radius can then be kept constant when imaging the samples of interest, provided the deformation of the sample is kept constant at ~ 3-4 nm via adaptation of the PeakForce setpoint. The indentation depth was intentionally kept low and below 10 nm in order to avoid as much as possible plastic deformation of the sample, high contact stress and viscoelasticity phenomena which are not taken into account in common elastic contact models. The calibrated parameters were kept constant for further mapping along the samples surface.

Given the complexity of the studied samples, consisting in fully polymeric or composite NTs randomly distributed over a PET filter, the favoured protocol consisted first in fast-scanning the sample surface until NTs were clearly spotted on the topographical channel. A set of representative f-d curves were then recorded independently on the PET zones of the sample and along the length of the NTs and subsequently treated offline with appropriate models to extract the relevant mechanical parameters. Real-time mapping of mechanical properties was indeed deemed poorly reliable due to inevitable discrepancies arising from the need for the AFM device to treat almost simultaneously zones with highly different properties. Raw force-distance curves were thus systematically recorded on areas of interest along each sample, and later treated using the Nanoscope and Igor softwares in order to estimate the sample's Young modulus. In practice, the retraction part of the force versus distance curves corresponding to the part of the indentation cycle where the probed surface elastically relaxes, pushing back against the tip to regain the equilibrium tip-sample distance, was fitted with the Derjaguin-Müller-Toporov (DMT) model to extract the reduced Young's modulus (*E**), given by:

$$\mathrm{F_{tip}} = \frac{4}{3} E^* \sqrt{R d^3} + \mathrm{F_{Adh}} \qquad \text{(VI.1)}$$

where $F_{tip}$ is the force applied on the tip, $F_{Adh}$ is the adhesion force, *R* is the tip apex radius and *d* is the tip-sample separation. Typically, only the region between 10% and 70% of the unload (retract) curve is included in the DMT

modulus fit. The resulting reduced modulus (*E**) can be converted into the sample Young's modulus ($E_s$) using the sample's Poisson's ratio:

$$E^* = \left[\frac{1-\nu_t^2}{E_t} + \frac{1-\nu_s^2}{E_s}\right]^{-1} \quad \text{(VI.2)}$$

where $\nu_t$ and $\nu_s$ are the Poisson's ratio of the tip and the sample, respectively; and $E_t$ and $E_s$ are the Young's modulus of the tip and sample, respectively. Assuming that the tip modulus is much larger than the sample's modulus and can be approximated as infinite, we get:

$$E^* = \frac{E_s}{1-\nu_s^2} \quad \text{(VI.3)}$$

Typical values for the Poisson's ratio usually range between 0.2 and 0.5. However, given that this value is merely an assumption, many publications only report the reduced modulus so as to avoid a source of uncertainty.

The described DMT model is widely used to characterize adhesive elastic contacts between a spherical indenter and a surface and considers only long-range attractive forces which act outside the sample-indenter contact zone. As a consequence, the adhesion force is treated as a simple addition to the external force applied on the probe whose main effect is to increase the contact radius. Application of the DMT model is particularly recommended in the case of a low and constant adhesion force generated when indenting a surface at shallow depth (indentation depth ~2-5 nm) with a small tip (apex radius of curvature <10 nm); as was the case in this study.

The methodology applied throughout this study consisted in using raw force curves recorded on the substrate phase (PET) or along the NTs of the same sample to independently determine the elastic modulus of the PET substrate and that of NTs. The average value obtained for the NTs modulus was then divided by that of the PET substrate, so as to yield a relative modulus. This procedure allows us to discard most uncertainties relative to the calibration process (notably the one associated with the relative calibration of the tip radius), to fully exclude any effect of the substrate on the determination of the modulus of the NTs it supports and, finally, renders useless the dubious conversion of the reduced modulus into Young's modulus.

## B) Evaluation of NTs rigidity based on morphological indices

Rigidity index $\frac{{R_{EE}}^2}{L^2}$

The sequence of atoms constitutive of polymer macromolecules can be modelled as a chain with a varying degree of flexibility. Polymers with a fixed structure, such as the DNA double helix or macromolecules involving many aromatic rings can better be apprehended as stiff ropes while macromolecules with a much greater freedom of movement, such as polyethylene, would better be described as soft, highly folded ropes. Compliant polymer chains having a high degree of movement freedom will have the tendency to bend and form loops, giving rise to a multitude of probable conformations, collectively termed 'random coil' conformations. On the contrary, highly stiff polymers will rather tend to keep a defined conformation. Hence, the end-to-end distance ($R_{EE}$) of the polymer chain, defined as the square root of the mean square distance between the two ends of the chain, will be close to the fully-extended length ($L$) of the polymer in each case involving a rigid macromolecule ($R_{EE} \sim L$) while it will take on a high number of possible values in the case of a soft polymer ($R_{EE} \leq L$).

Polymer chains are commonly schematized using a freely-jointed chain model where the polymer is considered as an ideal chain divided into $N$ independent segments of unit length $b$ (referred to as "Kuhn length") which can take any random orientation, independently of the directions taken by other segments. (Figure S5.14). The contour length, or fully-extended length ($L$) of the freely-jointed chain can be expressed as:

$$L = N.b \qquad \text{(VI.4)}$$

The square of the end-to-end distance of the freely-jointed chain is given by:

$${R_{EE}}^2 = N.b^2 = (N.b).b = L.b \qquad \text{(VI.5)}$$

In the case of flexible, wormlike polymer chains, $b = 2L_p$; where $L_p$ is the persistence length of the chain, defined as the mean distance along the chain

over which a correlation in the directions taken by adjacent segments is conserved. Equation (VI.5) thus gives:

$$R_{EE}{}^2 = L.b = L.2L_p \qquad \text{(VI.6)}$$

Given that for soft polymers, the persistence length is much smaller than the full contour length ($L_p << L$), it finally comes:

$$\frac{R_{EE}{}^2}{L^2} = \frac{L.2L_p}{L^2} = \frac{2L_p}{L} < 1 \qquad \text{(VI.7)}$$

On the contrary, for stiff, rod-shaped polymers, $R_{EE}{}^2 \sim L^2$, as explained in the first paragraph . Hence, it comes: $\frac{R_{EE}{}^2}{L^2} \sim 1$.

The $\frac{R_{EE}{}^2}{L^2}$ parameter thus takes on values comprised between ]0;1], with soft polymers showing a value strictly inferior to 1 while rigid ones oscillates around values very close to 1. Hence, the $\frac{R_{EE}{}^2}{L^2}$ ratio can be regarded as a quantitative indicator of a polymer degree of rigidity.

Following the lead of Saghazadeh et al.[43], this rigidity index initially defined for polymer chains can be extended to other anisotropic objects with varying degrees of flexibility, such as NTs. The rigidity index of the nanocomposite tubes synthesized during this thesis were thus routinely computed and compared as a first insight into their mechanical properties.

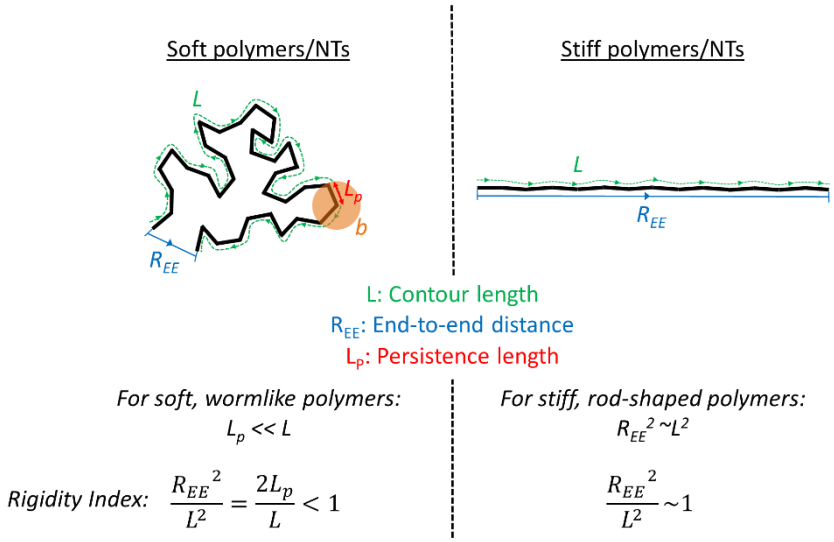


**Figure S5.14** *Schematic illustration of the rigidity index of soft and stiff polymers or NTs, defined as the ratio between the end-to-end distance and the contour length of the polymer or NT.*

Flattening index $\frac{D_{Tube}}{D_{Pore}}$

Once individual NTs are freed from their template via selective dissolution of the latter in DCM and filtered over a PET membrane, they tend to flatten due to the positive pressure applied during the filtration process. When imaged under the high vacuum conditions of the SEM, NTs are submitted to a negative pressure and further deformed. The lower the mechanical properties of the NTs, the more they will be affected by the applied pressure and the more they will deform and flatten upon filtration. These considerations lead us to define another quantitative parameter able to characterize the rigidity of NTs: the flattening index. This parameter is taken as the ratio between the average diameter of filtered NTs (diameter of NTs after filtration, $D_{Tube,AF}$) and the average diameter of the PC nanopores ($D_{Pore}$) from which they issue: $\frac{D_{Tube,AF}}{D_{Pore}}$. The initial diameter of the synthesized NTs (diameter of NTs before filtration, $D_{Tube,BF}$) is very close to the one of the templating membrane in which they are LbL-assembled ($D_{Tube,BF} \sim D_{Pore}$), and should stay that way after filtration for mechanically-stiff NTs (Figure

S5.15.a). On the contrary, the tube diameter can potentially evolve a lot upon filtration for very soft NTs (Figure S5.15.b).

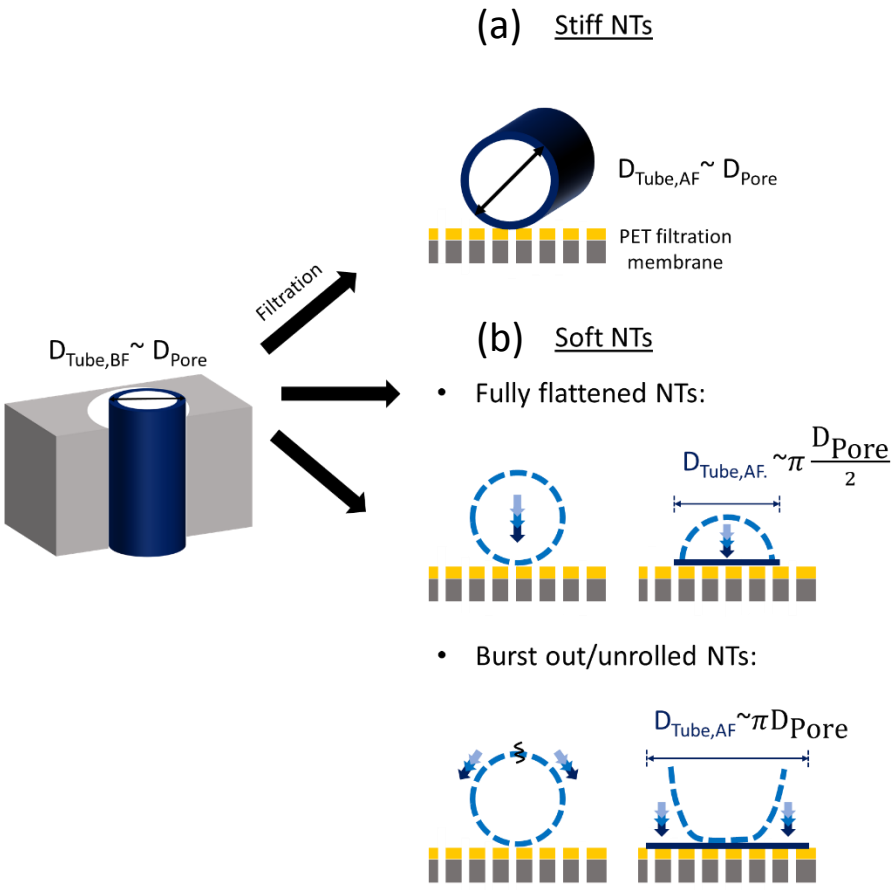


**Figure S5.15** *Schematic representation of the flattening index, defined as the ratio between the diameter of NTs measured after and before filtration for (a) stiff NTs and (b) soft NTs.*

The maximum length ($D_{Tube,AFMax}$) which can be obtained when measuring the diameter of a flattened nanocylinder of original diameter $D_{Tube,BF}$, can be computed as follows:

- If the NT is fully flattened, $D_{Tube,AFMax}$ becomes equal to the perimeter of the half-circle of diameter $D_{Tube,BF}$ ~ $D_{Pore}$: $D_{Tube,AFMax} = \frac{2\pi r_{pore}}{2} = \pi r_{pore} = \pi \frac{D_{Pore}}{2}$ (Figure S5.15.b). The flattening index thus becomes : $\frac{D_{Tube,AF}}{D_{Pore}} = \frac{\pi \frac{D_{Pore}}{2}}{D_{Pore}} = \frac{\pi}{2}$.

- If the NT is completely "broken down" and unrolled, $D_{Tube,AFMax}$ becomes equal to the perimeter of the full circle of diameter $D_{Tube,BF}$ ~ $D_{Pore}$ and it comes : $\frac{D_{Tube,AF}}{D_{Pore}} = \frac{\pi D_{Pore}}{D_{Pore}} = \pi$ (Figure S5.15.b).

Hence, the measured flattening index will range from ~ 1 for very rigid NTs to a maximum value of $\frac{\pi}{2}$ or $\pi$ for very soft NTs.

## 5.5 References

(1) Landoulsi, J.; Demoustier-Champagne, S.; Dupont-Gillain, C. Self-Assembled Multilayers Based on Native or Denatured Collagen: Mechanism and Synthesis of Size-Controlled Nanotubes. Soft Matter 2011, 7 (7), 3337. https://doi.org/10.1039/c0sm00918k.

(2) Mauquoy, S.; Dupont-Gillain, C. Combination of Collagen and Fibronectin to Design Biomimetic Interfaces: Do These Proteins Form Layer-by-Layer Assemblies? Colloids Surfaces B Biointerfaces 2016, 147, 54–64. https://doi.org/10.1016/j.colsurfb.2016.07.038.

(3) Weiner, S.; Wagner, H. D. THE MATERIAL BONE: Structure-Mechanical Function Relations. Annu. Rev. Mater. Sci. 1998, 28 (1), 271–298. https://doi.org/10.1146/annurev.matsci.28.1.271.

(4) Beniash, E. Biominerals—Hierarchical Nanocomposites: The Example of Bone. Wiley Interdiscip. Rev. Nanomedicine Nanobiotechnology 2011, 3 (1), 47–69. https://doi.org/10.1002/wnan.105.

(5) Silvester, L.; Lamonier, J.-F.; Vannier, R.-N.; Lamonier, C.; Capron, M.; Mamede, A.-S.; Pourpoint, F.; Gervasini, A.; Dumeignil, F. Structural, Textural and Acid–Base Properties of Carbonate-Containing Hydroxyapatites. J. Mater. Chem. A 2014, 2 (29), 11073–11090. https://doi.org/10.1039/C4TA01628A.

(6) Meagher, M. J.; Weiss-Bilka, H. E.; Best, M. E.; Boerckel, J. D.; Wagner, D. R.; Roeder, R. K. Acellular Hydroxyapatite-Collagen Scaffolds Support Angiogenesis and Osteogenic Gene Expression in an Ectopic Murine Model: Effects of Hydroxyapatite Volume Fraction. J. Biomed. Mater. Res. Part A 2016, 104 (9), 2178–2188. https://doi.org/10.1002/jbm.a.35760.

(7) Kasir, R.; Vernekar, V. N.; Laurencin, C. T. Inductive Biomaterials for Bone Regeneration. J. Mater. Res. 2017, 32 (6), 1047–1060. https://doi.org/10.1557/jmr.2017.39.

(8) Kikuchi, M.; Itoh, S.; Ichinose, S.; Shinomiya, K. Self-Organization Mechanism in a Bone-Like Hydroxyapatite / Collagen Nanocomposite Synthesized In Vitro and Its Biological Reaction In Vivo Self-

Organization Mechanism in a Bone-like Hydroxyapatite / Collagen Nanocomposite Synthesized in Vitro and Its Bio. Biomaterials 2001, 22, 1705–1711. https://doi.org/10.1016/S0142-9612(00)00305-7.

(9) Zhang, W.; Liao, S. S.; Cui, F. Z. Hierarchical Self-Assembly of Nano-Fibrils in Mineralized Collagen. Chem. Mater. 2003, 15 (16), 3221–3226. https://doi.org/10.1021/cm030080g.

(10) Tampieri, A.; Celotti, G.; Landi, E.; Sandri, M.; Roveri, N.; Falini, G. Biologically Inspired Synthesis of Bone-like Composite: Self-Assembled Collagen Fibers/Hydroxyapatite Nanocrystals. J. Biomed. Mater. Res. 2003, 67A (2), 618–625. https://doi.org/10.1002/jbm.a.10039.

(11) Maas, M.; Guo, P.; Keeney, M.; Yang, F.; Hsu, T. M.; Fuller, G. G.; Martin, C. R.; Zare, R. N. Preparation of Mineralized Nanofibers: Collagen Fibrils Containing Calcium Phosphate. Nano Lett. 2011, 11 (3), 1383–1388. https://doi.org/10.1021/nl200116d.

(12) Kokubo, T.; Takadama, H. How Useful Is SBF in Predicting in Vivo Bone Bioactivity? Biomaterials 2006, 27 (15), 2907–2915. https://doi.org/10.1016/j.biomaterials.2006.01.017.

(13) Kokubo, T.; Kushitani, H.; Sakka, S.; Kitsugi, T.; Yamamuro, T. Solutions Able to Reproducein Vivo Surface-Structure Changes in Bioactive Glass-Ceramic A-W3. J. Biomed. Mater. Res. 1990, 24 (6), 721–734. https://doi.org/10.1002/jbm.820240607.

(14) Marelli, B.; Ghezzi, C. E.; Zhang, Y. L.; Rouiller, I.; Barralet, J. E.; Nazhat, S. N. Fibril Formation PH Controls Intrafibrillar Collagen Biomineralization in Vitro and in Vivo. Biomaterials 2015, 37, 252–259. https://doi.org/10.1016/j.biomaterials.2014.10.008.

(15) Ikezawa, H. Glycosylphosphatidylinositol (GPI)-Anchored Proteins. Biol. Pharm. Bull. 2002, 25 (4), 409–417. https://doi.org/10.1248/bpb.25.409.

(16) Harrison, G.; Shapiro, I. M.; Golub, E. E. The Phosphatidylinositol-Glycolipid Anchor on Alkaline Phosphatase Facilitates Mineralization Initiation in Vitro. J. Bone Miner. Res. 2009, 10 (4), 568–573. https://doi.org/10.1002/jbmr.5650100409.

(17) Fosset, M.; Chappelet-Tordo; Lazdunski, M. Intestinal Alkaline Phosphatase. Physical Properties and Quaternary Structure.

Biochemistry 1974, 13 (9), 1783–1788. https://doi.org/10.1021/bi00706a001.

(18) Sabokbar, A.; Millett, P. J.; Myer, B.; Rushton, N. A Rapid, Quantitative Assay for Measuring Alkaline Phosphatase Activity in Osteoblastic Cells in Vitro. Bone Miner. 1994, 27 (1), 57–67. https://doi.org/10.1016/S0169-6009(08)80187-0.

(19) Dean, R. L. Kinetic Studies with Alkaline Phosphatase in the Presence and Absence of Inhibitors and Divalent Cations. Biochem. Mol. Biol. Educ. 2002, 30 (6), 401–407. https://doi.org/10.1002/bmb.2002.494030060138.

(20) Ngiam, M.; Liao, S.; Patil, A. J.; Cheng, Z.; Chan, C. K.; Ramakrishna, S. The Fabrication of Nano-Hydroxyapatite on PLGA and PLGA/Collagen Nanofibrous Composite Scaffolds and Their Effects in Osteoblastic Behavior for Bone Tissue Engineering. Bone 2009, 45 (1), 4–16. https://doi.org/10.1016/j.bone.2009.03.674.

(21) Ngiam, M.; Liao, S.; Patil, A. J.; Cheng, Z.; Yang, F.; Gubler, M. J.; Ramakrishna, S.; Chan, C. K. Fabrication of Mineralized Polymeric Nanofibrous Composites for Bone Graft Materials. Tissue Eng. Part A 2009, 15 (3), 535–546. https://doi.org/10.1089/ten.tea.2008.0011.

(22) Colaço, E. Design and Characterization of Biomimetic Biomineralized Nanomaterials, Université de Technologie de Compiègne.

(23) Richert, L.; Boulmedais, F.; Lavalle, P.; Mutterer, J.; Ferreux, E.; Decher, G.; Schaaf, P.; Voegel, J.-C.; Picart, C. Improvement of Stability and Cell Adhesion Properties of Polyelectrolyte Multilayer Films by Chemical Cross-Linking. Biomacromolecules 2004, 5 (2), 284–294. https://doi.org/10.1021/bm0342281.

(24) Monge, C.; Saha, N.; Boudou, T.; Pózos-Vásquez, C.; Dulong, V.; Glinel, K.; Picart, C. Rigidity-Patterned Polyelectrolyte Films to Control Myoblast Cell Adhesion and Spatial Organization. Adv. Funct. Mater. 2013, 23 (27), 3432–3442. https://doi.org/10.1002/adfm.201203580.

(25) Ren, K.; Crouzier, T.; Roy, C.; Picart, C. Polyelectrolyte Multilayer Films of Controlled Stiffness Modulate Myoblast Cell Differentiation. Adv. Funct. Mater. 2008, 18 (9), 1378–1389. https://doi.org/10.1002/adfm.200701297.

(26) Richert, L.; Engler, A. J.; Discher, D. E.; Picart, C. Elasticity of Native and Cross-Linked Polyelectrolyte Multilayer Films. Biomacromolecules 2004, 5 (5), 1908–1916. https://doi.org/10.1021/bm0498023.

(27) Boudou, T.; Crouzier, T.; Auzély-Velty, R.; Glinel, K.; Picart, C. Internal Composition versus the Mechanical Properties of Polyelectrolyte Multilayer Films: The Influence of Chemical Cross-Linking. Langmuir 2009, 25 (24), 13809–13819. https://doi.org/10.1021/la9018663.

(28) Schneider, A.; Obeid, R.; Schwinte, P.; Hemmerle, J.; Schaaf, P.; Voegel, J.; Senger, B.; Picart, C.; Dentaire, D. C.; Pasteur, L.; et al. Polyelectrolyte Multilayers with a Tunable Young ' s Modulus : Influence of Film Stiffness on Cell Adhesion. Langmuir 2006, 22 (3), 1193–1200.

(29) Smith, P. K.; Krohn, R. I.; Hermanson, G. T.; Mallia, A. K.; Gartner, F. H.; Provenzano, M. D.; Fujimoto, E. K.; Goeke, N. M.; Olson, B. J.; Klenk, D. C. Measurement of Protein Using Bicinchoninic Acid. Anal. Biochem. 1985, 150 (1), 76–85. https://doi.org/10.1016/0003-2697(85)90442-7.

(30) Wiechelman, K. J.; Braun, R. D.; Fitzpatrick, J. D. Investigation of the Bicinchoninic Acid Protein Assay: Identification of the Groups Responsible for Color Formation. Anal. Biochem. 1988, 175 (1), 231–237. https://doi.org/10.1016/0003-2697(88)90383-1.

(31) Brown, R. E.; Jarvis, K. L.; Hyland, K. J. Protein Measurement Using Bicinchoninic Acid: Elimination of Interfering Substances. Anal. Biochem. 1989, 180 (1), 136–139. https://doi.org/10.1016/0003-2697(89)90101-2.

(32) Krohn, R. I. The Colorimetric Detection and Quantitation of Total Protein. Curr. Protoc. Cell Biol. 2002, 15 (1), A.3H.1-A.3H.28. https://doi.org/10.1002/0471143030.cba03hs15.

(33) Weichselbaum, T. E. An Accurate and Rapid Method for the Determination of Proteins in Small Amounts of Blood Serum and Plasma. Am. J. Clin. Pathol. 1946, 10, 40–49.

(34) Gornall, A. G.; Bardawill, C. J.; David, M. M. Determination of Serum Proteins by Means of the Biuret Reaction. J. Biol. Chem. 1949, 177 (2), 751–766.

(35) Lowry, O. H.; Rosebrough, N. J.; Farr, A. L.; Randall, R. J. Protein

Measurement with the Folin Phenol Reagent. J. Biol. Chem. 1951, 193, 265–275.

(36) Legler, G.; Müller-Platz, C. M.; Mentges-Hettkamp, M.; Pflieger, G.; Jülich, E. On the Chemical Basis of the Lowry Protein Determination. Anal. Biochem. 1985, 150 (2), 278–287. https://doi.org/10.1016/0003-2697(85)90511-1.

(37) Bradford, M. M. A Rapid and Sensitive Method for the Quantitation of Microgram Quantities of Protein Utilizing the Principle of Protein-Dye Binding. Anal. Biochem. 1976, 72 (1–2), 248–254. https://doi.org/10.1016/0003-2697(76)90527-3.

(38) Schitter, G.; Menold, P.; Knapp, H. F.; Allgöwer, F.; Stemmer, A. High Performance Feedback for Fast Scanning Atomic Force Microscopes. Rev. Sci. Instrum. 2001, 72 (8), 3320–3327. https://doi.org/10.1063/1.1387253.

(39) Cappella, B.; Dietler, G. Force-Distance Curves by Atomic Force Microscopy. Surf. Sci. Rep. 1999, 34 (1–3), 1–104. https://doi.org/10.1016/S0167-5729(99)00003-5.

(40) Butt, H.-J.; Cappella, B.; Kappl, M. Force Measurements with the Atomic Force Microscope: Technique, Interpretation and Applications. Surf. Sci. Rep. 2005, 59 (1–6), 1–152. https://doi.org/10.1016/j.surfrep.2005.08.003.

(41) Cappella, B. Mechanical Properties of Polymers Measured through AFM Force-Distance Curves; Springer, Ed.; 2018.

(42) Rosa-Zeiser, A.; Weilandt, E.; Hild, S.; Marti, O. The Simultaneous Measurement of Elastic, Electrostatic and Adhesive Properties by Scanning Force Microscopy: Pulsed-Force Mode Operation. Meas. Sci. Technol. 1997, 8 (11), 1333–1338. https://doi.org/10.1088/0957-0233/8/11/020.

(43) Minne, S.; Hu, Y.; Hu, S.; Pittenger, B.; Su, C. NanoScale Quantitative Mechanical Property Mapping Using Peak Force Tapping Atomic Force Microscopy. Microsc. Microanal. 2010, 16 (S2), 464–465. https://doi.org/10.1017/S1431927610061829.

(44) Pittenger, B.; Erina, N.; Su, C. Mechanical Property Mapping at the Nanoscale Using PeakForce QNM Scanning Probe Technique. In

Nanomechanical Analysis of High Performance Materials. Solid Mechanics and its Applications; Tiwari, A., Ed.; Springer: Dordrecht, 2014; pp 31–51. https://doi.org/10.1007/978-94-007-6919-9_2.

(45) Shi, J.; Hu, Y.; Hu, S.; Ma, J.; Su, C. Method and Apparatus of Using Peak Force Tapping Mode to Measure Physical Properties of a Sample. 8,650,660, 2014.

(46) Lorenzoni, M.; Evangelio, L.; Verhaeghe, S.; Nicolet, C.; Navarro, C.; Pérez-Murano, F. Assessing the Local Nanomechanical Properties of Self-Assembled Block Copolymer Thin Films by Peak Force Tapping. Langmuir 2015, 31 (42), 11630–11638. https://doi.org/10.1021/acs.langmuir.5b02595.

(47) Young, T. J.; Monclus, M. A.; Burnett, T. L.; Broughton, W. R.; Ogin, S. L.; Smith, P. A. The Use of the PeakForce TM Quantitative Nanomechanical Mapping AFM-Based Method for High-Resolution Young's Modulus Measurement of Polymers. Meas. Sci. Technol. 2011, 22 (12), 125703. https://doi.org/10.1088/0957-0233/22/12/125703.

(48) Saghazadeh, S.; Zhang, S.; Lefèvre, D.; Le Beulze, A.; Jonas, A. M.; Demoustier-champagne, S. Universal Method to Transfer Membrane-Templated Nano-Objects to Aqueous Solutions. Langmuir 2015, 31 (26), 7264–7273. https://doi.org/10.1021/acs.langmuir.5b01648.

# Chapter 6

# Biofunctionalized and self-supported polypyrrole frameworks as nanostructured ECM-like biointerfaces

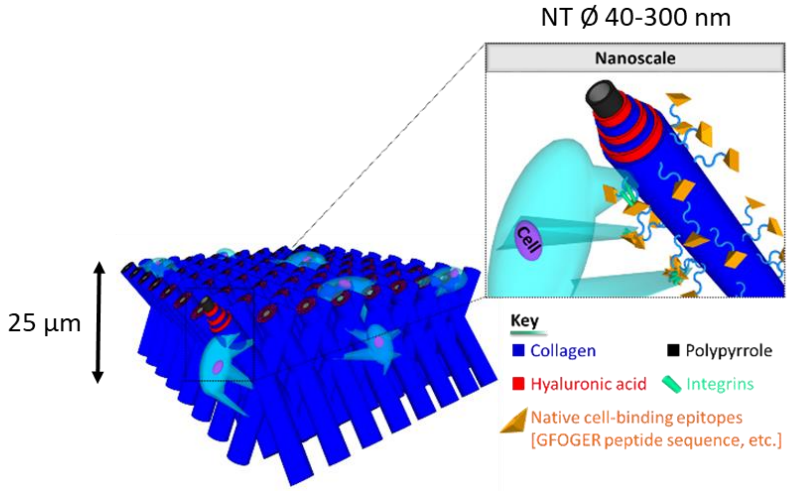


Based on the publication : Lefèvre, D., Louvegny, J., Naudin, M., Ferain, E., Dupont-Gillain, C. & Demoustier-Champagne, S. Biofunctionalized and self-supported polypyrrole frameworks as nanostructured ECM-like biointerfaces. RSC Advances 8, 22932-22943 (2018).

## Abstract

Hybrid nanobiointerfaces were designed as an original contribution to the challenge of synthesizing nanostructured biomaterials integrating a set of cell fate-determining cues, originally provided to cells by the extracellular matrix (ECM). The produced biointerfaces consist of a stiff framework of intersected polypyrrole (PPy) nanotubes supporting a soft multilayer composed of ECM-derived biomacromolecules: collagen (Col) and hyaluronic acid (HA). PPy frameworks with highly tunable characteristics were

synthesized through chemical oxidative polymerization of pyrrole monomers, templated within track-etched polycarbonate (PC) membranes featuring a network of intersected nanopores. PPy interfaces with a porosity of 80%, composed of nanotubes with an average diameter ranging from 40 to 300 nm, intersecting at an angle of 90°, were shown to be self-supported. These rigid PPy nanostructured interfaces were functionalized with a self-assembling (HA/Col) multilayer deposited via a layer-by-layer process. Biofunctionalized and unmodified PPy frameworks were both shown to promote sustained cell adhesion, therefore demonstrating the cytocompatibility of the engineered matrices. Such nanobiointerfaces, combining a mechanically-stable framework of tunable dimensions with a soft biopolymeric multilayer of highly versatile nature, pave the way towards cell-instructive biomaterials able to gather a wide range of cues guiding cell behavior. The developed self-supported structures could be used as a coating or as membranes bridging different tissues.

## 6.1 Introduction

Designing tissue engineering and regenerative medicine strategies remains challenging in modern nanosciences, their successful outcome being largely dependent on the availability of suitable biointerfaces able to artificially recreate down to the nanoscale the conditions ultimately guiding cell fate in vivo.[1–4] As the complex interplay of topographical, mechanical, biochemical and physicochemical stimuli controlling cell behaviour[5–10] is originally provided in nature through the extracellular matrix (ECM), current trends in tissue engineering mainly focus on the development of biomaterials mimicking the native ECM.[11–13] The complexity of the highly diverse cell-instructive cues found in vivo is reflected in the wide variety of bioinspired materials found in the literature, which attempt at replicating the 3-dimensional (3D) intricate network of fibrillary proteins, proteoglycans and glycoaminoglycans originally constituting the cell environment.[14,15] In particular, in view of the variety of roles played by collagen in different tissues, research has focused on developing novel collagen-based biomaterials to mimic the architecture of native collagen-based ECM. Among the different methods reported up to now for producing fibers of dimensions close to those of native ECM (diameters ranging between 50 and 500 nm), electrospinning appears as an attractive and widely used method.[16,17] This technique indeed allows to generate porous mats made of various synthetic and natural polymer fibers. However, due to the need of rather high electric fields and harsh solvents, electrospinning of collagen is still quite challenging when preservation of protein function is required.[18] Another approach consists in combining ECM-derived biomacromolecules for the design of biomimetic multilayers,[19–21] but their weak mechanical properties restrict their application to coatings of pre-existing biomaterials, as their in vivo transposition requires a supporting substrate. In an attempt to overcome the lack of mechanical integrity of biopolymers, different groups developed composite materials of collagen and multi-walled carbon nanotubes.[22,23] Even though these composites showed and appropriate macroporous architecture and were effective at enhancing cell proliferation, no clear control could be exerted over the nanoscale topography, which is a widely recognized cell-instructive agent.[2425] These examples illustrate the complexity in meeting the requirements for a mechanically-stable

architecture, easy to handle at the macroscale, while at the same time featuring the wide diversity of cell-regulating nanoscale tags found in native ECM.

Here, we report on an original contribution to this current challenge. Hybrid mechanically-stable and self-supported polymer networks made of core-shell nanotubes, combining the biocompatibility and bioactivity of naturally-derived biomacromolecules with the mechanical stability of a rigid polymer core were designed and synthesized through a versatile template-based fabrication method (Figure 6.1). For that purpose, flexible nanoporous membranes featuring a peculiar network of intersected nanopores[26,27] were prepared through sequential polycarbonate (PC) film irradiation with heavy energetic ions at different incident angles, followed by chemical etching of the ion tracks created within the polymer film (see Figure 6.1a). These membranes exhibit tunable properties such as membrane thickness (ranging from 5 to 25 µm), pore density (107 to 1010 pores.cm$^{-2}$), average pore diameter (ranging from 30 to 400 nm) and angle of intersection between crossing ion tracks (random or set at a fixed value).Next, polypyrrole (PPy), a stiff[28], electroactive and biocompatible[29–32] polymer was synthesized within the pores of these PC membranes, used as templates, through a fast and easy chemical polymerization route[33] (Figure 6.1b, step 1). After removal of the PC template, arrays of intersected PPy nanotubes (Figure 6.1b, step 2) with well-controlled architecture were obtained. A range of properties of the PC template were optimized to get freestanding nanofibrous interfaces. In a third step, engineered stiff PPy networks were functionalized with a self-assembled multilayer based on the alternate adsorption of two ECM-derived biopolymers: hyaluronic acid (HA) and type I collagen (Col) (Figure 6.1b, Step 3). Col is the most abundant protein in mammals and is ubiquitously present as a structural protein in the ECM.[34,35] Type I Col, in particular, is well-known for featuring peptide sequences (i.e. GFOGER[13,36] and DGEA[37,38] motifs, etc.) responsible for triggering integrin-mediated cell adhesion[39,40] and was also demonstrated to play a role in cellular differentiation, especially towards the osteoblastic lineage.[37,41] In order to benefit from these bioactive properties, Col was thus specifically chosen to decorate the outermost layer of the biofunctionalized interfaces. HA, a linear glycosaminoglycan copolymer of D-glucuronic acid and N-acetyl-D-glucosamide also abundantly present in native ECM[42] was more recently discovered to be granted with numerous

biological functions. HA is indeed involved in cell signalling, including proliferation,[43] migration[44] and adhesion.[45,46] HA was therefore selected as second partner for the layer-by-layer (LbL) assembly of the biomimetic multilayer, in combination with Col. Although the great interest of these two biomolecules has been clearly demonstrated, reports focusing on the LbL assembly of Col and HA remain scarce in the literature,[47–50] probably due to the complexity of the selection of adequate assembling conditions. Using the optimal conditions described in chapter 4 to trigger the self-assembly of Col & HA, the construction of the biomimetic (HA/Col) multilayer was initiated on the rigid PPy nanotube networks to yield a core-shell structure. The osteogenic properties of Col in combination with the hybrid core-shell structure of the engineered biointerfaces encouraged us to evaluate their potential as bone matrix mimics.[51] The cytocompatibility of these new nanostructured biointerfaces was thus assessed through preliminary cell adhesion tests with murine MC3T3-E1 pre-osteoblasts, chosen as typical model cells whose behaviour (adhesion, proliferation, differentiation) highly depends on bone matrix organization.

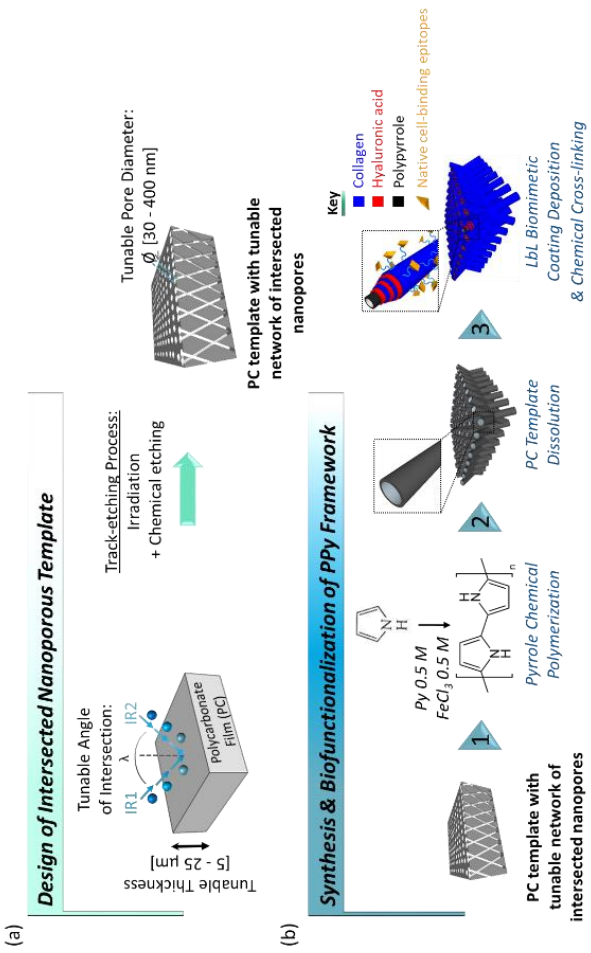


**Figure 6.1** *Schematic of (A) the track-etching process for the production of nanostructured polycarbonate membranes featuring a network of intersected nanochannels. (B) the elaboration of engineered nano-biointerfaces mimicking the structure of native ECM. The network of interconnected nanopores of the PC template is first replicated through oxidative polymerization of pyrrole monomers (step 1). After dissolution of the sacrificial template (step 2), the resulting framework of intersected polypyrrole nanotubes is functionalized with a (HA/Col) multilayer via LbL deposition. The biopolymer shell is finally chemically cross-linked (step 3). The whole process yields biointerfaces with a core-shell structure.*

## 6.2 Results and discussion

### 6.2.1 Template synthesis of self-supported PPy frameworks

In order to select the set of template characteristics most likely to yield mechanically-stable, self-supported frameworks of intersected PPy nanotubes, chemical polymerization of Py was performed inside the pores of various PC membranes (PCT1-5, *see* Table 6.1). To evaluate the morphology and mechanical integrity of the resulting PPy nanostructures, they were collected through selective dissolution of the PC template and imaged by SEM. Pictures from Fig.6.2 clearly demonstrate that architectures made of intersected PPy nanotubes were produced in all cases, with dimensions matching those of the used PC template. The first framework (Fig.6.2a), issued from template PCT1 with an average pore diameter of 400 nm and random angles of intersection between nanotubes, shows a microporous architecture (Fig.6.2.a1), as could be expected with a porosity as high as 90%. When zooming in (Fig.a2), we can clearly distinguish widely spaced yet interconnected sheets of nanotubes, responsible for the microporous lamellar structure of the whole interface. When observing the framework sideways (Fig.a3), the lamellar structure originating from these interconnected nanotube sheets is even more blatant. Although such an interface combining a microporous structure and nanotopographical cues could turn out to be particularly interesting to study and control cell behaviour, it does not fulfil the requirement for a self-supported architecture. The lack of mechanical stability is clearly a consequence of the too high porosity of the intersecting network, which is in turn the result of a too low pore density of the original templating PC membrane. When designing template PCT2, the density of nanopores was therefore increased while the average pore diameter was left unchanged. The resulting second network is slightly less porous than the first one: a highly homogeneous interface is obtained, both at the micro- and macroscale (Fig.b1). At higher magnification (Fig.b2), some intersections between nanotubes are clearly visible. However, images of the edge of the nanostructured framework (Fig.b3) reveal that the network is partially collapsing. The still high porosity (~86%) is again responsible for the low mechanical strength of the structure. So as to impart better mechanical stability, the overall porosity was further

decreased while the number of intersections between nanotubes was increased. For that purpose, a third PC template was designed with a lower pore diameter (Ø = 150 nm) coupled to a higher pore density (template PCT3 of Table 6.1). A highly homogeneous framework, both at the macro- and microscale, resulted again from the polymerization of Py within this template (Fig.c1 and c2). Nonetheless, the sides of the PPy network were unstable (Fig.c3), as nanotubes were still collapsing. Further detailed observations evidenced that this instability can be attributed to a too low density of nanotube intersections, which is a side effect of the reduction of the average nanotube diameter. To conciliate these two conflicting requirements, a new parameter was adjusted, i.e. the angle at which nanotubes intersect (λ). A new PC template (template PCT4 of Table 6.1) was therefore designed to combine a level of porosity set at 80% with an intermediate pore diameter of 300 nm. The angle of intersection between tubes was set at 90°. This implies the PC film to be irradiated twice with an ion beam aligned at +45° and -45° with respect to the normal of the template surface. The resulting PPy framework shows a highly uniform and well-organized architecture, with PPy nanotubes intersecting at an angle of 90° (Fig.d1-d3). Furthermore, the intersected PPy network meets the requirements for a self-supported material (see inset in Figure d1) and is therefore optimal to pursue the targeted applications. Further exploiting the set of refined parameters (i.e., intersecting angle λ = 90°, average porosity ~ 80-85%), freestanding PPy networks composed of nanotubes with a diameter as low as 40 nm were successfully synthesized (Fig.e1-e3), strongly evidencing the possibility to finely tune the nanotopography presented by the nanostructured PPy platforms.

**Table 6.1** *Characteristics of the PC membranes used as template for the preparation of frameworks of intersected PPy NTs. Tunable key parameters of these PC templates with intersected nanopores include the average diameter of nanopores [Ø], the pore density [ρ], the thickness of the template [L], the angle at which the pores intersect [λ] and the average porosity [P] of the obtained framework, computed as follows:*

$$\mathrm{P} = \left(1\text{-}\rho \times \left(\frac{\emptyset}{2}\right)^2 \times \pi\right) \times 100$$

| PC template | Pore diameter : Ø (nm) | Pore density : ρ (# pores per cm$^2$) | Template thickness : L (µm) | Angle of intersection : λ (°) | Computed porosity of resulting framework: P (%) |
|---|---|---|---|---|---|
| **PCT1** | 400 | 6.4 x $10^7$ | 25 | Random (0 ≤λ ≤90) | ~ 90 |
| **PCT2** | 400 | 1.05 x $10^8$ | 25 | Random (0 ≤λ ≤90) | ~ 86 |
| **PCT3** | 150 | 1 x $10^9$ | 25 | Random (0 ≤λ ≤90) | ~ 82 |
| **PCT4** | 300 | 2.8 x $10^8$ | 25 | ~ 90 | ~ 80 |
| **PCT5** | 40 | 1.2 x $10^{10}$ | 25 | ~ 90 | ~ 85 |

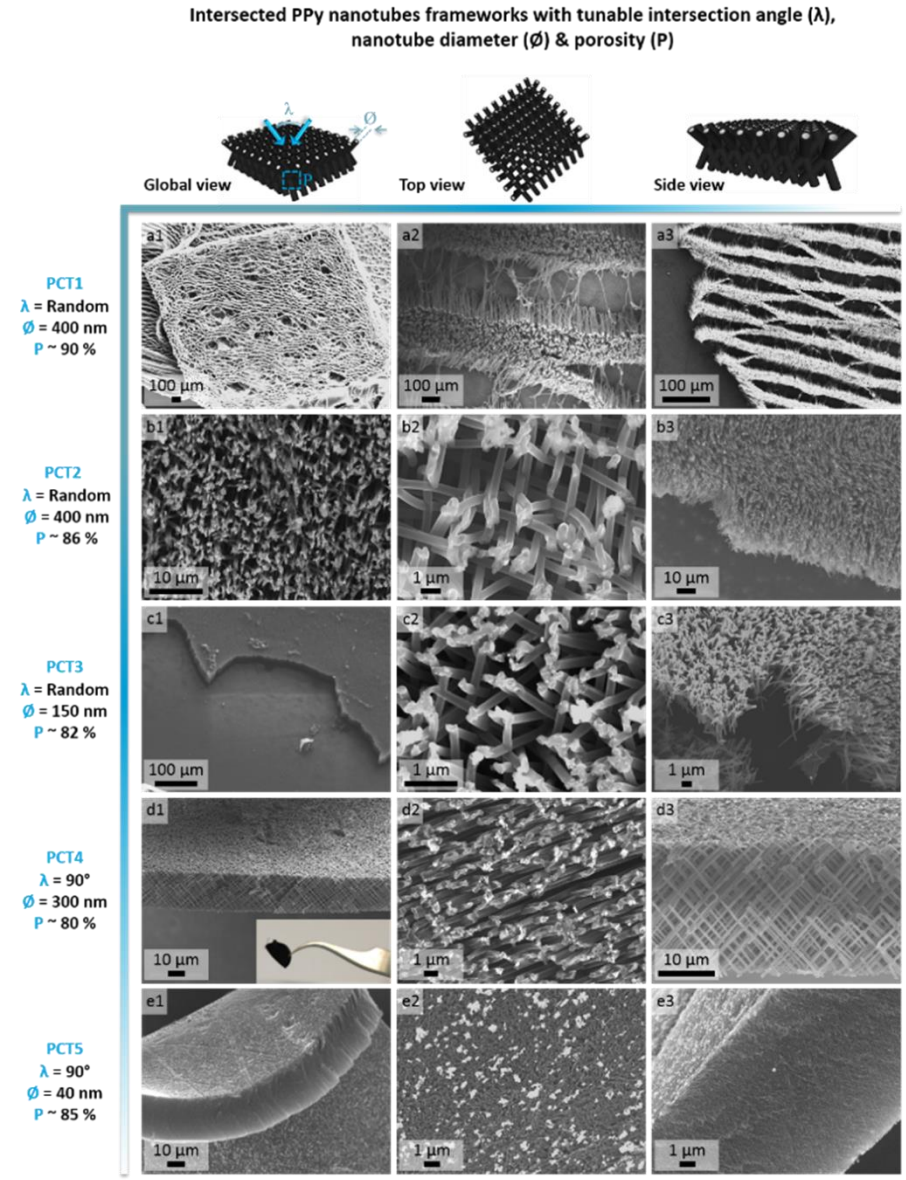


**Figure 6.2** *SEM images of (a-e) chemically polymerized frameworks of intersected PPy nanotubes with different intersection angles [λ], average nanotube diameter [Ø] and porosity [P]. (1) : global view, (2) : top view and (3) : side view of the synthesized frameworks. The inset in d1 shows the typical macroscale morphology of the self-supported PPy frameworks derived from PCT4.*

### 6.2.2 Biofunctionalization of PPy frameworks

*a) Exploratory phase*

An exploratory phase was first conducted to evaluate the feasibility of functionalizing stiff PPy NTs with a soft polymer multilayer *via* a LbL process. Rather than using matrices of intersected NTs, this preliminary stage was carried out using individual PPy NTs (Ø 500nm, L 21 µm), derived from the polymerization of Py inside a PC template with parallel nanopores. Two distinct processes were considered in order to coat the rigid PPy core. The first method is a fully templated approach, referred to as "pre-polymerization coating" process, as the polymer multilayer is first LbL-assembled inside the template nanopores prior to initiating the polymerization of the PPy core. The second approach entails, first, the templated polymerization of PPy NTs, the consecutive dissolution of the PC template and collection of the NTs over a PET filter and, finally, dipping of the supported NTs into solutions of oppositely-charged polymers to assemble the soft polymer shell. Hence, this process is referred to as "post-polymerization coating" approach. Following the unsuccessful outcome of the pre-polymerization coating process (*see* S.I.6.1), only the post-polymerization approach was deemed satisfactory and further used throughout the present work.

*b) Main results*

In order to produce ECM-like biointerfaces, the alternate adsorption of HA and Col was initiated on the optimally designed self-supported PPy frameworks derived from template PCT4 (*see* Table 6.1). The biomimetic (HA/Col) shell was deposited on the NT network in a stepwise, LbL fashion carried out in UPW at pH 4.0. These conditions were favored over higher ionic strength conditions (i.e., $I$ = 0.15 M), following the observation that the network of NTs was more homogeneously coated with the biopolymers when they were assembled in UPW as compared to 0.15 M NaCl conditions (*see* SI, Figure S6.3). The build-up of the (Col/HA) multilayer in UPW pH 4.0 was further monitored on reference quartz substrates via QCM-D (Figure 6.3). Figure 6.3 (a) displays the gradual evolution of the mass adsorbed at the crystal surface following the stepwise adsorption of HA and Col. The relatively linear increase in $\Delta f$ upon injection of each biopolymer confirms

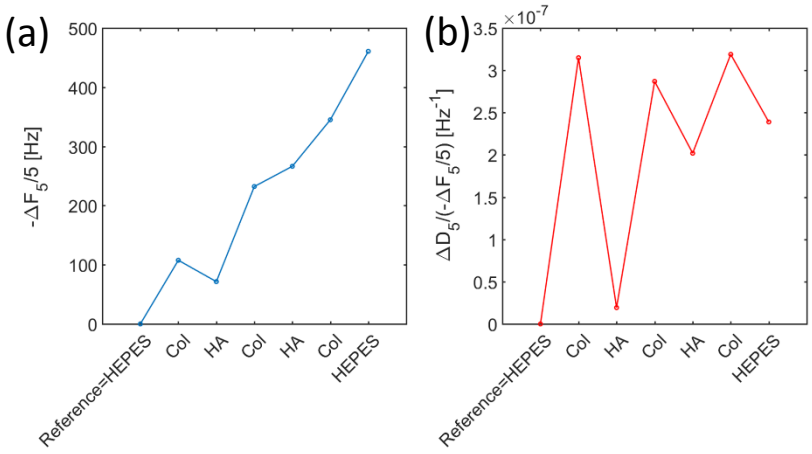


**Figure 6.3** *Cumulated (a) -Δf₅/5 (proportional to the adsorbed wet mass) and (b) ΔD₅/(-Δf₅/5) extracted from the real time QCM-D monitoring of the construction of the (Col/HA)$_{2.5}$ film [Col & HA 1 mg.mL$^{-1}$ in UPW pH 4.0].*

the capacity of these molecules to interact together, in order to create complex multilayered architectures in a LbL fashion. The high dissipation increase (Figure 6.3 (b)) recorded after each Col injection step is characteristic of the adsorption of Col as a soft and viscoelastic layer, as previously described by Landoulsi *et al*.[52]. Circulation of HEPES buffer (10 mM, NaCl 0.15 M, pH 7.4) on the self-assembled (Col/HA) multilayer leads to a swelling of the biopolymer multilayer, without causing any subsequent multilayer deconstruction. The (Col/HA) multilayer built in the chosen conditions is thus stable under physiological conditions, in contrast to the previous conclusions of Johansson *et al*.[48]. SEM images showing the PPy interface sideways, before (Fig.6.4 a-c) and after (Fig.6.4 d-f) LbL assembly of 6 bilayers of the (HA/Col) system, clearly highlight the effective construction of a biopolymer shell surrounding the nanotubes (Fig.6.4 d-f). Furthermore, Figure 6.4 (c & f) confirms the tubular nature of the framework building blocks, as central open pores can be distinguished. Aerial views of the scaffolding PPy platforms further emphasize the presence of the polymer coating (Fig.S6.4 c and S6.4 d).

The growth of the biomimetic (HA/Col) multilayer was further investigated by SEM, as the rigid PPy network was submitted to the deposition of an increasing number of (HA/Col) bilayers (starting from 3 up to 12 bilayers) (Fig.6.5-sideways and S6.5-aerial views). While the growth of

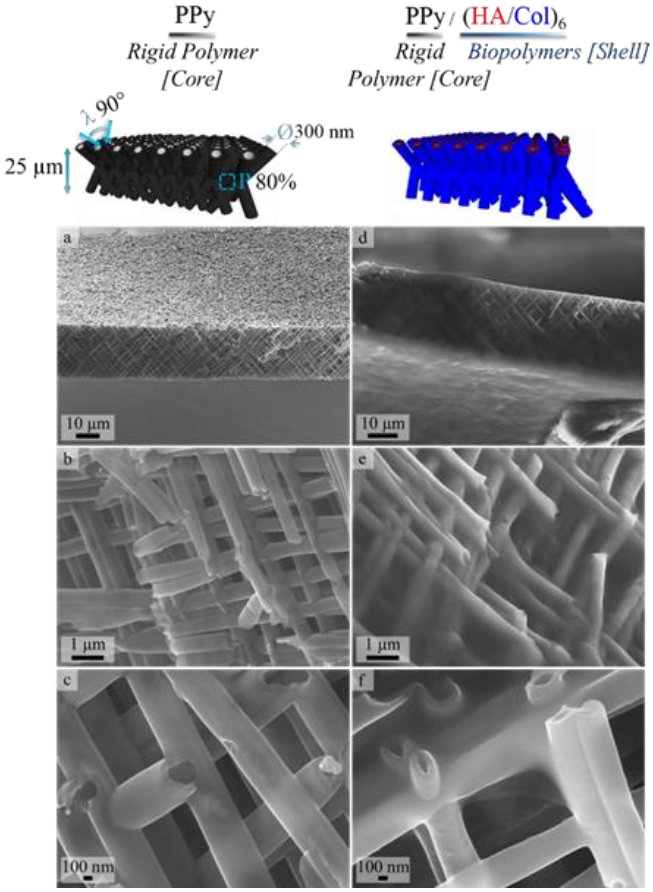


**Figure 6.4** *SEM images showing a side view of PPy framework (a-c) before biofunctionalization [increasing magnification from a to c] and (d-f) after LbL deposition of 6 bilayers of HA & Col.*

the $(HA/Col)_n$ system appears to be first limited, in the early stages of the deposition process, to a soft polymer adlayer directly covering the nanotubes surface (Fig.6.5 a & b), it rapidly expands towards the intertubular space, finally merging after deposition of 12 bilayers into a dense polymer gel completely masking the constituting tubules (Fig.6.5 d-sideways and Fig.S6.5 d-aerial view). The fibrillar structure of the polymer crust can be attributed to the fibrillation of Col, a phenomenon commonly reported under the studied conditions.[49,53] The progressive growth of the HA/Col multilayer further opens the opportunity to tune the thickness of the biomimetic shell functionalizing the rigid PPy interface.

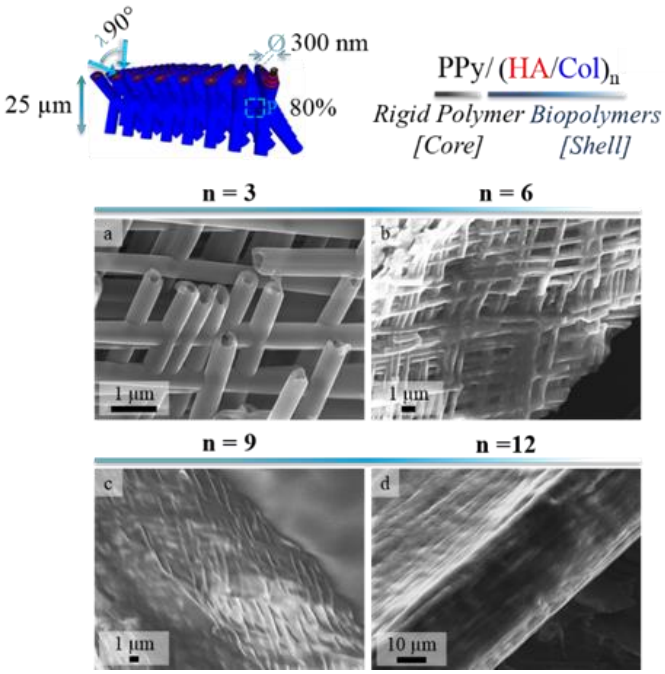


**Figure 6.5** *SEM images showing a side view of PPy frameworks after deposition of an increasing number of (HA/Col) bilayers : (a) 3 bilayers, (b) 6 bilayers, (c) 9 bilayers and (d) 12 bilayers.*

The mass of Col effectively deposited on the PPy frameworks was further evaluated using a µBCA assay (Figure 6.6) and compared to that adsorbed on reference quartz substrates *via* QCM-D monitoring (Table 6.2). It is striking to observe that the mass of Col deposited on the PPy framework with 40-nm diameter NTs is much lower than that adsorbed on larger 300-nm diameter NTs and remains below the detection limit of the assay whatever the number of assembled bilayers. While at first glance, this might be attributed to the lower superficial area available to Col adsorption on individual 40-nm diameter tubes as compared to 300-nm diameter ones, this argument does not hold when taking into account the total superficial area developed by each matrix. Indeed, the total superficial area developed by the PPy platforms with intersected NTs of 40-nm diameter was computed to be over 5 times greater than that of the matrices with 300-nm diameter NTs (103 versus 580 $cm^2$ for the matrix with 300-nm and 40-nm tube diameter, respectively; *see Th.A.5.III & 5.IV*). The diffusion and adsorption of the Col

biomacromolecule within PPy frameworks displaying a lower density of larger diameter NTs must therefore be eased compared to the case of matrices with a higher density of smaller diameter tubes. The average size of the porosity is indeed visibly lower in the latter case (Figure 6.2 d3 versus e3), which might drastically impair the diffusion of the Col molecule being highly extended under low *I* conditions. Moreover, the diameter of the 40-nm diameter NTs might be too small compared to the dimensions of the extended Col molecule in UPW (~ 300 nm long) to allow proper adsorption of the biopolymer.

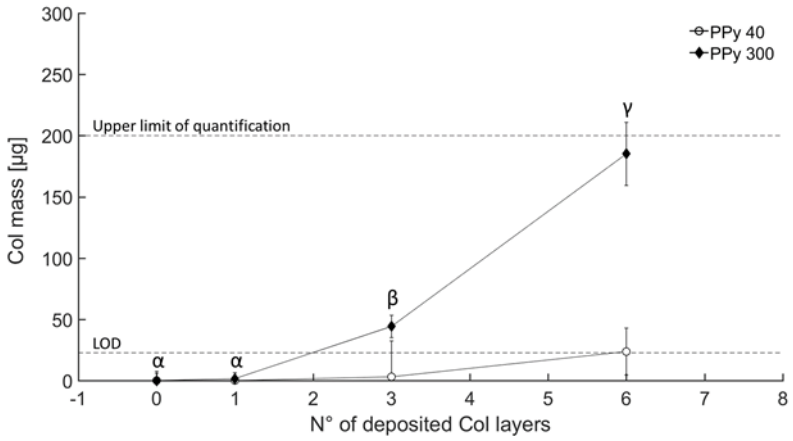


**Figure 6.6** *Mass of Col (µg), as determined via µBCA assay, effectively deposited over PPy frameworks (average tube diameter of 40 nm, open circles, and 300 nm, black diamonds) as a function of the number of LbL-assembled (HA/Col) bilayers. The solid line connecting individual data points is added as a guide to the eye. Error bars represent standard deviation (n=3). Bars topped with different greek letters indicate significant difference (p-value < 0.05 as computed via consecutive Welch's ANOVA and Games-Howell post hoc tests). Limit of detection, LOD, was experimentally determined to be 22.64 µg. Upper limit of quantification was experimentally determined to be 200 µg.*

Dividing the values obtained from the µBCA test plotted in Figure 6.6 by the superficial area of the custom-made PPyØ300nm framework (0.0103 $m^2$; Th.A.5.III) enables a comparison to be made between the mass of Col incorporated in flat multilayered thin films (derived from QCM-D data) and that deposited over nanostructured PPy interfaces (derived from µBCA data). In a similar fashion as the observations made in Chapter 5 for composite biointerfaces, the amount of Col adsorbed per square centimeter of 3D interface is much lower than the amount of Col adsorbed per square centimeter of quartz crystal. A hypothesis can be formulated to explain this observation : frameworks of intersected NTs most probably oppose a higher resistance to the diffusion of large Col & HA biomacromolecules in comparison with flat substrates. This higher diffusion barrier is coupled to a much higher surface area available to adsorption in the case of 3D interfaces (~ 100 $cm^2$ for a PPy framework with 300-nm diameter intersected tubes versus ~ 1 $cm^2$ for a quartz crystal). The combined effect of a low concentration of diffusing molecules reaching into a meshwork of tremendously high surface area might favor the adsorption of biopolymers under a low spatial density regime, the molecules adsorbing under an extended conformation so as to maximize the number of interaction sites with the surface and thus leading to thinner layers. The validity of this hypothesis is further reinforced by the evidence that the mass of protein adsorbed on the 40-nm NT interface, displaying both a porosity of lower size and a higher total surface area, is even lower than that on the 300-nm NT interface. In addition, one has to keep in mind that whereas QCM-D measures the total wet mass of molecules adsorbed over the crystal surface in a non-specific manner, the µBCA test specifically determines the dry mass of proteins. It therefore makes sense that the wet protein mass extracted from QCM-D data should be higher than the dry mass obtained through µBCA assay.

**Table 6.2** *Comparison between the cumulated areal mass and cumulated thickness of the Col layer(s) incorporated in flat multilayered thin films (QCM-D date) or assembled over nanostructured PPy interfaces (µBCA data)*

| N° of deposited Col layer(s) | Cumulated areal mass (ng.cm$^{-2}$) | | Cumulated thickness (nm) | |
|---|---|---|---|---|
| | QCM-D | µBCA | QCM-D | µBCA |
| **1** | 1906 | 15 | 19 | 0 |
| **2** | 4752 | / | 48 | / |
| **3** | 6145 | 429 | 62 | 4 |
| **6** | / | 1797 | / | 18 |

Information regarding the surface chemistry of (un)coated PPy biointerfaces was obtained using Fourier-transform infrared spectroscopy with an attenuated total reflection system (ATR-FTIR). FTIR spectra of uncoated and $(HA/Col)_6$-biofunctionalized PPy frameworks are compared in Figure 6.7 (a & b, respectively). The native PPy interface displays the typical fingerprint of naked PPy, with characteristic absorbance peaks like the band centered around 1550 cm$^{-1}$ representing the Py ring vibration, the C-N stretching vibration peak at ~1470 cm$^{-1}$, the C-H vibration band at ~1040 cm$^{-1}$ and the absorbance peak at ~1320 cm$^{-1}$ attributed to the C-C stretching vibration.[54,55] The change in interfacial chemistry upon introduction of the biomimetic $(HA/Col)_6$ multilayer is clearly visible in the FTIR spectrum and confirms the successful biofunctionalization of the PPy network. Indeed, whereas the peaks characteristic of PPy disappear, a set of absorbance bands highly characteristic of proteins and polysaccharides can be identified[56,57]: the amide I, II and III bands centered at ~1650 cm$^{-1}$, ~1550 cm$^{-1}$ and ~1320 cm$^{-1}$, respectively; the absorbance peak located around 1150 cm$^{-1}$, attributed to the antisymmetric C-O-C stretching of glycosidic groups present in carbohydrate moieties; the vibration band of carboxylate groups at ~1410 cm$^{-1}$; as well as the broad and intense band located at ~3250 cm$^{-1}$ which corresponds to N-H and O-H groups engaged in hydrogen bonds in both HA and Col.

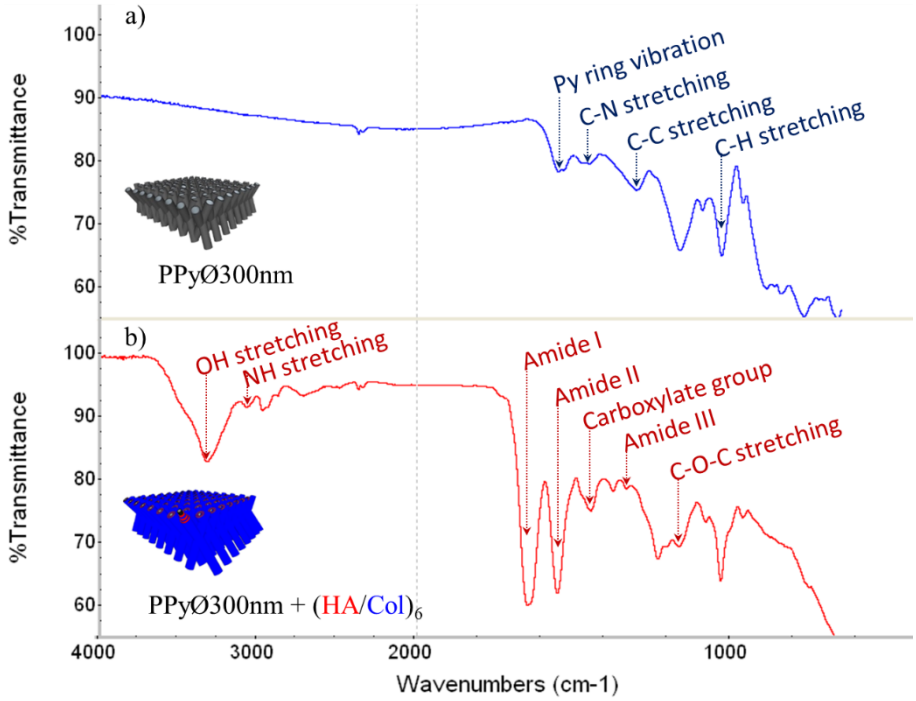


**Figure 6.7** *ATR-FTIR spectra of (a) native and (b) $(HA/Col)_6$-coated PPy framework (PPyØ300 nm obtained from PCT4, Table 6.1).*

### 6.2.3 Mechanical properties of bare and biofunctionalized PPy frameworks

In order to have an idea of the mechanical stiffness which cells will experience once seeded on the engineered ECM-like matrices, their reduced modulus was measured through nanoidentation using AFM. With the goal of extracting an elastic modulus as representative as possible of the cell-matrix interactions, the AFM cantilever was functionalized with a microcolloidal probe having a size (i.e., 5-µm diameter) in the same order of magnitude as that of the cell body. Such a spherical indenter of micrometer size allows to contact and thus take into account the contribution of many of the nanotubular heads constitutive of the substrate, hence yielding a modulus representative of the entire surface. The reduced modulus was determined instead of the Young's modulus, given that the studied system is a hybrid between polymers of different mechanical properties for which the Poisson's ratio is unknown. The moduli measured for the native and coated

frameworks were found to be clearly distinct, the reduced modulus of the biofunctionalized system being more than twice that of the native one (Figure 6.8 a).

The assembly of the biomimetic (HA/Col) coating on the PPy platforms thus increases the stiffness of the system. It has to be noted that the value of the elastic modulus recorded for the native framework of PPy NTs (i.e., ~ 66 MPa) is much smaller than the values commonly reported in the literature. Indeed, Cuenot *et al.* reported values in the range of 1.2 and 3.2 GPa (at least 18 times greater than the values measured in this work) for PPy NTs with a diameter greater than 100 nm[28], in line with the values previously recorded on flat PPy films.[58,59] The moduli reported here are also lower than the values reported for the elastic modulus of individual Col fibers, their reduced modulus being in the range from 5 to 11.5 GPa in air.[60] The data recorded in this work are, however, much closer to the values found in the literature for LbL-assembled thin films measured in water or highly hydrated NTs measured in air. Indeed, Cuenot *et al*. reported a Young's modulus of about 115 MPa for LbL-assembled PE NTs in air[61], while Picart *et al*. recorded values as low as 0.8 MPa for a chemically cross-linked PLL/HA multilayer in aqueous medium.[62] In view of this, although the numerical values of the moduli recorded for our systems might be underestimated, it can be fairly assumed that the stiffness of the biofunctionalized PPy meshwork is significantly greater than the native one, which might further influence the behavior of the seeded cells. As for the measured adhesion force (Figure 6.8 b), it is observed to be much more negative in the case of the biofunctionalized interface, which logically relates to the fact that the crosslinked biomimetic coating displays some elastomeric properties. The LbL-assembled and cross-linked multilayer is indeed likely to glue the colloidal probe and apply a tension force to it whenever it retracts away from the surface.

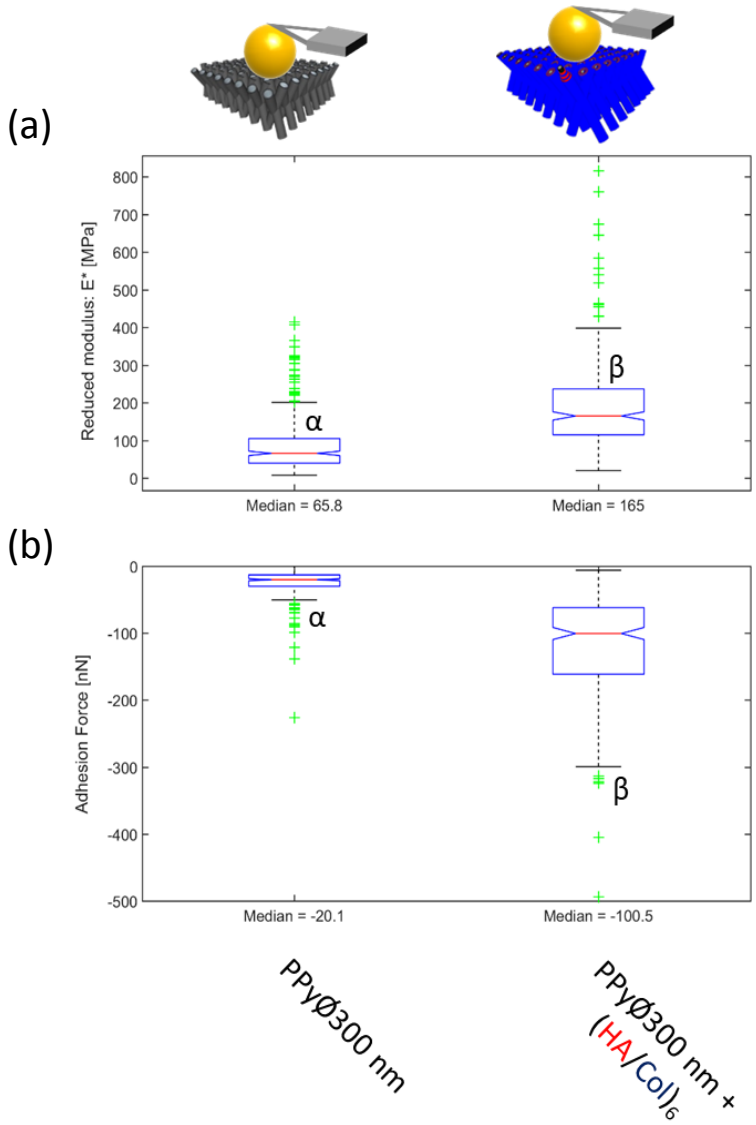


**Figure 6.8** *Notched boxplot presenting the full distribution (n = 300) of (a) the reduced modulus, E* (MPa) and (b) the adhesion force (nN), extracted from force-distance curves recorded during the AFM nanoindentation of both native and biofunctionalized PPy frameworks using a nanocolloidal probe (i.e., gold-coated $SiO_2$ colloid of 5-µm diameter). The red line displays the median of each population, the length of the whiskers represent 1.5 x interquartile range (IQR), the width of the notches represent the 95% confidence interval on the median while the outliers are represented by the green '+' signs. Bars topped with different greek letters indicate significant difference between the population means (p-value < 0.05 as computed via consecutive Welch's ANOVA and Games-Howell post hoc test).*

### 6.2.4 Preliminary study of cell adhesion, proliferation & osteogenic differentiation

*a) Adhesion and proliferation*

Murine MC3T3-E1 pre-osteoblasts, widely used as model cell line for bone tissue engineering applications,[63,64] were selected to evaluate *in vitro* the potential of (un)modified PPy frameworks as cell-instructive biointerfaces. The number of (HA/Col) bilayers decorating the PPy core was set at 6 for all cellular tests, to avoid masking the underlying nanotopography. When seeded at a density of 60,000 cells per mL and after 24 h of culture, cells were found to adhere to both uncoated and $(HA/Col)_6$-biofunctionalized nanostructured PPy frameworks (Fig.S6.6.C & D).

Given the specificities of the engineered biointerfaces (opaque black color, high developed specific surface area, non-uniformly smooth surface, *etc.*), cell densities were difficult to assess based solely on microscopic analyses. Cells seeded on the PPy networks were indeed found to interact both with the tips of the constituting nanotubes as well as with their cylindrical body, as cells were adhering to the vertical edges of the biointerfaces (Figure 6.10 C2 and Figure 6.9 B3). In contrast, a 2D surface only was explored by cells on glass. Total DNA quantification was therefore selected as an objective parameter for the comparison of samples (Figure 6.11). In the absence of serum supplementation, the produced biointerfaces were shown to promote cell adhesion to an extent similar to or higher than uncoated glass (i.e., the positive control), which is known for its cytophilic properties.[65] In particular, the biomimetic $(HA/Col)_6$ multilayer was evidenced to positively impact cell adhesion, as it was significantly increased compared to bare glass. No significant difference in terms of cell-adhesivity could be observed between the bare and the biofunctionalized PPy matrices but, nevertheless, both of these systems showed performances similar to that of the positive control. As a means of comparison, when seeding cells at a density of 100,000 cells.$mL^{-1}$ on a negative control (i.e., highly hydrophobic poly(tetrafluoroethylene) (PTFE) membranes), no living cell could be detected on the substrate after 3 days of culture (Figure S6.8). In addition to demonstrating the cytocompatibility of the engineered biointerfaces, these results emphasize the ability of the biomimetic (HA/Col) coating to be an

efficient substitute (at least during the initial adhesion phase) for the undefined mixture of proteins found in serum while ensuring a similar cell adhesion level. Serum-supplemented cultures did not show any significant differences in cell adhesion and proliferation depending on sample type, all the samples eliciting a cell-adhesiveness as high as the one of glass. After 6 days of culture, cells had proliferated on all substrates and were well-spread (Figure 6.10). The morphology of the seeded cells was found to be influenced by their supporting substrate. They adopted a polygonal shape, characteristic of the MC3T3-E1 cells[50,66], when cultured on uncoated glass slides (Fig.S6.6 A2 & A4), whereas they were found to adopt a more stellate shape both on $(HA/Col)_6$-coated glass slides and (un)coated PPy frameworks (Fig.S6.6 B2, B4 & C2, C4). In particular, cells formed many pseudopods in presence of the biomimetic $(HA/Col)_6$ coating (fig.S6.6 B1, B4 & D1, D4), which might be due to the specific anchorage of cells to the integrin-binding cues located on collagen molecules, non-uniformly distributed on the substrate.64 On nanostructured interfaces, the formation of filopodia might be increased as adherent cells have to contact multiple nanotubular heads to anchor themselves on the surface. The heterogeneous distribution of cell-adhesive cues and nanotopography might be both at play in dictating the morphology of cells adhering to $(HA/Col)_6$-functionalized nanobiointerfaces. SEM analyses (Fig.6.9) further highlight the presence of numerous cell protrusions, which wrap themselves around the tubules (Fig.6.9 B2 & B4). This observation opens perspectives for the use of the hollow cavity of the tubes, which is directly in contact with the cytoplasmic projections, to deliver bioactive agents. A dense fibrillar network is found on biofunctionalized systems, fully covering the samples (Fig.6.9 C2). It is attributed to a reorganization of the $(HA/Col)_6$ multilayer upon dehydration rather than to a *de novo* synthesis of ECM macromolecules by the adherent cells (as demonstrated in Fig.S6.9). When increasing the seeded cell density to 1,000,000 cells per mL, pre-osteoblast cells were found to fully colonize the surface of all (un)coated PPy interfaces after 6 days in culture, illustrating the cytocompatibility of the produced biointerfaces (Fig.6.10 B, C & D).

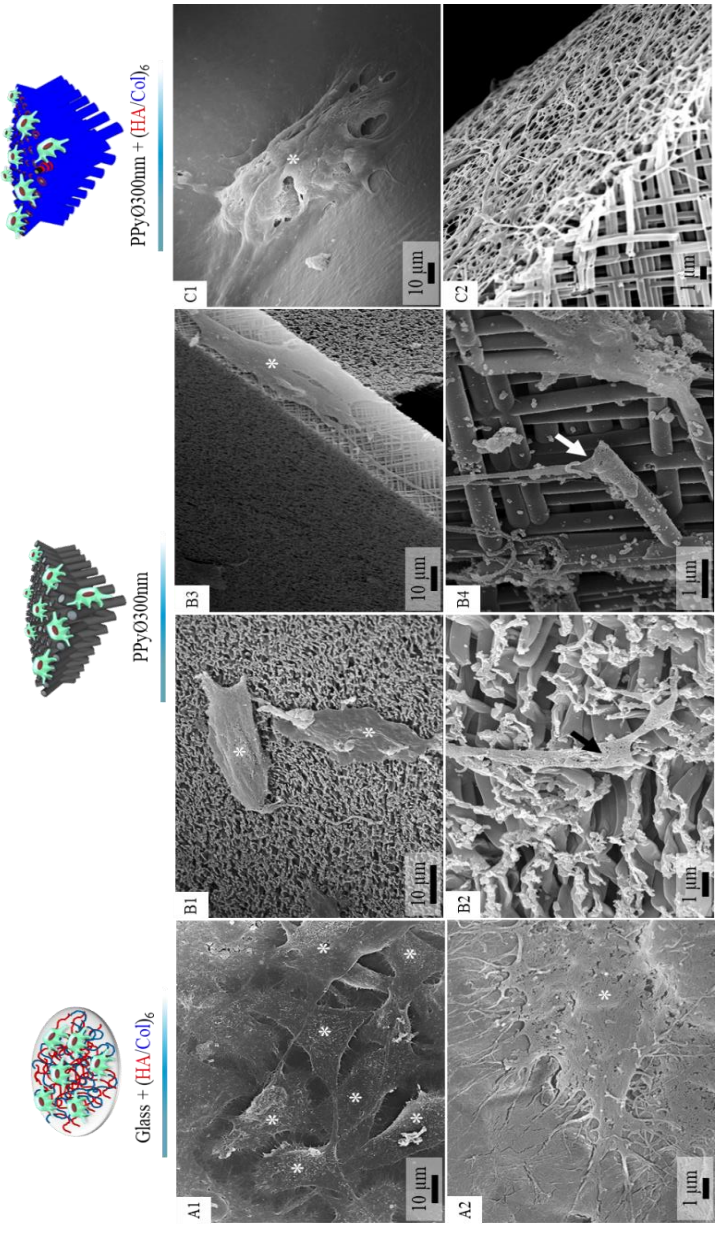


**Figure 6.9** *SEM images of cell-seeded biointerfaces after 6 days of in vitro culture (seeding density 60,000 cells per mL): cells (asterisk) adhering on bare glass slide (positive control, Fig. S6.7), (A 1-2) $(HA/Col)_6$-coated glass slide, (B 1-4) bare PPy framework with 300-nm diameter NTs (cytoplasmic elongations are shown to interact with NTs [arrows]), (C 1-2) $(HA/Col)_6$-coated PPy framework with 300-nm diameter NTs.*

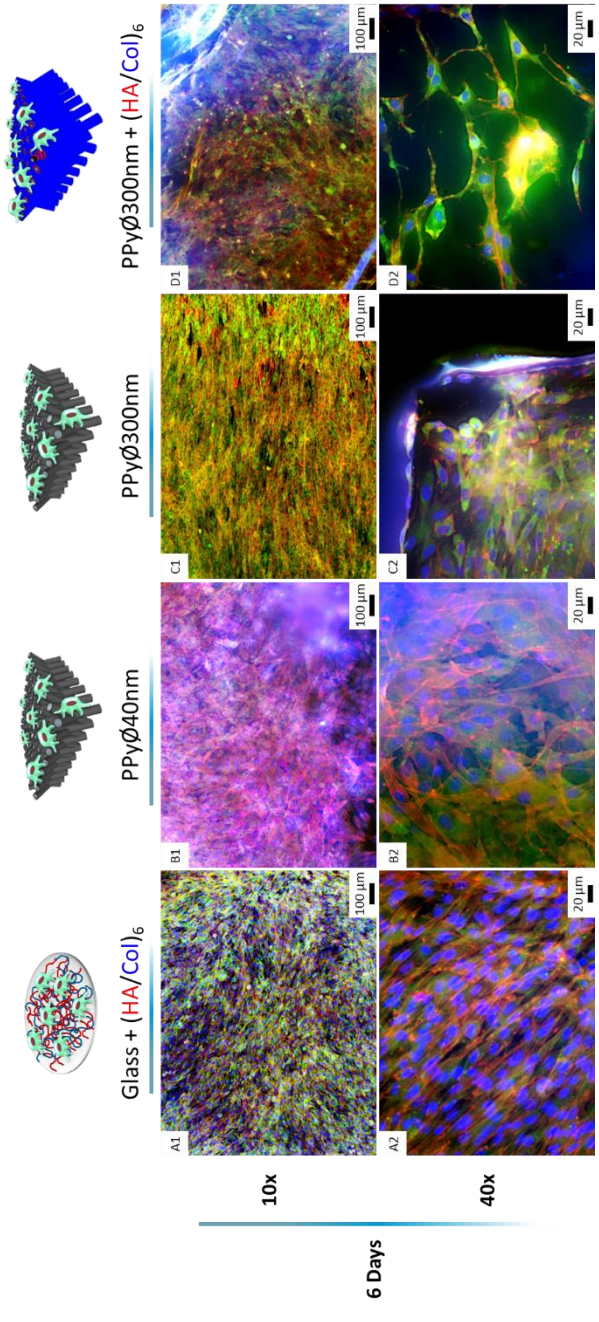


**Figure 6.10** *Epifluorescence microscopy images of immunostained MC3T3-E1 cells cultured for 6 days (seeding density 1,000,000 cells per mL) on (A 1-2) $(HA/Col)_6$-coated glass ; (B 1-2) bare PPy framework with 40 nm-diameter NTs ; (C 1-2) bare PPy framework with 300-nm diameter NTs ; (D 1-2) $(HA/Col)_6$-coated PPy framework with 300-nm diameter NTs. Images are a combination of red (actin, cytoskeleton), green (vinculin, FA) and blue (DNA, nucleus) channels.*

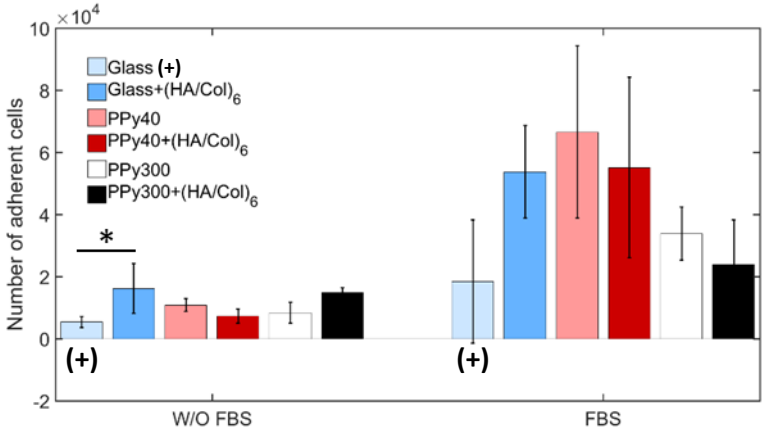


**Figure 6.11** *Number of MC3T3-E1 cells adhered on the studied systems after 24 hours of culture in the presence (FBS, right) or absence (W/O FBS, left) of 10% foetal bovine serum supplementation. Error bars represent standard deviation computed for triplicates. *p-value < 0.05 as computed via consecutive ANOVA and Tukey's HSD post hoc tests.(+) indicates positive control (i.e., glass).*

### *b) Osteogenic differentiation*

The engineered biointerfaces displaying a cytophilicity at least as good as that of the positive control (i.e., glass), their ability to further influence the differentiation of the seeded cells, i.e. osteogenic precursor cells, into mature osteoblasts was investigated. To this end, MC3T3-E1 pre-osteoblast cells were first seeded on the different substrates and cultured for 7 days under normal conditions until reaching ~ 90% confluence on all substrates (i.e., marking the end of the proliferation phase); after which the differentiation phase was initiated by adding chemical osteogenesis inducers (i.e., ascorbic acid and β-glycerophosphate ; osteogenic medium) to the medium of all samples. The activity of the ALP enzyme, an early marker of osteoblastic differentiation, was then measured after 7, 14 and 21 days of culture in the osteogenic medium. In parallel with the quantification of the ALP activity, the number of adherent cells on each sample was quantified and used to normalize the ALP data, so as to express the level of ALP activity per adherent cell.

***Influence of the NT diameter on the osteogenic differentiation of MC3T3-E1 cells***

The differentiation ability of seeded cells was first investigated for bare PPy frameworks displaying intersected NTs of either 40 or 300 nm diameter (Figure 6.12). No clear distinction could be made between the results obtained for time periods below 21 days, which is probably indicative of the fact that the onset of the differentiation phase is located somewhere in the period between 14 and 21 days. After 21 days of incubation within the osteogenic medium, significant differences were evidenced as the level of ALP activity remained close to 0 for the cells seeded on glass whereas the amount of active ALP present in the cells grown on both intersected PPy systems (either with 40-nm or 300-nm diameter tubes) was appreciably higher. Although no particular influence of the NT diameter on the differentiation of cells could be highlighted from the collected data, it is clear that the nanostructured interfaces favored the expression of ALP to a higher extend than did the glass substrate.

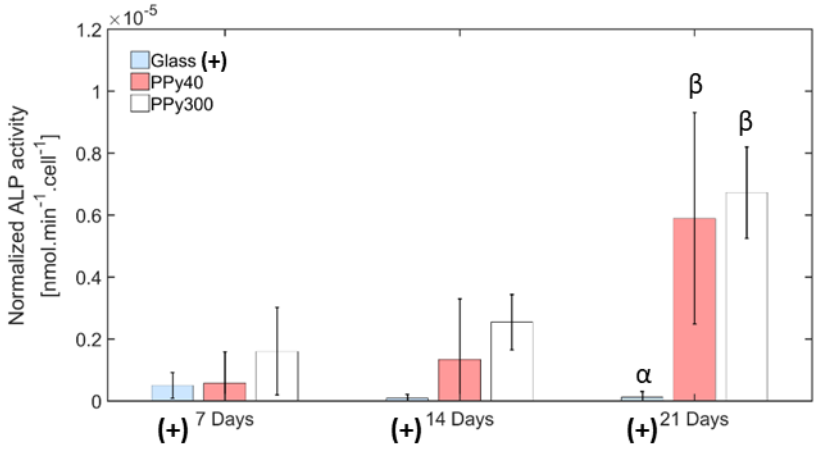


**Figure 6.12** *Normalized ALP activity measured from cells cultured for 7, 14 and 21 days on bare PPy frameworks (40-nm or 300-nm diameter NTs) or glass (positive control) and in the presence of osteogenic medium. Error bars represent the standard deviation (n=3). Considering each timepoint individually, bars topped with different Greek letters indicate statistical significance (p-value < 0.05, as computed via consecutive ANOVA and Tukey HSD post hoc test).*

***Influence of the biomimetic (HA/Col) multilayer on the osteogenic differentiation of MC3T3-E1 cells***

The influence of the biomimetic (HA/Col) multilayer on the differentiation ability of osteoprogenitor cells was next examined. Following conclusions drawn from the results discussed hereabove (Figure 6.12), the focus was placed on larger differentiation times (i.e., 14 and 21 days). After 14 days of incubation within the osteogenic medium, the ALP activity was found to be significantly increased in cells hosted on biofunctionalized PPy frameworks compared to those seeded on bare frameworks or either on bare and biofunctionalized glass slides (Figure 6.13). 21 days after introduction of the osteogenic inducers, the ALP activity on bare glass slightly increases and the difference with the nanostructured interface, highlighted at day 14, falls below the limit of statistical significance. The significant influence of bare PPy frameworks on the differentiation of cells, highlighted in Figure 6.12 at day 21, could not be observed anymore from the results displayed in Figure 6.13. Quite surprisingly, functionalizing the glass substrate with a biopolymer multilayer did not result in an increase of the ALP activity for any of the probed timepoints. This observation seems to point towards the conclusion that the biomimetic coating alone has no influence on the differentiation ability of pre-osteoblast cells. However, the evidence of a synergistic effect played by the biomimetic coating combined with the nanoscaled topography of PPy frameworks seems to emerge as the coated biointerfaces were found to promote an early rise in ALP activity. Indeed, a significant rise in ALP activity was observed after only 14 days of culture on biofunctionalized PPy nanostructures (Figure 6.13) whereas a significant increase was only recorded after 21 days of culture for bare nanostructures (Figure 6.12).

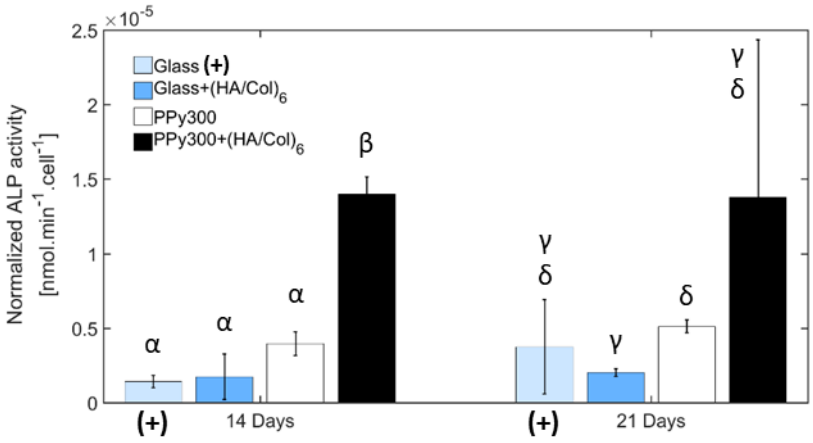


**Figure 6.13** *Normalized ALP activity measured from cells cultured for 14 and 21 days on bare and biofunctionalized PPy frameworks (300-nm diameter NTs) or glass (positive control) and in the presence of osteogenic medium. Error bars represent standard deviation of the mean (n=3). Considering each timepoint individually, bars topped with different Greek letters indicate statistical significance (p-value < 0.01, as computed via consecutive ANOVA and Tukey HSD post hoc test or consecutive Welch's ANOVA and Games-Howell post hoc test).*

***Pooled results : influence of the NT diameter, the biomimetic multilayer and the presence of HyAp on the osteogenic differentiation of MC3T3-E1 cells***

In order to further segregate and more clearly evidence the potential effects, outlined in Figure 6.12 and 6.13, of the nanostructured architecture and the biomimetic multilayer on osteogenic differentiation, experiments were reiterated independently several times (up to a number of independent repetitions N = 3). To enable a comparison to be made between results extracted from independent experiments, the mean of the normalized ALP activity measured for each sample category was divided by the highest normalized activity measured on the positive control (i.e., bare glass after 14 days of osteogenic supplementation), taken as reference. Pooled results are thus expressed as dimensionless "relative osteoblastic differentiation" values ; the mean value of the positive control (i.e., bare glass at day 14), taken as reference, being equal to 1 (Figure 6.14). Most of the engineered biointerfaces, whether functionalized or not with a (HA/Col) multilayer showed a higher tendency to promote osteogenic differentiation than bare

and biofunctionalized glass at all investigated timepoints. It is fair to assume that glass (bare or biofunctionalized) showed no particular ability to influence cell differentiation, as the ALP activity remained close to 0 throughout the investigations. This statement is further reinforced when looking at the evolution of the number of cells adhered to each system throughout the differentiation period (Figure 6.15). Indeed, the number of cells remained quite steady for all samples (indicative of the fact that cells effectively exited the proliferation phase to enter the differentiation phase), except for glass where the number of adhered cells kept on growing throughout the 21 days which lasted the differentiation experiments. Similarly, the biomimetic (HA/Col) multilayer, when considered independently from other parameters, was unable to trigger the differentiation of cells; judging by the fact that coated glass showed similar or even lower enzymatic activities than bare glass. In contrast, our ECM-like matrices displayed values up to 8 times higher than the best value recorded on glass. 7 days after the first addition of osteogenic inducers, the mean relative differentiation measured on the biofunctionalized PPy frameworks with 300-nm diameter NTs is already 5 times that observed on the positive control (significant difference, p-value < 0.05). The biomimetic coating seems to have a positive impact on differentiation when assembled on the nanostructured interfaces, as :

- The biofunctionalized PPy frameworks with 40-nm diameter NTs display better or similar values as bare PPy for all assayed periods (difference not statistically significant).

- The biofunctonalized PPy frameworks with 300-nm diameter NTs display, in general, higher differentiation values than the frameworks with identically-sized NTs lacking the biofunctionalization (difference statistically significant at day 7, Figure 6.14).

- The PPy frameworks (300-nm diameter NTs) functionalized with both the biomimetic multilayer and HyAp (CaP) crystals display similar values to the biofunctionalized frameworks lacking HyAp but; in general, higher values than the bare frameworks (difference statistically significant after 14 days under soft statistical treatment

(Figure S6.10) and after 21 days under hard statistical treatment (Figure 6.14)).

A synergistic effect of the biomimetic coating combined to the nanostructured topography can thus be highlighted. No specific influence of the NT diameter could be unveiled as the differentiation ratios obtained on both biointerfaces with intersected 40-nm and 300-nm diameter NTs were statistically similar for all time periods. Furthermore, no particular effect of the addition of co-precipitated CaP minerals could be detected, as the frameworks presenting CaP on their surface showed similar results to those without CaP.

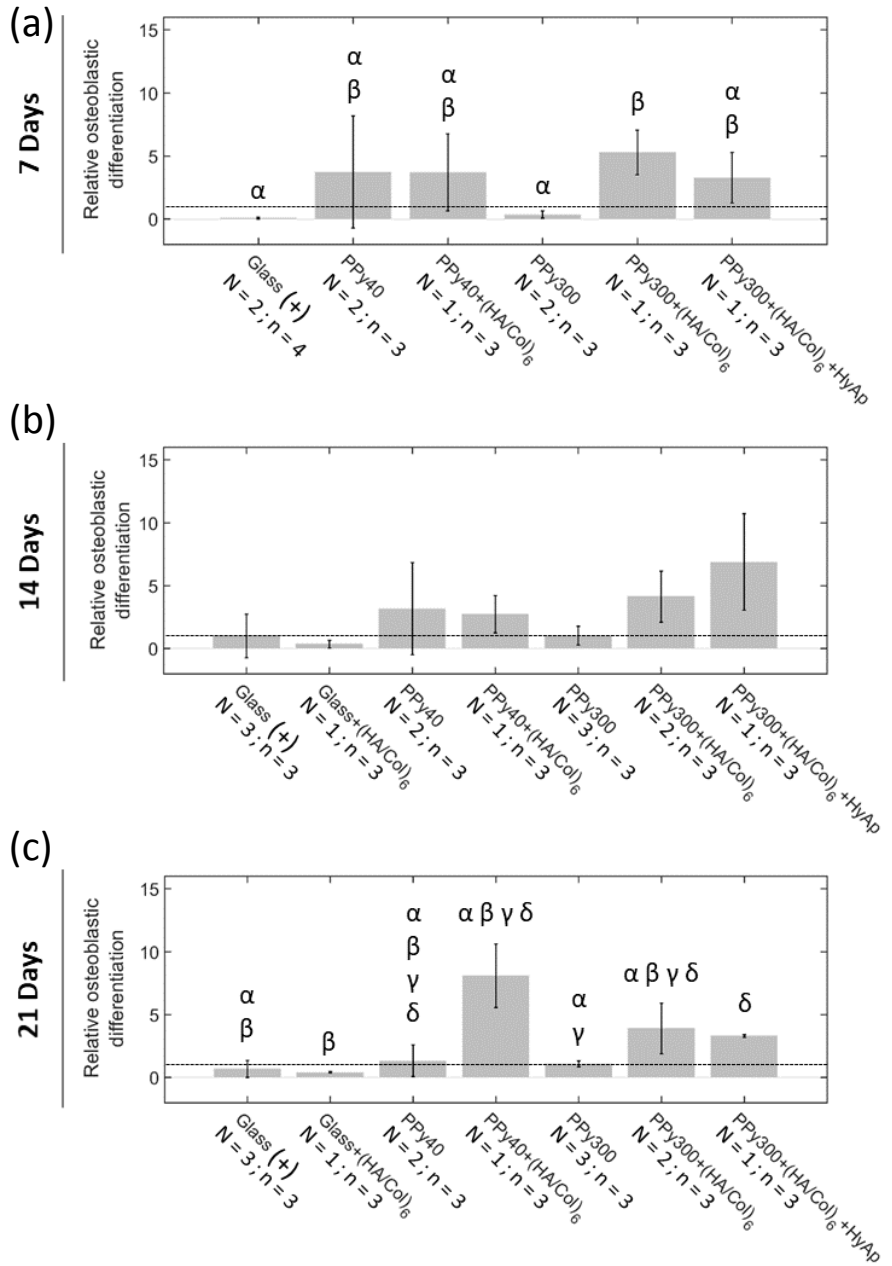


**Figure 6.14** *Relative osteoblastic differentiation (reference = bare glass at day 14) of cells cultured on the studied samples in the presence of osteogenic medium for (a) 7 days, (b) 14 days, and (c) 21 days. Error bars represent standard deviation. Bars topped with different Greek letters indicate statistical significance (p-value < 0.05, as computed following consecutive Welch's ANOVA and Games-Howell post hoc test). N indicates the number of independent iterations and n the number of replicates tested per iteration. The black dotted line represents the value of the reference (i.e., bare glass at day 14).*

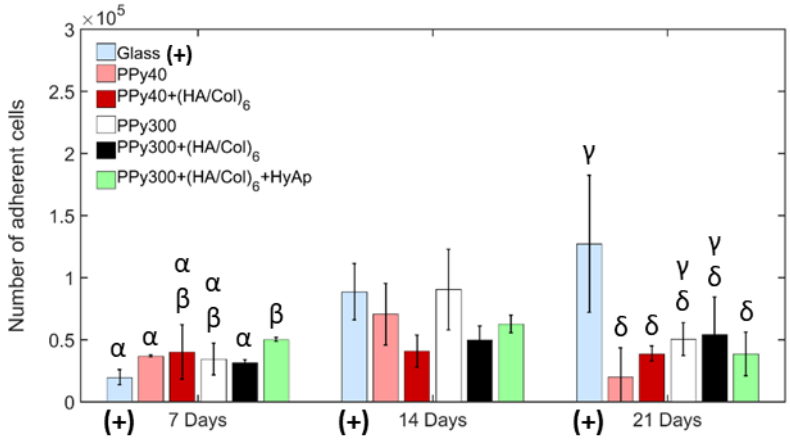


**Figure 6.15** *Number of MC3T3-E1 cells adhered on the studied systems after 7 days of culture within proliferation medium followed by either 7, 14, or 21 days of culture within differentiation (i.e., osteogenic) medium. Error bars represent standard deviation computed for triplicates. Considering each timepoint individually, bars topped with different Greek letters indicate statistical significance (p-value < 0.05 as computed via consecutive Welch's ANOVA and Games-Howell post hoc test).*

## 6.3 Conclusions and future prospects

Biofunctional rigid nanostructured PPy frameworks with highly tunable features were reproducibly fabricated using the simple and cost-effective hard-templating process combined with the versatile LbL technique. In particular, mechanically-stable frameworks made of intersected PPy NTs with a diameter of 40- or 300-nm and an angle of 90° between crossing tubes were successfully synthesized. These self-supported PPy architectures were further functionalized with a biomimetic coating, therefore combining two often antagonistic factors : mechanical stability and bioactivity. Such hybrid systems were shown to elicit good cell adhesion and cytocompatibility. Murine MC3T3-E1 pre-osteoblasts cells were indeed able to adhere and proliferate on both bare and $(HA/Col)_6$-functionalized PPy nanostructures to an extent similar to the performances of highly cytophilic glass. These synthesized hybrid nanostructures hold many advantages, including : highly tunable geometry, nanotopography (values ranging from 40 to 300 nm were selected in this work, but the range of achievable nanotube diameters can be considerably extended), interconnected porosity and potentially electrical

conductivity (which could be modulated by varying the tubular diameter), together with biocompatibility and high versatility of the LbL-deposited functional coating (HA and Col, ECM-derived biopolymers, were selected in the present work to be the components of the LbL-assembled multilayer, but many other polyelectrolyte combinations could be used). Such biointerfaces could provide further cell-signalling cues through the incorporation of bioactive molecules either inside the tubular PPy core or directly within the biomimetic shell. We thus foresee that this new type of nanobiointerfaces could be useful as cell-instructive materials.

In addition to the demonstration of the cytophilicity of both biofunctionalized and bare PPy matrices, the preliminary differentiation assays which were carried out promisingly indicate that the synthesized ECM-like biointerfaces favored the osteogenic differentiation of osteoblast progenitor cells compared to bare and biofunctionalized glass which had no effect. The biointerfaces indeed seemed to push cells to exit the proliferative phase and enter the differentiation one, whereas cells seeded on glass (bare or biofunctionalized) seemed to be blocked in a proliferative activity. The overall positive impact highlighted for the biointerfaces is a general one, no clear effect could indeed be assigned to the diameter of the intersected tubes nor to the biomimetic coating or the presence of HyAp *per se*. Only a synergistic effect of the biomimetic coating combined with the nanostructure could be highlighted. It is particularly difficult to segregate the independent influence of parameters such as nanomechanical properties, nanotopography and surface chemistry which are intimately interlinked in the design of nanostructured interfaces. For instance, AFM nanoindentation tests revealed that the biofunctionalized frameworks are also the more rigid ones. More control substrates should therefore be assayed in parallel to enable to clearly identify the impact of each parameter. A non-exhaustive list of such interesting controls would be : biofunctionalized surfaces tailored to display an elastic modulus identical to that of bare interfaces, flat substrates having a similar modulus to nanostructured interfaces, commercially available ECM-derived matrices (e.g., Matrigel®), etc. Studying the ability of the biointerfaces to trigger the differentiation of cells in the absence of osteogenic inducers (i.e., L-ascorbic acid and β-glycerophosphate) would also be interesting to consider.

Furthermore, it is important to emphasize that the differentiation experiments carried out in the framework of this thesis are only preliminary

tests, based on the detection of an early marker of osteogenic differentiation. The collected data should thus be further refined and corrected through comparisons with other markers, such as : osteocalcin, osteopontin, mineralization state of the *de novo* matrix produced by the seeded cells (i.e., calcium content), etc.[67–69] Priority should be given to markers which do not require optical characterization as this is complicated by the opaque black character of the studied systems. Comparing the gene transcripts of seeded cells at various timepoints would also be recommended.

The present study could also be extended to the use of multipotent stem cells. An interesting area of research indeed opens up to determine whether their differentiation could be oriented towards different tissues by appropriately tailoring the set of cues presented by the bioengineered interfaces, which could be used as a coating on biomaterials or as membranes bridging different tissues. Finally, an interesting parameter which was left unexplored in this work is the electrical conductivity of PPy, which could be further exploited to stimulate the hosted cells with electrical cues and investigate their resulting effects on cell differentiation (in particular using neuronal cell lines, for instance).

## Highlights of the chapter

- Self-supported frameworks of intersected NTs reproducibly produced, displaying a porosity of ~80% and NTs with an average diameter of either 40 or 300 nm
- A biomimetic (HA/Col) multilayer was assembled in a LbL fashion on the self-supported nanostructures, yielding biointerfaces combining increased mechanical stability and bioactivity
- Indentation modulus of biofunctionalized samples observed to be significantly higher than bare frameworks *via* microcolloidal AFM indentation tests
- Bare and biofunctionalized interfaces with intersected NTs of 300-nm or 40-nm diameter evidenced to be at least as cytophilic as glass
- ECM-like matrices with 300-nm diameter NTs coated with a $(HA/Col)_6$ biomimetic multilayer, those coated with the multilayer and further functionalized with HyAp and those with biofunctionalized 40-nm diameter NTs all significantly favored the advent of the early osteogenic differentiation phase in murine osteoprogenitor cells compared to glass (after a period of 7, 14 and 21 days respectively)

## 6.4 Experimental section

### 6.4.1 Synthesis of nanostructured frameworks of intersected PPy NTs

***Materials*.** Ferric chloride [$FeCl_3$], 2-(N-morpholino)ethanesulfonic acid monohydrate [MES], aluminium oxide [aluminium oxide, basic, for chromatography, 50-200 µm] and pyrrole monomer [Py, 99%, extra pure] were purchased from Acros. Alpha alumina powder (average diameter ~ 1 µm) was provided by CH instruments. Sodium hydroxide [NaOH, reagent grade, 97% powder] was bought from Sigma-Aldrich. Nanoporous PC templates as well as PET filtration membranes were kindly supplied by it4ip [Louvain-la-Neuve, Belgium, http://www.it4ip.be]. Frameworks of intersected PPy nanotubes were synthesized using polycarbonate (PC) templates featuring a network of intersected nanopores. The characteristics of all the PC templates used throughout this work are detailed in Table 1. PET membranes used for sample deposition had an average pore diameter of 200 nm, with a pore density of $5.10^8$ pores.cm$^{-2}$ and a thickness of 23 µm.

***Chemical oxidative polymerization of PPy nanostructures***. A piece of PC template featuring a network of intersected cylindrical nanopores, was inserted between the two compartments of a diffusion cell. One compartment was first filled with a solution of Py monomers (Py 0.5 M in MES buffer, 100 mM pH 5.5) which was allowed to diffuse within the membrane pores for 20 min. The oxidizing solution of $FeCl_3$ was then introduced in the second compartment and the polymerization reaction was carried out for 5 min. As these two solutions are allowed to diffuse towards each other through the template pores, Py monomers get oxidized by the initiator and start to polymerize along the pore walls[70]. The PC membrane filled with PPy nanotubes was finally recovered and abundantly rinsed with UPW. Polymerization of Py not only takes place inside the template pores, but also on the top and bottom surfaces of the template, resulting in undesired PPy crusts

clogging the nanopores. In order to remove these unwanted crusts, both faces of the template were gently rubbed on a polishing pad covered with alumina paste [alumina micropowder (average diameter ~ 1 µm) mixed with UPW]. Both surfaces of the template were then abundantly rinsed with UPW and dried in air for a few minutes.

***Release of PPy intersected nanotubes frameworks***. PET membranes were metallized with a supporting layer of chromium (3 nm) further coated by a gold layer (20 nm). PC templates in which nanostructured PPy frameworks were polymerized were deposited over metallized PET membranes. Large amounts of fresh dichloromethane (Vol. ~ 30 mL) were then poured dropwise over the template until complete dissolution of PC was achieved. The released PPy frameworks supported over PET membranes were finally air-dried at room temperature for about 1h prior to microscopy analysis.

***SEM and STEM Observations***. Samples were observed with a field-emission scanning electron microscope (JSM-7600F, JEOL) equipped with a transmission detector. Observations were performed at 15 keV.

### 6.4.2 Biofunctionalization of PPy nanostructures

***Polymers & other material supplies*.** Dried sodium hyaluronate [HA, Mw ~ 151-300 kDa] was purchased from Lifecore Biomedical. Type I Collagen G from bovine calf skin [Col, 0.4% solution in 15 mmol/L HCl, 4 mg/mL] was purchased from Biochrom AG. Cross-linking agents, 1-(3-dimethylaminopropyl)-3-ethylcarbodiimide hydrochloride [EDC, 98+%] and N-hydroxysulfosuccinimide sodium salt [s-NHS, ≥ 98%] were purchased from Acros and Sigma-Aldrich, respectively. Sodium chloride [NaCl, ACS reagent, ≥ 99%] and hydrochloric acid solution [HCl, 0.1 N in aqueous solution] were purchased from Sigma-Aldrich, while sodium hydroxide solution [NaOH, 0.1 N in aqueous solution] was bought from VWR.

***Biomimetic LbL (Col/HA) coating of PPy nanostructures***. Col solutions were prepared at a final concentration of 1 mg/mL by diluting the stock solution in UPW, and the pH of this solution was further adjusted at pH 4 (using HCl 0.1 N). HA solutions were prepared at a concentration of 1 mg/mL and pH was further adjusted at pH 4 (using NaOH 0.1 N). All solutions were freshly prepared and gently stirred for at least 20 min right before use. The cross-linking solution was prepared, right before use, by adding EDC and s-NHS at a final concentration of 100 mg/mL and 11 mg/mL respectively, to UPW adjusted at pH 4 (using HCl 0.1 N). After their release from PC templates, self-supported PPy frameworks were successively dipped in a solution of HA for 30 min, then rinsed for 5 min in the construction medium (UPW adjusted at pH 4), prior to being immersed in a Col solution for 2 h. Dipping time in Col solution was set at 2 h, following recommendations from the previous work of Landoulsi *et al*.[71] This process of alternate dipping of PPy nanostructures in solutions of HA and Col was cycled 3 to 18 times until the desired number of [Col/HA] bilayers was achieved (6 bilayers were most commonly deposited). The LbL deposition was carried out at 4 °C. Right after completion of the LbL construction, coated PPy nanostructures were immersed in the cross-linking solution [EDC 100 mg/mL & s-NHS 11 mg/mL in UPW pH 4] and stored at 4 °C for at least 48 h, following an adaptation of the protocol of Picart *et al*.[72] After cross-linking, the coated samples were rinsed 4 times for 10 min each in UPW at pH 4 to avoid any harmful effect of unreacted EDC/s-NHS on cells. Samples were then transferred to the construction medium (UPW pH 4) and stored at 4 °C until further characterization.

***QCM-D monitoring of the biomimetic (Col/HA) LbL build-up***. The self-assembly of the chosen biomacromolecules on reference substrates was monitored step by step using quartz crystal microbalance with dissipation monitoring (QCM-D). The LbL construction was carried out on gold-coated quartz crystals [AT-cut 5 MHz crystals coated with 100 nm Au, Q-Sense, Gothenburg (Sweden)]. Crystals were first cleaned in a piranha solution [$H_2O_2$ 30% (Prolabo, VWR, Leuven, Belgium)/$H_2SO_4$ 95% (Prolabo, VWR, Leuven, Belgium), 1:2 v:v] for 20 min, before being

thoroughly rinsed with ultrapure water and dried under nitrogen flow. All measurements were performed in a Q- Sense E4 system [Gothenburg, Sweden] following the same protocol: resonance frequencies of the crystals were obtained under buffer for the different overtones, and the shifts of frequency (Δf) and of dissipation (ΔD) were both monitored as a function of time upon stepwise injection of each of the two biopolymers.

***Adsorbed protein mass quantification*:** The total mass of protein (i.e., Col) adsorbed the nanostructured PPy frameworks was quantified using a Micro BCA™ Protein Assay Kit (Thermo Scientific). This kit allows dilute protein concentrations (0.5-20 µg/mL) to be determined, relying on the colorimetric detection of cuprous ions ($Cu^{+}$), produced through the reduction of $Cu^{2+}$ ions by proteins under alkaline conditions. Briefly, the kit protocol was adapted as follows: the PPy frameworks were first immersed in test tubes filled with 1 mL of pH 11.25 buffer (MA reagent of Micro BCA™ kit, Thermo Scientific. Probable composition [Ref.4.7.a]: aqueous solution of 8% $Na_2CO_3.H_2O$, 1.6% NaOH, 1.6% $Na_2$ tartrate and sufficient $NaHCO_3$ to adjust the pH to 11.25) containing 1% v/v sodium dodecyl sulfate (SDS), thoroughly vortexed and incubated for 2 h at 60°C in a water bath, so as to trigger the deconstruction of the Col/HA multilayer and the solubilisation of the Col protein. After solubilisation of the multilayer compounds, 1 mL of working reagent was added to each tube, which was consecutively vortexed and incubated 1 h at 60°C. The working reagent itself was freshly prepared by mixing a bicinchoninic acid (BCA) solution (MB reagent of Micro BCA™ kit, Thermo Scientific. Probable composition [Ref.4.7.a]: aqueous solution of 4% $CuSO_4.5H_2O$) and SDS in the proportions 50/47/2/1% v/v. After 1 h of reaction, the tubes were cooled to room temperature, and thoroughly vortexed before 1 mL of each sample-specific tube was transferred to a cuvette whose absorbance was read at 562 nm using a UV/Vis. spectrophotometer. Collagen standards with a concentration ranging from 3.13 µg/mL to 100 µg/mL were prepared by successive dilution of a Col stock solution (4 mg/mL) in a 1% v/v SDS solution within the kit pH 12 buffer. A standard curve, relating each standard absorption at 562 nm to its known Col content, was finally plotted and used to infer the Col content of the biointerfaces. The absorbance of a bare PPy framework, containing no protein and incubated in the working reagent, was used as blank and

substracted from the 562 nm reading of all other samples. All samples absorbance was measured within 10 minutes.

***Fourier Transform Infrared analysis***. The *in-situ* Fourier transform infrared (FTIR) spectroscopy in attenuated total reflection (ATR) mode experiments were performed with a Nexus 870 FT-IR spectrometer (Nicolet, USA) coupled to a Continuum microscope (Thermo Spectra-Tech, USA). Unmodified and biofunctionalized PPy frameworks were deposited on a Si crystal and ATR-FTIR spectra, averaged over 128 scans, were recorded in the range of 400-4000 $cm^{-1}$ with 8 $cm^{-1}$ resolution. The spectra were analysed using the software OMNIC.

***AFM colloidal probe nanoindentation tests.*** The reduced modulus and adhesion force of bare and biofunctionalized PPy frameworks was estimated using the Force-Volume mode equipped on a Bruker Dimension-Icon system. Micro -colloidal probes consisting in a silica sphere (5-µm diameter) mounted on a silicon cantilever was purchased from Novascan (PT.$SiO_2$.SI.f) and used for all measurements. A triangular modulation of 1 Hz was applied to the piezoelectric scanner so as to bring the colloidal probe in contact with the sample surface, indent it and subsequently withdraw from the surface. The calibration process was carried out as follows: the spring constant (k) was determined via thermal tuning (3.66 N/M). The deflection sensitivity (89.09 nm/v) was obtained by imaging a silicon wafer. All reference samples were provided by Bruker. The force setpoint was set at a value of 40 nN. The calibrated parameters were kept constant for further mapping along the sample surface. The bead functionalizing the probe having a diameter of 5 µm, a force-distance curve was recorded forevery 5-µm square area within a 50 x50 µm array of the sample surface. 300 force-curves were recorded for each sample category and later treated using the Nanoscope and Igor softwares to estimate the reduced modulus and adhesion force.

### 6.4.3 Cell adhesion and proliferation tests

***In vitro* cell culture of MC3T3-E1**. Progenitor cells of the MC3T3-E1 Subclone 14 pre-osteoblast cell line, derived from mouse calvaria (ATCC® CRL-2594TM) were used in this study. MC3T3-E1 cells were

routinely cultured in α-MEM medium supplemented with 10% (v/v) foetal bovine serum (FBS, Lonza) (excluded from FBS-free adhesion tests), 1% (v/v) sodium pyruvate (solution 100 mM, Sigma-Aldrich) and 1% (v/v) pen-strep (10,000 U/mL penicillin & 10,000 µg/mL streptomycin, Gibco®) at 37 °C with 5% $CO_2$. The supplemented culture medium was renewed every 3 days and confluent cells were subcultured through trypsinization (Trypsin EDTA, Lonza) until reaching passage 23, where the cells were seeded either on nanostructured PPy frameworks (uncoated or $(HA/Col)_6$-coated) or control substrates (virgin or $(HA/Col)_6$-coated circular glass slides, Ø 10 mm, Thermo Scientific). All samples were sterilized with 70% ethanol for 30 min followed by 4 times rinsing with sterile PBS prior to cell seeding. The samples were kept in a 24-well plate (Costar® Ultra-low attachment 24 well plate from Corning), and 500,000 cells were seeded per well (volume of solution per well = 1 mL).

***Cell morphology observation***. To observe cell attachment and spreading on PPy frameworks (both uncoated and $(HA/Col)_6$-coated) and control substrates (both uncoated and $(HA/Col)_6$-coated glass slides), MC3T3-E1 cells were seeded on the samples and cultured for 24 h and 6 days. At both time points, cells were fixed with a 4% (w/v) paraformaldehyde solution in PBS for 20 min at room temperature. The samples were then washed 2 times with a 0.05% Tween-20 solution in PBS (rinsing buffer). The cells were permeabilized using a 0.1% (v/v) Triton X-100 solution in PBS for 5 min. The samples were then rinsed twice and incubated in 1% BSA (Sigma-Aldrich) solution in PBS (blocking buffer) for 30 min at room temperature, to prevent non-specific binding. Subsequently, immunostaining of cells was initiated: in order to label focal contacts, cells were incubated with a solution of mouse anti-vinculin antibody (1:175 in blocking buffer) (FAK100, Millipore) during 1 h at room temperature. Cells were then washed 3 times and reacted with (FITC)-conjugated secondary antibody (1:150 in PBS) (AP124F, FITC-conjugated goat anti-mouse IgG, Millipore) for 1 h at room temperature. To detect actin filaments simultaneously, (TRITC)-conjugated phalloidin (1:100 in PBS) (FAK100, Millipore) was added in the secondary antibody solution. Finally, the substrates were washed 3

times before being mounted in Vectashield containing DAPI (Vector Laboratories, Peterborough, UK) to stain the nuclei. Immunolabeled cells were observed using an epifluorescence microscope (Olympus, IX71). In order to further analyse the cell-material interactions by SEM, cell-seeded samples were washed three times with PBS, gradually dehydrated in 20, 40, 60, 80 and 100% ethanol for 5 min each, covered with hexamethyldisilazane and left to dry overnight in a fumehood. The samples were finally sputter-coated with 10 nm gold prior to imaging.

***DNA quantification***. The number of adherent cells on the substrates after 24 h of culture (initial seeding density: 500,000 cells/well) with or without 10% FBS (Lonza), was quantified using a CyQUANT® Proliferation Assay kit (Molecular Probes, USA).After 24 h of culture, adherent cells were rinsed twice with sterile PBS before being detached from their corresponding substrate using trypsin and collected in a cryotube. Cell suspensions were then centrifuged at 1500 RPM for 5 min at 4 °C to recover cell pellets. After being washed with sterile PBS to remove all traces of phenol red (which might interfere with the CyQUANT® kit) and subsequently centrifuged, cells pellets were frozen at -80 °C. Before the start of the assay, the concentrated cell lysis buffer (CLB) provided with the CyQUANT® kit was diluted 20 times in ultrapure water. A reagent solution was then freshly prepared by diluting 80 times the CyQUANT® DNA-labelling GR dye with the prepared CLB solution, and kept protected from light. Cell pellets were thawed and resuspended in 200 µL of the CLB/GR dye solution. The obtained cell suspensions were independently transferred to a 96-well microplate. One well containing only the CLB/GR dye solution (i.e., with no cell) was used as blank. The fluorescence intensity of each well was then measured with a Tecan Infinite M200-PRO microplate reader with an excitation and emission wavelength set at 480 nm and 520 nm, respectively. In order to build a calibration curve displaying the fluorescence intensity as a function of the cell number, reference pellets containing 500,000 MC3T3-E1 cells were resuspended in CLB and serially diluted (by a factor 2) in the wells of a 96-well microplate, so as to span cell numbers from 244 to 250,000 cells. CLB/GR dye

solution was then added to each well to reach a final volume of 200 µL, whose fluorescence intensity was measured. Three repetitions of the calibration curve were achieved per sample group (i.e., with or without addition of FBS). For each repetition, a well containing only the CLB/GR dye solution (i.e., with no cells) was used as blank.

### 6.4.4 Cell differentiation tests

***Cell seeding, proliferation and induction of differentiation*.** MC3T3-E1 cells at passage 23 were seeded at a density of 500,000 cells/well on all samples on the same day for all tested durations (i.e., 7, 14 and 21 days) following the classical procedure described above. One specific 24-well plate (Costar® Ultra-low attachment 24 well plate from Corning) was used per incubation time (i.e., one specific plate for the 7-day period, another for the 14-day period and a last one for the 21-day period). Cells seeded on the samples were first allowed to proliferate within proliferation medium for 7 days before being switched to differentiation medium. The proliferation medium was the classical culture medium previously described (i.e., α-MEM supplemented with 10% (v/v) FBS, 1% (v/v) sodium pyruvate and 1% (v/v) pen-strep). During this 7-day proliferation phase, the culture medium was renewed every 2 to 3 days. At the end of the 7-day proliferation phase, differentiation of the cells was induced by replacing the proliferation medium with an osteogenic medium. The osteogenic medium was obtained by supplementing the proliferation medium with 400 µM L-ascorbic acid and 10 mM β-glycerophosphate. Solutions of L-ascorbic acid and β-glycerophosphate were prepared by solubilizing respectively L-ascorbic acid powder (Sigma) and β-glycerophosphate powder (Sigma) in Dulbecco's Phosphate-buffered saline (DPBS, Gibco). Prior to their use, both solutions were autoclaved and sterile filtered. The three differentiation periods investigated (i.e., 7, 14 and 21 days) started on the same day, at the moment at which the osteogenic medium was added (day 0 of the differentiation test, 7 days after initial cell seeding). The osteogenic medium was renewed every 2 to 3 days. Throughout the proliferation and differentiation protocols, the cells were maintained in culture in an incubator at 37°C with 5% $CO_2$ and 95% humidity. At the end of each differentiation period, cells and culture media from the corresponding plate were retrieved and frozen at -80°C.

***ALP activity quantification*.** The level of intracellular ALP activity was quantified by a colorimetric assay using para-nitrophenylphosphate (p-NPP), a chromogenic substrate for phosphatase enzymes such as ALP. In basic conditions and in the presence of divalent cationic cofactors (e.g., $Mg^{2+}$ or $Zn^{2+}$), ALP catalyzes the hydrolysis of p-NPP wich liberates an inorganic phosphate and p-nitrophenol. Unlike p-NPP which is colorless, p-nitrophenol under alkaline conditions has a yellow color and a strong absorbance at 405 nm. Therefore, the amount of p-nitrophenol produced from p-NPP can be extracted from absorbance measurements at 405 nm using an absorbance/p-nitrophenol calibration curve. ALP activity is thus defined as the quantity of p-nitrophenol produced per unit time [$nmol.min^{-1}$]. Prior to starting the assay, the following solutions were freshly prepared. For the establishment of the absorbance/p-nitrophenol calibration curves, a solution of 20 mM p-nitrophenol (4-nitrophenol, spectrophotometric grade, Sigma) was prepared within the cell lysis buffer (CLB) provided in the CyQUANT™ proliferation assay kit (*see* DNA quantification). A CLB/GR-dye 5X solution was also prepared (*see* DNA quantification). The reagent solution containing 10 mM p-NPP (4-nitrophenyl phosphate disodium salt hexahydrate for enzyme immunoassay, Sigma) and 10 mM $MgSO_4$ (Magnesium sulfate hepta-hydrate, ≥99% purity, Sigma-Aldrich) was prepared on a carbonate/bicarbonate buffer at pH 10.5. The carbonate/bicarbonate buffer was itself prepared by solubilizing sodium carbonate (Sodium carbonate decahydrate, ≥99% purity, Fluka) and sodium bicarbonate (Sodium bicarbonate, 99.7+%, for analysis ACS, Acros Organics) into UPW. The reagent solution was protected from light throughout the assay. A stop solution containing 0.1 M NaOH and 0.1 M ethylenediaminetetraacetic acid (EDTA, Titriplex III, Millipore) was prepared in UPW. The stop solution was used to disrupt the enzymatic reaction at the end of the allocated reaction time. Indeed, the high pH of the solution combined with the presence of EDTA chelating the divalent cofactor has the effect of disturbing the enzyme and stopping the reaction. In order to establish the absorbance/p-nitrophenol calibration curve, serial dilutions (with factor 2) of the p-nitrophenol solution were performed in the wells of a 96-well plate so as to span p-nitrophenol concentrations ranging from 0.007 to 18 mM. The stop solution was then added to bring the total volume to 200 µL. For each triplicate of the calibration curve, one well containing only the CLB and stop solution (i.e., without any p-nitrophenol) was used as a blank. In order to

quantify the intracellular ALP activity, cell pellets retrieved from each specific samples which were frozen at -80°C were thawed. Given that the number of cells present in each cell pellet needed to be quantified in parallel with the ALP activity (*see* DNA quantification, hereunder), the thawed cells were resuspended in the CLB/GR-dye solution. After thorough vortexing, 100 µL of each cell suspension were transferred into the wells of the 96-well microplate. 80 µL of the reagent solution were then sequentially added to each well. The enzymatic reaction was left to occur for 30 min at 37°C, after which 20 µL of stop solution were sequentially added to each well to disrupt the reaction. One well filled with a cell suspension to which the stop solution was added prior to the reagent solution in order to prevent any reaction, was used as a blank. Readout of the absorbance at 405 nm was then performed with a Tecan infinite M200-PRO plate reader.

***DNA quantification*.** In order to normalize the ALP activity measured for each sample by the respective number of cells adhering on that sample, a fluorometric DNA quantification assay was performed in parallel with the ALP assay. As for the cell adhesion tests, a CyQUANT$^{TM}$ Proliferation Assay kit (Molecular Probes) was used. What remained of each sample lysate after the ALP assay was diluted four times in CLB and 200 µL of the resulting diluted lysate were dispensed into the wells of a 96-well plate. The same protocol of DNA quantification as the one described for the cell adhesion tests (*see* DNA quantification in section 6.3.3 hereabove)was then applied.

***Normalized ALP activity computation*.** The ALP activity of each sample was computed from the absorbance/p-nitrophenol calibration curve whereas the number of cells adhered on each sample was determined from the fluorescence/cell number calibration curve. In order to normalize the ALP activity measured for each sample and enable their comparison, the ALP activity of each sample was divided by its respective cell number, resulting in a normalized ALP activity expressed in [nmol.min$^{-1}$.cell$^{-1}$].

***Relative osteoblastic differentiation values computation.*** In order to enable a comparison to be drawn between normalized ALP activities measured from independent iterations, the normalized ALP activities measured at a given timepoint (i.e., 7, 14 or 21 days) were pooled as a function of the sample category and their mean was further divided by a reference value. This reference value was chosen as the highest mean normalized ALP activity

measured for a positive control (i.e., the normalized ALP activity of bare glass at day 14).

***Statistical analyses.*** All the results presented for the cellular tests (i.e., cell number, normalized ALP activity and relative osteoblastic differentiation) are expressed as mean ± standard deviation. Levene's test was used to assess the equality of variances (homoscedasticity) between the compared groups. A difference between the variances of the populations was deemed significant for a p-value < 0.05. Whenever the homoscedasticity hypothesis had to be rejected, Welch's ANOVA (exempt from any assumption regarding the equality of variances between the compared groups, on the contrary to the classical ANOVA) was used to detect a significant difference between the means of groups. A difference between the mean of groups was deemed significant for a p-value < 0.05. Welch's ANOVA was followed by a Games-Howell post hoc test (alternative to the Tukey-Kramer post hoc test on the equality of the means of two populations in the cases where the data violate the assumption of homogeneity of variances) for multiple pairwise comparisons of the means. Differences were considered significant whenever p-value < 0.05. Whenever the homoscedasticity hypothesis was respected, a classical one-way ANOVA was used to compare the means of groups. The classical ANOVA was followed by a Tukey's Honestly Significant Difference procedure for multiple pairwise comparisons of the means. Differences were again considered significant for a p-value < 0.05.

# Supporting information 6

## S.I.6.1 Pre- versus post-polymerization coating of PPy NTs

**Pre-polymerization coating process of individual PPy NTs**. In order to functionalize the outermost surface of PPy NTs which will be polymerized during the second stage of the process, the first step entails the LbL assembly of a polymer multilayer inside PC templates with parallel nanopores. This LbL construction was achieved *via* sequential dipping of the template into solutions of oppositely-charged polymers. Polymers used consisted of fluorescent-tagged PEs, so as to easily track the soft polymer coating with epifluorescence microscopy. It is noteworthy to mention that, following evidences that PPy exerts a fluorescence-quenching effect (*see* section S.I.6.2 and Fig.S6.2), a spacing interlayer consisting of non-fluorescent synthetic PEs (PAH and PSS) was intercalated between the PPy NT surface and the fluorescent multilayer to avoid direct energy transfer. Dissolution of the PC template after completion of the LbL assembly, collection of the tubular multilayers over a PET filter and epifluorescence imaging of the system clearly evidenced the synthesis of a high number of soft fluorescent NTs of ~ 21 µm long (in accordance with the thickness of the PC template) (Figure S6.1 B1). Reaching the second phase of the process, Py monomers were chemically polymerized inside the previously-assembled polymer multilayers embedded in their template. The resulting NTs were freed from their template, collected over a PET filter and imaged using epifluorescence microscopy (Fig. S6.1 B2). Two distinct populations of NTs could be observed : soft and fluorescent polymer NTs (corresponding to the soft LbL-assembled polymer shell) on the one hand, and dark rigid NTs (identified as the PPy core) on the other hand. Further imaging this system under SEM (Fig. S6.1 B3) and STEM (Fig. S6.1 B4) modes allowed us to formulate a hypothesis regarding these observations. Most NTs were observed to either consist in highly flexible, soft polymer NTs (i.e., the fluorescent multilayers observed under optical microscopy) with no trace of a stiffening PPy core or, on the opposite, in stiff PPy NTs (i.e., the dark and rigid NTs observed under optical microscopy) showing no trace of a soft polymer coating. A small minority of NTs, displayed in Figures S6.1 B3 & B4, were evidenced to display a hybrid

structure with a small portion of stiff PPy core embedded at the ends of a soft shell. The portion of stiff PPy core was observed to be strictly limited to the first few micrometers inside of the soft polymer shell. This lead to the hypothesis that polymerization of Py monomers inside the LbL multilayer was somehow impaired due to the very nature of the soft polymer multilayer. Indeed, under aqueous conditions such as the ones used throughout the Py polymerization process, the PEM initially covering the template nanopore walls is likely to swell and give rise to a highly hydrated gel, which might prevent the diffusion and adsorption of Py monomers along the functionalized pore walls. This assertion is further demonstrated by the observation, under STEM (Fig. S6.1 B4), of a clear demarcation line (i.e., corresponding to the diffusion front of the Py monomers inside the soft PEM) between the dark and opaque PPy and the rest of the soft PEM shell. It can therefore be concluded that the pre-polymerization coating approach is a failure because the swollen nature of the PEM in such a confined environment as a nanopore, prevents the further diffusion and polymerization of Py monomers. The presence of 3 distinct populations of NTs can thus be explained as follows. Most PEMs totally block the diffusion of Py monomers which results into soft and fluorescent NTs with no trace of PPy core. As a consequence, Py monomers are left to diffuse and polymerize mostly in nanopores where the self-assembly of PEs was unsuccessful or not fully complete, yielding rigid PPy NTs with no trace of LbL functionalization. Finally, a minority of hybrid structures are created whenever Py monomers manage to diffuse and polymerize a few micrometers into the PEM-functionalized pores.

**Post-polymerization coating process of individual PPy NTs.** The post-polymerization coating process entails, first, the polymerization of Py monomers inside the PC template, subsequent dissolution of the template and collection of the resulting NTs over a PET filter which is then alternately dipped in solutions of oppositely-charged PEs. Epifluorescence imaging of the supported PPy NTs before (Fig. S6.1 C1) and after (Fig. S6.1 C2) LbL assembly clearly highlights the presence of the soft polymer coating functionalizing the PPy core, as the NTs become embedded in a fluorescent multilayer.

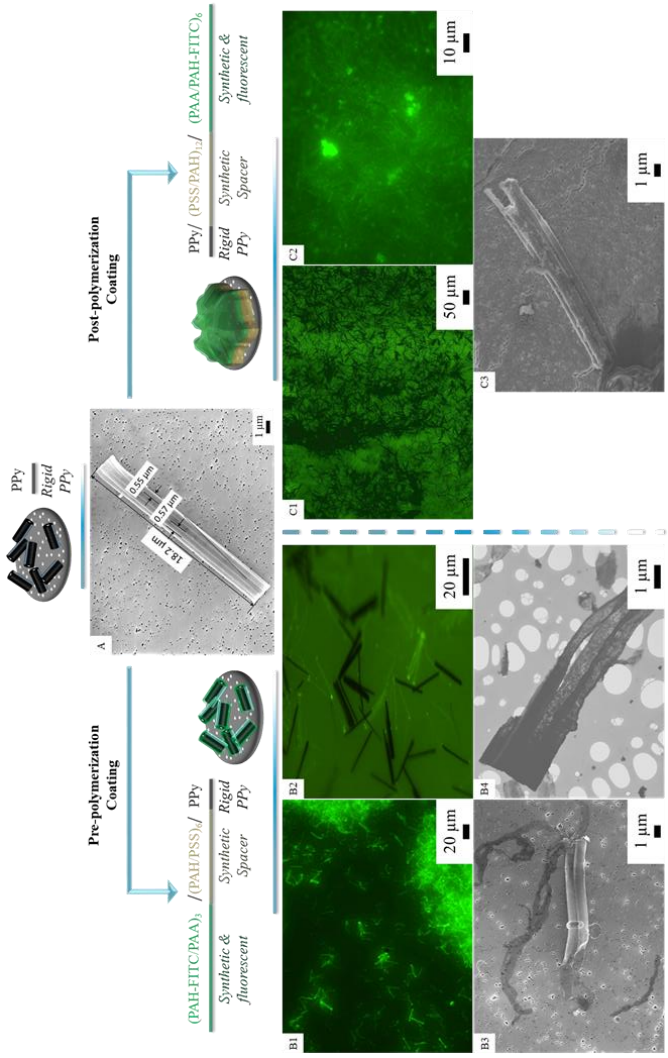


**Figure S6.1** *(A) SEM picture of individual PPy NTs before coating. (B 1-4) Pre-polymerization coating process. Epifluorescence micrographs of fluorescent (PAH-FITC/PAA)$_3$/(PAH/PSS)$_6$ polymer multilayer before (B1) and after (B2) Py polymerization. SEM (B3) and STEM (B4) micrographs of fluorescent (PAH-FITC/PAA)$_3$/(PAH/PSS)$_6$ polymer multilayer after Py polymerization. (C 1-4) Post-polymerization coating process. Epifluorescence micrographs of individual PPy NTs, before (C1) and after (C2) assembly of the fluorescent (PSS/PAH)$_{12}$/(PAA/PAH-FITC)$_6$ polymer multilayer. (C3) SEM micrograph of individual PPy NTs after assembly of the polymer multilayer.*

## S.I.6.2 Fluorescence-quenching effect of PPy

The fluorescence-quenching effect exerted by PPy was evidenced both on flat substrates and NTs. While adsorbing a fluorescent-labelled (PAA/PAH-FITC)$_3$ multilayer on a flat PC membrane in a LbL fashion gives rise to a homogeneously green-fluorescent coating (Figure S6.2 A1), polymerizing a crust of PPy over the PC template prior to initiating the LbL assembly of the fluorescent multilayer totally suppresses the fluorescent signal (Fig. S6.2 A2). This phenomenon is to be attributed to the dissipation of the energy which should have been released as fluorescence as resonance into the resonating aromatic rings of the PPy core (PPy being highly conductive to electron and energy transfer). Intercalating an insulating multilayer of non-fluorescent PEs having a thickness of only a few nanometers between the PPy and the fluorescent coating, allows to restore the fluorescent signal (Fig. S6.2 A3), further proving our point. The fluorescence emission is not homogeneous over the entire surface, as it is probably restricted to areas where the multilayered spacer homogeneously covers the PPy. The same phenomenon was observed when coating PPy NTs with a fluorescent multilayer. In absence of an interlayer able to insulate the PPy from the fluorescent shell, no fluorescent signal could be detected in the vicinity of the PPy NTs (Figure S6.2 B2). In contrast, upon adsorption of an insulating multilayer, a clear fluorescence emission coming from the functionalized PPy NTs could be detected (Fig. S6.2 B3).

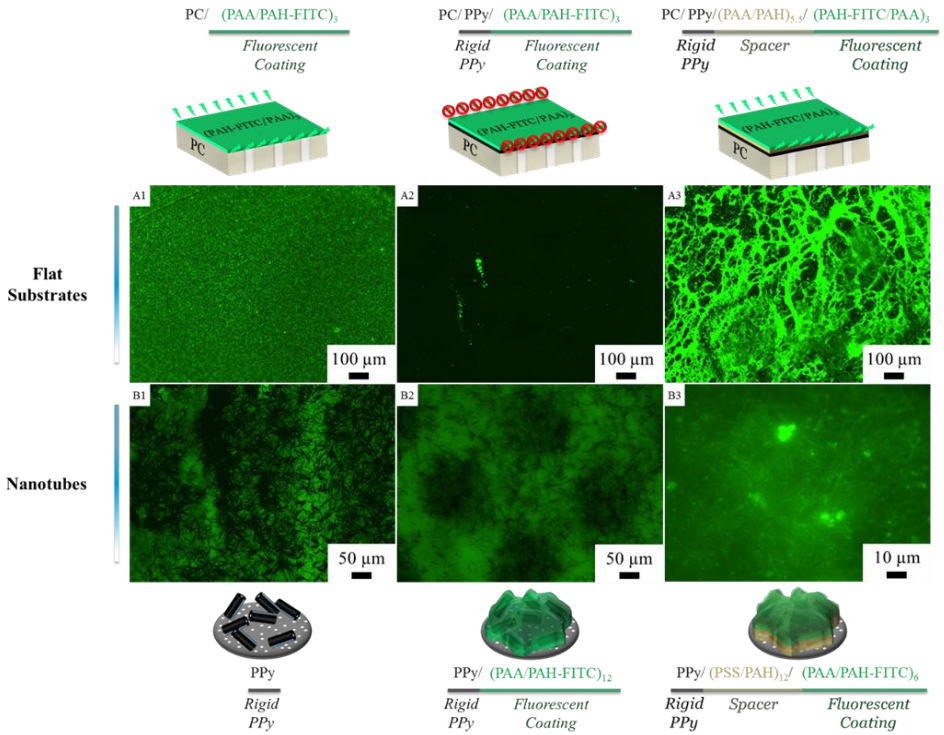


**Figure S6.2** Epifluorescence images of (A) flat PC membrane coated with (A1) 3 bilayers of a fluorescent-labelled PE: $(PAA/PAH\text{-}FITC)_3$; (A2) a PPy crust further covered with 3 bilayers of the fluorescent multilayer and (A3) a PPy crust covered with 5.5 bilayers of an insulating (PAA/PAH) multilayer followed by 3 bilayers of the fluorescent multilayer. (B) PPy NTs collected over a PET membrane in their native state (B1), or coated with either 12 bilayers of the fluorescent (PAA/PAH-FITC) multilayer (B2) or 12 bilayers of an insulating (PSS/PAH) multilayer followed by 6 bilayers of the fluorescent multilayer.

## S.I.6.3 Optimal ionic strength conditions for the assembly of a (HA/Col) multilayer on nanostructured PPy frameworks

In line with the conclusions drawn in Chapter 4 regarding the optimal conditions to trigger the self-assembly of Col and HA, their assembly on matrices of intersected PPy NTs was carried out at pH 4.0 either under low (i.e., UPW, $I = 10^{-4}$ M) or physiological ionic strength (i.e., NaCl 0.15 M, $I$ = 0.15 M). When deposited at high $I$ (Figure S6.3 a-b), the biomimetic multilayer was observed to coat the PPy NTs less homogeneously ; some parts of the network showing no visible presence of a soft polymer coating (Fig. S6.3 a), whereas other areas of the same sample displayed a granular adlayer gluing tubes together (Fig.S6.3 b). In contrast, coating the PPy matrices under low $I$ required fewer deposited bilayers (6 versus 12 bilayers in a 0.15 M NaCl environment) to give rise to a microscopically detectable soft polymer shell, smoothly covering all the NTs (Figure S6.3 c). The higher reliability of the self-assembly conducted under low $I$ contrasts with the previous observation that higher $I$ was needed ($I$ = 0.15 M) to drive the assembly of tubular multilayers inside porous templates displaying a nano-confined environment (*see* Chapter 4). However, it is perfectly in line with the conclusions drawn from QCM-D experiments where the assembly of Col and HA on flat substrates was evidenced to yield a thicker multilayer in the absence of salt (*see* Table 4.1, Chapter 4). The diffusion of biomacromolecules through the highly porous network of PPy NTs is more than probably eased compared to the situation of template nanopores and, as a result, the interaction of Col and HA and their subsequent adsorption under a rod-shaped conformation is enhanced in an environment with low charge-screening capacity. Nanostructured PPy frameworks thus display a similar regime of biopolymer-coating as quartz microcrystals due to their high porosity which lowers the diffusion barrier to macromolecules even when in an elongated state.

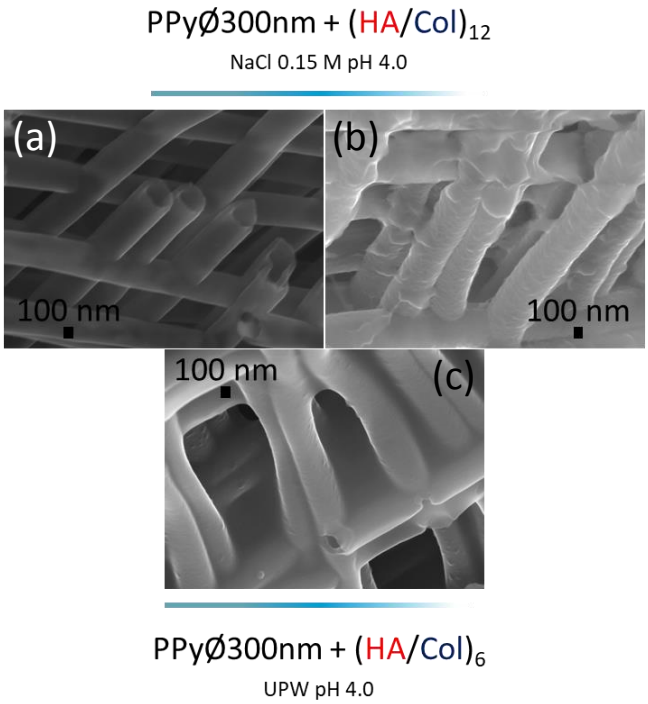


**Figure S6.3** *SEM images showing a side view of a PPy framework coated with (a & b) 12 bilayers of HA & Col assembled in 0.15 M NaCl pH 4.0 and (c) 6 bilayers of HA & Col assembled in UPW pH 4.0.*

## S.I.6.4 Aerial views of bare and biofunctionalized PPy frameworks

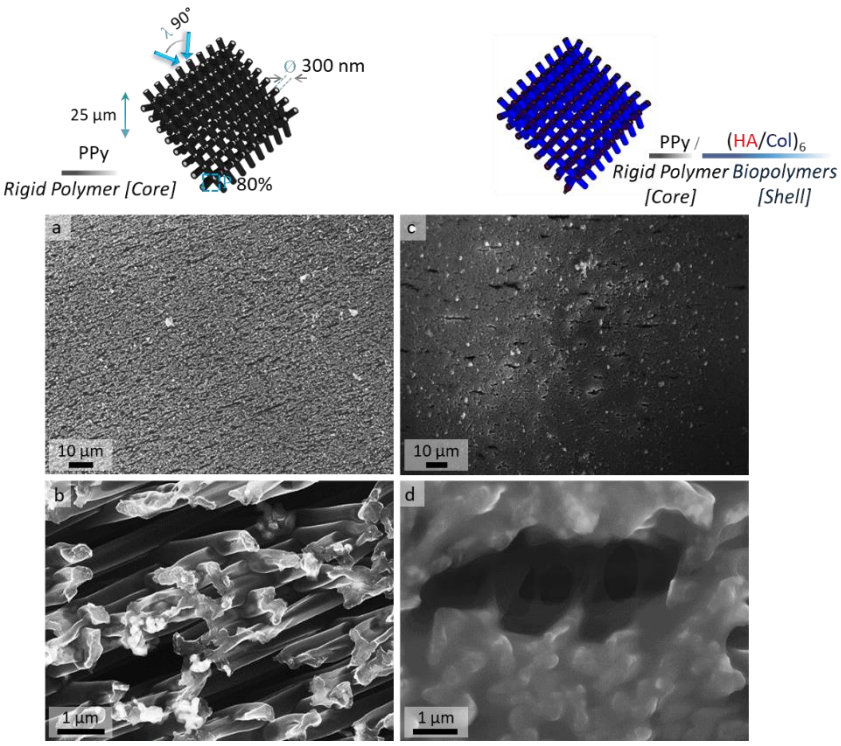


**Figure S6.4** *SEM images showing an aerial view of PPy frameworks (a & b) before biofunctionalization [a : low magnification and b : high magnification] and (c & d) after LbL deposition of 6 bilayers of HA & Col.*

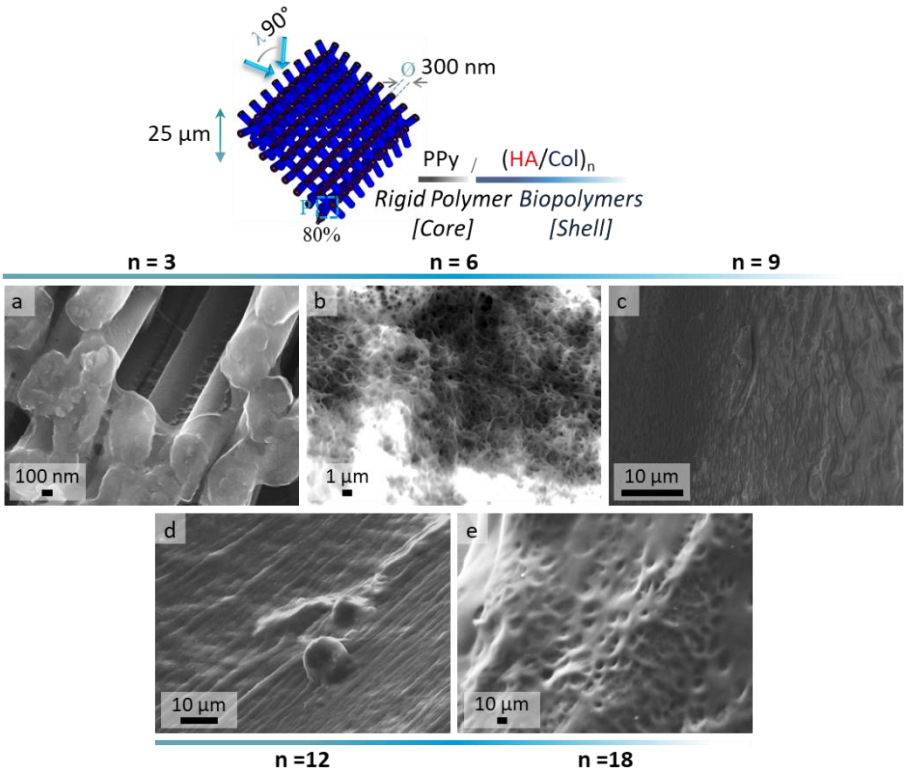


**Figure S6.5** *SEM images showing an aerial view of PPy frameworks after deposition of an increasing number of (HA/Col) bilayers : (a) after 3 bilayers, (b) 6 bilayers, (c) 9 bilayers, (d) 12 bilayers and (e) 18 bilayers. Different magnifications are purposely displayed to highlight the homogeneous coverage of the PPy NT networks with the biomimetic (HA/Col) multilayer.*

## S.I.6.5 Adhesion of MC3T3-E1 pre-osteoblast cells

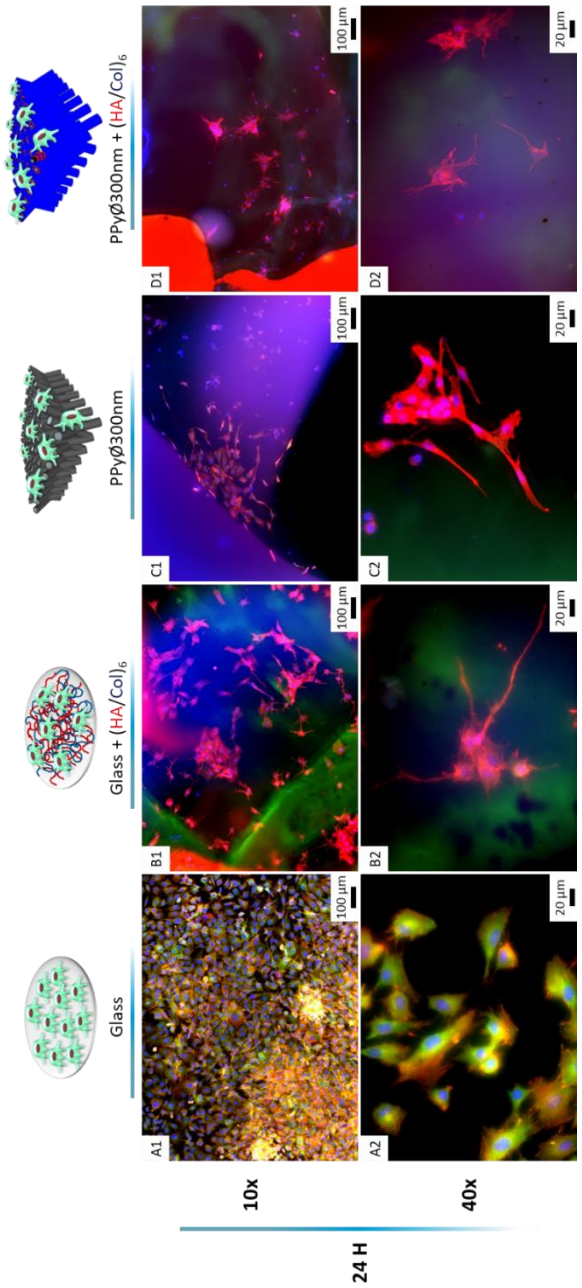


**Figure S6.6** *Epifluorescence microscopy images following immunostaining of MC3T3-E1 cells cultured for 1 day on (A) glass, (B) $(HA/Col)_6$-coated glass, (C) Bare PPy framework with 300-nm diameter NTs, and (D) $(HA/Col)_6$-coated PPy framework with 300-nm diameter NTs. Images are a combination of red (actin, cytoskeleton), green (vinculin, FA) and blue (DNA, nucleus) channels.*

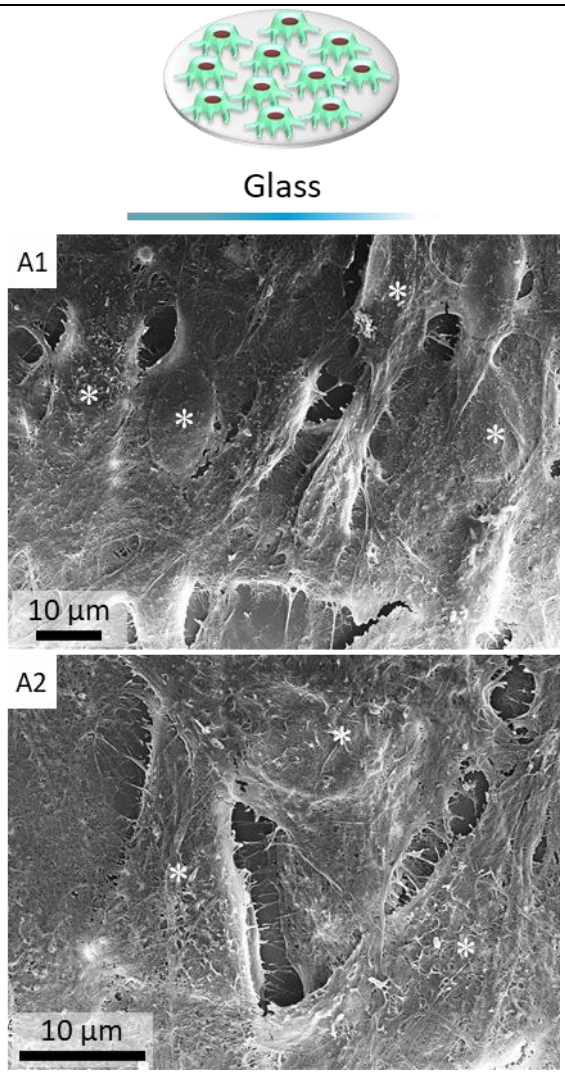


**Figure S6.7** *SEM images of cell-seeded biointerfaces after 6 days of culture in vitro (initial seeding density 60,000 cells per mL): cells (asterisk) adhering on (A 1-2) bare glass slide [positive control].*

## S.I.6.6 Negative control for cell adhesion tests : PTFE membranes

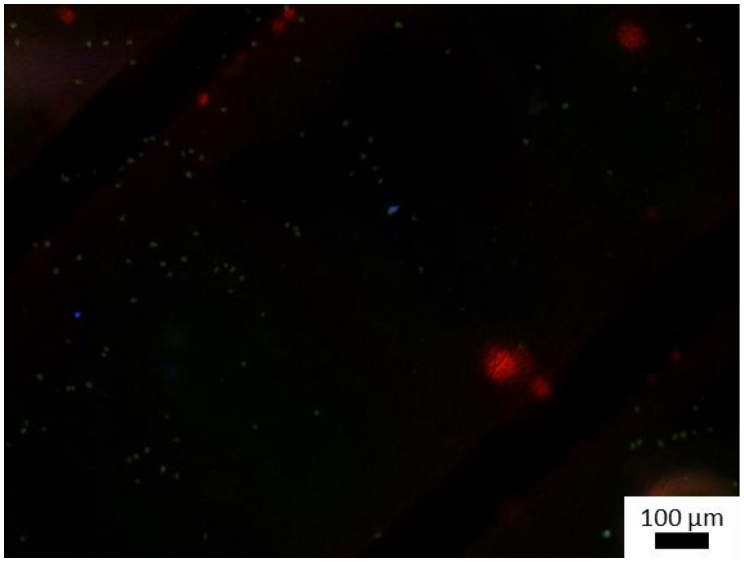


**Figure S6.8** *Epifluorescence microscopy image of immunostained MC3T3-E1 cells cultured for 3 days on PTFE membrane (negative control) [initial seeding density 100,000 cells.mL$^{-1}$]. The image is a combination of red (actin, cytoskeleton), green (vinculin, FA) and blue (DNA, nucleus) channels.*

## S.I.6.7 Evidence of a structural change of the biomimetic coating undergoing dehydration

Figure S6.9 evidences that the fibrillary network spotted on biofunctionalized samples has to be attributed to a structural change of the $(HA/Col)_6$ coating upon dehydration [serial immersion in ethanol solutions and hexamethyldisilazane, *see* Experimental section] rather than to a *de novo* synthesis of ECM by the seeded cells. Indeed, this fibrillary network is observed both on interfaces which did and did not contact cells, but only provided that they are functionalized with a biomimetic (HA/Col) coating and underwent a dehydration process (Figure S6.9 C1-2 & D1-2). In contrast, no fibrillary network could be observed on unmodified samples (Figure S6.9 A1-2) whereas (HA/Col)-coated systems which did not undergo the dehydration process displayed a biofunctionalizing multilayer with a typical highly hydrated, gel-like morphology (Fig. S6.9 B1-2).

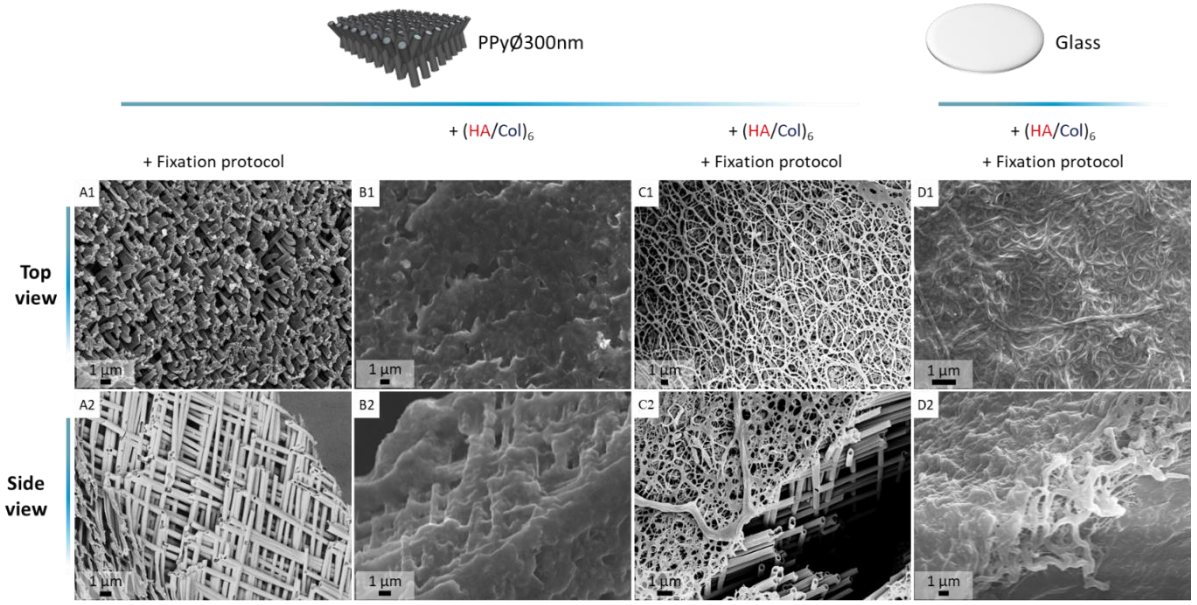


**Figure S6.9** *SEM images of (A-C) a bare network of intersected PPy NTs not contacted with cells and having undergone (A) a dehydration protocol [serial immersion in alcohol and hexamethyldisilazane; see Experimental section] (A1 : top view and A2 : side view) ; (B & C) assembly of the $(HA/Col)_6$ biofunctionalizing multilayer without consecutive dehydration (B) and after consecutive dehydration (C). (D) SEM images of a glass slide not contacted with cells and having undergone consecutively the assembly of the $(Col/HA)_6$ biomimetic multilayer and dehydration.*

## S.I.6.8 Soft statistical treatment of osteogenic differentiation data

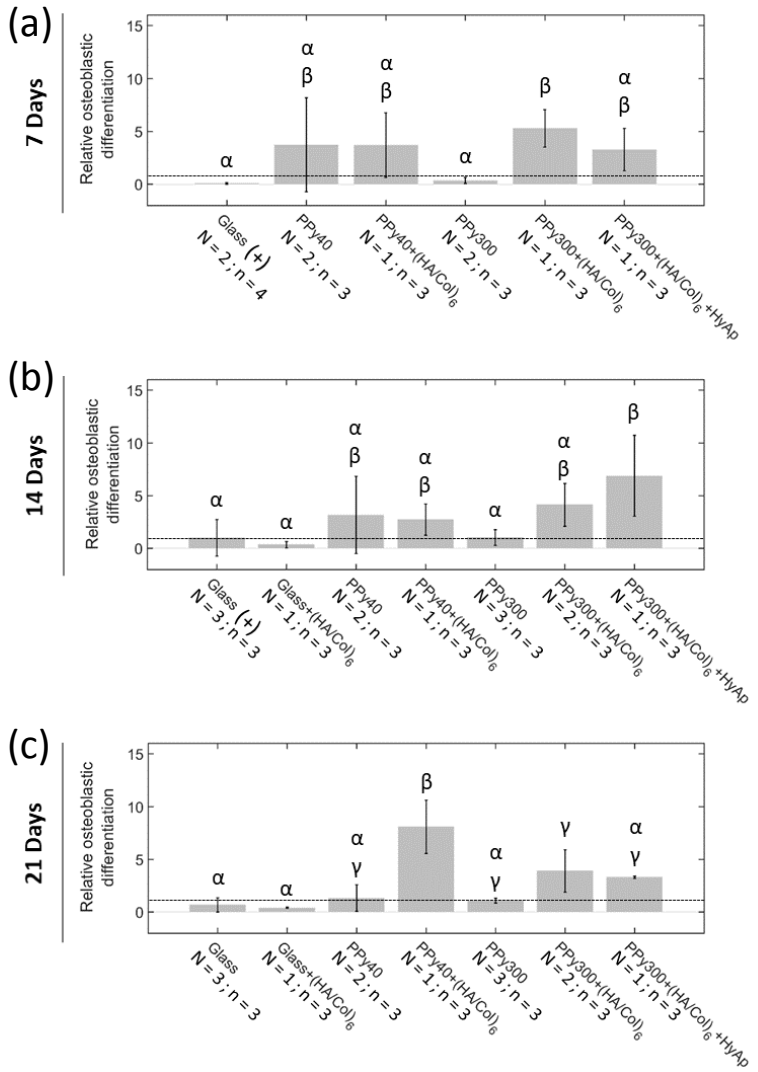


**Figure S6.10** *Relative osteoblastic differentiation (reference = bare glass at day 14) of cells cultured on the studied samples in the presence of osteogenic medium for (a) 7 days, (b) 14 days, and (c) 21 days. Error bars represent standard deviation. Bars topped with different Greek letters indicate statistical significance when ignoring unequal variances (p-value < 0.05 computed via consecutive ANOVA and Tukey HSD post hoc test). The black dotted line represents the value of the reference (i.e., bare glass at day 14).*

## 6.5 References

(1) Shah, S.; Solanki, A.; Lee, K. B. Nanotechnology-Based Approaches for Guiding Neural Regeneration. *Acc. Chem. Res.* **2016**, *49* (1), 17–26. https://doi.org/10.1021/acs.accounts.5b00345.

(2) Dalby, M. J.; Gadegaard, N.; Oreffo, R. O. C. Harnessing Nanotopography and Integrin-Matrix Interactions to Influence Stem Cell Fate. *Nat. Mater.* **2014**, *13* (6), 558–569. https://doi.org/10.1038/nmat3980.

(3) Mager, M. D.; LaPointe, V.; Stevens, M. M. Exploring and Exploiting Chemistry at the Cell Surface. *Nat. Chem.* **2011**, *3* (8), 582–589. https://doi.org/10.1038/nchem.1090.

(4) Liu, X.; Wang, S. Three-Dimensional Nano-Biointerface as a New Platform for Guiding Cell Fate. *Chem. Soc. Rev.* **2014**, *43* (8), 2385–2401. https://doi.org/10.1039/c3cs60419e.

(5) Chen, C. S.; Mrksich, M.; Huang, S.; Whitesides, G. M.; Ingber, D. E. Geometric Control of Cell Life and Death. *Science (80-. ).* **1997**, *276* (5317), 1425–1428. https://doi.org/10.1126/science.276.5317.1425.

(6) Yao, X.; Peng, R.; Ding, J. Cell – Material Interactions Revealed Via Material Techniques of Surface Patterning. *Adv. Mater.* **2013**, *25*, 5257–5286. https://doi.org/10.1002/adma.201301762.

(7) Engler, A. J.; Sen, S.; Sweeney, H. L.; Discher, D. E. Matrix Elasticity Directs Stem Cell Lineage Specification. *Cell* **2006**, *126*, 677–689. https://doi.org/10.1016/j.cell.2006.06.044.

(8) Fu, J.; Wang, Y. K.; Yang, M. T.; Desai, R. A.; Yu, X.; Liu, Z.; Chen, C. S. Mechanical Regulation of Cell Function with Geometrically Modulated Elastomeric Substrates. *Nat. Methods* **2010**, *7* (9), 733–736. https://doi.org/10.1038/nmeth.1487.

(9) Wen, J. H.; Vincent, L. G.; Fuhrmann, A.; Choi, Y. S.; Hribar, K. C.; Taylor-Weiner, H.; Chen, S.; Engler, A. J. Interplay of Matrix Stiffness and Protein Tethering in Stem Cell Differentiation. *Nat. Mater.* **2014**, *13* (10), 979–987. https://doi.org/10.1038/nmat4051.

(10) Yang, C.; Tibbitt, M. W.; Basta, L.; Anseth, K. S. Mechanical Memory and Dosing Influence Stem Cell Fate. *Nat. Mater.* **2014**, *13* (6), 645–652. https://doi.org/10.1038/nmat3889.

(11) Ma, P. X. Biomimetic Materials for Tissue Engineering. *Adv. Drug Deliv. Rev.* **2008**, *60* (2), 184–198. https://doi.org/10.1016/j.addr.2007.08.041.

(12) Gjorevski, N.; Sachs, N.; Manfrin, A.; Giger, S.; Bragina, M. E.; Ordonnez-Moran, P.; Clevers, H.; Lutolf, M. P. Designer Matrices for Intestinal Stem Cell and Organoid Culture. *Nature* **2016**, *539* (7630), 560–564. https://doi.org/10.1038/nature20168.

(13) Von Der Mark, K.; Park, J.; Bauer, S.; Schmuki, P. Nanoscale Engineering of Biomimetic Surfaces: Cues from the Extracellular Matrix. *Cell Tissue Res.* **2010**, *339* (1), 131–153. https://doi.org/10.1007/s00441-009-0896-5.

(14) Fernandes, H.; Moroni, L.; van Blitterswijk, C.; de Boer, J. Extracellular Matrix and Tissue Engineering Applications. *J. Mater. Chem.* **2009**, *19* (31), 5474. https://doi.org/10.1039/b822177d.

(15) Frantz, C.; Stewart, K. M.; Weaver, V. M. The Extracellular Matrix at a Glance. *J. Cell Sci.* **2010**, *123*, 4195–4200. https://doi.org/10.1242/jcs.023820.

(16) Schofer, M. D.; Boudriot, U.; Wack, C.; Leifeld, I.; Gräbedünkel, C.; Dersch, R.; Rudisile, M.; Wendorff, J. H.; Greiner, A.; Paletta, J. R. J.; et al. Influence of Nanofibers on the Growth and Osteogenic Differentiation of Stem Cells: A Comparison of Biological Collagen Nanofibers and Synthetic PLLA Fibers. *J. Mater. Sci. Mater. Med.* **2009**, *20* (3), 767–774. https://doi.org/10.1007/s10856-008-3634-8.

(17) Prabhakaran, M. P.; Venugopal, J.; Ramakrishna, S. Electrospun Nanostructured Scaffolds for Bone Tissue Engineering. *Acta Biomater.* **2009**, *5* (8), 2884–2893. https://doi.org/10.1016/j.actbio.2009.05.007.

(18) Walters, B. D.; Stegemann, J. P. Strategies for Directing the Structure and Function of Three-Dimensional Collagen Biomaterials across Length Scales. *Acta Biomater.* **2014**, *10* (4), 1488–1501. https://doi.org/10.1016/j.actbio.2013.08.038.

(19) Silva, J. M.; Reis, R. L.; Mano, J. F. Biomimetic Extracellular

Environment Based on Natural Origin Polyelectrolyte Multilayers. *Small* **2016**, *12* (32), 4308–4342. https://doi.org/10.1002/smll.201601355.

(20) Ren, K.; Crouzier, T.; Roy, C.; Picart, C. Polyelectrolyte Multilayer Films of Controlled Stiffness Modulate Myoblast Cell Differentiation. *Adv. Funct. Mater.* **2008**, *18* (9), 1378–1389. https://doi.org/10.1002/adfm.200701297.

(21) Picart, C. Polyelectrolyte Multilayer Films: From Physico-Chemical Properties to the Control of Cellular Processes. *Curr. Med. Chem.* **2008**, *15* (7), 685–697. https://doi.org/10.2174/092986708783885219.

(22) da Silva, E. E.; Della Colleta, H. H. M.; Ferlauto, A. S.; Moreira, R. L.; Resende, R. R.; Oliveira, S.; Kitten, G. T.; Lacerda, R. G.; Ladeira, L. O. Nanostructured 3-D Collagen/Nanotube Biocomposites for Future Bone Regeneration Scaffolds. *Nano Res.* **2009**, *2* (6), 462–473. https://doi.org/10.1007/s12274-009-9042-7.

(23) Hirata, E.; Uo, M.; Takita, H.; Akasaka, T.; Watari, F.; Yokoyama, A. Development of a 3D Collagen Scaffold Coated with Multiwalled Carbon Nanotubes. *J. Biomed. Mater. Res. - Part B Appl. Biomater.* **2009**, *90 B* (2), 629–634. https://doi.org/10.1002/jbm.b.31327.

(24) Park, J.; Bauer, S.; von der Mark, K.; Schmuki, P. Nanosize and Vitality: TiO2 Nanotube Diameter Directs Cell Fate. *Nano Lett.* **2007**, *7* (6), 1686–1691.

(25) Hirata, E.; Uo, M.; Takita, H.; Akasaka, T.; Watari, F.; Yokoyama, A. Multiwalled Carbon Nanotube-Coating of 3D Collagen Scaffolds for Bone Tissue Engineering. *Carbon N. Y.* **2011**, *49* (10), 3284–3291. https://doi.org/10.1016/j.carbon.2011.04.002.

(26) Rauber, M.; Alber, I.; Muöller, S.; Neumann, R.; Picht, O.; Roth, C.; Schoökel, A.; Toimil-Molares, M. E.; Ensinger, W. Highly-Ordered Supportless Three-Dimensional Nanowire Networks with Tunable Complexity and Interwire Connectivity for Device Integration. *Nano Lett.* **2011**, *11* (6), 2304–2310. https://doi.org/10.1021/nl2005516.

(27) Piraux, L.; Antohe, V.; Ferain, E.; Lahem, D. Self-Supported Three-Dimensionally Interconnected Polypyrrole Nanotubes and Nanowires for Highly Sensitive Chemiresistive Gas Sensing. *RSC Adv.* **2016**, *6*,

21808–21813. https://doi.org/10.1039/C6RA03439J.

(28) Cuenot, S.; Demoustier-Champagne, S.; Nysten, B. Elastic Modulus of Polypyrrole Nanotubes. *Phys. Rev. Lett.* **2000**, *85* (8), 1690–1693. https://doi.org/10.1103/PhysRevLett.85.1690.

(29) Guimard, N. K.; Gomez, N.; Schmidt, C. E. Conducting Polymers in Biomedical Engineering. *Prog. Polym. Sci.* **2007**, *32* (8–9), 876–921. https://doi.org/10.1016/j.progpolymsci.2007.05.012.

(30) Wei, Y.; Mo, X.; Zhang, P.; Li, Y.; Liao, J.; Li, Y.; Zhang, J.; Ning, C.; Wang, S.; Deng, X.; et al. Directing Stem Cell Differentiation via Electrochemical Reversible Switching between Nanotubes and Nanotips of Polypyrrole Array. *ACS Nano* **2017**, *11* (6), 5915–5924. https://doi.org/10.1021/acsnano.7b01661.

(31) Liu, X.; Yue, Z.; Higgins, M. J.; Wallace, G. G. Conducting Polymers with Immobilised Fibrillar Collagen for Enhanced Neural Interfacing. *Biomaterials* **2011**, *32* (30), 7309–7317. https://doi.org/10.1016/j.biomaterials.2011.06.047.

(32) Zeng, J.; Huang, Z.; Yin, G.; Qin, J.; Chen, X.; Gu, J. Fabrication of Conductive NGF-Conjugated Polypyrrole-Poly(l-Lactic Acid) Fibers and Their Effect on Neurite Outgrowth. *Colloids Surfaces B Biointerfaces* **2013**, *110*, 450–457. https://doi.org/10.1016/j.colsurfb.2013.05.012.

(33) Duchet, J.; Legras, R.; Demoustier-Champagne, S. Chemical Synthesis of Polypyrrole : Structure – Properties Relationship. *Synth. Met.* **1998**, No. 98, 113–122. https://doi.org/10.1016/S0379-6779(98)00180-5.

(34) Beckman, M. J.; Shields, K. J.; Diegelmann, R. F. Collagen. *Encyclopedia of Biomaterials and Biomedical Engineering*; Wnek, G. E., Bowlin, G. L., Eds.; New-York, 2004; pp 324–334. https://doi.org/10.1081/E-EBBE120007271.

(35) Piez, K. A. Collagen. *Encyclopedia of Polymer Sciences and Engineering*; Kroschwitz, J., 1985; pp 699–727.

(36) Emsley, J.; Knight, C. G.; Farndale, R. W.; Barnes, M. J.; Liddington, R. C. Structural Basis of Collagen Recognition by Integrin A2β1. *Cell* **2000**, *101* (1), 47–56. https://doi.org/10.1016/S0092-8674(00)80622-4.

(37) Mizuno, M.; Fujisawa, R.; Kuboki, Y. Type I Collagen-Induced Osteoblastic Differentiation of Bone-Marrow Cells Mediated by Collagen-A2β1 Integrin Interaction M. *J. Cell. Physiol.* **2000**, *184*, 207–

213.

(38) Mizuno, M.; Kuboki, Y. Osteoblast-Related Gene Expression of Bone Marrow Cells during the Osteoblastic Differentiation Induced by Type I Collagen. *J. Biochem* **2001**, *129* (1), 133–138.

(39) Nykvist, P.; Tu, H.; Ivaska, J.; Ka, J.; Pihlajaniemi, T. Distinct Recognition of Collagen Subtypes by A1β1 and A2β1 Integrins. *J. Biol. Chem.* **2000**, *275* (11), 8255–8261.

(40) Schiro, J. A.; Chan, B. M. C.; Roswit, W. T.; Kassner, P. D.; Pentland, A. P.; Hemler, M. E.; Eisen, A. Z.; Kupper, T. S. Integrin A2β1 (VLA-2) Mediates Reorganization and Contraction of Collagen Matrices by Human Cells. *Cell* **1991**, *67* (2), 403–410. https://doi.org/10.1016/0092-8674(91)90191-Z.

(41) Salasznyk, R. M.; Williams, W. A.; Boskey, A.; Batorsky, A.; Plopper, G. E. Adhesion to Vitronectin and Collagen I Promotes Osteogenic Differentiation of Human Mesenchymal Stem Cells. *J. Biomed. Biotechnol.* **2004**, *2004* (1), 24–34. https://doi.org/10.1155/S1110724304306017.

(42) Laurent, T. C.; Laurent, U. B.; Fraser, J. R. The Structure and Function of Hyaluronan: An Overview. *Immunol. Cell Biol.* **1996**, *74*, A1–A7. https://doi.org/10.1002/yea.

(43) Yoneda, M.; Shimizu, S.; Nishi, Y.; Yamagata, M.; Suzuki, S.; Kimata, K. Hyaluronic Acid-Dependent Change in the Extracellular Matrix of Mouse Dermal Fibroblasts That Is Conducive to Cell Proliferation. *J. Cell Sci.* **1988**, *90 ( Pt 2)*, 275–286.

(44) Nishida, T.; Nakamura, M.; Hiroshi, M.; Otori, T. Hyaluronan Stimulates Corneal Epithelial Migration. *Exp. Eye Res.* **1991**, *53* (6), 753–758.

(45) Turley, E. A.; Noble, P. W.; Bourguignon, L. Y. W. Signaling Properties of Hyaluronan Receptors. *J. Biol. Chem.* **2002**, *277* (7), 4589–4592. https://doi.org/10.1074/jbc.R100038200.

(46) Underhill, C. B.; Toole, B. P. Binding of Hyaluronate to the Surface of Cultured Cells. *J. Cell Biol.* **1979**, *82* (2), 475–484.

(47) Ao, H.; Xie, Y.; Tan, H.; Yang, S.; Li, K.; Wu, X.; Zheng, X.; Tang, T. Fabrication and in Vitro Evaluation of Stable Collagen/Hyaluronic Acid

Biomimetic Multilayer on Titanium Coatings. *J. R. Soc. Interface* **2013**, *10* (84), 20130070. https://doi.org/10.1098/rsif.2013.0070.

(48) Johansson, J. Å.; Halthur, T.; Herranen, M.; Söderberg, L.; Elofsson, U.; Hilborn, J. Build-up of Collagen and Hyaluronic Acid Polyelectrolyte Multilayers. *Biomacromolecules* **2005**, *6* (3), 1353–1359. https://doi.org/10.1021/bm0493741.

(49) Zhang, J.; Senger, B.; Vautier, D.; Picart, C.; Schaaf, P.; Voegel, J. C.; Lavalle, P. Natural Polyelectrolyte Films Based on Layer-by Layer Deposition of Collagen and Hyaluronic Acid. *Biomaterials* **2005**, *26* (16), 3353–3361. https://doi.org/10.1016/j.biomaterials.2004.08.019.

(50) Li, X.; Luo, Q.; Huang, Y.; Li, X.; Zhang, F.; Zhao, S. The Responses of Preosteoblasts to Collagen/Hyaluronic Acid Polyelectrolyte Multilayer Coating on Titanium. *Polym. Adv. Technol.* **2012**, *23* (4), 756–764. https://doi.org/10.1002/pat.1953.

(51) Anselme, K. Osteoblast Adhesion on Biomaterials. *Biomaterials* **2000**, *21* (7), 667–681. https://doi.org/10.1016/S0142-9612(99)00242-2.

(52) Landoulsi, J.; Demoustier-Champagne, S.; Dupont-Gillain, C. Self-Assembled Multilayers Based on Native or Denatured Collagen: Mechanism and Synthesis of Size-Controlled Nanotubes. *Soft Matter* **2011**, *7* (7), 3337. https://doi.org/10.1039/c0sm00918k.

(53) Dupont-Gillain, C. C. Understanding and Controlling Type I Collagen Adsorption and Assembly at Interfaces, and Application to Cell Engineering. *Colloids Surfaces B Biointerfaces* **2014**, *124*, 87–96. https://doi.org/10.1016/j.colsurfb.2014.08.029.

(54) Jiang, S.; Sun, Y.; Cui, X.; Huang, X.; He, Y.; Ji, S.; Shi, W.; Ge, D. Enhanced Drug Loading Capacity of Polypyrrole Nanowire Network for Controlled Drug Release. *Synth. Met.* **2013**, *163* (1), 19–23. https://doi.org/10.1016/j.synthmet.2012.12.010.

(55) Li, C.; Hsu, Y.; Hu, W. The Regulation of Osteogenesis Using Electroactive Polypyrrole Films. *Polymers (Basel).* **2016**, *8* (7), 1–12. https://doi.org/10.3390/polym8070258.

(56) Gilli, R.; Kacuráková, M.; Mathlouthi, M.; Navarini, L.; Paoletti, S. FTIR Studies of Sodium Hyaluronate and Its Oligomers in the Amorphous Solid Phase and in Aqueous Solution. *Carbohydr. Res.* **1994**, *263*, 315–

326. https://doi.org/10.1016/0008-6215(94)00147-2.

(57) Belbachir, K.; Noreen, R.; Gouspillou, G.; Petibois, C. Collagen Types Analysis and Differentiation by FTIR Spectroscopy. *Anal. Bioanal. Chem.* **2009**, *395* (3), 829–837. https://doi.org/10.1007/s00216-009-3019-y.

(58) Gandhi, M.; Spinks, G. M.; Burford, R. P.; Wallace, G. G. Film Substructure and Mechanical Properties of Electrochemically Prepared Polypyrrole. *Polymer (Guildf).* **1995**, *36* (25), 4761–4765. https://doi.org/10.1016/00323-8619(59)92912-.

(59) Sun, B.; Jones, J. J.; Burford, R. P.; Skyllas-Kazacos, M. Stability and Mechanical Properties of Electrochemically Prepared Conducting Polypyrrole Films. *J. Mater. Sci.* **1989**, *24* (11), 4024–4029. https://doi.org/10.1007/BF01168967.

(60) Wenger, M. P. E.; Bozec, L.; Horton, M. A.; Mesquidaz, P. Mechanical Properties of Collagen Fibrils. *Biophys. J.* **2007**, *93* (4), 1255–1263. https://doi.org/10.1529/biophysj.106.103192.

(61) Cuenot, S.; Alem, H.; Louarn, G.; Demoustier-Champagne, S.; Jonas, a. M. Mechanical Properties of Nanotubes of Polyelectrolyte Multilayers. *Eur. Phys. J. E* **2008**, *25* (4), 343–348. https://doi.org/10.1140/epje/i2007-10291-3.

(62) Richert, L.; Engler, A. J.; Discher, D. E.; Picart, C. Elasticity of Native and Cross-Linked Polyelectrolyte Multilayer Films. *Biomacromolecules* **2004**, *5* (5), 1908–1916. https://doi.org/10.1021/bm0498023.

(63) Yazid, M.; Ariffin, S.; Senafi, S.; Razak, M.; Wahab, R. Determination of the Differentiation Capacities of Murines' Primary Mononucleated Cells and MC3T3-E1 Cells. *Cancer Cell Int.* **2010**, *10* (1), 42. https://doi.org/10.1186/1475-2867-10-42.

(64) Wang, J.; de Boer, J.; de Groot, K. Proliferation and Differentiation of MC3T3-E1 Cells on Calcium Phosphate / Chitosan. *J. Dent. Res.* **2008**, *87* (7), 650–654.

(65) Gronowicz, G.; McCarthy, M. B. Response of Human Osteoblasts to Implant Materials: Integrin-Mediated Adhesion. *J Orthop Res* **1996**, *14* (6), 878–887. https://doi.org/10.1002/jor.1100140606.

(66) Wu, S.; Liu, X.; Yeung, K. W. K.; Liu, C.; Yang, X. Biomimetic Porous

Scaffolds for Bone Tissue Engineering. *Mater. Sci. Eng. R Reports* **2014**, *80* (1), 1–36. https://doi.org/10.1016/j.mser.2014.04.001.

(67) Choi, J.-Y.; Lee, B.-H.; Song, K.-B.; Park, R.-W.; Kim, I.-S.; Sohn, K.-Y.; Jo, J.-S.; Ryoo, H.-M. Expression Patterns of Bone-Related Proteins during Osteoblastic Differentiation in MC3T3-E1 Cells. *J. Cell. Biochem.* **1996**, *61* (4), 609–618. https://doi.org/10.1002/(SICI)1097-4644(19960616)61:4<609::AID-JCB15>3.0.CO;2-A.

(68) Zhang, Y.; Gong, H.; Sun, Y.; Huang, Y.; Fan, Y. Enhanced Osteogenic Differentiation of MC3T3-E1 Cells on Grid-Topographic Surface and Evidence for Involvement of YAP Mediator. *J. Biomed. Mater. Res. Part A* **2016**, *104* (5), 1143–1152. https://doi.org/10.1002/jbm.a.35648.

(69) Wang, D.; Christensen, K.; Chawla, K.; Xiao, G.; Krebsbach, P. H.; Franceschi, R. T. Isolation and Characterization of MC3T3-E1 Preosteoblast Subclones with Distinct In Vitro and In Vivo Differentiation/Mineralization Potential. *J. Bone Miner. Res.* **1999**, *14* (6), 893–903. https://doi.org/10.1359/jbmr.1999.14.6.893.

(70) Demoustier-Champagne, S.; Duchet, J.; Legras, R. Chemical and Electrochemical Synthesis of Polypyrrole Nanotubules. *Synth. Met.* **1999**, *101*, 20–21.

(71) Landoulsi, J.; Roy, C. J.; Dupont-Gillain, C.; Demoustier-Champagne, S. Synthesis of Collagen Nanotubes with Highly Regular Dimensions through Membrane-Templated Layer-by-Layer Assembly. *Biomacromolecules* **2009**, *10* (5), 1021–1024. https://doi.org/10.1021/bm900245h.

(72) Richert, L.; Boulmedais, F.; Lavalle, P.; Mutterer, J.; Ferreux, E.; Decher, G.; Schaaf, P.; Voegel, J.-C.; Picart, C. Improvement of Stability and Cell Adhesion Properties of Polyelectrolyte Multilayer Films by Chemical Cross-Linking. *Biomacromolecules* **2004**, *5* (2), 284–294. https://doi.org/10.1021/bm0342281.

# Chapter 7

# Conclusions and future prospects

This last chapter will summarize the main achievements obtained throughout this work as well as suggest new avenues of investigation.

In the first result-oriented chapter, ***Chapter 4,*** optimal conditions leading to the successful LbL assembly of two biomacromolecules, Col & HA, were identified. Assembly was shown to occur at pH 4.0, whether under low (UPW) or high ionic strength (NaCl 0.15 M) conditions, owing to the opposite polarity of the global charge carried by the two molecules in these conditions. Evidences were further raised regarding the substrate-dependence of the optimal conditions triggering this assembly. On flat substrates, a thicker film was obtained when assembling the biopolymers at low ionic strength whereas a higher ionic strength was required to initiate the construction within confined nano-environments (i.e., template nanopores). We hypothesized that the increased thickness deposited on flat substrates at low ionic strength is the result of a more sustainable LbL process under these conditions, the biomolecules interacting more strongly with each other and the substrate under low charge-screening conditions. Moreover, this increased interaction probably further reduces the tendency of the polymers to leave the surface in the form of soluble complexes. The need for higher charge-screening conditions to trigger the assembly within nanopores was attributed to the prevalence of the hydrodynamic radius as limiting factor for the diffusion of macromolecules along the nanopores. Based on this observation, biomimetic (Col/HA) NTs were reproducibly synthesized but were evidenced to lack the adequate mechanical properties to give rise to self-supported supramolecular architectures.

In order to confirm the conclusions drawn from **Chapter 4,** monitoring the assembly of the macromolecules under a broader range of ionic strength values both on flat substrates and within templates with different pore sizes would be of great interest.

Following the evident lack of mechanical stability of the matrices built using biopolymers, two strategies were developed with a view to impart increased mechanical properties while preserving bioactivity.

The first strategy, discussed in **Chapter 5,** consisted in adding ceramic nanoparticles to the LbL buildup so as to synthesize composite materials. After careful optimization of the assembly parameters (concentration of the colloidal phase, method of incorporation and location within the polymer multilayer), both individual and matrices of intersected composite NTs were successfully produced. Both mechanical (i.e., based on AFM nanoindentation tests) and morphological (i.e., based on visual observations) indices pointed out to the successful stiffening of the NTs, as the composite NTs were shown to display a less flexible morphology (evidenced by the lower data dispersion around the median value for morphological indices) and a significantly increased (~38 % higher) elastic modulus compared to native biopolymer NTs. Microscopic observations seem to indicate that a certain level of control is possible regarding the location of NPs incorporation within the polymer multilayer. Indeed, NTs with a soft outer layer were achieved when silica colloids were incorporated within the internal layers of the tubes whereas a rough external surface was evidenced when adding the particles to the external layers. However, no difference in the mechanical properties of the resulting constructs could be highlighted.

Cell culture investigations and, all the more biomedical applications are conditional on the availability of a easy-to-handle material. The synthesized nanocomposite interfaces are still too fragile to fall in that category, which has impeded their biological characterization in this work. Any method which would further improve the mechanical properties of the structures by addressing their brittleness and tendency to delaminate would be of high interest. Starting from the premise that, on one hand, the natural ECM mostly consists of a meshwork of intertwined proteins embedded within a highly viscoelastic gel of polysaccharides and that, on the other hand, the interconnected porosity of our engineered matrices is dispensable given that its size is too low for cells to penetrate it; we could think of embedding the interfaces within a biodegradable gel in an attempt to overcome their brittleness. The production of this gel would have to be strictly controlled so as to make sure it is restricted to the inner porosity of the matrices and does not mask the topography (i.e., extremities of the NTs) which would be left sticking out of the gel to interact with cells.

Even though the foreseen applications in tissue engineering and regenerative medicine might be out of reach at this point, the engineered

composite matrices still offer outstanding opportunities as multifunctionalizable nanostructured platforms bridging the gap between mechanical stability and preservation of the bioactivity of native biomacromolecules. The tremendously high specific surface area of these matrices, developed both at the microscale by the well-ordered array of intersected NTs they are made of and at the nanoscale, by the high amount of silica colloids contained in each tubular building block, could be taken advantage of in the following applications:

(i) Provided that the $SiO_2$ NPs are proven biocompatible, they could be pre-incubated with valuable drugs, so as to create complexes, before being integrated in the LbL assembly of the nanotube arrays which could then be used as implantable or skin-contacting drug-delivery platforms with a high exchange surface area.

(ii) Similarly, functionalizing the colloids with proteins known to bind a specific ligand with high affinity (i.e., enzymes, antibodies, etc.) and finding a way to translate the binding event into a detectable signal (e.g., an electrical signal) could lead to opportunities of using the synthesized frameworks as biosensing devices with high sensitivity. Such interfaces could also be used *in vitro* as highly sensitive membranes for immunoassays (e.g., ELISA, etc.).

(iii) The use of the composite nanostructures as nanocatalytic platforms enabling the high-throughput transformation of pollutants or the synthesis of products of high added value could also be considered, provided that the colloidal ceramic phase is adequately functionalized.

The second approach developed with a view to improve the mechanical properties of artificial matrices of intersected NTs was discussed in **Chapter 6** and involved the polymerization of a rigid framework of intersected PPy NTs which were further biofunctionalized with a biomimetic (HA/Col) multilayer. This strategy resulted in self-supported matrices displaying tunable features (i.e., average tube diameter, porosity and thickness). Two very different tube diameters (i.e., 40 and 300 nm) were investigated and both yielded self-supported PPy architectures. These interfaces were robust enough to be used for cell culture assays and were thus biologically characterized. Both bare and biofunctionalized systems of either tube

diameter were evidenced to be as cytocompatible as glass (a common positive control for cell culture). A preliminary differentiation test assayed the ability of the synthesized biointerfaces to influence the early events (i.e., ALP expression) of differentiation in murine pre-osteoblast cells and evidenced a general positive impact of the biointerfaces on cell differentiation. Indeed, most artificial matrices triggered a higher relative osteodifferentiation than glass (although not always statistically significant). In particular, ECM-like matrices with 300-nm diameter NTs coated with a $(HA/Col)_6$ biomimetic multilayer, those coated with a multilayer and further functionalized with HyAp and those with biofunctionalized 40-nm diameter NTs all significantly favored the advent of the early osteogenic differentiation phase in MC3T3-E1 cells (after a period of 7, 14 and 21 days, respectively). These results tend to highlight a synergistic effect of the biomimetic coating combined with the nanotopography, as all the best performing systems are actually coated and nanostructured. However, no distinctive effect of either the coating alone or the average diameter of the nanotopographical cues could be extracted.

The differentiation test presented in this work is a preliminary assay as it only involved the quantification of a single osteogenic marker. Hence, the collected results should be further corrected and refined through quantification of other differentiation markers (e.g., osteocalcin, osteopontin, bone sialoprotein, etc.). Furthermore, in addition to the quantification of the protein marker in itself, the relative quantities of the messenger RNAs specific to each of these proteins could be compared. In order to segregate the specific effect of interlinked parameters such as surface chemistry, mechanical properties and nanotopography, a set of differentiation tests should be carried out in parallel on several controls (e.g., surfaces with various tailored nanotopographies and constant elastic modulus, substrates of constant stiffness but varying chemistry,etc.). As the ALP activity is known to peak at the beginning of the osteogenic differentiation, it would be interesting to probe differentiation periods shorter than 7 days. In addition, more biologically-relevant controls should be added to the tests as a way to compare the performances of the ECM-like matrices designed in this work with those of commercially available products (e.g., matrigel®, demineralized bone matrix, etc.). Up to know, the biological relevancy of the biointerfaces were only assessed using murine

osteoprogenitor cells. It would be highly interesting to carry out a similar study with related cell types issued from another organism (e.g., osteoprogenitor cells of human origin) and multipotent cells (i.e., stem cells of human and/or murine origin).

Finally, even though tissue engineering applications of these ECM-like systems might still be years away from present day; more straightforward applications for such multifunctionalizable nanostructures of high surface area could be found in the fields of drug delivery, biosensing or nanocatalysis.